Sensing Using Fluorescent-Core Microcapillaries

by

Stephen Alexander Lane

A thesis submitted in partial fulfillment of the requirements for the degree of

Doctor of Philosophy

Department of Physics
University of Alberta

ABSTRACT

This thesis covers microfluidic sensing using whispering gallery modes supported in silica microcapillaries coated with a fluorescent film, hereby called fluorescent core microcapillaries (FCMs). We give an introduction to this class of device, and describe how it can be built and used effectively in microfluidic sensing. We then discuss the theory and experimental observations of these modes, including their shape, origin, wavelength, efficiency, and refractometric sensitivity. The thickness of the fluorescent film is a key factor in optimizing FCM-based detection, as is the polarization and order of the mode analyzed. Next, the effect of thermal fluctuations within a WGM is discussed. Film thickness, film composition, and analyte solvent play key roles in the thermal response of this device, and complete thermal stability is theoretically shown and approximately demonstrated. We developed a method for functionalization of the channel surface using a polyelectrolyte strategy, and subsequently demonstrate nanomolar detection of neutravidin. We conclude with a discussion of outstanding obstacles and potential avenues for further research. The appendix contains initial research on an organic lasing chromophore that may be a future component of the fluorescent film.

PREFACE

This thesis is an original work by me, Stephen Lane. Chapters 3 to 5 and Appendix A are slightly modified from published research. I am the main contributor to each paper and did most of the experimental work. Each co-author in the publications contributed to the experiment or analysis. In Chapter 3, Judy Chan helped with the experimental work, Torrey Thiessen implemented the data analysis algorithm, the peak-fitting and Q-factor analysis, and helped with experimental work. Al Meldrum laid out the WGM theory and the theoretical mode predictions. In Chapter 4, Yanyan Zhi and Al Meldrum developed the theoretical shift maps, and Al Meldrum and Frank Marsiglio developed the thermal equations and WGM theory. In Chapter 5, Peter West helped with the experimental work and data analysis algorithms. Alexander François helped with the functionalization and biochemistry implementation and Al Meldrum helped with the protein detection theory. In Appendix A, Sergei Vagin led the synthesis of the chromophore, with contributions from Wernor Heinz to both the synthesis and methods. Hui Wang assisted with the optics work, and led the work on the emissive films with contributions from Yina Zhao. William Morrish contributed to the chromaticity and data analysis. Bernard Rieger made enabling contributions to the project. My supervisor, Al Meldrum, contributed intellectually and to the writing and experimental concept of all publications.

Reaching to yon bookshelf to get Ye Flaske, you reveal in the dimness behind it, Ye Dustiy Tome. Intrigued, you lay it open and pore over the ancient script within. It is a chronicle by a cave-dwelling Mage of Light in his last moments of sanity. Although his runes be arcane, they use many of the human glyphs known to scholars like yourself. You turn the page and begin to read...

ACKNOWLEDGEMENTS

Thank you to Al, for being my supervisor and mentor for these past seven years, and not kicking me out for melting your furnace and writing bad. You taught me not only about physics, but also research, people, and life in general. You are truly a gentleman and a scholar.

Thank you to my family, for food, care packages, visits, phone calls, and peanut butter cups. Thank you, Mom and Dad, for your patient and gentle advice, for talking me back from the edge, and for the foundation you gave me to make this possible. Thank you, Theresa and Heather, for keeping me humble and cultured, and for being as intrinsically cool as you were a decade ago.

Thank you to Roshani, for your persistent love and kindness, for challenging me, and for being a partner in insanity.

Thank you to my colleagues and friends: William; Kirsty & Annika and the Wee Beasties; Hui; Rose; Ross; Torrey; Sergei; Kyle Reid; Kyle Foster; Lohrasp; Kerri; Roshan; and all the unlisted others, for years of entertaining and interesting conversations, for reminding me to sleep and eat, and for tolerating/encouraging my existential crises. It has been a pleasure.

Thank you to Jon and Mark for teaching me so much about chemistry, magnetism, curiosity, and being a scientist. Thank you also specifically for the support of ATUMS, and for sponsoring the TA bootcamp that allowed me to research post-secondary physics teaching.

Thank you to Mike, for taking me as a student despite my low marks. Your encouragement, enthusiasm, and patient guidance throughout the molybdenum research project is the reason I went to graduate school. You introduced me to real science.

Thank you to God, for such a difficult yet beautiful world and life, and for the beginning of knowledge.

Table of Contents

List of Tables **x**

List of Figures **xxiii**

1 Introduction **1**

1.1 Microfluidics 1

1.1.1 Label-based sensing 2

1.2 Optical label-free sensing platforms 4

1.2.1 Surface plasmon resonance sensors 4

1.2.2 Whispering-gallery-based sensors 8

1.3 Basic theory of WGMs 10

1.3.1 Mode classification 11

1.3.2 Theory of WGMs: basic equations 11

1.3.3 TE modes 16

1.3.4 The Bessel solutions 19

1.3.5 TM modes 23

1.3.6 Sensitivity and limit of detection 25

1.3.7 Fluorescent layer properties: SiQDs 27

1.3.8 Q-factor and loss mechanisms 28

1.3.9 Mode volume and the Purcell effect 30

1.3.10 Important parameters of WGM spectra 31

1.4 Types of WGM cavities 33

1.4.1 Fibers 33

1.4.2 Microspheres 34
1.4.3 Liquid-core optical ring resonators 36
1.4.4 Other types of WGM resonator structures 37
1.4.5 Fluorescent-core microcapillaries 37
1.5 FCM-based biosensing 38
1.5.1 Biomolecule detection 38
1.5.2 Surface functionalization methods 40
1.5.3 Building on functional groups 46
1.5.4 Assays 49
1.5.5 Interaction rates 55
1.6 Summary and subsequent chapters 58

2 Experimental **60**
2.1 FCM fabrication 60
2.2 Formation of silicon nanocrystal layers 61
2.3 Selecting microfluidic components 62
2.4 Mounting FCMs onto the microscope stage 63
2.5 Minimizing mechanical and thermal drift 65
2.6 Locating modes and spectrometer alignment 66
2.7 Solution pumping 67

3 Whispering gallery mode structure and refractometric sensitivity of fluorescent capillary-type sensors **69**
3.1 Abstract 69
3.2 Introduction 70
3.3 Materials and methods 72
3.4 Results and discussion 76
3.4.1 WGM field calculations 76
3.4.2 Comparison with experiment 83
3.5 Conclusions 89
3.6 Acknowledgements 90

4 Refractometric sensitivity and thermal stabilization of fluorescent core microcapillary sensors: theory and experiment 91
4.1 Abstract . . . 91
4.2 Introduction . . . 92
4.3 Experiment . . . 94
4.4 Theory . . . 95
4.5 Results and discussion . . . 103
4.6 Conclusions . . . 112
4.7 Acknowledgements . . . 113

5 Protein biosensing with fluorescent microcapillaries 114
5.1 Abstract . . . 114
5.2 Introduction . . . 115
5.3 Experimental . . . 117
5.4 Results and discussion . . . 121
5.5 Conclusions . . . 134
5.6 Acknowledgements . . . 135

6 Conclusions and outlook 136
6.1 Summary of contents . . . 136
6.2 Advances in FCM-based sensing . . . 138
6.3 Future work . . . 139

Bibliography 141

A Wide-gamut lasing from a single organic chromophore 183
A.1 Abstract . . . 183
A.2 Introduction . . . 184
A.3 Materials and methods . . . 186
A.3.1 Synthesis of Np-P4VB . . . 187
A.3.2 Preparation of dye solutions . . . 189
A.3.3 NMR spectroscopy and other analytics . . . 189

A.3.4 Preparation of emissive polyelectrolyte films 190
A.3.5 Absorption and photoluminescence spectroscopy 191
A.3.6 Photoluminescence dynamics 191
A.3.7 Absolute quantum yield 191
A.3.8 Lasing 192
A.4 Results and discussion 193
A.5 Acknowledgements 203
A.5.1 Conflict of interests 203
A.5.2 Contributions 204
A.6 Supplemental information 204

List of Tables

A.1 Summary of Np-P4VB absorption and emission properties. The first absorption peak in the green and yellow emission was overwhelmed by the nitrate absorption. 200

List of Figures

1.1 Example of surface plasmon resonance (SPR) excitation using the Kretschmann configuration. 5
1.2 Diagram of LSPR being stimulated. Republished with permission of Annual Reviews, from Ref. [1]; permission conveyed through Copyright Clearance Center, Inc. 7
1.3 Photograph of the Whispering Gallery walkway in St. Paul's Cathedral. Photo by photographer Grant Smith at www.grant-smith.com, reproduced here with permission. 9
1.4 Diagram of WGM path. The WGM ray traces a red line by repeatedly reflecting off the boundary (black line). Reprinted from Ref [2] under a Creative Commons License (CC-BY-4.0). 10
1.5 Simulated cross-sectional profile of TE-polarized cylindrical WGMs with radial orders $n = 1$ (a), $n = 2$ (b), $n = 3$ (c), and angular order $l = 15$. Electric field maxima and minima are represented as bright and dark, respectively. Simulation and image courtesy of A. Meldrum, reproduced here by permission. 11
1.6 Diagram illustrating the structure of a fluorescent-core micro-capillary. The inner channel has a radius of a, down from its original radius of b, caused by a fluorescent layer with thickness $b - a$. 21

1.7 Graph showing the normalized electric field magnitude across the three regions (channel, layer, and glass). This field is in a capillary with a 17.2 μm radius, a 600 nm film, and is for the $n = 1$, $l = 206$ WGM. 23
1.8 Diagram of spiral mode geometry. The difference in path length between the two rays causes constructive or destructive interference. 32
1.9 Diagram of a fluorescent-doped fiber supporting WGMs, excited using free-space illumination. Adapted from Ref. [3] and reprinted under a Creative Commons License (CC-BY-NC). . 34
1.10 Diagram of a crossed fibers; one carrying light to excite WGMs and the other supporting WGMs around its periphery. Reprinted with permission from Ref. [4], © 2000 IEEE. 35
1.11 Diagram of an LCORR structure. The path of the WGM is around the wall of the structure (not-to-scale), while here a DNA-based assay is performed in the microfluidic channel. Reprinted from Ref. [5], with permission from Elsevier. 36
1.12 Layer buildup on the inner surface of a LCORR. Here we see subsequent buildup of a crosslinker, a protein, an antibody, and a biomarker (the sensing target). Reprinted from Ref. [6] with permission from Elsevier. 39
1.13 Build-up of two polyelectrolytes (a polycation and polyanion) on a positively-charged substrate. 43
1.14 Graph of polyelectrolyte-based layer thickness using different salinity solutions. Reprinted from Ref. [7] by permission from Springer Nature Customer Service Centre GmbH. 44
1.15 Graph of polyelectrolyte-based layer thicknesses, indicating incomplete initial layer. Reproduced with permission of A. François from Ref. [8] 45

1.16 Schematic of the multi-tiered structure of the protein PCNA (proliferating cell nuclear antigen). In the primary structural level, amino acids abbreviated as "Val", "Lys", etc. are shown forming a chain. Reproduced under a Creative Commons License (https://creativecommons.org/licenses/by/4.0/legalcode) from Thomas Shafee at [9]. 47
1.17 Structure of an antibody showing the distinctive Y-shape and antigen-binding region. Image public domain, modified for this work. 48
1.18 Diagram of a direct ELISA, showing an analyte on a surface, with an antibody bound to it. An enzyme conjugated to the antibody causes a substrate in solution to change or emit colour. 51
1.19 Diagram of a sandwich ELISA, showing an antibody on a surface, and a successive chain of antigen, primary antibody, and secondary antibody stacked on top of it. A substrate in solution reacts with the enzyme. 52
1.20 Diagram showing a competition ELISA with (top) and without (bottom) analyte antibodies. Note that both enzyme-conjugated and unconjugated antibodies are present. In this diagram, the substrate is purple when reacted with the enzyme and this colour correlates inversely with the analyte concentration. . . . 54
1.21 Measurements of nonspecific adsorption on a functionalized fiber for given protein concentrations when unblocked versus using two varieties of BSA. Reprinted with permission from Ref. [10], © 2017 American Chemical Society. 55

2.1 Photograph of a capillary mounted over a microscope objective. A syringe pump dispenses analyte into PTFE tubing that feeds a microcapillary. 64

2.2 Diagram of the slit and capillary orientations. (A) shows a fluorescence image of the FCM, with purple and blue boxes indicating possible alignments for the spectrometer slit. Each box is labeled to show the dimension that will appear in the y-axis of the spectrometer output. (B) shows a spectral image of the WGMs taken in the perpendicular orientation (purple box). The x-axis is wavelength and the y-axis is the spatial coordinate across the radius of the capillary. (C) shows a spectral image taken in the parallel direction (blue box). The x-axis is wavelength and the y-axis is the spatial coordinate along the length of the capillary. 67

3.1 Cross sectional diagram of the FCM structure, which consists of a high-index fluorescent layer (m_2) coated onto the channel wall of a glass capillary (m_3). The analyte (m_1) flows within the channel. The electric field profile of a WGM resonance is represented schematically by the black line. 71

3.2 Diagram illustrating the experimental setup. 73

3.3 Electric field amplitude profile of a second-order mode ($n = 2$, $l = 195$, TE polarization) of a capillary with a radius of 15 μm and a film thickness of 0.8 μm. The coating is bounded by the vertical gray lines. This is an example of a low-Q mode ($Q = 430$), as evidenced by the large evanescent extension. . . 75

3.4 First-order mode profiles (angular mode number $l = 195$) for different film thicknesses, for a glass ($m_3 = 1.45$) capillary of inner radius 15 μm, with water in the channel ($m_1 = 1.33$). The coating thicknesses correspond to 0.2, 0.4, 0.6, 0.8, and 1.0 μm, and the refractive index is 1.67. The resonance wavelength for these modes is close to 770 nm. 77

3.5 Resonance wavelength, Q-factor, and sensitivity for the first-order $l = 165, 180$, and 195 WGMs, as a function of layer thickness. In the center plot, the $l = 180$ mode occurs between the other two, but is not labeled. Solid red lines indicate TE, and dashed blue lines indicate TM polarization. 79
3.6 Second-order mode profiles (angular mode number $l = 195$) for different film thicknesses, for a glass ($m_3 = 1.45$) capillary of inner radius 15 μm, with water in the channel. The coating thicknesses are 0.6, 0.8, and 1.0 μm and the refractive index is 1.67. The peak wavelength for these modes is close to 705 nm. For the 600 μm film, the Q-factor is only ~ 60. 80
3.7 A comparison of the resonance wavelength, Q-factor, and sensitivity for the first three radial orders ($l = 195$, TM polarization). 82
3.8 Resonance Q-factor for the first-order $l = 190$ WGM, as a function of absorbing layer thickness. The extinction coefficient steps in units of 0.0002. Solid red lines indicate TE, and dashed blue lines indicate TM polarization. The inset shows the Q-factor at saturation, as a function of extinction coefficient for a 2 μm thick coating. 83
3.9 Resonance Q-factor for the first-order $l = 190$ WGM, as a function of analyte absorption. Solid red lines indicate TE, and dashed blue lines indicate TM polarization. 84
3.10 Fluorescence spatial-spectral map (left) of a section of microcapillary and its corresponding TM spectrum. The inset shows finer mode structure in the thick region. The right side shows a fluorescence image of the capillary channel with the position scale approximately aligned to the spectral map. 84

3.11 TE (a) and TM (b) polarized fluorescence spectra for thin (black lines) and thick (green lines) films on the microcapillary, with water in the channel. Data is offset for clarity. The inset in (a) shows the experimental $l = 206$ TM mode for the thin film on the microcapillary fit with the modified skewed Lorentzian function (Eq. 3.6). The sidebar (c-f) illustrates the agreement between experiment (data points) and theory (line) for films with a thickness of 695 nm (thin) and 930 nm (thick). 85

3.12 The experimental $l = 206$ TM mode for different coating thicknesses. The data has been offset for clarity. The top inset shows the spectral map from which the measurements were taken, with the line profiles color-coded to match the main spectra. The WGM Q-factor appears to increase as the skew modes become increasingly well resolved for the thicker coatings. 87

3.13 Measured (blue) and calculated (red) sensitivities as a function of angular mode number, for FCMs with a thin (695 nm) or thick (930 nm) QD coating. Note the variation in the sensitivities of alternating angular modes that is especially apparent in the thin film TM case. The theoretical sensitivity closely matches the lower-sensitivity group of modes. In the other cases, this alternating behavior is not as clear, and but all the modes are more sensitive to changes in the core index than would be predicted by theory. Error bars were calculated from the uncertainty in the peak fitting procedure for each WGM. . 88

4.1 (a) Cross-sectional diagram of an FCM illustrating the channel analyte (refractive index m_1), the high-index fluorescent layer (index m_2), and the capillary wall (index m_3). The QD film thickness is given by $t = a - b$. The electric field of the WGM extends into the analyte region, as illustrated by the red shading and the white "wave" that represents the electric field profile of a resonance. (b) Diagram of the experimental setup. 93

4.2 Refractometric sensitivity maps (TM polarization, $n = 1$ radial modes) for a 15-μm-radius capillary with a QD coating of thickness t and index $m_2 = 1.67$, for ethylene glycol (left) and water (right) in the channel. The angular orders, $L = 190 - 200$, cover a wavelength range of $\sim$ 720-770 nm. TE maps were essentially similar but had slightly lower sensitivities. 104

4.3 Map of thermal shifts and detection limits for various film thicknesses, for an EG- or water-filled capillary. (a1) Thermal shift map for EG solvent. (a2) Thermal-fluctuation-limited detection limit for EG. The arrows point into the zero DL valley. (b1) and (b2) Same as above, except for a water solvent. 105

4.4 (a1), (b1) Thermal sensitivity and (a2), (b2) corresponding detection limit for thermal fluctuations of 1 K. The white arrows in (a2) and (b2) point toward the zero-DL valley. The top panels are for a 360-nm-thick QD film, and the bottom ones correspond to a 400 nm film. 107

4.5 (a) Spectral map of the modes in a section of the capillary, in which the WGMs appear as bright lines. The resonance wavelengths change along the capillary length, due to variations in the QD coating thickness. (b) Luminescence image showing a length of capillary. The color fluorescence image must be taken on a different setup in our laboratory, so although the capillary is the same one, the region shown in (b) does not necessarily correlate with the spectra in (a) or (c). (c) Typical mode spectrum, representing an intensity profile along a horizontal dashed line (thin) in (a). These structures have experimental Q-factors of $\sim$ 1500 and free spectral range of $\sim$ 3.2 nm, depending on the QD film thickness. 108

4.6 Wavelength shifts for different solvents in the capillary channel, relative to the case for air, for regions of the film, corresponding to lines labeled "thick" and "thin" in Fig. 4.5. The thin regions of the film have greater sensitivity, as do the TM-polarized modes, in agreement with theory. The inset shows a representative normalized WGM spectral peak for each solvent in the "TM thin" case. The solvents used were, in order, air, water, ethanol, and ethylene glycol from left to right. 109

4.7 Experimental WGM shifts with different solvents in the channel of an FCM (TM modes). The results for the thick film region are shown in panel (a), while a thin region is illustrated in (b). In the latter case, thermal stability was achieved with ethanol in the capillary channel. In some cases the error bars are smaller than the symbols. 110

5.1 Diagram of the capillary and the experimental setup. In the cross-sectional diagram of the capillary, the refractive indices m_1, m_2, and m_3 refer to the analyte, fluorescent layer, and capillary wall, respectively. Radius "b" is measured to the QD layer while "a" is the capillary's original inner radius (*i.e.*, prior to QD layer deposition). The white wave represents a WGM electric field profile. 118

5.2 Diagram of the polyelectrolyte surface functionalization for the biosensing experiments corresponding to steps 1-10 below. The NaOH-treated glass surface has a polyelectrolyte trilayer, with the final PAH layer capturing biotin. 120

5.3 (a) Fluorescence image of the capillary channel. The red glow is due to the QD emission. The representative slit direction (perpendicular to the channel) is diagrammed. (b) A typical WGM emission spectrum over the range from 760 to 780 nm. . 122

5.4 WGM wavelength shift as a function of NaOH etching time. As the QD film becomes thinner, the WGMs gradually blueshift. The upper-right inset shows sensorgrams for the water-to-ethanol transition at different etching times. The sensitivity of a single fluorescent microcavity observed at many different etching times is shown in the lower-left inset. 123

5.5 (a) Calculated 2D electric field amplitude for an $n = 1$, $l = 310$ TM mode for a 50-μm diameter capillary with 500-nm-thick QD film (marked by the black lines). Only part of the circumference is shown. (b) 1D intensity profile for the same conditions as in (a). The discontinuities in the field profile are due to the TM boundary conditions. The sensitivity of this structure is calculated from Eq. 5.4 to be 23.7 nm/RIU. 126

5.6 Sensorgram showing the deposition of alternating layers of PAH (red points) and PSS (yellow), followed by cleaning with 10 M NaOH solution (pink). Water is in blue, labeled a to e. The inset shows representative spectra corresponding to steps a and e. 127

5.7 Sensorgram showing the 13-step functionalization and biosensing experiment. The numbers label the steps according to the list given in Section 5.3. The key step is (12), corresponding to the specific binding of neutravidin. 129

5.8 (a) Sensorgram for control sample 1. The sequence is identical to that in Fig. 5.7, except that the neutravidin (step 12) had been pre-biotinylated before being pumped into the microcavity. The slight spread in data near the start of step 10 is likely caused by a bubble in solution. (b) Sensorgram for control sample 2. Here, there is a slight redshift (grey points, step 12), likely due to a small amount of electrostatic binding of neutravidin to the PAH layer. 130

5.9 Sensorgrams for neutravidin binding, for four different concentrations. These data show only step 12 of the reaction process; for each data set the capillary was cleaned with 10 M NaOH and steps 1-11 were performed prior to the running the neutravidin solution. The black lines are fits using first-order reaction kinetics (Eq. 5.10). The inset shows k_{obs} plotted against the neutravidin concentration, along with a linear fit. 132

A.1 Chemical structures of a) DSB (PPV), b) P2VB, and c) Np-P4VB. The key change between DSB and P2VB is the pyridine ring on each end. The difference between the P2VB and P4VB structures is the position of the nitrogen in the pyridine rings. The Np-P4VB synthesized here is similar to P4VB but with the addition of branched neopentyloxy groups on the central benzene ring. 186

A.2 Scheme showing the intermediate products during the synthesis of Np-P4VB. The products are numbered according to the step of the synthetic route. Step 4 shows the Wittig-Horner-type reaction which produces Np-P4VB. 189
A.3 Simplified diagram of the laser cavity setup. Cuvette #1 is placed in the tunable lasing cavity and is excited with 337-nm pulses from a nitrogen laser. The lasing output is directed through Cuvette #2 for further amplification before entering the spectroscopy system. 193
A.4 Crystals of Np-P4VB in transmitted light (left) and fluorescence (right). The scale bar is 100 μm. 194
A.5 Photograph of the Np-P4VB chromophore (2 mM) in solution taken under a black light (a) dissolved on cyclohexane (blue); (b) dissolved in DMF (teal); (c) dissolved in DMF with the addition of $Zn(NO_3)_2$ (green); (d) dissolved in DMF with the addition of $Hg(NO_3)_2$ (yellow); and (e) dissolved in acidified DMF (orange-red). 194
A.6 a) Normalized absorption spectra of 0.07 mM Np-P4VB in DMF containing various concentrations of $Zn(NO_3)_2$. The dashed line shows the absorption of a 500 mM $Zn(NO_3)_2$ solution in DMF. b) Absorption spectra of Np-P4V in DMF with various concentrations of HCl. 195
A.7 Absorption (dashed) and photoluminescence (solid) spectra of Np-P4VB in (a) cyclohexane, (b) pure DMF, (c) DMF with 500 mM $Zn(NO_3)_2$, (d) DMF saturated ($\sim$100 mM) with $Hg(NO_3)_2$, and (e) DMF with 500 mM HCl. The concentration of the chromophore for absorption measurements was 0.1 mM, while that for PL measurements was 2 mM (0.7 mM for cyclohexane). The insets show photographs of the luminescence corresponding to the spectrum for each panel. 197

A.8 (a) Lifetimes of pure, HCl (acid) doped, and $Zn(NO_3)_2$ doped solutions of Np-P4VB (3 mM). The small "blip" at $\sim$ 10 ns is a PMT afterpulse. (b) Output pulse power of various concentrations of Np-P4VB in DMF. (c) Threshold behavior of 2 mM solution of Np-P4VB in DMF when stimulated at 337 nm by an N_2 laser. The inset shows a double-slit interference pattern from the laser emission. Panels (d), (e), (f), and (g) show the Np-P4VB laser emission wavelengths for blue (0.7 mM Np-P4VB in cyclohexane) teal (2 mM Np-P4VB in DMF), green (2 mM Np-P4VB/DMF with 500 mM $Zn(NO_3)_2$), and red lasing (2 mM Np-P4VB/DMF with 0.1 M HCl) solutions. 199

A.9 (a) Lasing wavelengths for Np-P4VB in DMF achievable by tuning the laser cavity. The lasing intensity was normalized across the different groups for ease of visualization. (b) CIE 1931 chromaticity diagram showing the achievable color space from the Np-P4VB laser tuned optimally for 442 nm, 514 nm, and 695 nm, compared with the (Adobe) Wide Gamut RGB and the standard RGB color spaces. 201

A.10 Photograph (raw unprocessed data) of red-orange, yellow-green, teal, and white polyelectrolyte bilayer films containing dissolved Np-P4VB. A hand-held overhead blacklight was used for excitation. Corresponding PL spectra are shown in Fig. A.11. The wafers are 1 cm in diameter. 202

A.11 Normalized photoluminescence spectra of the teal, green-yellow, and orange polyelectrolyte films. 202

A.12 Compound 1: ^{1}H-NMR (300 MHz, $CDCl_3$, 300 K): δ (ppm) = 6.85 (s, 4H, Harom), 3.56 (s, 4H, -CH_2), 1.04 (s, 18H, -CH_3). Signals of solvent impurities ($CHCl_3$, H_2O) are marked with asterisk. 204

A.13 Compound 2: ^{1}H-NMR (300 MHz, $CDCl_3$, 300 K): δ (ppm) = 6.86 (s, 2H, Harom), 4.57 (s, 4H, -CH_2Br), 3.65 (s, 4H, -OCH_2), 1.11 (s, 18H, -CH_3). Signals of solvent impurities ($CHCl_3$, H_2O) are marked with asterisk. 205
A.14 Compound 3: ^{1}H-NMR (300 MHz, $CDCl_3$, 300 K): δ (ppm) = 6.95 (s, 2H, Harom), 4.09 – 3.96 (m, 8H, -OCH_2CH_3), 3.59 (s, 4H, -OCH_2), 3.26 (d, $^{2}J_{H-P}$ =20.3 Hz, 4H, -CH_2P), 1.25 (t, $^{3}J_{H-H}$ = 7.1 Hz, 12H, -OCH_2CH_3), 1.06 (s, 18H, -CH_3). Signals of solvent impurities ($CHCl_3$, H_2O) are marked with asterisk. . 205
A.15 Compound Np-P4VB: ^{1}H-NMR (300 MHz, CD_2Cl_2, 300 K): δ (ppm) = 8.55 (d, 3J = 6.2 Hz, 4H, $py - H_{ortho}$), 7.75 (d, ^{3}J = 16.5 Hz, 2H, inner vinylene H), 7.39 (d, ^{3}J = 6.2 Hz, 4H, py-H_{meta}), 7.17 (s, 2H, -CH_{arom}), 7.15 (d, ^{3}J = 16.5 Hz, 2H, outer vinylene H), 3.75 (s, 4H, -OCH_2), 1.15 (s, 18H, -CH_3). Signals of solvent impurities ($CHDCl_2$), H_2O) are marked with asterisk. 206
A.16 Compound Np-P4VB: ESI-MS (MeCN): 229 $[M+2H]^{2+}$, 457 $[M+H]^{+}$, 499 $[M+Na]^{+}$. 206

Chapter 1

Introduction

In this chapter we review some of the background of microfluidic biosensing and the transduction methods commonly applied in sensors based on whispering gallery modes. The main themes expand upon and elucidate the published chapters of this thesis.

1.1 Microfluidics

Microfluidics is the description of fluid-carrying and fluid-manipulating systems that are on the micrometer scale. Since the mid-1900s, miniaturization has been one of the key components for increasing measurement speed, accuracy, and accessibility. Hydraulic and pneumatic systems were long used for control in industrial machines, and the natural progression of this technology eventually led to micro-scale fluidic systems.

Microfluidics was at one point considered a method of control, signal transmission, and computation that could compete with nascent electronics [11] [12] [13] [14]. Ultimately, electronics won out due to immense speed and miniaturization advantages. However, microfluidic devices remained of immense interest for sensing and analytic purposes [15] [16]. Currently, microfluidics is often used in lab-on-a-chip applications, where fluidic channels allow sample control [17] and basic computation [18], and provide a miniature self-contained

platform for medical diagnostics [19] [20].

The fluidic element of microfluidics is what establishes its niche in sensing applications. In biology the vast majority of samples are processed in aqueous conditions because cells and viruses both generally need moisture to survive. In addition, many chemical samples are processed in aqueous flow or solution. The liquid state offers natural sample compatibility through solvation and a controllable flow and mixing platform.

Microfluidics works in the laminar flow regime. Flow is often described by the Reynolds number, approximated for incompressible fluids as

$$R = \frac{bv}{\nu} \tag{1.1}$$

where b is the tube diameter, v is the velocity, and ν is the fluid kinematic viscosity (the ratio of dynamic viscosity to density). The laminar-to-turbulent transition lies near a Reynolds number of 1000. For water, which has $\nu = 1$ $\frac{m^2}{s}$, flowing at 10 $\frac{m}{s}$ through a tube of 100 μm diameter, the Reynolds number is 0.001, placing it squarely in a viscosity-dominated non-turbulent regime. Much lower speeds common to microfluidics are even further into the laminar flow regime.

Microfluidics, which handles fluid volumes of the μL scale, offers the ability to analyze typical volumes of biological samples. For example, a standard blood glucose test uses 0.3 μL of sample. Single-well culture plates offer volumes ranging from 1 μL to 1 mL. Additionally, microfluidics as it is known today operates on a size scale readily compatible with optical microscopy. Finally, on smaller scales (*i.e.*, nanofluidics), biological analysis becomes difficult due to the size limit imposed by single cells, which have cross-sections on the order of μm and so would clog such devices.

1.1.1 Label-based sensing

Many sensors aimed at biological detection use a form of labeled sensing [21]. Here, a solution containing an analyte undergoes a chemical reaction where the

analyte molecules are bound or strongly associated with a detectable marker or label. The label chosen depends on the application – it could be a gold nanoparticle [22] [23], enzyme [24], engineered cell [25], fluorophore [26] [27] [28] [29], or radioisotope [30] [31] [32] [33]. Often the label is attached through a series of ligands, antibodies, antigens, and other biomolecules.

Many biological assays use a fluorescent label to identify the analyte. This type of labeling can be used in sandwich and direct enzyme-linked immunosorbent assays (ELISA), which will be discussed in Section 1.5.4. In the simplest implementation, fluorescent labels are attached to a target molecule, and a measurement of the fluorescence intensity is used as a proportional indication of the analyte present. More complex techniques can be used – a fluorescent dye might be injected into a cell or cell culture which then preferentially uptakes it into cells or organelles based on a certain biochemical condition being met. Förster energy transfer methods are commonly applied in fluorescent labeling schemes. Fluorescence lifetime, imaging, and spectroscopy techniques can be used to identify the labeled target.

While ubiquitous, label-based detection has some drawbacks. In some cases, it requires precise delivery of the label to a particular part of the sample, especially for in-cell detection or dye-based imaging. In others, attaching the label requires prior access to the analyte and the completion of a multi-step reaction. Many samples degrade over time and are unstable enough to prevent accurate labeling. Some may not tolerate labels, or may not have a reaction site that would attach specifically to a label. The number of fluorescent labels is far smaller than the number of possible analytes, and many combinations will not bind to each other. Thus, while fluorescent labeling techniques are well established, there is considerable interest in unlabeled analyses that do not require chemical modification of the analyte.

Microfluidic assays using label-based detection are widely used in the bioanalytic industry. Established protocols allow microfluidic sensing to be used to measure chemical binding rates, determine affinities of different biomolecules including proteins and enzymes, and measure the physical parameters of a

solution including temperature and refractive index. These protocols may be applied to modern detection platforms, including those utilizing optical sensors.

1.2 Optical label-free sensing platforms

The development of label-free sensors has been an important step in developing fast and widely-accessible assays [34]. These methods often involve the ability to detect an analyte directly on a sensor head. In many cases, the sensor head is pre-treated so that specific analytes will bind or accumulate on its surface. There are several modern technologies that offer the ability to perform label-free sensing optically. Here, we will focus on two of the most commonly applied research techniques: surface-plasmon-based sensing and sensing based on the whispering gallery modes of an optical cavity. Although this thesis does not involve surface plasmon resonances (SPR), there has been a considerable amount of work in which SPR is coupled to whispering gallery modes in order to enhanced sensing performance.

1.2.1 Surface plasmon resonance sensors

Surface plasmons are electromagnetic waves in the nearly-free surface electrons of a metal [35] [36]. This wave, which propagates along the surface of the metal, is polarized with its electric field normal to the metal surface. The resonant wavelength, λ_{SPP}, supported on the metal surface is a function of the dielectric constants of the metal and the adjacent medium according to the following equation [37]:

$$\lambda_{SPP} \approx \sqrt{\frac{\varepsilon_1'(\lambda_0) + \varepsilon_2(\lambda_0)}{\varepsilon_1'(\lambda_0)\varepsilon_2(\lambda_0)}}\lambda_0. \tag{1.2}$$

Here the dielectric constant of each region is given by $\varepsilon = \varepsilon' + i\varepsilon''$, with the metal defined by subscript 1 and the sample (with a real dielectric constant)

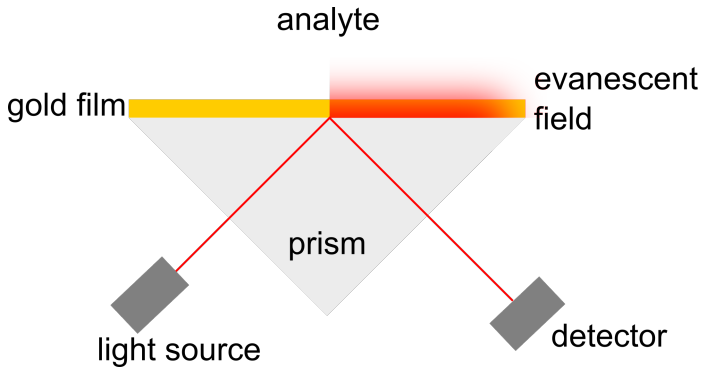

Figure 1.1: Example of surface plasmon resonance (SPR) excitation using the Kretschmann configuration.

defined by subscript 2. The wavelength of the light in a vacuum, is given by λ_0, as usual.

Gold is widely used because its surface plasmon resonance lies in the visible spectrum (*e.g.*, at around 700 nm for an interface with water [38]). Other metals featuring plasmons near the visible spectrum are copper ($\sim$ 700 nm) and silver ($\sim$ 650 nm) [38]. As the plasmon propagates, it has an evanescent component extending outward from the surface (Fig. 1.1). This evanescent component samples out to a distance of $\sim$ 500 nm into the sample near a wavelength of 600–700 nm [37].

There are several ways to interrogate the plasmon resonance in order to extract information about the interface properties. In general, light is introduced to the system, coupled into a surface plasmon wave, and the resulting changes in the properties of the reflected light are detected (Fig. 1.1). The degree to which light couples to the plasmon is affected by its wavelength and angle of incidence [39]. This degree of coupling can be measured by the intensity of the light reflected from the interface.

In angle-variance mode, for example, a constant-wavelength beam of light is swept through different incident angles while the reflectance from the metal surface is measured. Minimum reflectance indicates maximum coupling. The

angle at which this occurs is given by [40]:

$$\theta = sin^{-1}\left(\frac{1}{m_p}\sqrt{\frac{\varepsilon_1\varepsilon_2}{\varepsilon_1+\varepsilon_2}}\right), \tag{1.3}$$

where ε_1 and ε_2 are the dielectric constants of the metal and the sample, respectively, and m_p is the refractive index of the medium used to couple the light to the metal (*e.g.*, a prism in the configuration in Fig. 1.1). Eq. 1.3 can be used to extract the dielectric constant of the sample once θ has been measured. The alternative wavelength-variance measurement is accomplished by observing the wavelength associated with maximum coupling (*i.e.*, minimum reflectance) while holding the angle of the light source constant.

Because the surface of a metal film may be functionalized with a particular chemical group, SPR methods are capable of performing surface-based biosensing [41]. A plethora of tools, methods, and procedures exist for accomplishing this, particularly for gold, which employs the thiol-gold binding methodology [42]. A binding event will change the refractive index near the gold surface through the difference in polarizability between the solvent and the analyte [43]. Many of the chemistry challenges are similar to those of labeled assays except that the analyte requires no preparatory reaction.

SPR sensing technologies have been rapidly developed over the last two decades and are now considered the gold standard in label-free microfluidic sensing for proteins, vitamins, and antibodies. This method has also become commercially viable, and has even been implemented as a smart-phone extension utilizing the camera as a detector and the flash as a light source [44] [45].

Localized SPR (LSPR) is a phenomenon in nanoparticles that are much smaller than the wavelength of the incident light [1] [46] [47] (Fig. 1.2). Here, the plasmon is confined to the nanoparticle, rather than propagating along the surface of a film as for SPR. The LSPR resonance is affected by the size and shape of the nanoparticles, as well as the optical constants of the particle and its surroundings. LSPR can be measured by passing white light through

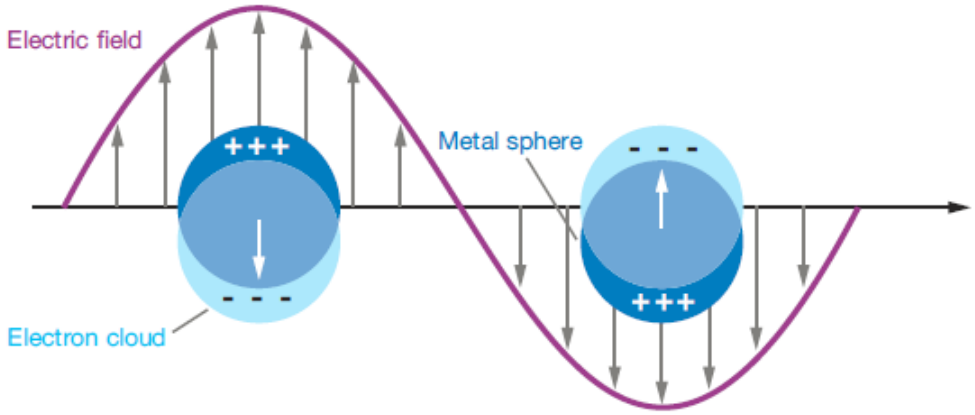

Figure 1.2: Diagram of LSPR being stimulated. Republished with permission of Annual Reviews, from Ref. [1]; permission conveyed through Copyright Clearance Center, Inc.

a suspension of nanoparticles and measuring the transmission spectrum. The extinction spectrum of these nanoparticles (the combination of absorption and scattering effects) is described by [1]

$$e(\lambda) = \frac{24\pi^2 a^3 \varepsilon_2^{3/2}(\lambda_0)}{ln(10)\lambda_0} \left[\frac{\varepsilon_1''(\lambda_0)}{(\varepsilon_1'(\lambda_0) + \chi\varepsilon_2)^2(\lambda_0) + \varepsilon_1''(\lambda_0)^2} \right], \tag{1.4}$$

where λ_0 is the wavelength, a is the radius of the particle, $\varepsilon_1(\lambda_0) = \varepsilon_1'(\lambda_0) + \varepsilon_1''(\lambda_0)$ is the dielectric function of the particle, and $\varepsilon_2(\lambda_0)$ is the dielectric function of the surrounding medium.

Excitation of the LSPR produces a strong electromagnetic field at the surface of the nanoparticle. The localized LSPR field is amplified by a factor of 10 to 100 compared to the incident field, and extends to a distance of ~ 20 nm from the surface of the particle [48] [49]. As a result of this field enhancement, the LSPR is exceptionally sensitive to changes in the surrounding dielectric. This makes the LSPR well-suited to detect surface-binding events such as biomolecule adsorption. Metal nanoparticles supporting LSPR can also be used to create individual electromagnetic hot-spots in optical resonators, increasing the sensitivity of the resonator at the location of the nanoparticle [50].

1.2.2 Whispering-gallery-based sensors

Named for a famous acoustic phenomenon found in the dome of St. Paul's Cathedral in London (Fig. 1.3), a whispering gallery transmits sounds waves efficiently by a series of reflections along the inside edge of an enclosed space. Although many geometries are possible, including polygons and ellipses, the most "effective" whispering galleries form a circular path (Fig. 1.4).

Similar to the acoustic case, optical whispering gallery modes (WGMs) can occur in transparent dielectric materials like raindrops or glass beads. WGMs can be described using a basic ray-optics approach. Light passing from a medium with refractive index (RI) of m_1 to another medium with an RI of m_2 less than m_1 will experience total internal reflection if the angle of incidence is sufficiently large. Repeated reflections can generate an optical standing wave when light travels an integer number of wavelengths around the circumference of a circular structure. Any change in the effective path length around the cavity will thus cause the resonant frequencies and wavelengths to shift. These changes can occur when the medium inside the whispering gallery undergoes a change in refractive index, or if the gallery itself changes in size. This leads to a transduction mechanism, where wavelength or frequency shifts in the WGM spectrum are used to measure changes in the properties of the cavity, including analytes passed through or around it.

There are several advantages to WGM-based sensing schemes. First, they can be designed to perform sensing in a localized fluid volume [51]. WGM cavities can have a diameter as small as a few microns, compared to a standard SPR sensor having dimensions of mm to cm. WGM-based sensors are sensitive; they have been used to show individual virus detection [52] and single-molecule binding events [53]. WGMs can also be used to perform detection through multiple methods simultaneously, for example by observing both the modal wavelength and the spectral shape of the mode. Finally, WGM-based devices can support lasing, which can improve the detection capability through better mode visibility and a high signal-to-noise ratio.

Figure 1.3: Photograph of the Whispering Gallery walkway in St. Paul's Cathedral. Photo by photographer Grant Smith at www.grant-smith.com, reproduced here with permission.

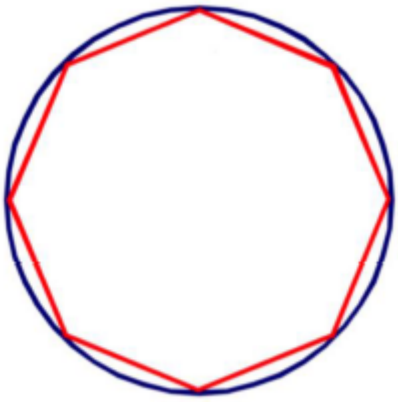

Figure 1.4: Diagram of WGM path. The WGM ray traces a red line by repeatedly reflecting off the boundary (black line). Reprinted from Ref [2] under a Creative Commons License (CC-BY-4.0).

However, there are also several drawbacks. Microcavity devices are often fabricated from glass and are surrounded by air or fluid in a sensing environment, making them fragile and difficult to handle. WGM-based sensors can also require expensive equipment such as a scanning laser or high-resolution optical spectrum analyzer in order to accurately measure the resonances. Finally, many WGM-based sensors are fairly involved to fabricate, in contrast to commercially available SPR designs [44] [45]. The sensors we examine in this thesis offer possible solutions to some of these drawbacks.

1.3 Basic theory of WGMs

In this section, the whispering gallery resonances of a cylindrical capillary-type structure, relevant to the main thesis work, are derived using standard and well-known methods. First, the mode classification scheme will be given. Then Maxwell's equations and the Helmholtz equation will be combined in cylindrical coordinates to give an equation that describes the resonances. Solutions based on Bessel functions will be used to yield expressions from which the mode parameters can be extracted. Finally, the terms used for spectral characterization of the modes will be explained.

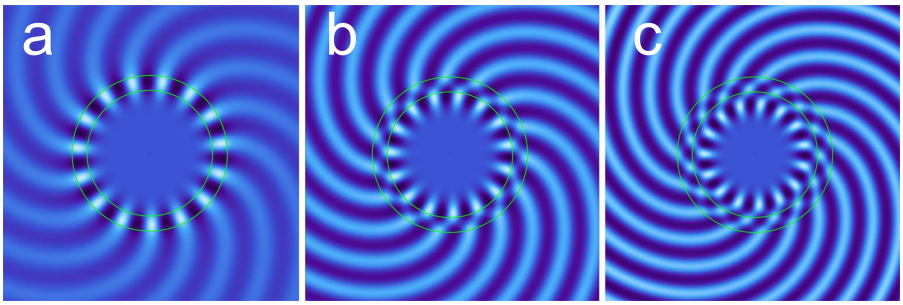

Figure 1.5: Simulated cross-sectional profile of TE-polarized cylindrical WGMs with radial orders $n = 1$ (a), $n = 2$ (b), $n = 3$ (c), and angular order $l = 15$. Electric field maxima and minima are represented as bright and dark, respectively. Simulation and image courtesy of A. Meldrum, reproduced here by permission.

1.3.1 Mode classification

Cylindrical WGMs are classified using three parameters: The radial mode number n is used to describe the number of intensity maxima in the radial direction (Fig. 1.5). The angular mode number l is used to describe the number of wavelengths that fit around the circumference of the whispering gallery (Fig. 1.5). Each mode can also have one of two polarizations, either transverse electric (TE) or transverse magnetic (TM). We define TE as the polarization where the electric field of the WGM is transverse to the plane of propagation (*i.e.*, it is parallel to the cylinder axis). Similarly, TM polarization implies that the magnetic field is transverse to the plane of propagation (E-field radial or tangential).

1.3.2 Theory of WGMs: basic equations

Cylindrical WGMs can be completely described by manipulating Maxwell's equations and Ohm's Law, given the wave equation and the appropriate boundary conditions. While these solutions have been well-known for nearly a century, they bear repeating here since the result provides a consistent mathematical description of the WGMs.

Maxwell's equations are

$$\nabla \cdot \mathbf{D} = \rho \tag{1.5}$$

$$\nabla \cdot \mathbf{B} = 0 \tag{1.6}$$

$$\nabla \times \mathbf{E} = -\frac{\partial \mathbf{B}}{\partial t} \tag{1.7}$$

$$\nabla \times \mathbf{H} = \frac{\partial \mathbf{D}}{\partial t} + \mathbf{J}, \tag{1.8}$$

where $\mathbf{E}$ is the electric field in free space, $\mathbf{D}$ is the electric field in a medium of dielectric constant ϵ, $\mathbf{B}$ is the magnetic flux density, ρ is the bound charge density, $\mathbf{J}$ is the displacement current, $\mathbf{H}$ is the magnetic field, and t is time. The field in the dielectric $\mathbf{D}$ is related to the field in free space $\mathbf{E}$ according to the formula

$$\mathbf{D} = \epsilon \mathbf{E} = \epsilon_o \epsilon_r \mathbf{E}. \tag{1.9}$$

Here the material dielectric constant ϵ is defined as the vacuum dielectric constant ϵ_o multiplied by the real relative dielectric constant of the material ϵ_r. A similar equation exists where the magnetic field inside a material, $\mathbf{B}$, is related to that outside, $\mathbf{H}$, according to the formula

$$\mathbf{H} = \frac{\mathbf{B}}{\mu}, \tag{1.10}$$

where μ is the magnetic permeability.

The Laplacian for cylindrical coordinates can be expanded as

$$\nabla^2 \mathbf{E} = \frac{1}{r}\frac{\partial}{\partial r}(r\frac{\partial \mathbf{E}}{\partial r}) + \frac{1}{r^2}\frac{\partial^2 \mathbf{E}}{\partial \phi^2} + \frac{\partial^2 \mathbf{E}}{\partial z^2}. \tag{1.11}$$

Meanwhile, we also have the relationship of Ohm's Law

$$\mathbf{J} = \sigma \mathbf{E}, \tag{1.12}$$

where σ is the conductivity of a substance supporting current $\mathbf{J}$ under electric field $\mathbf{E}$.

By operating on Eq. 1.7 we obtain

$$\begin{aligned} \nabla \times (\nabla \times \mathbf{E}) &= \nabla \times (\frac{-\partial \mathbf{B}}{\partial t}) \\ &= -\mu \frac{\partial}{\partial t}(\nabla \times \mathbf{H}) \\ &= -\mu \frac{\partial}{\partial t}(\mathbf{J} + \frac{\partial \mathbf{D}}{\partial t}) \\ &= -\mu \frac{\partial \mathbf{J}}{\partial t} - \frac{-\mu \partial^2 \mathbf{D}}{\partial t^2} \\ &= -\mu \frac{\sigma \partial \mathbf{E}}{\partial t} - \frac{-\mu \epsilon \partial^2 \mathbf{E}}{\partial t^2}. \end{aligned} \tag{1.13}$$

The identity

$$\nabla \times (\nabla \times \mathbf{E}) = \nabla(\nabla \cdot \mathbf{E}) - \nabla^2 \mathbf{E} \tag{1.14}$$

will shortly be used to change the form of the left-hand-side of Eq.1.13. For a structure with no free carriers the charge density is zero, which can be expressed as

$$\nabla \cdot \mathbf{D} = \rho = 0, \tag{1.15}$$

so the first term on the right hand side of Eq. 1.14 reduces to zero. Substituting Eqs. 1.13 and 1.15 into Eq. 1.14 yields

$$\nabla^2 \mathbf{E} = \mu \sigma \frac{\partial \mathbf{E}}{\partial t} + \mu \epsilon \frac{\partial^2 \mathbf{E}}{\partial t^2}. \tag{1.16}$$

For the magnetic field there is a similar relationship given by

$$\nabla \cdot \mathbf{H} = \nabla \cdot \frac{\mathbf{B}}{\mu}, \tag{1.17}$$

and

$$\nabla \cdot \mathbf{B} = 0. \tag{1.18}$$

Following similar steps as for the electric field

$$\begin{aligned} \nabla \times (\nabla \times \mathbf{H}) &= \nabla \times (\mathbf{J} + \frac{\partial \mathbf{D}}{\partial t}) \\ &= \nabla \times \sigma \mathbf{E} + \nabla \times \frac{\partial \mathbf{D}}{\partial t} \\ &= -\sigma \frac{\partial \mathbf{B}}{\partial t} + \nabla \times \frac{\partial \epsilon \mathbf{E}}{\partial t} \\ &= -\sigma \frac{\partial \mathbf{B}}{\partial t} + \epsilon \frac{\partial}{\partial t}(\nabla \times \mathbf{E}) \\ &= -\sigma \frac{\partial \mathbf{B}}{\partial t} + \epsilon \frac{\partial}{\partial t}(-\frac{\partial \mathbf{B}}{\partial t}) \\ &= -\sigma \frac{\partial \mathbf{B}}{\partial t} - \epsilon \frac{\partial^2 \mathbf{B}}{\partial t^2} \\ &= -\sigma \mu \frac{\partial \mathbf{H}}{\partial t} - \epsilon \mu \frac{\partial^2 \mathbf{H}}{\partial t^2}. \end{aligned} \tag{1.19}$$

We write the same mathematical identity as used for Eq. 1.14 for the magnetic field

$$\nabla \times \nabla \times \mathbf{H} = \nabla(\nabla \cdot \mathbf{H}) - \nabla^2 \mathbf{H}. \tag{1.20}$$

Substituting Eqs. 1.6 and 1.19 into Eq. 1.20 gives

$$-\nabla^2 \mathbf{H} = -\sigma \mu \frac{\partial \mathbf{H}}{\partial t} - \epsilon \mu \frac{\partial^2 \mathbf{H}}{\partial t^2}. \tag{1.21}$$

Eqs. 1.16 and 1.21 are in a form that can be used in the Laplacian for cylindrical coordinates (Eq. 1.11) in order to find solutions of the Helmholtz equation.

Here we note that the magnetic Reynolds number is given by the equation

$$R_m = LV\sigma\mu, \tag{1.22}$$

where L is length ($\sim 10^{-3}$ for large resonators), V is velocity (on the order of c, or 10^8), μ is the permeability (on the order of 10^{-7}), and σ is the conductivity (on the order of 10^{-6} for silica [54]), each in SI units. This gives a magnetic Reynolds number for a silica-based resonator on the order of 10^{-8}, or $R_m \ll 1$. Thus the term $\frac{\partial \mathbf{H}}{\partial t}$ is extremely small in Eq. 1.21.

We now return to the electric field, and assume a time-harmonic solution where ω is the frequency of the wave so that the electric field function becomes

$$\mathbf{E}(t, x, y, z) \Rightarrow \mathbf{E} = \mathbf{E}_o e^{-i\omega t}, \tag{1.23}$$

which has derivatives given by

$$\frac{\partial \mathbf{E}}{\partial t} = -i\omega \mathbf{E}_0 e^{-i\omega t} \tag{1.24}$$

and

$$\frac{\partial^2 \mathbf{E}}{\partial t^2} = -\omega^2 \mathbf{E}_0 e^{-i\omega t}. \tag{1.25}$$

Eqs 1.24 and 1.25 can be substituted into Eq. 1.16, giving

$$\nabla^2 \mathbf{E} = \left(-i\mu\sigma\omega\mathbf{E} - \omega^2\mu\epsilon\mathbf{E}_o\right) e^{-i\omega t}. \tag{1.26}$$

Simplifying this further yields

$$\begin{aligned} \nabla^2 \mathbf{E}_0 e^{-i\omega t} &= -i\omega\mu\sigma\mathbf{E}_o e^{-i\omega t} - \omega^2\mu\epsilon\mathbf{E}_0 e^{-i\omega t} \\ \nabla^2 \mathbf{E} &= -i\omega\mu\sigma\mathbf{E} - \omega^2\mu\epsilon\mathbf{E} \\ &= -\omega\mu(i\sigma + \omega\epsilon)\mathbf{E} \\ &= -\omega^2\epsilon\mu\left(\frac{\sigma}{\omega\epsilon}i + 1\right)\mathbf{E}. \end{aligned} \tag{1.27}$$

Since

$$c = \frac{1}{\sqrt{\mu\epsilon}}, \tag{1.28}$$

$$k = \frac{\omega}{c}, \tag{1.29}$$

where c is the speed of light in vacuum, the real (non-attenuative) part of the refractive index can be given as

$$m^2 = \frac{c^2 k^2}{\omega^2}, \tag{1.30}$$

where k is the wavevector and m is refractive index, Eq. 1.27 becomes

$$\nabla^2 \mathbf{E} + k^2 m^2 \mathbf{E} = 0. \tag{1.31}$$

Eq. 1.31 is the Helmholtz equation, which can be solved using separation of variables. We assume a separable function in terms of cylindrical coordinates:

$$\mathbf{E}(r, \theta, z) = R(r)\Phi(\phi)Z(z). \tag{1.32}$$

The solutions of the separable Helmholtz equation will describe the WGMs, provided we apply the correct polarization requirements and boundary conditions.

1.3.3 TE modes

We first choose the TE polarization. Accordingly, the electric and magnetic fields are defined by

$$E_r(R) = 0 \qquad H_r(R) \neq 0 \tag{1.33}$$

$$E_\phi(R) = 0 \qquad H_\phi(R) \neq 0 \tag{1.34}$$

$$E_z(R) \neq 0 \qquad H_z(R) = 0. \tag{1.35}$$

Here, Z indicates a direction along the cylinder axis, ϕ is the angular direction around the cylinder circumference, and r is along the radius. Thus the Laplacian (Eq. 1.11) becomes

$$\nabla^2 E_z = \frac{\partial^2 E_z}{\partial z^2} + \frac{1}{r^2}\frac{\partial^2 E_z}{\partial \phi^2} + \frac{1}{r}\frac{\partial}{\partial r}\left(r\frac{\partial E_z}{\partial r}\right). \tag{1.36}$$

One assumes a capillary that has angularly-constant refractive index, thus

$$E(r, \phi, z) = E_z e^{il\varphi}, \tag{1.37}$$

where φ is the phase change of a wave travelling around the circumference of a capillary, or "azimuthal phase change". The azimuthal boundary conditions require constructive interference, such that the net phase change of a wave having travelled one circumference in refractive index n_{eff} around a resonator with radius R is

$$\Delta\phi = 2\pi k_o n_{eff} R. \tag{1.38}$$

The phase of the wave must have changed by a multiple of 2π, thus

$$E(\phi) = E(\phi + 2\pi l), \tag{1.39}$$

which can be written as a cyclic boundary condition that is a modification of Eq. 1.37

$$\Rightarrow E(r, \phi, z) = E_z e^{il\phi}, \tag{1.40}$$

where l is an integer as defined previously. This is a no-loss approximation since it assumes that the field propagating azimuthally retains its initial amplitude. We now evaluate the Laplacian in Eq. 1.36 using the steady-state solution and the phase condition of constructive interference (Eq. 1.40). For the first term

we assume that there is no axial variation in the field, thus,

$$\frac{\partial^2 E_z}{\partial z^2} = 0. \tag{1.41}$$

For the second term in Eq. 1.36, we substitute our time-independent field solution (Eq. 1.40) to yield the result and subsequent simplification steps

$$\begin{aligned} \frac{1}{r^2}\frac{\partial^2 E_z}{\partial \phi^2} &= \frac{1}{r^2}\frac{\partial^2 E_z(r,\phi)e^{il\phi}}{\partial \phi^2} \\ &= \frac{1}{r^2}E_z(r)ilile^{il\phi} \\ &= -\frac{1}{r^2}E_z(r)l^2e^{il\phi} \\ &= -\frac{l^2}{r^2}E_z(r,\phi). \end{aligned} \tag{1.42}$$

Substituting the time-independent solution (Eq. 1.40) for the third term in Eq. 1.36, we find the result and performing subsequent simplifications yields

$$\begin{aligned} \frac{1}{r}\frac{\partial}{\partial r}\left(r\frac{\partial E_z}{\partial r}\right) &= \frac{1}{r}\frac{\partial}{\partial r}\left(re^{il\phi}\frac{\partial E_z}{\partial r}\right) \\ &= \frac{e^{il\phi}}{r}\frac{\partial}{\partial r}\left(r\frac{\partial E_z}{\partial r}\right) \\ &= \frac{e^{il\phi}}{r}\left[r\frac{\partial^2 E_z}{\partial r^2} + \frac{\partial E_z}{\partial r}\right] \\ &= \frac{1}{r}\left[r\frac{\partial^2 E_z(r,\phi)}{\partial r^2} + \frac{\partial E_z(r,\phi)}{\partial r}\right]. \end{aligned} \tag{1.43}$$

Substituting the results of Eqs 1.41, 1.42, and 1.43 back into 1.36 yields the expression

$$0 + -\frac{l^2}{r^2}E_z(r,\phi) + \frac{1}{r}\left[r\frac{\partial^2 E_z(r,\phi)}{\partial r^2} + \frac{\partial E_z(r,\phi)}{\partial r}\right] + k_0^2 m^2 E_z = 0, \tag{1.44}$$

where we use k_0 to denote a constant wavevector of a particular cavity resonance rather than the variable k. By separation of variables we obtain

$$k_0^2 m^2 - \frac{l^2}{r^2}E_z(r,\phi) + \frac{\partial^2 E_z(r,\phi)}{\partial r^2} + \frac{1}{r}\frac{\partial E_z}{\partial r} = 0. \tag{1.45}$$

Multiplying through by r^2 gives

$$e^{il\phi}\left[(k_0^2 r^2 m^2 + l^2)E_z(r) + r^2\frac{\partial^2 E_z(r)}{\partial r^2} + r\frac{\partial E_z}{\partial r}\right] = 0. \tag{1.46}$$

Making the substitution $R = mkr \Rightarrow dR = mkdr$, and assuming the refractive index and wavevector are radially invariant yields

$$e^{il\phi}\left[(R^2 - l^2)E_z(R) + R^2\frac{\partial E_z(R)}{\partial R^2} + R\frac{\partial E_z}{\partial R}\right] = 0. \tag{1.47}$$

The solutions to this equation will be time-independent electromagnetic waves in the cylindrical resonator, *i.e.*, the whispering gallery modes.

1.3.4 The Bessel solutions

Bessel's equation is

$$(x^2 - p^2)y + \frac{x^2 d^2 y}{dx^2} + x\frac{dy}{dx} = 0, \tag{1.48}$$

which matches the form of Eq. 1.47 with the substitutions

$$x = R, \tag{1.49}$$

$$p = l, \tag{1.50}$$

and

$$y = E_z(R). \tag{1.51}$$

The solutions to Bessel's equation are known and given by the functions

$$y(R) = AJ_p(R) \tag{1.52}$$

and

$$y(R) = BY_p(R), \tag{1.53}$$

where J_p and Y_p are Bessel functions of the first and second kinds, respectively, of integer order p. The coordinate R denotes the radial position in a polar coordinate system. The terms A and B are arbitrary scaling constants.

Equation 1.48 is also satisfied by Bessel functions of the third kind (the Hankel functions) [55] [56]. These are complex linear combinations of the Bessel functions of the first and second kinds, expressed as

$$H_l^{(1)}(R) = A_1 J_l(R) + A_2 i Y_l(R) \tag{1.54}$$

$$H_l^{(2)}(R) = B_1 J_l(R) - B_2 i Y_l(R). \tag{1.55}$$

Here we have written the Bessel functions in terms of order l, as defined before.

We now take the specific case of the fluorescent-core microcapillary (FCM). The FCM is a thick-walled glass tube with inner radius b, a fluorescent layer of thickness $t = b - a$, and an outer radius a (Fig. 1.6). Each region (*i.e.* the channel, fluorescent layer, or glass) has a different refractive index m_r, making the refractive index of the device m_r a piecewise function:

$$m(r) = \begin{array}{ll} m_1 & r < a \\ m_2 & a < r \leq b \\ m_3 & r > b \end{array} \tag{1.56}$$

where the channel, layer, and glass are labeled as regions 1, 2, and 3 respectively (Fig 1.6). The refractive index m_2 must be higher than that of the glass wall m_3 in order to support total internal reflection at that interface.

As a result, the electric field $E_z(R)$ will also be piecewise defined by functions that satisfy Eq. 1.47. In region 2, the outgoing and incoming waves are described by the Hankel functions of the first and second kind, respectively [55]. The Bessel function of the second kind has a singularity at $r = 0$, so the

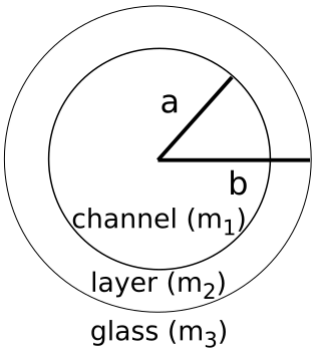

Figure 1.6: Diagram illustrating the structure of a fluorescent-core microcapillary. The inner channel has a radius of a, down from its original radius of b, caused by a fluorescent layer with thickness $b - a$.

Bessel function of the first kind is chosen for this region in order to avoid unphysical results. In region 3, we consider only the outward-propagating fields for a thick-walled cylinder, so we use the Hankel function of the first kind. The solutions for the fields can thus be written:

$$\begin{cases} A_l J_l(m_1 k_0 r) & r \leq a \\ B_l H_l^{(2)}(m_2 k_0 r) + C_l H_l^{(1)}(m_2 k_0 r) & a < r \leq b \\ D_l H_l^{(1)}(m_3 k_0 r) & r > b, \end{cases} \tag{1.57}$$

where the constants (A_l, B_l, C_l, and D_l) are arbitrary scaling factors that will be related to each other through the boundary conditions.

Across the boundaries between regions 1, 2, and 3, the electric field E_z and its derivative must be continuous for the TE polarization [55]. By setting the solutions (Eq. 1.57) equal to each other at the boundaries $r = a$ and $r = b$, we obtain

$$A_l J_l(m_l k_0 a) = B_l H_l^{(2)}(m_2 k_0 a) + H_l^{(1)}(m_2 k_0 a) \tag{1.58}$$

and

$$B_l H_l^{(2)}(m_2 k_0 b) + H_l^{(1)}(m_2 k_0 b) = D_l H_l^{(1)}(m_3 k_0 b). \tag{1.59}$$

Similarly, by setting the derivatives of the solutions (Eq. 1.57) equal to each other at the boundaries $r = a$ and $r = b$, we obtain

$$m_1 A_l J_l'(m_l k_0 a) = m_2 B_l H_l^{(2)\prime}(m_2 k_0 a) + m_2 H_l^{(1)\prime}(m_2 k_0 a) \tag{1.60}$$

and

$$m_2 B_l H_l^{(2)\prime}(m_2 k_0 b) + m_2 H_l^{(1)\prime}(m_2 k_0 b) = m_3 D_l H_l^{(1)\prime}(m_3 k_0 b), \tag{1.61}$$

where the J' and H' denote the derivatives of the Bessel and Hankel functions with respect to the position coordinate r.

At the boundary $r = b$ one can write

$$\frac{m_3 H_l^{(1)\prime}(m_3 k_0 b)}{H_l^{(1)}(m_3 k_0 b)} = \frac{m_2 B_l H_l^{(2)\prime}(m_2 k_0 a) + m_2 H_l^{(1)\prime}(m_2 k_0 a)}{B_l H_l^{(2)}(m_2 k_0 b) + H_l^{(1)}(m_2 k_0 b)}, \tag{1.62}$$

while at boundary $r = a$ we have the expression

$$\frac{A_l J_l(m_1 k_0 a)}{m_1 A_l J_l'(m_1 k_0 a)} = \frac{B_l H_l^{(2)}(m_2 k_0 a) + H_l^{(1)}(m_2 k_0 a)}{m_2 B_l H_l^{(2)\prime}(m_2 k_0 a) + m_2 H_l^{(1)\prime}(m_2 k_0 a)}. \tag{1.63}$$

Eq. 1.63 can be rearranged to give an expression for B_l, which can then be substituted back into Eq. 1.62.

The resulting expression can be solved numerically via rootfinding algorithms. The solutions for a given angular order l, refractive indices (m_1, m_2, m_3), and capillary size parameters (a, b) yield wavevectors k_0 of a whispering gallery resonance. Multiple solutions exist for each set of parameters, and are differentiated according to the WGM radial order n. An example radial profile of a TE WGM (using Eq. 1.57) is shown in Fig. 1.7.

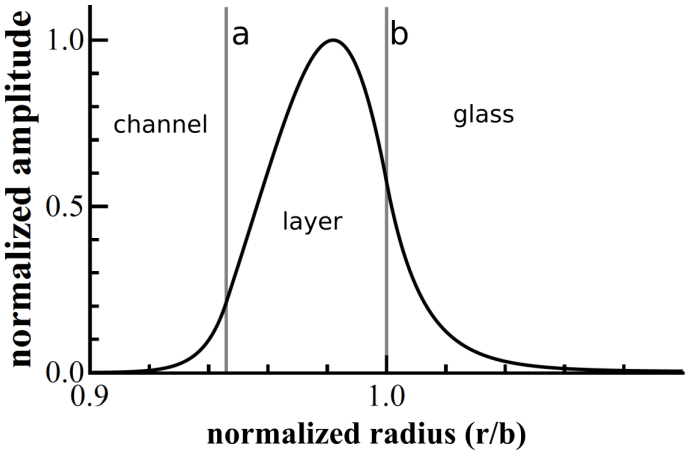

Figure 1.7: Graph showing the normalized electric field magnitude across the three regions (channel, layer, and glass). This field is in a capillary with a 17.2 μm radius, a 600 nm film, and is for the $n = 1$, $l = 206$ WGM.

1.3.5 TM modes

A similar procedure can be applied in order to find the TM modes, which have electric and magnetic fields given by

$$E_r(R) \neq 0 \qquad H_r(R) = 0 \tag{1.64}$$

$$E_\phi(R) \neq 0 \qquad H_\phi(R) = 0 \tag{1.65}$$

$$E_z(R) = 0 \qquad H_z(R) \neq 0. \tag{1.66}$$

Applying the Helmholtz equation (Eq. 1.31), we find

$$\nabla^2 H_z(r,\phi) + k_0^2 m^2 H_z(r,\phi) = 0, \tag{1.67}$$

which, as for the TE case, can be solved via the Bessel and Hankel functions using the same process outlined in Section 1.3.3 [55]. The solutions to the

wave equations in the different regions are given in this case by [55]

$$
\begin{cases}
E_l J_l(m_1 k_0 r) & r \leq a \\
F_l H_l^{(2)}(m_2 k_0 r) + G_l H_l^{(1)}(m_2 k_0 r) & a < r \leq b \\
I_l H_l^{(1)}(m_3 k_0 r) & r > b,
\end{cases} \tag{1.68}
$$

where E_l, F_l, G_l, and I_l are proportionality constants and J_l and H_l are the Bessel functions of the first- and third-kinds with order l, as before.

The first boundary condition for the TM solution is that H_z must be continuous across the boundaries at a and b, yielding

$$E_l J_l(m_l k_0 a) = F_l H_l^{(2)}(m_2 k_0 a) + G_l H_l^{(1)}(m_2 k_0 a) \tag{1.69}$$

and

$$F_l H_l^{(2)}(m_2 k_0 b) + G_l H_l^{(1)}(m_2 k_0 b) = I_l H_l^{(1)}(m_3 k_0 b). \tag{1.70}$$

The second boundary condition for the TM field is that the derivative of the field has discontinuities across the boundaries $r = a$ and $r = b$ according to [55] [57]:

$$\frac{1}{m_1} E_l J_l'(m_l k_0 a) = \frac{1}{m_2} F_l H_l^{(2)\prime}(m_2 k_0 a) + \frac{1}{m_2} G_l H_l^{(1)\prime}(m_2 k_0 a) \tag{1.71}$$

and

$$\frac{1}{m_2} F_l H_l^{(2)\prime}(m_2 k_0 b) + \frac{1}{m_2} G_l H_l^{(1)\prime}(m_2 k_0 b) = \frac{1}{m_3} I_l H_l^{(1)\prime}(m_3 k_0 b). \tag{1.72}$$

These equations can be simplified as for the TE case, yielding [55]

$$\frac{m_2 H_l^{(1)\prime}(m_3 k_0 a)}{m_3 H_l^{(1)}(m_3 k_0 a)} = \frac{F_l H_l^{(2)\prime}(m_2 k_0 a) + H_l^{(1)\prime}(m_2 k_0 a)}{F_l H_l^{(2)}(m_2 k_0 a) + H_l^{(1)}(m_2 k_0 a)} \tag{1.73}$$

and

$$F_l = \frac{-m_1 J_l(m_1 k_0 b) H_l^{(1)\prime}(m_2 k_0 b) + m_2 J_l'(m_1 k_0 b) H_l^{(1)}(m_2 k_0 b)}{m_1 J_l(m_1 k_0 b) H_l^{(2)\prime}(m_2 k_0 b) - m_2 J_l'(m_1 k_0 b) H_l^{(2)}(m_2 k_0 b)}. \tag{1.74}$$

As with Eqs. 1.62 and 1.63, one can use a numerical root finder to determine the mode wavevectors k_0 from Eqs. 1.71 and 1.72.

1.3.6 Sensitivity and limit of detection

The refractometric sensitivity is defined as the magnitude of the shift of the WGM wavelength for a given change in refractive index experienced by the mode field. For FCMs, the changing refractive index is that inside the channel (region 1). Thus, the refractometric sensitivity for the FCM can be written as

$$S = \frac{\partial \lambda}{\partial m_1}, \tag{1.75}$$

where λ is the WGM resonant wavelength and m_1 is the channel refractive index.

In order to predict the sensitivity of a mode, we will first find an expression for λ. We approximate a resonant wavelength as

$$\lambda = \frac{2\pi b m_{eff}}{l}, \tag{1.76}$$

where b is the inner radius of the capillary wall (Fig. 1.6), l is the angular order of the WGM, and m_{eff} is the refractive index of the resonator, given by

$$m_{eff} = I_1 m_1 + I_2 m_2 + I_3 m_3. \tag{1.77}$$

Here I_1, I_2, and I_3 are the fractions of the WGM field intensity in each region, and m_1, m_2, and m_3 are the refractive indices defined as before (Fig. 1.6). Once the wavevector, k_0, of a mode has been found, the electric field amplitude (or intensity) profiles can be obtained from Eq. 1.57. One can then write Eq.

1.76 in terms of the effective index in Eq. 1.77:

$$\lambda = \frac{2\pi b}{l}(I_1 m_1 + I_2 m_2 + I_3 m_3). \tag{1.78}$$

The analyte RI, m_1, is the quantity changing during a measurement. Thus, the sensitivity $\partial\lambda/\partial m_1$ (Eq. 1.75) can be written by differentiating Eq. 1.78 with respect to m_1. We assume that the intensity profiles I are functions of the refractive index of the channel m_1.

$$\frac{\partial\lambda}{\partial m_1} = \frac{2\pi b}{l}\left(I_1 + \frac{\partial I_2 m_2}{\partial m_1} + \frac{\partial I_3 m_3}{\partial m_1}\right), \tag{1.79}$$

If we assume that the changes in I_2 and I_3 due to changes in m_1 are small [58], Eq. 1.79 simplifies to

$$\frac{\partial\lambda}{\partial m_1} = \frac{2\pi b}{l} I_1. \tag{1.80}$$

We rearrange Eq. 1.76 to solve for angular order l, giving $l = \frac{2\pi b m_{eff}}{\lambda}$, which we substitute in Eq. 1.80 to find a final expression for the FCM sensitivity:

$$S = \frac{\partial\lambda}{\partial m_1} = \frac{\lambda I_1}{m_{eff}}, \tag{1.81}$$

Eq. 1.81 estimates the wavelength shift response of a WGM to refractometric changes in the analyte. Higher sensitivities are, obviously, better.

The limit of detection (LoD), that is the smallest detectable change in the analyte index, depends on the sensitivity S and the smallest measurable WGM shift $\Delta\lambda_{min}$. $\Delta\lambda_{min}$ is defined to be three standard deviations (3σ) of the measured wavelength shift when m_1 is not changing (*i.e.*, 3σ of the noise). The LoD is given by [59]:

$$LoD = \frac{\Delta\lambda_{min}}{S}. \tag{1.82}$$

Thus, a low limit of detection requires low noise in the WGM peak position

(small $\Delta\lambda_{min}$) and a high sensitivity.

1.3.7 Fluorescent layer properties: SiQDs

The inner surface of the FCM channel is coated in a fluorescent layer (region 2). In this work, region 2 is composed of silicon quantum dots (SiQDs) embedded in an oxide matrix. This material was chosen because it is biocompatible, photochemically and physically stable, and resists bleaching. In addition, a method for coating the channel with a SiQD layer was recently established in our lab [60] [61]. A review of SiQDs and their use in other biosensing platforms may be found in Ref. [62].

SiQDs have been extensively investigated before [63] [64] [65] [66] [60]. While their properties are not the main topic of this work, a brief overview is provided here. Oxide-embedded SiNCs exhibit a size- [63] and surface-dependent [67] [68] fluorescence spectrum centered between 650-950 nm. They have a quantum efficiency up to 5% [69] [70], a PL lifetime on the order of tens of microseconds [71] [72], and they are absorbing in the blue and UV parts of the spectrum. The SiQDs in this work have diameters of 3.4 ± 0.7 nm [64].

SiQDs have several advantages over fluorescent dyes. First, they are relatively photostable and thermally stable and do not bleach or thermally decompose like many dyes [73]. This makes them suitable for long-term measurements and gives them a good storage life. Second, quantum dots tend to be less sensitive to their environment than fluorescent molecules [73]. Many fluorescent markers change their emission properties depending on solvent polarity, viscosity, and the presence of other molecules or surfactants. Finally, quantum dots are less prone to aggregation-based quenching [73].

There are several advantages to using silicon-based quantum dots in particular. First, silica and SiQDs are biocompatible, showing low cytotoxicity and high pH-stability [74] [75] [76]. This contrasts with the relatively high toxicity of other quantum dots including cadmium selenide [77], cadmium telluride, and other III-V and IV-VI semiconductor quantum dots [78] [79]. Second, the

silica matrix encapsulates the SiQDs, stabilizing and protecting the quantum dots from the solvents flowing through the capillary. Notable exceptions are hydrofluoric acid and strong bases like potassium and sodium hydroxides [80] [81], which dissolve the silica matrix.

The fluorescent layer using silica and SiQDs has been measured by ellipsometry to have a refractive index of ~ 1.67 [61]. However, this measurement is not specific to the layer inside the FCM, but is for a similar layer deposited on a wafer via spin-coating. Moreover, the indices of the SiQDs are higher than the index of the surrounding oxide so the estimated refractive index used in simulations and calculations is both an approximation and an average.

1.3.8 Q-factor and loss mechanisms

The Q-factor of an optical resonator is a measure of how efficiently it stores electromagnetic energy. It is defined as

$$Q = 2\pi \frac{E_{stored}}{E_{lost\,per\,cycle}} \tag{1.83}$$

A high Q-factor corresponds to a resonator with low loss per cycle. However, this definition of the Q-factor does not lend itself easily to experimental measurement [58]. In the high-Q limit, the Q-factor becomes [82]:

$$Q = \frac{f_0}{\delta f} = \frac{\lambda_0}{\delta \lambda}, \tag{1.84}$$

where f_0 is the resonant frequency, δf is the spectral width, λ_0 is the resonant wavelength, and $\delta\lambda$ is the spectral width. These parameters are easily measured.

Several processes affect the energy lost from the resonator. The most important ones with respect to FCMs will be briefly discussed. Reflection at the curved inner wall leads to an outward-radiating wave. This resulting radiation loss is larger for more strongly curved surfaces (*i.e.*, smaller cylinder radius) [83] [55]. The limiting Q-factor, Q_{rad}, can be determined from Eqs. 1.62 and

1.63 via [71]:

$$Q_{rad} = \frac{Re[k_0]}{2Im[k_0]}. \tag{1.85}$$

In FCMs of diameters ranging from 30–50 μm, Q_{rad} ranges from 10^6–10^9.

Loss also occurs in FCMs through absorption in the SiQD film. The extinction coefficient has been measured for a flat SiQD film to be $\kappa \approx 6 \times 10^{-4}$ at 800 nm [84], with the resulting loss coefficient $\alpha_{abs} = \frac{4\pi\kappa}{\lambda_0}$ where λ_0 is the wavelength, κ is the extinction coefficient, and c is the speed of light [85]. The Q-factor in the loss-limited (*i.e.*, not radiation-limited) regime is estimated by [71] [86]:

$$Q_{abs} \approx \frac{2\pi m_{eff}}{\lambda_0 \alpha_{sca}}, \tag{1.86}$$

which for a wavelength of 800 nm and a m_{eff} of 1.67 gives a value of $\alpha_{sca} \approx 94$ cm^{-1}, giving $Q_{abs} \approx 1300$. Alternatively, the imaginary part of the refractive index, κ, can be included in Eqs 1.62 and 1.63 to find a complex wavevector k_0. This complex wavevector can be used in Eq. 1.85 to find the total Q-factor, *i.e.*, a combination of Q_{rad} and Q_{abs}. If Q_{rad} is known for the non-absorbing structure (*e.g.*, via Eq. 1.85), Q_{abs} can then be determined. Using this numerical method, Q_{abs} is on the order of $\sim$ 1400–1700 for FCMs, depending on the SiQD film thickness.

Optical losses also occur due to scattering from surface roughness. The scattering-related loss coefficient is [71] [86] [87]

$$\alpha_{sca} = \varphi^2(r)(m_2^2 - 1)\frac{k_0^3}{8m_2^2}\sigma^2\sqrt{\frac{\pi}{m_{eff} - 1}}, \tag{1.87}$$

where φ is the value of the normalized electric field at the resonator surface, m_{eff} is the effective index of the cavity, m_2 is the index of the fluorescent layer, and σ is the root-mean-square roughness. For a typical SiQD layer thickness of 600 nm, we find $\varphi^2 \approx 0.3$. Using a SiQD RMS roughness of 3.4 nm [88] [89], a wavelength of 800 nm, $m_2 = 1.67$, and $m_{eff} = 1.41$ [87] one obtains

$\alpha_{sca} \approx 0.05$ cm^{-1} [87]. As before, we can estimate the Q-factor using Eq. 1.86 to yield a Q_{sca} of 5×10^4 for a typical FCM.

The total Q-factor (Q_{total}) can be found from the Q-factors associated with each specific loss mechanism , according to [88]:

$$\frac{1}{Q_{total}} = \frac{1}{Q_{rad}} + \frac{1}{Q_{abs}} + \frac{1}{Q_{sca}} + ..., \tag{1.88}$$

where other losses could include interband absorption, ohmic heating in the walls of the resonator, Auger recombination, and scattering off SiQDs. The limiting Q-factor from interband absorption has been estimated for similar structures as on the order of Q_{sca}, or 10^5 [86]. Loss from Ohmic heating only becomes relevant at Q-factors on the order of 10^7, and then only in special circumstances (GHz excitation, plasmon-hybrid devices) [90] [91]. As a result, these are neglected here. For FCMs, Q_{abs} represents the limiting loss mechanism.

1.3.9 Mode volume and the Purcell effect

The mode volume V_0 is the volume occupied by the WGM electromagnetic field. It is defined as the intensity of the WGM electric field integrated over all space normalized to the maximum intensity [86] [92]:

$$V_0 = \frac{\int_{all\ space} \varepsilon(r)|\mathbf{E}(r)|^2 d^3r}{Max[(\varepsilon(r)|\mathbf{E}(r)|^2)]}, \tag{1.89}$$

where $\mathbf{E}$ is the electric field and ε is the dielectric constant. The electric field propagating outward from the resonator through all space causes the result of this integral to diverge, and so the integral is arbitrarily truncated at $r \gg b$ [92] [86] [58]. For spherical and cylindrical WGM-based resonators utilizing a SiQD film, mode volumes are estimated by simulation to be on the order of 100 μm^3 [93] [86] [58].

The Purcell effect describes a modification of the radiative lifetime of a particle inside a resonant cavity [94]. The Purcell factor is the ratio of the

in-cavity to the spontaneous radiative emission rate for an emitter located spectrally and physically on a cavity resonance:

$$F_p = \frac{w_{cav}}{w_{free}}, \tag{1.90}$$

where w_{cav} is the emission rate of the particle when emitting into a cavity resonance and w_{free} is the emission rate into free space. The Purcell factor can be derived using Fermi's Golden Rule [95] [96] from the density of states and transition matrix element, yielding for a spectrally narrow emitter on resonance with a cavity:

$$F_p = \frac{3Q(\frac{\lambda_0}{m_{eff}})^3}{4\pi^2 V_0}. \tag{1.91}$$

Here Q is the resonator Q-factor, m_{eff} is the effective refractive index as usual and V_0 is the mode volume of the WGM. This further assumes that only a single emitter exists, with a single emission frequency, positioned within a resonant cavity having a single mode. Violations of these assumptions would result in a lower Purcell enhancement. This is likely the case for an FCM, since the fluorescent layer is composed of an ensemble of SiQDs, which have a distribution of emission wavelengths [97] and are positioned at various locations with respect to the cavity and resonances. Although the Purcell factor has not been measured for SiQDs in WGM resonators, other optical microresonators have shown Purcell factors from 1 to 46 depending on Q-factor, resonator size, and emitter type [98] [99] [100] [101] [97] [102] [103] [104].

1.3.10 Important parameters of WGM spectra

WGMs appear as a set of peaks in a fluorescence spectrum. They have a Lorentzian lineshape given by

$$I(\omega) = \frac{\Delta\omega^2}{2\pi}\frac{1}{(\omega-\omega_0)^2 + (\frac{\Delta\omega}{2})^2}, \tag{1.92}$$

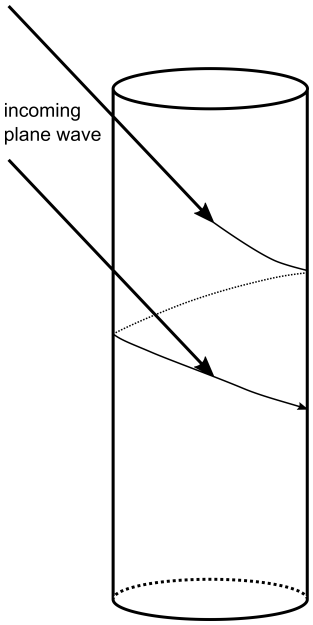

Figure 1.8: Diagram of spiral mode geometry. The difference in path length between the two rays causes constructive or destructive interference.

where $\Delta\omega$ and ω_0 are the FWHM and central frequency of the peak, respectively [105]. However, we found that the fluorescence WGMs often display a tail extending to shorter wavelengths. This is attributed to axial-propagating modes known as spiral modes [106] [107]. These are launched in the capillary at an angle θ with respect to the equatorial plane and are blueshifted from the equatorial WGMs by an amount $\Delta\lambda$, according to [107]

$$\Delta\lambda \approx \frac{\pi b}{m_{eff} l}\theta^2, \tag{1.93}$$

where l is the angular order of the mode, m is refractive index of the fluorescent layer, and b is the FCM radius. Since the spiral modes can have any angle, the result is an apparent short-wavelength skewing of the main fluorescence WGMs. Although the existing references and theory discuss the spiral mode phenomenon with reference to external illumination, we believe a similar effect is achieved through spiralling of florescence inside the FCM walls.

The free spectral range (FSR) of a resonant cavity is

$$\Delta f_{FSR} = \frac{c}{m_{eff} L}, \tag{1.94}$$

where L is the length of a cavity round-trip.. Expressed in terms of wavelength, the FSR at a wavelength λ_0 is

$$\Delta \lambda_{FSR} = \frac{\lambda_0^2 \Delta f_{FSR}}{c} = \frac{\lambda_0^2}{m_{eff} L}. \tag{1.95}$$

The visibility is a parameter that describes the contrast between the resonance and the background signal, given by:

$$V = \frac{I_{max} - I_{min}}{I_{max} + I_{min}}. \tag{1.96}$$

where I_{max} is the intensity at a peak and I_{min} is the intensity between two modes. A high spectral visibility is desirable for more reliably tracking WGM spectral shifts.

1.4 Types of WGM cavities

Many types of structures with circular cross-sections can be utilized for WGM-based sensing. Here, we mention some commonly-studied types of WGM resonators.

1.4.1 Fibers

One of the simplest WGM platforms is an optical fiber. Cylindrical whispering gallery modes can propagate around the circumference of the fiber via internal reflection along the glass-air boundary (Fig. 1.9). Light must be coupled into a fiber in order to excite WGMs, and coupled back out to provide sensing information. In-coupling can be done in three ways: using free-space illumination with a laser or LED, using a fluorescent coating on the resonator surface

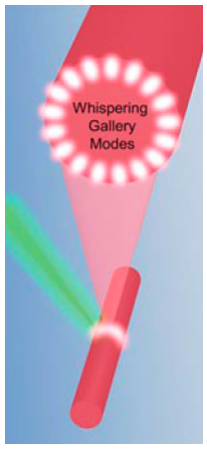

Figure 1.9: Diagram of a fluorescent-doped fiber supporting WGMs, excited using free-space illumination. Adapted from Ref. [3] and reprinted under a Creative Commons License (CC-BY-NC).

[87], or using evanescent coupling from another fiber or waveguide (Fig. 1.10) [4]. Outcoupling can be accomplished in the first two cases by observing light scattered out of the fiber modes. In the third case, the out-coupling can be accomplished using the same fiber or waveguide as for in-coupling.

Optical fibers have some advantages with regard to sensing. Fibers innately support WGMs and can be purchased commercially in bulk, so no special fabrication for this platform is needed. In addition, because the evanescent field of a fiber WGM lies directly at the interface between the fiber and its environment, they can have sensitivities on the order of 300 nm/RIU [3]. However, they also have some limitations. There is no simple capability for remote sensing, since fiber-based WGMs do not propagate along the length of the fiber, although this could be overcome by an outcoupling method like that in Fig. 1.10. Additionally, fibers are not inherently microfluidic, meaning that a fiber-based sensor must be immersed in an external reservoir containing the analyte.

1.4.2 Microspheres

Dielectric microspheres or droplets support spherical WGMs. These resonators are commonly made of silica [108] [109] [110] [111] [112] [113] [114], polymers

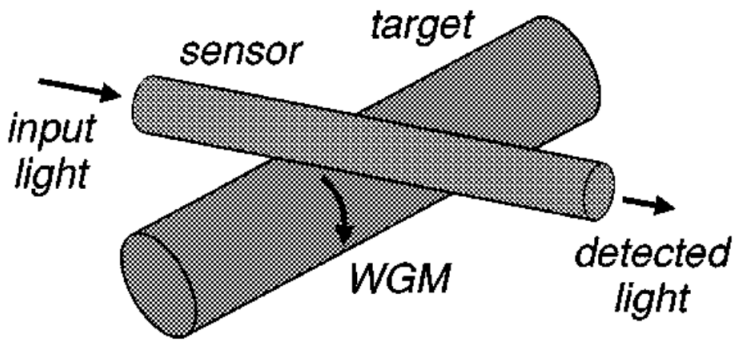

Figure 1.10: Diagram of a crossed fibers; one carrying light to excite WGMs and the other supporting WGMs around its periphery. Reprinted with permission from Ref. [4], © 2000 IEEE.

[115] [116] [117], or liquid droplets [118] [119]. As with optical fibers and other types of WGM microcavities, light can be coupled into microsphere WGMs via free-space, fluorescent, or evanescent excitation.

Microspheres have the advantage of being naturally formed via surface tension, allowing them to be fabricated in various ways. Glass can be formed into microspheres by melting. Polymers can form microspheres in solution and then be cured or solidified. Furthermore, reflow fabrication techniques can reduce the surface roughness of microsphere resonators, which improves their efficiency over etched resonators [120]. Finally, microspheres have been shown to exhibit the carousel effect, where analyte particles placed in solution around a microsphere become polarized by the WGM field [121]. When they are surrounded by a medium with a lower relative dielectric constant, this draws them toward the microsphere, thus improving their likelihood of detection.

There are also several limitations to microsphere-based sensing. Microspheres are fragile when fabricated on the end of fibers, due to a small neck separating the sphere from the fiber. When free-standing, they are difficult to individually manipulate. When measuring microsphere WGMs with a tapered fiber or using a spectrometer, the measurement is sensitive to the latitude. Last, similar to fibers, microspheres require adaption for liquid sensing since

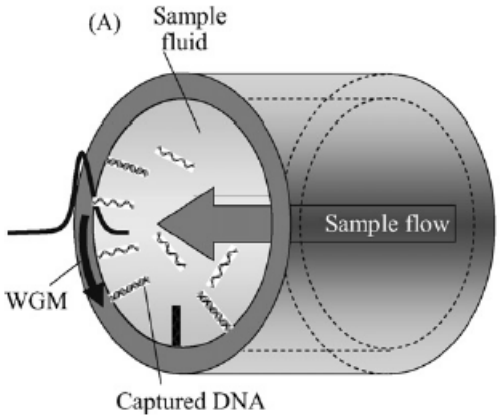

Figure 1.11: Diagram of an LCORR structure. The path of the WGM is around the wall of the structure (not-to-scale), while here a DNA-based assay is performed in the microfluidic channel. Reprinted from Ref. [5], with permission from Elsevier.

they are not inherently microfluidic.

1.4.3 Liquid-core optical ring resonators

The liquid-core optical ring resonator (LCORR) is a thin-walled glass tube supporting WGMs at its outer boundary [122] [123] (Fig. 1.11). It is hollow, allowing analyte to flow through it and making it well-suited for microfluidics. Because the WGMs propagate at the outer surface of the LCORR, the LCORR wall must be thin enough that the analyte (at the inner wall) lies within the WGM field. As a result, LCORR walls must be less than 5 microns thick [122]. In contrast with FCMs, LCORRs may utilize second-order radial modes because of their extremely thin walls and relatively high ($\sim 10^5$) Q-factors [124].

LCORRs are inherently microfluidic; they contain the analyte and do not require an outside reservoir. They can be excited via evanescent coupling through tapered fibers or lithographically-fabricated waveguides, using a tunable laser to scan the resonances [124]. However, LCORRs are exceptionally fragile and are sensitive to pressure fluctuations in the sample-delivery system. They expand in response to a pressure increase, causing spurious WGM shifts

[125] [126].

1.4.4 Other types of WGM resonator structures

Many other platforms for WGM-based detection exist, including toroids [127] [128], microdisks [129] [130] [131], bubble resonators [132] [133], and bottle resonators [134] [135]. Like the types mentioned already, these have a circular cross-section to support WGMs through total internal reflection. They offer various features depending on the platform, including lithographic fabrication, high sensitivity, and optomechanical coupling. Other than bubble resonators, however, none of them are inherently microfluidic.

1.4.5 Fluorescent-core microcapillaries

The fluorescent-core microcapillary (FCM) is the main subject of this work [136] [137] [61] [138] [139]. Like the LCORR, the FCM is a hollow glass tube carrying a fluidic analyte. The distinguishing feature of the FCM is a thin, high-index layer of fluorescent material that coats the inside channel wall. This layer provides the RI contrast necessary for total internal reflection at the inner wall of the glass capillary [84] [56]. The fluorescent layer also serves to couple light into the resonances of the FCM and obviates the need to have thin walls.

The FCM has several advantages. First, like the LCORR, it is inherently microfluidic. Second, it does not require evanescent coupling, which removes the need for fiber thinning and micropositioning equipment. Finally, the FCM is durable and easy to handle [140]. However, the FCM has a low Q-factor ($\sim 10^3$ vs. $\sim 10^6$ for the LCORR [126]), which makes it more difficult to resolve spectral shifts.

1.5 FCM-based biosensing

To achieve WGM-based biosensing in a fluorescent-core microcapillary, the inner walls of the capillary must capture target molecules from solution. Once enough binding events have occurred, a shift in the WGM wavelengths will become apparent in the fluorescence spectrum. The wavelength shifts are due to the excess polarizability of the bound biomolecules as they interact with the circulating optical field. The main purpose of this section will be to describe the methods used to attach these biomolecules.

1.5.1 Biomolecule detection

The simplest method of biochemical sensing in FCMs is to dissolve a target species in a solvent, flow it through the FCM channel, and observe the refractometric shift. The dissolved species will change the refractive index of the solution as a function of the target's concentration. This refractive index change is detected by shifts in the spectral locations of the WGMs. Thus, if the refractive index of the solvent and the analyte species are each known, the concentration can be determined.

More sensitive measurements can be achieved by adsorbing a layer of biomolecules onto the surface of a sensor. Instead of being distributed in solution, the biomolecules are concentrated on the inner wall of the FCM, resulting in a larger refractometric shift. This layer forms because of chemical interactions between the biomolecules and the channel wall of the FCM. The properties of the channel wall may be modified in order to facilitate the formation of this layer, which is called functionalization.

Ideally, a WGM-based biosensor will have the desired qualities of any sensor: sensitivity, stability, specificity (or selectivity), and re-usability [141] [142]. The sensitivity depends on the mode field interaction with the analyte and on the density and thickness of the biomolecular layer formed. Stability here refers to the sensor output remaining constant when no change is induced. This depends on many factors including the device configuration but is also affected

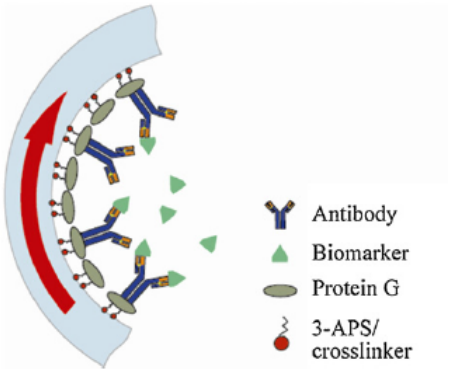

Figure 1.12: Layer buildup on the inner surface of a LCORR. Here we see subsequent buildup of a crosslinker, a protein, an antibody, and a biomarker (the sensing target). Reprinted from Ref. [6] with permission from Elsevier.

by whether the biomolecule layer degrades over time. Specificity pertains to a unique property, affinity, or behaviour that allows for differentiation of one analyte species from another. We discuss specificity briefly here, and will mention the other biosensor qualities later in the context of the functionalization methods.

Biosensing may be performed nonspecifically by creating a sensor surface where a wide spectrum of biomolecules may adsorb (or stick, in general terms). However, this does not differentiate biomolecule species and so is only suitable for samples with a single species to be analyzed. These types of measurements have been used as a proof of principle in detecting bovine serum albumin (BSA), and various cancer-associated proteins [143] [144] [145] [146] [122] [147].

Biosensing may also be accomplished specifically, *i.e.*, showing a high degree of selectivity. Biomolecules are typically classified and differentiated by their particular function or role within the living system that created them. For example, hormones give feedback to endocrine systems, enzymes catalyze particular reactions, antibodies target the antigens they were made for, and so forth. Creating an environment in which the target biomolecule or its counterpart will react allows for potential sensing mechanisms. An antibody could be deposited on a surface in order to cause its specific corresponding antigen to be detected. Thus, the particular interaction that characterizes a biomolecule

is the key to a specific detection mechanism, provided other nonspecific mechanisms can be suppressed. This interaction and subsequent attachment is known as bioaffinity.

1.5.2 Surface functionalization methods

Functionalization for biosensing involves the formation of a chemically active layer on the sensor surface so that biomolecules may be anchored to it. We will discuss three categories of functionalization corresponding to different intermolecular interactions: physisorption, covalent bonding, and ionic bonding [148]. We will first discuss physisorption, which can be used to anchor biomolecules through weak interactions such as dipole-dipole interactions, hydrogen bonding, and van der Waals forces. Next, we will discuss covalent bonding via silanes. These involve well-defined bonds where electrons are shared between biomolecules and the underlying surface. Finally, we will discuss ionic functionalization via polyelectrolyte deposition, which is mediated by electrostatic interaction between charged groups on biomolecules and the surface to be functionalized. Each of these methods offers a different degree of specificity. Furthermore, each functionalization step may form the basis for a later functionalization step – in fact, the path to anchoring a particular molecule often involves a multi-tiered approach.

Physisorption

The first method of attaching a material to a surface is to allow it to stick nonspecifically. Many molecules experience instantaneous dipole moments that create attractive van der Waals forces. Large molecules like proteins, with diameters on the order of 10 nm, provide many site where this can occur. Furthermore, if one part of a protein sticks to the surface, it draws other parts of the protein closer to the surface as well, increasing the likelihood of binding at multiple sites. This is perhaps the simplest path for functionalizing a surface.

Physisorption is straightforward to implement. No special ingredients,

chemistry, or reaction are required, and it can be readily extended to a wide variety of biomolecules, including proteins and antigens. It is also reasonably fast, with molecules sticking to the surface in a matter of seconds or minutes versus the hours needed for some other processes [148].

Physisorption forms layers with relatively poor long-term mechanical stability [148]. The rate of attaching and detaching is concentration-dependent with forward and backward reactions stabilizing at an intermediate equilibrium. Similar to Le Chatelier's principle for perturbed reaction equilibria, a decrease in concentration of molecules in solution may result in the adsorbed population of these molecules gradually desorbing. In our case, the biomolecule layer steadily desorbs once exposed to a solution that does not contain the same biomolecules. This is significant in physisorbed layers over those anchored by other bonds, and can be accelerated by environmental conditions including pH, temperature, and other ions in the solution [149].

The stability of physisorbed layers can be improved by pre-treating or modifying the substrate surface [150] [151] [152]. For example, many proteins adsorb more strongly to hydrophobic surfaces [153]. Thus, an appropriately treated surface may improve the physisorption mechanism for specific applications.

Physisorbed functionalization is easily removed [148]. Surfaces coated in physisorbed molecules can be cleaned using soaps and detergents, organic solvents like acetone or methanol, or strong bases. This makes physisorbing sensors easy to re-use and re-functionalize for repeated measurements.

Covalent attachment via silanes

A surface may be functionalized using covalent bonds to anchor a biomolecule. These are commonly employed to link silica surfaces to organic molecules via silanes and to link gold surfaces to organic molecules via thiol chemistry in WGM-based and SPR-based sensors, respectively. These bonds can take hours rather than the minutes or seconds for physisorption [148]. However, they provide bonds that do not dissociate during biosensing.

Silanization is widely used for functionalizing biosensors that employ silica surfaces. Silanization can be accomplished on silica using alkoxysilanes. One proposed mechanism is that these chain terminations hydrolyze to Si-O-H groups, which then react with a hydroxylated silica surface (Si-O-H) to form siloxane bonds (Si-O-Si) [154] [155].

Silanization often causes a decrease in the functional area of a surface. The successful formation of silane films depends on many factors, including surface cleanliness, reaction temperature, and the presence of water, which catalyzes the reaction, or alcohol [156] [157] [158]. In particular, an excess of water favours interlinking of silanes rather than binding to the substrate [154] [159]. As a result, the silane film is often patchy, clumped, or sparse, which in turn decreases the density of subsequent biomolecular layers and causes poor sensor performance [160] [161] [162].

Nevertheless, silanization is relatively stable. Silanated sensor surfaces can be cleaned, or rejuvenated, using a 50:50 mixture of methanol (MeOH) and hydrochloric acid (HCl), and with mixtures of sulfuric acid and hydrogen peroxide (known sometimes as Piranha) [125] [139]. This is a double-edged sword – although the silane bonds are difficult to break, more chemistry is needed in order to rejuvenate the sensor head.

Silanes are most widely applied to oxide surfaces. For example, silanization has limited application to polystyrene (PS) and poly methyl methacrylate (PMMA), which are also used for WGM-based sensors [163]. Similarly, SPR-based sensors usually build on a gold substrate, for which thiol chemistry is used for functionalization. Thus, for many surfaces methods other than silanization may be preferred.

Ionic attachment via polyelectrolytes

A third type of surface functionalization utilizes the ionic nature of polyelectrolytes. Polyelectrolytes are long-chain molecules (often up to 20,000 amu) consisting of charged monomers. When dissolved, the polyelectrolyte can be accumulated on positively or negatively charged surfaces depending on the

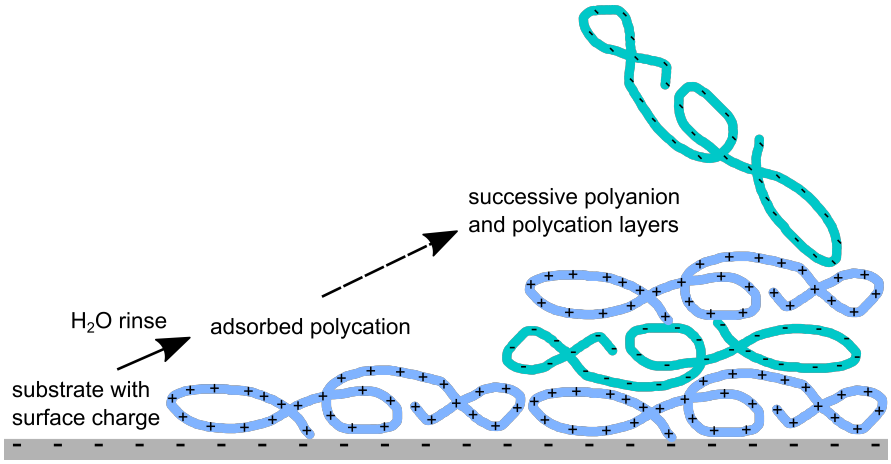

Figure 1.13: Build-up of two polyelectrolytes (a polycation and polyanion) on a positively-charged substrate.

charge of each of the polyelectrolyte and surface. This ionic interaction can be used to build layer-by-layer polyelectrolyte films [164].

The process of polyelectrolyte layering (Fig. 1.13) requires a surface with a slight residual charge [164]. This can be accomplished for silica by silanization. It is also done by treating the silica surface with a strong base to provide an oxide-terminated surface with a negative charge [165] [81]. The oxide is then exposed to a solution containing a polyelectrolyte with a positive charge, which then accumulates on the surface by coulombic attraction. The layer formed can be monomolecular, with a thickness on the order of 1–2 nm. Thus, depositing the polyelectrolyte layer effectively reverses the surface charge. A second polyelectrolyte (with the same charge as the original substrate, which is negative in this case) is then applied, forming a new layer and reversing the surface charge again (Fig. 1.13). This procedure may be repeated hundreds of times, all the while preserving surface functionality, layer regularity, and layer stability [166] [164]. The final layer can be chosen to contain some particular functional group (carboxylic acids, amines, etc.).

The thickness of polyelectrolyte layers may be controlled by adding NaCl to the polyelectrolyte solutions [7]. The conformation of the polyelectrolytes in pure water tends to be flat, making a thin layer on the substrate. However,

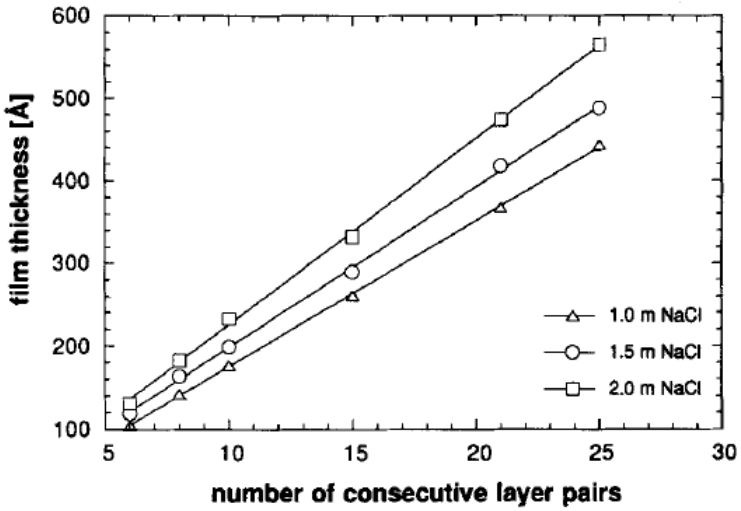

Figure 1.14: Graph of polyelectrolyte-based layer thickness using different salinity solutions. Reprinted from Ref. [7] by permission from Springer Nature Customer Service Centre GmbH.

as the salinity of the solvent rises, the polyelectrolyte units take on a bunched, crumpled formation [7]. This configuration persists after the polyelectrolyte attaches to the substrate, which results in a thicker monolayer. Thus, the layer thickness can be precisely-controlled (Fig. 1.14), ranging from <1 to 5 nm per layer.

Polyelectrolyte functionalization preserves the functional area of a substrate. The initial layer in the polyelectrolyte functionalization scheme is often incomplete, with occasional bare patches [8]. However, polyelectrolyte molecules will attach to the surface even if only a few ionic bonds form. Furthermore, once one side of a polyelectrolyte has bound, its opposite side retains all of its ionic sites, making a subsequent layer easier to deposit and more complete. Thus, the effective charge of the surface and the surface coverage increases with successive layers until the surface is homogenous [8].

Polyelectrolyte molecules in layered films do not retain their shape indefinitely, and respond to changes in salinity [167]. A deposited multilayer of polyelectrolyte can be annealed, which decreases its defects and makes it more homogenous) by alternating rinses of saline and pure water. The proposed

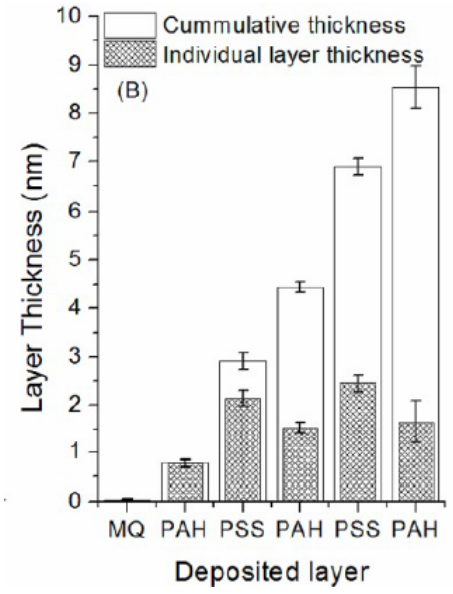

Figure 1.15: Graph of polyelectrolyte-based layer thicknesses, indicating incomplete initial layer. Reproduced with permission of A. François from Ref. [8]

mechanism is one in which the dissolved salt causes small breakages or dissociations within and between molecules where there are pre-existing weaknesses [167]. A subsequent pure water rinse then returns the polyelectrolytes to their flat configuration, packing these loose components into an ultimately smoother layer. This has the desirable effect of healing a layer. An undesirable side effect is variations in solution salinity may cause an adsorbed polyelectrolyte layer to swell or shrink, which can manifest as a shift in WGM-based sensor data.

Polyelectrolyte-functionalized sensors are straightforward to clean and thus rejuvenate in preparation for a different measurement. The most commonly used method is flowing a concentrated base like sodium hydroxide or potassium hydroxide over the sensor head. This has proved effective with base concentrations ranging from 0.1 to 10 M, and takes only minutes [168].

1.5.3 Building on functional groups

The purpose of the initial functionalization method is to allow subsequent attachment of molecules, *e.g.* antigens, antibodies, vitamins, or other biomolecular species. This bait is chosen for its affinity to the desired detection target. The most widely-used bait is an antibody, which is a protein of the immune system. In this section, we introduce the structure of a protein and explain the different cross-linking sites. We do this with specific reference to antibodies because of their use in immunoassays, which are used extensively in biochemical sensing.

Protein/antibody structure

Proteins are composed of amino acids, which are organic chains containing an amine (NH_2 group) and a carboxylic acid (COOH group) [169]. When the amine of one amino acid links with the carboxylic group of another to form an amide, they create a peptide that can be extended as a polypeptide chain. These polypeptides can form into sheets or helices, with bonds forming between adjacent strands. These structures may fold into 3D shapes depending on the composition of each level of the protein. Finally, these 3D structures can cluster with others to give a final layer of complexity. Proteins are often further modified at the strand and sheet level by various processes, including glycosylation (the addition of carbohydrates), phosphorylation (the addition of a phosphorus-containing group), or ubiquitination (the addition of a smaller, different class of proteins). The structural tiers of a protein are illustrated in Fig. 1.16.

Antibodies are a Y-shaped protein used by a host's immune system to attack (bind to) antigens [170]. The tail region of an antibody (the stem of the Y) is known as the Fc or fragment crystallisable region (Fig. 1.17). This region is characteristic of the species of host that produced the antibody, and allows an antigen-antibody complex to be taken up by immune cells. The forked section of the Y, the Fab or fragment antigen binding region, is

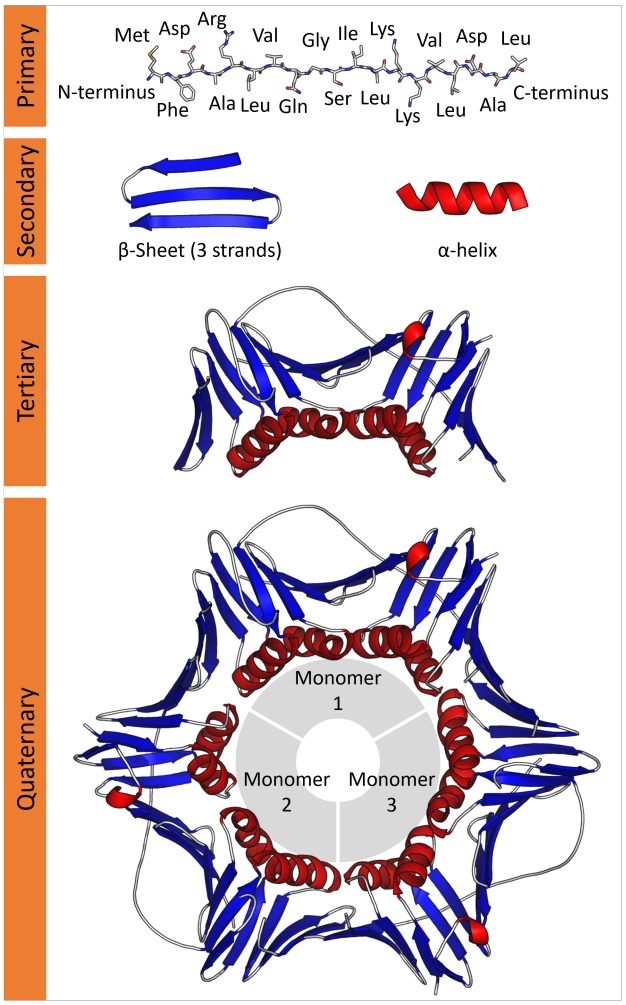

Figure 1.16: Schematic of the multi-tiered structure of the protein PCNA (proliferating cell nuclear antigen). In the primary structural level, amino acids abbreviated as "Val", "Lys", etc. are shown forming a chain. Reproduced under a Creative Commons License (https://creativecommons.org/licenses/by/4.0/legalcode) from Thomas Shafee at [9].

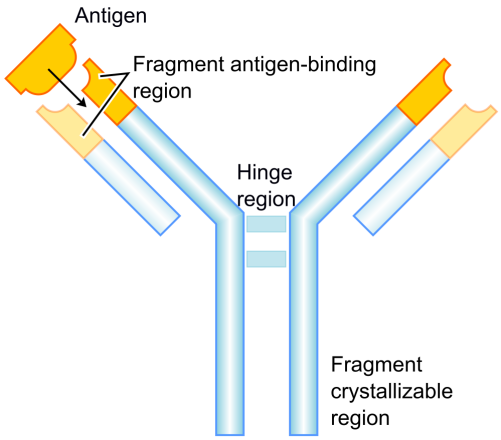

Figure 1.17: Structure of an antibody showing the distinctive Y-shape and antigen-binding region. Image public domain, modified for this work.

connected to the Fc region through a hinge section. The Fab arms terminate in a moiety that chemically recognizes and binds to the signature of a particular biomolecule (its target antigen). The antibody's target can be tailored by exposing an organism to the target so that antibodies are created against it. The resulting antibody-antigen interaction is extremely specific [171].

Biomolecular anchor sites

Antibodies can be bound to surfaces via amine, sulfhydryl, and carbonyl groups [170]. Amine groups are the most widely accessible moiety on most proteins, and protocols exist to link them with both amines and carboxylic acids [172]. Amine-amine coupling can be achieved using an imidoester, but this involves a reactive intermediary and elevated pH, and produces a less stable bond than amine-carboxyl bonds [173]. Amine-carboxyl crosslinking can be accomplished using N-hydroxysuccinimide (NHS) and sulfo-NHS esters [174], or by using ethyl dimethylaminopropyl carbodiimide (EDC). NHS and EDC can also be employed together in some protocols, as Chapter 5 of this thesis. Because amines are widely available on the surface of proteins, amine-based linking is widely-applicable. However, this also means amine-based linking does not offer control over the protein orientation.

Disulfide bonds between peptide chains on certain amino acid species can be split to create sulfhydryl groups [175], providing another anchoring site. In antibodies, sulfhydryls are available in the hinge region, and accessing them involves cleaving the antibody Y vertically down the middle. The malemide group is used to bind to sulfhydryls via a sulfur-carbon bond, attaching an alkyl chain. This alkyl chain will have a group with affinity to amines, carboxylic acids, or some other moiety. Because disulfide bonds only exist at particular locations, the orientation of the antibody will be controlled. However, there are downsides to this method. Disulfides are not accessible in all proteins, making this a limited-scope technique outside of antibodies. Second, the protein must be partially denatured in order to expose the sulfhydryl groups, and in an antibody specifically there must be a complete split.

In antibodies, carbonyl groups exist in the peptide bonds as well as on the side chain of some amino acids (aspartic and glutamic acid), offering a third binding site. They can also be found in carbohydrates, which are a component of glycosylated proteins. In antibodies, carbohydrates are accessible in the Fc region. The carbonyl groups are utilized by oxidizing them to produce reactive aldehydes and ketones. The process starts with the addition of periodic acid or sodium metaperiodate, and can be halted by the addition of glycerol. These newly-created carbonyls may be joined to amines via hydrazide linkers. The advantage of this technique is that it offers a degree of protein orientation control, since carbohydrate-linked residues are only on specific regions of proteins. Antibodies will only be anchored at their Fc region, leaving the antigen-reactive Fab end free. The disadvantage is that the required oxidization will eventually destroy the protein; thus the reaction must be carefully controlled.

1.5.4 Assays

Assays are overall procedures used for detection of a particular biomolecule. They typically begin with the functionalization of a surface, exploit the bioaffin-

ity of an antibody or other protein, and require a transduction mechanism where the presence of the biomolecule becomes a measurable signal. Here we present the most common assays used for antibody-mediated detection, known as enzyme-linked immunosorbent assays (ELISAs). In a WGM-based sensor like that demonstrated in this thesis, the method of transduction is different from a classic ELISA but the other steps remain the same.

Direct ELISA

The simplest implementation of the ELISA protocol is the direct ELISA (Fig. 1.18). This begins with functionalization, which is accomplished by physisorbing an analyte nonspecifically onto the sensor surface. The adsorbed analyte molecules are then used to create a detectable signal. This is accomplished by exposing the adsorbed analyte to antibodies that target them, building up a layer of antibodies on the surface of the sensor. In an ELISA, the antibody will have been pre-conjugated to an enzyme such as horseradish peroxidase (HRP) [176]. This enzyme acts on a substance known in biochemistry as the substrate, not to be confused with the physical underlying structure. The enzyme causes the substrate to photoactivate, fluoresce, or exhibit some other measurable behaviour [177] [178]. Thus, substrate addition results in a signal correlated with the amount of enzyme present, which in turn is correlated with the amount of adsorbed analyte.

Sandwich ELISA

The sandwich ELISA avoids nonspecific analyte adsorption and the antibody-enzyme conjugate of the direct ELISA (Fig. 1.18). Here, the surface is functionalized using primary antibodies. These primary antibodies are then exposed to a solution containing the target antigen, which in turn forms a layer on the antibody. However, antigens can be bound from multiple sides simultaneously; during an immune response, antigens are swarmed with antibodies until they are rendered inert. The top of the antigen layer is then saturated us-

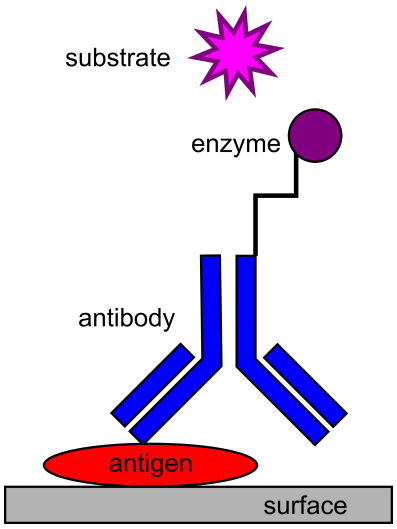

Figure 1.18: Diagram of a direct ELISA, showing an analyte on a surface, with an antibody bound to it. An enzyme conjugated to the antibody causes a substrate in solution to change or emit colour.

ing antibodies of the same type as those initially attached to the surface. This forms an antigen sandwich, with the tails or Fc regions (with a species-specific signature) of the top layer of primary antibodies facing upward. A final layer is made using an antibody-enzyme conjugate that targets the species of the animal from which the primary antibodies are derived. The substrate can then be applied to complete the assay as before.

There are several advantages of the sandwich ELISA. First, the antigen adsorption is specific, *i.e.*, it is mediated by the primary antibody, which increases the accumulation of antigen. Second, the sandwich ELISA is cost-efficient. In the direct ELISA, the antibody-enzyme conjugate contains an antibody that targets a particular antigen. Thus, for every antigen a new conjugate must be made. In the sandwich ELISA, the antibody in the conjugate targets a species marker. For example, many different experiments for different targets can be performed using rat antibodies, and each can be resolved using a goat anti-rat set of conjugates. This avoids having to manufacture multiple conjugates.

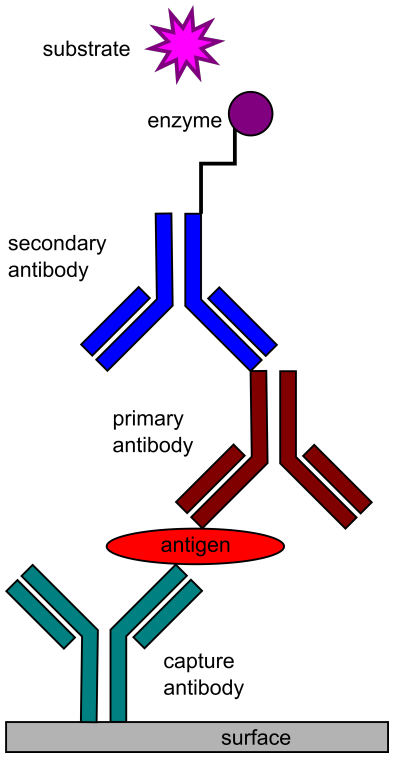

Figure 1.19: Diagram of a sandwich ELISA, showing an antibody on a surface, and a successive chain of antigen, primary antibody, and secondary antibody stacked on top of it. A substrate in solution reacts with the enzyme.

Competition Assay

A variant of the ELISA utilizes competition between antigen contained in a sample, and a quantified portion of antigen added to the sample (a "spike") [179] (Fig. 1.19). First, a sensor head is pre-coated with antigen either specifically or nonspecifically. The sensor is then exposed to a mixture of two antibodies that both target the antigen. One group of antibodies comprises the sample to be analyzed, while the other is a pre-prepared antibody-enzyme conjugate. The antibodies then compete for binding sites, and the resulting signal of the enzyme substrate is inversely proportional to the amount of analyte in the solution. The procedure can also be reversed, with antibodies initially on the sensor head and enzyme-conjugated antigens competing for binding sites. This technique is useful when an antigen is too small to bind to multiple antibodies, which prevents the use of a sandwich ELISA.

Applications to WGM sensors

The assays described above are the workhorses of analytical biochemistry [180] [181] [182]. They can be applied to various platforms by utilizing the same underlying principles. The molecule under investigation need not be part of an antibody-antigen pair; it can be an enzyme-substrate pair, an aptamer-protein system, a vitamin-protein pair, and so forth. The key element is a degree of biorecognition. Similarly, the transduction mechanism need not be enzymatic, and has been implemented using both radio-isotopes [183] and fluorescent markers [184].

WGM-based platforms offer potential improvements over conventional ELISA deployment. ELISA is done using multiple reaction wells, in which samples are analyzed in parallel using different concentrations of substrate, antibody, or antigen. However, the ELISA protocol centers on the amplification of signal from adsorbed analyte. In WGM-based sensors, a layer of antibodies or antibody-sized antigens can be detected directly through the mode wavelength shifts. A WGM-deployed sandwich ELISA, can be stopped while still open-

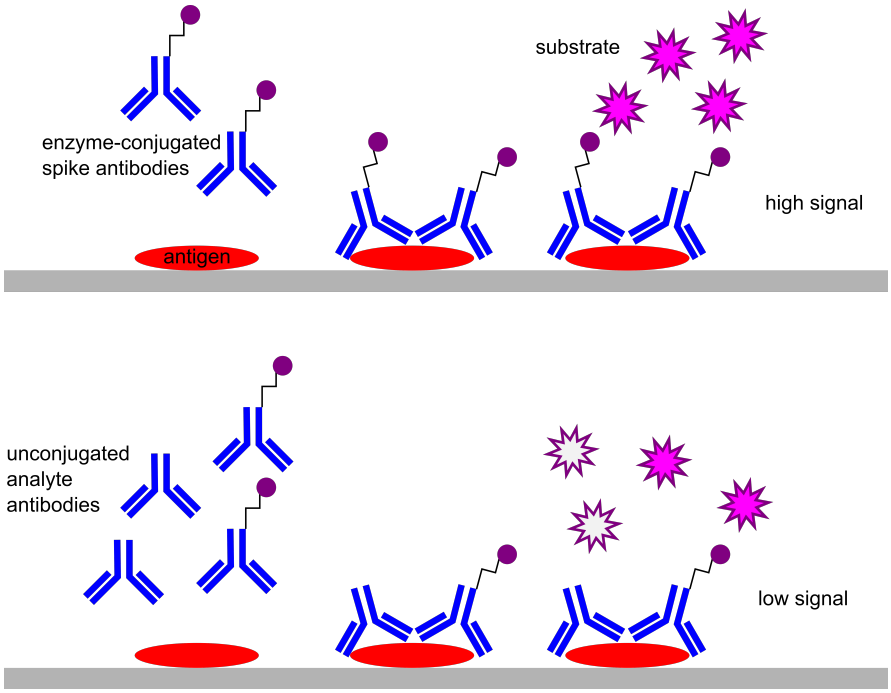

Figure 1.20: Diagram showing a competition ELISA with (top) and without (bottom) analyte antibodies. Note that both enzyme-conjugated and unconjugated antibodies are present. In this diagram, the substrate is purple when reacted with the enzyme and this colour correlates inversely with the analyte concentration.

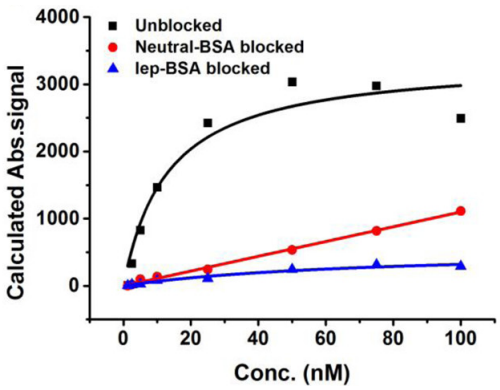

Figure 1.21: Measurements of nonspecific adsorption on a functionalized fiber for given protein concentrations when unblocked versus using two varieties of BSA. Reprinted with permission from Ref. [10], © 2017 American Chemical Society.

face, eliminating the need for a second primary antibody, a conjugate, or an enzyme.

Specificity and blocking

Nonspecific layer formation is a risk in antibody-based biosensing. Antibodies may adsorb nonspecifically to locations that are not functionalized with antigen. In order to correct this, blocking may be performed. This involves a cheap, minimally-reactive protein such as bovine serum albumin (BSA) [10]. BSA is composed of the same chemicals as other proteins, and will similarly bind nonspecifically to a surface. However, BSA is chosen because it is notoriously unreactive, which means other proteins in turn will not adsorb to it. This reduces the level of nonspecific binding that occurs during antibody layer formation (Fig. 1.21).

1.5.5 Interaction rates

Dissolved protein will be brought into contact with the sensor head either by being flowed directly over the sensor surface or by eventual diffusion through the solution. We can estimate whether biosensing in the FCM operates in a

diffusion-limited regime, by using the equation

$$\langle x^2 \rangle = q_i D t \tag{1.97}$$

where $\langle x^2 \rangle$ is the mean squared displacement of a particle, q_i is a dimensional constant (4 for 2-dimensional diffusion), D is the diffusion coefficient of a particle, and t is time [185]. For a protein in aqueous solution, the diffusion coefficient is on the order of $10^{-10} \frac{m^2}{s}$ [185]. This gives a protein speed of $\sim 4 \times 10^{-5} \frac{m}{s}$. The flow of solution through the FCM is at a rate of ~ 0.002 mL/min, which for a 50 μm capillary gives a fluid flow of $2 \times 10^{-2} \frac{m}{s}$. As a result, the time scale of diffusion within the solution is negligible compared to the time for the capillary to be refilled with a fresh solution. Thus, the concentration of the protein in solution may be considered constant during solution flow.

The rate of a biosensing reaction may be used to evaluate the concentration of an analyte. A simple biosensing reaction is described by the equation

$$A + B \rightleftharpoons AB, \tag{1.98}$$

where the analyte is represented by A, a surface-modifying ligand that targets the analyte is represented by B, and their conjugate on the surface is AB. The forward rate of the reaction is given by [186]

$$\frac{d[AB]}{dt} = k_a [A]^x [B]^y, \tag{1.99}$$

where the concentrations of A, B, and AB are denoted by $[A]$, $[B]$, and $[AB]$ respectively, $\frac{d[AB]}{dt}$ is the time rate of change of [AB], and k_a is a constant of proportionality known as the association constant. The constants x and y are experimentally-determined parameters that give the order of the reaction with respect to each reactant [186]. The reverse rate is correspondingly defined by

$$\frac{-d[AB]}{dt} = k_d [AB]^z, \tag{1.100}$$

where k_d is the dissociation constant. The combined reaction rate is then

$$\frac{d[AB]}{dt} = k_a[A]^x[B]^y - k_d[AB]^z. \tag{1.101}$$

The binding rate can be used to extract concentration information in a reaction that is essentially one-directional. Perhaps the simplest case is for a reaction with one reagent undergoing a zeroth order reaction. Eq. 1.99 then reduces to

$$\frac{d[A]}{dt} = -k[A]^0. \tag{1.102}$$

This describes a concentration-independent reaction, where a reactant concentration can be graphed as a straight line with slope k [187]. An example of this behaviour could involve a saturated catalyst. For the case of a first-order reaction, integration yields $[A] = [A]_0 e^{-k_a t}$ where $[A]_0$ is the initial concentration. The graph of the first-order reaction is exponential, allowing the rate constant to be obtained from the slope after linearization. The order of the reaction must be determined experimentally from a graph of the reaction rate, and gives clues to the reaction mechanism [187].

These rates may also be used when association and dissociation balance each other in an equilibrium. For many biosensing mechanisms, the reaction is zeroth-order with regard to the functionalized surface [188]. In the case of the proof-of-principle biotin-avidin interaction, the reaction is first-order ($x = 0$) with respect to avidin concentration ($[A]$) [189]. This simplifies Eq. 1.101 to the form

$$k_{obs} = k_a[A] - k_d, \tag{1.103}$$

where we have made the substitution $k_{obs} = \frac{d[AB]}{dt}$, the observed rate constant. This can be found by fitting data from a biosensor to the equation

$$R(t) = [1 - e^{-k_{obs}t}], \tag{1.104}$$

where $R(t)$ is the signal from the sensor head during layer formation [168]. The parameter $[A]$ in Eq. 1.103 may be found by using solutions with known concentration. Once $R(t)$ and $[A]$ are known, Eq. 1.103 allows determination of k_a and k_d for the sensor head, effectively calibrating the biosensor. At this point, unknown analyte concentrations may be measured.

1.6 Summary and subsequent chapters

In this chapter, we introduced the microfluidic measurement regime, along with two label-free optical sensing mechanisms: surface plasmon resonance and whispering gallery modes (WGMs). We then showed how optical WGMs arise in a cylinder from solutions to Maxwell's equations and the wave equation. We discussed the particular structure known as the fluorescent-core microcapillary (FCM), which utilizes a fluorescent silicon quantum-dot (SiQD) film to drive its WGMs. Next, we explained how the mode wavelengths can be used to measure the refractive index of a fluidic sample, and summarized the loss mechanisms and several parameters of a WGM spectrum.

We then described several WGM sensing platforms including fibers, microspheres, and two types of capillary-based resonators. We introduced the principle of biosensing using surface-sensitive devices, and set forth several methods and principles for surface functionalization. Finally, we discussed how this surface functionalization can be used in biochemical assays to perform detection of specific biomolecules. The use of standard assays means that WGM-based devices can detect particular molecules in solution, being sensitive only to predefined targets. Furthermore, the application of established assay techniques to WGM-based sensors suggests and important role improving detection capability in the biomedical industry.

In Chapter 2, we describe how to fabricate the FCM. We explain how to adapt it to microfluidic measurement using stable mounting techniques and chemically-resistant components. Next, in Chapter 3, we explore how the SiQD layer thickness and WGM order chosen affect refractometric measure-

ments with the FCM. In Chapter 4, thermal effects within the FCM are investigated, and we show that by engineering the SiQD layer and solvent, the FCM can be made thermally stable. In Chapter 5, we apply the principles of biosensing to measure the presence and concentration of a specific protein in solution.

Chapter 2

Experimental

In this section, the procedure for making, mounting, and performing measurements on a fluorescent-core microcapillary (FCM) will be described. We start by discussing the methods of fabricating the capillary itself, then mounting the fabricated capillary on a stage, and minimizing measurement noise. We then address how to find the modes and options for capillary orientation. We finish with brief notes on pumping fluidic samples through the FCM.

2.1 FCM fabrication

The FCM was made from bulk silica capillary stock. In this work we chose those with ~ 320 μm outer diameter (OD) in order to match tubing with sizes corresponding to standard gauges, and 10–100 μm inner diameter (ID), in order to provide WGMs with a clearly-resolvable FSR. The capillary material must first be cut into usable lengths of ~ 5 cm by scoring it using a ceramic blade and then snapping it to produce a cleave. Nitrile gloves were worn to avoid contamination of the capillary surface.

The capillary stock was shipped from Polymicro Technologies® with a polyimide coating, which must be removed. This can be accomplished in two ways. The first was via a bath of 300 °C 18 M sulfuric acid, which will dissolve the polyimide coating but not the silica capillary [61]. The second was to burn

off the coating using a furnace fed with an oxygen-rich atmosphere. In this work the latter method was used.

40–50 lengths of capillary were placed into a silica or alumina furnace boat (1200 or 1800 °C rating, respectively). The boat was placed in the furnace chamber, which was evacuated with a roughing pump and refilled with high-purity oxygen. The furnace temperature was ramped to 600 °C over 20 minutes, held at temperature (the dwell function) for 45 minutes, then cooled, all under flowing oxygen. Following this, the capillaries were ready to be coated with a fluorescent layer.

2.2 Formation of silicon nanocrystal layers

The SiQDs used in this work were formed using solutions of hydrogen silsesquioxane (HSQ), a material developed as a photoresist and electron-beam resist for soft lithography [64] [66] [65]. The HSQ was dissolved in m-xylene or methyl isobutyl ketone (MIBK) at a concentration of 15–20% w/w [162]. These solutions were made in-house using HSQ synthesized by our collaborators [162], or purchased from Dow Corning under the trade name FOx-15, which consists of MIBK containing 15–18% w/w of HSQ. Capillaries were filled by touching their end to an HSQ solution to draw the solution inside via surface tension.

The HSQ was thermally processed in order to form SiQDs [63] [64] [65]. This was accomplished by placing the filled capillaries in a furnace, which was raised at a rate of 20 °C per minute to 1100 °C under an atmosphere of N_2 with 5% H_2. The solvent evaporated as the furnace heated, depositing a layer of HSQ on the channel walls. This layer then decomposed to form SiNCs embedded in a silica matrix [63] [60]. The processes taking place during the thermal processing of HSQ were extensively investigated in recent work [63] [60].

It was difficult to create a film of SiQDs with consistent thickness along the length of the capillary. The thickness of the film affected the WGM profile, wavelength, and sensitivity [84] [58], so a uniform film was generally desired.

However, for a capillary with smaller ID, the SiQD films tended to exhibit increasingly variable thicknesses, PL intensity, and colour, and sometimes had regions without luminescent SiQDs. The success rate of fabricating WGM-supporting capillaries with an ID of 50 μm was 30–50%, while the success rate of 30 μm capillaries was below 1%. Thus, 50 μm capillaries were used extensively for this work.

The SiQD film thickness can be controlled in two ways. Capillaries with a larger channel surface-area-to-volume ratio (*i.e.*, smaller IDs) result in thinner QD films, since the HSQ will cover a proportionally larger surface. Alternatively, one can form a thick film and subsequently etch it using strong NaOH to eat away the silica [58] [168] [81]. Another proposed method explored in other work is to use a different concentration of HSQ [162].

2.3 Selecting microfluidic components

Analyte solutions were transferred to and from the FCMs by gluing lengths of tubing on each end. Polytetrafluoroethylene (PTFE) was used because it is resistant to organic solvents such as acetone and toluene, as well as to concentrated NaOH. The tubing should have an ID close to the OD of the capillary in order to attach snugly.

The tubing was glued to the capillary in order to form a tight seal. UV-curable adhesive Norland Optical Adhesive 76 (NOA76) was chosen for this purpose. It is resistant to organic solvents, strong acids and strong bases, and also binds well to both glass and PTFE. It is damaged by chlorinated solvents (chloroform, dichloromethane, tetrachloroethylene) or to temperatures above $\sim$ 70 °C , but none of these were present during the sensing experiments.

The gluing procedure began by placing the end of the capillary inside the tubing. A small drop of NOA76 was applied to the boundary between tubing and capillary, and the capillary was rotated by hand to spread the glue into a film. The capillary should be slowly pushed further into the tubing (1-2 mm) as it is rotated, causing the glue to be drawn along the inner wall of the tubing.

The glue will then begin to wick along this boundary toward the capillary end. It was then cured using a UV lamp, becoming firm to the touch and showing a slight yellow tinge. A second curing step was performed by heating the glued sample in an oven to 60 °C for $\sim$ 10 hours.

Syringes with volumes of 1–3 mL were used with a syringe pump to push analytes through the tubing at rates of 0.002 to 0.005 mL/min. Polycarbonate or polypropylene syringes are suitable for pumping aqueous samples and bases, but dissolve with organic solvents. For organic solvents and acids, glass syringes with glass plungers can be used, but the plunger seal is often unable to maintain the pressure needed to push the analyte solution through the capillary. Glass syringes using a PTFE-coated gasket and plunger were preferred because of a stronger seal and chemical inertness.

Needles with gauges ranging from 26 to 28 depending on the tubing size were used to interface the syringe end with the capillary tubing. Needles were chosen with bases that attached to the syringes using the standard Luer-Lok format. The needle tips were slid into the capillary tubing, where they fit snugly. Half-inch stainless steel needles with polycarbonate bases were used for aqueous solutions, but the bases not sufficiently resistant to organic solvents. Polychlorotrifluoroethylene (PCTFE) needle bases with stainless steel tips were a suitable alternative in these cases. PCTFE has chemical resistance similar to that of PTFE, but with sufficient rigidity to be attached to a Luer-Lok mount.

2.4 Mounting FCMs onto the microscope stage

The glued capillary was then mounted on a home-built stage for holding FCM devices (Fig. 2.1). The capillary was held by its ends in grooved bars with its middle over the microscope objective. Several methods may be used to hold the capillary in the grooves, including by using a thin neodymium magnet. It takes only seconds to attach or release a capillary, but it seldom fits the groove perfectly and can shift during an experiment. Plastic tape can hold

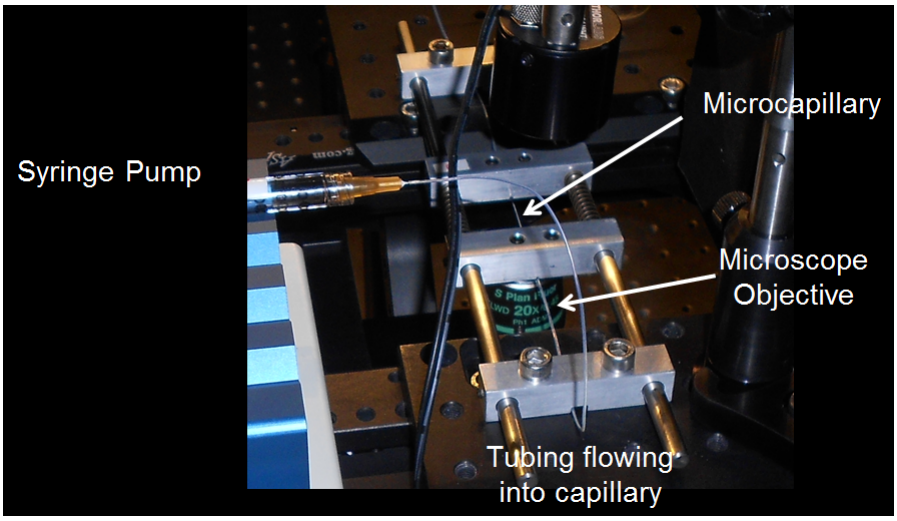

Figure 2.1: Photograph of a capillary mounted over a microscope objective. A syringe pump dispenses analyte into PTFE tubing that feeds a microcapillary.

the capillary more firmly, but it is not rigid and still allows the FCM to move. The tape may also leave adhesive on the FCM that makes it more difficult to handle afterward. Both magnet- and tape-based mounting can be improved slightly by shimming the capillary with tissue or ~ 1 mil. latex glove strips.

Glue can also be used to provide a more stable mounting option. Craft glue can be applied to the groove, and then the capillary placed in the groove as the glue dries. However, this requires waiting for the glue to dry, which can take up to an hour, and unmounting requires immersing the stage in water to dissolve the glue, which can take up to a day. The second option is to use NOA76, which can be cured in seconds. However, unmounting is difficult and requires either elevated temperature or simply breaking the capillary to remove it. A third option was to use transmission electron microscopy mounting wax, which melts near 60 °C. Small pieces of wax were liquified by placing them on the stage grooves and heating the whole stage. Once the stage was removed from heat, the wax solidified around the capillary. Unmounting the capillary was accomplished by simply heating the stage again. Thus, the wax method was finally chosen as the most optimal.

2.5 Minimizing mechanical and thermal drift

Once the capillary was mounted, the stage frame was bolted to the microscope stage, anchoring it at four corners using cross-tightened bolts. The stage could be observed to drift by tens of microns relative to the microscope objective over ~ 1 day. Thus, the stage was left overnight before attempting microfluidic sensing measurements.

Heating arising from laser illumination can cause shifts in WGMs through thermo-optic effects and thermal expansion. The former is dominant in an FCM [56], but the contribution from thermal expansion has not been specifically measured. It is possible that WGM shifts occur due to a combination of effects, including nonlinearities such as the Kerr effect [190]. For this reason, lower-intensity light sources such as LEDs or lasers attenuated by filters were most often used for excitation. It was also important for the capillary to thermally equilibrate under illumination for tens of minutes before acquiring data. Note that this does not remove thermal noise caused by random fluctuations of the atoms constituting the FCM. Such thermal noise is not a measurable factor in FCMs due to the low Q-factor and long spectral collection times ($\sim$ 20 seconds), but has been measured in other WGM-based sensors [191] and is discussed at length in Ref. [192]. More discussion of detection limits and analysis methods for similar structures may be found in Ref. [58].

Thermal and mechanical fluctuations can also be caused by air currents. To minimize this effect, the entire microscope assembly (apart from the capillary itself) was wrapped in a thin plastic sheet like that used to wrap food. The capillary itself had a rigid aluminum or cardboard form placed over it, since the plastic wrap would have caused mechanical drift if put in direct contact with it. Thermal fluctuations may also result from a cold analyte solution. Biomolecules in cold storage (*i.e.* a refrigerator or freezer) were therefore allowed to equilibrate to room temperature before flowing them through the FCM.

2.6 Locating modes and spectrometer alignment

FCMs were qualitatively screened via microscopic inspection. Some may support WGMs all along their length, or, due to inhomogeneities in the film quality, only in isolated regions. If a region of the capillary appeared dim or showed a speckled colour or texture, then it was unlikely to support WGMs. Good candidate locations show a thin, uniform line of bright red fluorescence along the channel wall.

The spectrometer slit may be aligned perpendicular to the capillary axis (Fig. 2.2). The imaging spectrometer then produces a 2D spectral image where the y-axis is a spatial coordinate along the length of the slit and the x-axis is wavelength. WGMs were most visible at the edge of the capillary channel. This configuration (with the slit perpendicular to the capillary axis) minimizes the effects of FCM drift, since the drift was usually in the sideways direction, *i.e.*, radially with respect to the capillary. Thus, the spectral image will show the same modes as before the shift, only at a slightly different y-coordinate in the image.

The capillary may also be mounted so it is parallel to the spectrometer slit, with the edge of the channel and the spectrometer slit aligned (Fig. 2.2). In this case, the spectral image has a y-coordinate corresponding to axial distance along the capillary. With this orientation, the fluorescence from large regions along the edge of the channel may be measured simultaneously. However, this orientation makes the measurement susceptible to drift. If the capillary shifts radially, the slit will no longer be aligned with the edge of the channel and the WGMs will no longer be observable. Thus, this configuration offers broad measurement capability but is susceptible to sample instability.

Although WGMs are sometimes identified by angular order in subsequent chapters, these labels are not the result of experimental measurement. This is not possible because the fundamental mode is not visible and nodes and antinode locations are not distinctly localized in the FCM. Instead, the mode

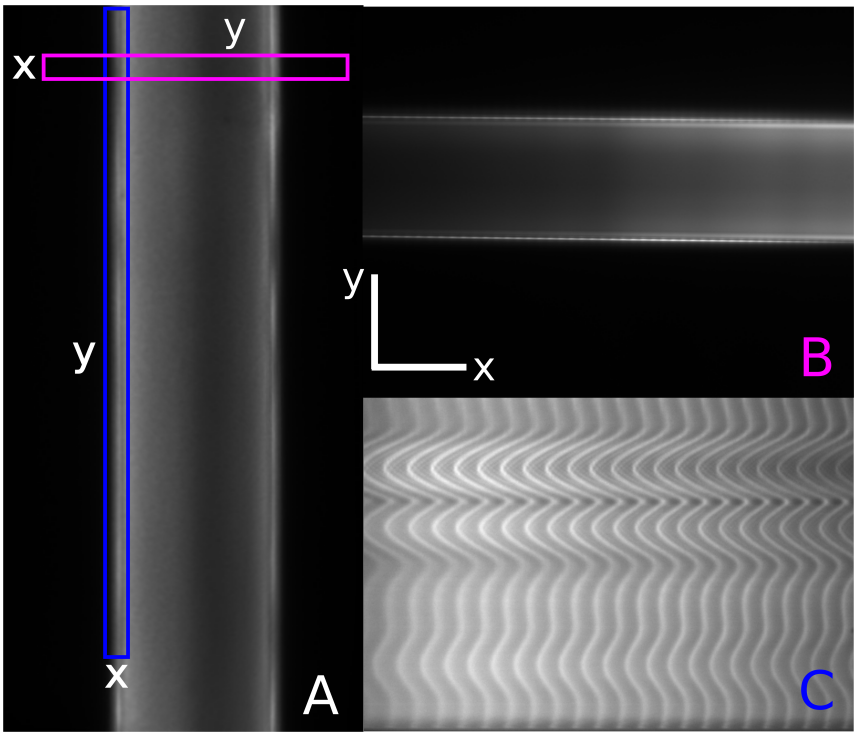

Figure 2.2: Diagram of the slit and capillary orientations. (A) shows a fluorescence image of the FCM, with purple and blue boxes indicating possible alignments for the spectrometer slit. Each box is labeled to show the dimension that will appear in the y-axis of the spectrometer output. (B) shows a spectral image of the WGMs taken in the perpendicular orientation (purple box). The x-axis is wavelength and the y-axis is the spatial coordinate across the radius of the capillary. (C) shows a spectral image taken in the parallel direction (blue box). The x-axis is wavelength and the y-axis is the spatial coordinate along the length of the capillary.

assignments are found by comparison with simulation or numerical evaluation of the Bessel functions previously described.

2.7 Solution pumping

A variety of solutions were pumped through FCMs in order to functionalize, clean, or determine sensitivity. Although solutions may initially appear clear, they often contain microscopic dust and debris from the various solutes. This debris can block the narrow channel of the capillary. As a result, solutions

were let stand until any undissolved material settled to the bottom, allowing clean solution to be drawn off the top. For large quantities of solution or fine contaminants, a circular filter with 10 μm pores was used. This filter would be folded into a cone over a sample reservoir, and the solution allowed to drip through it by gravity.

Care must also be taken to avoid pumping bubbles into the capillaries. These tend to slow the rate of analyte flow through the tubing and capillary. Bubbles can be created between solutions when one needle is removed from the end of the tubing and another introduced. In order to avoid this, a syringe should be gently squeezed as its needle is removed, in order to backfill the space previously occupied by the needle. Done properly, a small droplet of solution will extend from the end of the tubing. The next needle can then be introduced to the tubing without forming bubbles. Bubbles introduced during the loading of a syringe were removed by tapping them free from the syringe walls, tilting the syringe mouth upward, and pressing the plunger slightly. Degassing procedures to remove bubbles already in solution were not employed, but could be investigated if required.

Using these techniques, a single FCM could be used for weeks without blocking. Typically the capillary would be mounted and a series of solutions with known refractive index used to determine its sensitivity. Following this, the device could be used for several experiments with cleaning steps between, and then un-mounted with little risk of breaking.

This chapter described some of the experimental work that was not reported in the published papers. Several of the apparently inconsequential but nevertheless significant experimental hurdles were discussed, along with several tricks of the trade that were learned as the work proceeded. The discovery of several behavioural quirks of FCMs was important to improving the fabrication success rate, locating WGMs, and pumping solutions for biosensing. Using the techniques described above, measurements in subsequent papers can be more easily replicated or advanced.

Chapter 3

Whispering gallery mode structure and refractometric sensitivity of fluorescent capillary-type sensors

A modified version of this chapter was published in Sensors and Actuators B: Chemical 190 752-759 (2014) by S. Lane, J. Chan, T. Thiessen, and A. Meldrum.

3.1 Abstract

Fluorescent core microcapillary (FCM) structures present an alternative to optofluidic ring resonators for refractometric or biosensing applications. Instead of a thin-walled capillary that needs to be probed with a tuneable laser, FCMs are comprised of a fluorescent coating deposited on the channel walls of a microcapillary. The high refractive index of the coating serves to confine the fluorescence and leads to the development of whispering gallery modes (WGMs) whose field profile extends into the capillary channel. This work first investigates theoretically the conditions required to optimize the refractomet-

ric sensitivity of these structures. The optimal fluorescent coating thickness ultimately represents a trade-off between sensitivity and the mode Q-factors. We then use a spectral–spatial mapping method to obtain WGM information along the length of a capillary with variable film thickness. The maps agreed well with the theoretical predictions with one main exception: the experimental sensitivities were higher than the predicted values for some modes, possibly owing to interference modulation effects.

3.2 Introduction

Capillary-based devices have numerous existing and developing sensor applications [193]. In one example, capillaries can be used in microfluidic arrangements to sense local changes of the refractive index of liquid analytes in microfluidic devices [123] [194] [122] [61]. In the refractometric mode, a capillary sensor measures only the change in the local index of refraction of the fluid in the channel; whereas in the biosensing mode, the channel surfaces must be chemically pre-treated or functionalized to bind target biomolecules. Many applications have been explored, including disease detection [6], pesticide sensing [195], protein detection [196], and capillary electrophoresis [197]. Furthermore, microcapillary sensors can be compatible with dense, viscous fluids [198]. Capillary-based sensors can be classified into two broad types: liquid-core optical ring resonators (LCORRs) or fluorescent-core microcapillaries (FCMs).

The LCORR, or optofluidic ring resonator, is comprised of a thin-walled glass capillary [122] [61] [6] [195] [197] [198] [199]. Light from a tunable laser is confined by total internal reflection at the interface between the outer wall and the outside air, leading to the development of the cylindrical resonances known as whispering gallery modes (WGMs). Because the walls of the LCORR are thin (*i.e.*, 1–5 μm), a part of the electric field of the WGM extends into the capillary channel, where it can interact with an analyte. This interaction causes a shift of the resonance frequencies, which forms the fundamental sensor

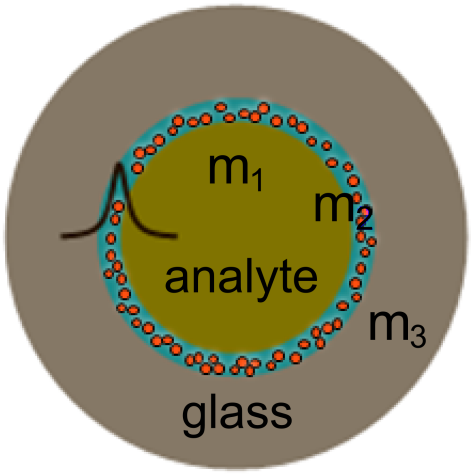

Figure 3.1: Cross sectional diagram of the FCM structure, which consists of a high-index fluorescent layer (m_2) coated onto the channel wall of a glass capillary (m_3). The analyte (m_1) flows within the channel. The electric field profile of a WGM resonance is represented schematically by the black line.

transduction mechanism.

In contrast, the FCM makes use of a high-refractive-index fluorescent layer that coats the capillary channel walls (Fig. 3.1) [61] [198] [200] [201] [140]. The WGMs develop because of the index contrast between the fluorescent layer and the glass wall. In this case a tunable laser is not needed, since the electric field is built up via fluorescence in the coating, which can be excited with a diode laser or LED. These devices are robust, but it is difficult to control the thickness of the coating [61] [201], which can affect the sensitivity of the structure to analytes pumped into the channel region. Thus, an objective of the present work was to perform a theoretical and experimental analysis of the effects of the fluorescent coating thickness on the sensitivity of the FCM structure. This can determine the geometries (*e.g.* film thickness and capillary diameter) required for optimal sensing performance.

3.3 Materials and methods

Microcapillaries with a fluorescent quantum dot layer coating the channel were prepared using methods previously described [140]. Briefly, capillaries from Polymicro Technology with a nominally 30±2 μm inner diameter were first heated for 45 min at 650 °C in flowing O_2 to ash the polyamide jacket. Next, the capillaries were filled with a solution of hydrogen silsesquioxane (HSQ) dissolved in methyl isobutyl ketone (MIBK). The capillaries were then annealed in a two-step procedure: 3 hours at 300 °C to evaporate the MIBK, and a subsequent hour at 1100 °C to cause the remaining HSQ to separate into a coating consisting of fluorescent silicon quantum dots embedded in a silica film. Some of the fluorescent capillaries formed with this method contain films that have varying thickness along the length of the capillary. A single capillary showing considerable variation in film thickness along its length was chosen for these experiments.

An approximately 4-cm-long capillary was supported such that it extended over a microscope objective. The ends of the capillary were glued to Teflon tubing (using Norland #76 adhesive) and a syringe pump was used to inject fluids into the tube. The fluorescence was excited using a 445-nm diode laser incident on the capillary via free space, focused to a spot size on the capillary of several hundred μm^2. The fluorescence was collected through the objective (Fig. 3.2) and sent to an SGS imaging spectrometer from the Santa Barbara Instruments Group. In this instrument, first optic is a mirror with a 100-μm entrance slit located in the center. One camera (the "tracking CCD") is aligned to accept images reflected from the mirror (which will contain a dark image of the slit superimposed on the microscope image). Light that passes through the slit enters the spectrograph part of the instrument and the spectrum is recorded by a second imaging CCD.

The capillary was carefully rotated so that its axis would be parallel to the spectrometer entrance slit, as observed on the tracking image (see Fig. 3.2). This orientation permits a spectral map to be obtained along the length of

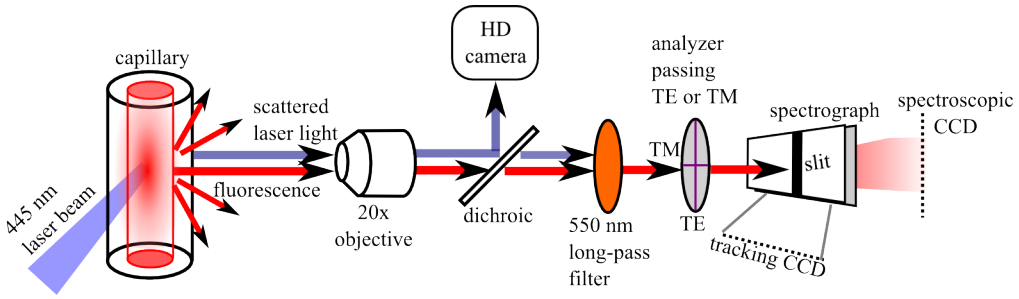

Figure 3.2: Diagram illustrating the experimental setup.

the capillary; the resulting spectral map has wavelength on the horizontal axis and distance (parallel to the capillary length) on the vertical one. Initially, the capillary tended to settle or drift slightly in its mounting, a tendency that caused some difficulty in obtaining data from the identical region of the capillary over long time periods. This behavior was minimized by mounting the capillary firmly using a low-melting-temperature wax and waiting for several hours before starting data collection.

In order to measure the refractometric sensitivity, deionized water and then ethanol were pumped into the channel while fluorescence spectra were being collected. The collection time was 20 seconds per spectrum. Dispersion effects are quite small over the wavelength range of 790–850 nm over which the spectra were collected, so we used fixed values of $m_{water} = 1.329$ and $m_{ethanol} = 1.357$ to estimate the experimental sensitivity. All spectra were calibrated for wavelength and intensity, by using an HgAr calibration lamp and a blackbody source (the LS1 from Ocean Optics), respectively.

We use the work of Teraoka and Arnold [202] [203] as the starting point for understanding layered capillary structures. Their work showed how the refractometric sensitivity of a layered sphere can be controlled by film thickness. One of the most interesting results was that there was an optimal film thickness at which the sensitivity of a layered microsphere reaches a maximum. Essentially, when the high-index coating is very thin, it tends to "pull" the electric field from the inside toward the sphere surface and allows a greater fraction to extend outward into the analyte, increasing the sensitivity. However, as

the high-index layer is made thicker, the evanescent field in the analyte also begins to contract inward toward the film and the sensitivity is reduced. Lin et al. subsequently extended the work toward a sensitivity and temperature analysis of the LCORR structure [204], and Franchimon et al. examined the WGM frequency shifts induced by nearby waveguides or fiber tapers [205].

Here, we follow the work of Teraoka and Arnold [202] [203], extending it toward capillary structures with an absorbing layer. Accordingly, for a capillary with a single channel layer, the electric field profile can be written as:

$$E_z(r) = \begin{cases} AJ_l(m_1 k_0 r) & r \leq a - t \\ BH_l^{(2)}(m_2 k_0 r) + CH_l^{(1)}(m_2 k_0 r) & a - t < r \leq a \\ DH_l^{(1)}(m_3 k_0 r) & r > a, \end{cases} \tag{3.1}$$

where a is the inner radius of the capillary and t is the film thickness. Applying the appropriate boundary conditions leads to the following two equations for the transverse electric (TE) and transverse magnetic (TM) polarizations:

$$TE: \frac{m_3 H_l^{(1)\prime}(m_3 k_0 a)}{m_2 H_l^{(1)}(m_3 k_0 a)} = \frac{(B_l/C_l)H_l^{(2)\prime}(m_2 k_0 a) + H_l^{(1)\prime}(m_2 k_0 a)}{(B_l/C_l)H_l^{(2)}(m_2 k_0 a) + H_l^{(1)}(m_2 k_0 a)} \tag{3.2}$$

$$TM: \frac{m_2 H_l^{(1)\prime}(m_3 k_0 a)}{m_3 H_l^{(1)}(m_3 k_0 a)} = \frac{(B_l/C_l)H_l^{(2)\prime}(m_2 k_0 a) + H_l^{(1)\prime}(m_2 k_0 a)}{(B_l/C_l)H_l^{(2)}(m_2 k_0 a) + H_l^{(1)}(m_2 k_0 a)}. \tag{3.3}$$

In Eqs. 3.1 and 3.3, J_l and $H_l^{(1),(2)}$ are the cylindrical Bessel and Hankel functions of order l, where l is the angular mode number of the WGM, defining the number of wavelengths that "fit" around the capillary circumference. The prime indicates the radial derivative of the function, as usual. The polarizations are defined with respect to the WGM plane, so that E (TE) and H (TM)

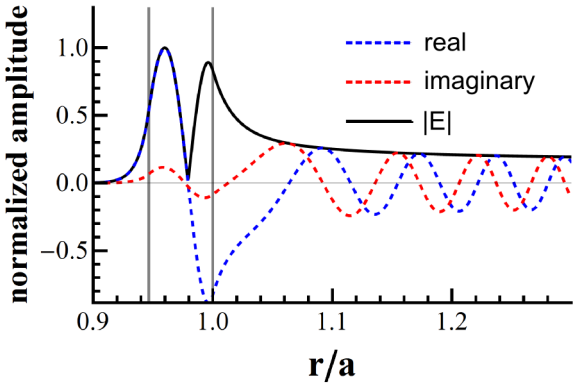

Figure 3.3: Electric field amplitude profile of a second-order mode ($n = 2$, $l = 195$, TE polarization) of a capillary with a radius of 15 μm and a film thickness of 0.8 μm. The coating is bounded by the vertical gray lines. This is an example of a low-Q mode ($Q = 430$), as evidenced by the large evanescent extension.

are parallel to the capillary axis. The ratios B_l/C_l are given by:

$$\left(\frac{B_l}{C_l}\right)_{TE} = \frac{-m_2 J_l(m_1 k_0 z) H_l^{(1)\prime}(m_2 k z) + m_1 J_1'(m_1 k_0 z) H_l^{(1)}(m_2 k_0 z)}{m_2 J_l(m_1 k_0 z) H_l^{(2)\prime}(m_2 k z) - m_1 J_l'(m_1 k_0 z) H_l^{(2)}(m_2 k_0 z)} \tag{3.4}$$

$$\left(\frac{B_l}{C_l}\right)_{TM} = \frac{-m_1 J_l(m_1 k_0 z) H_l^{(1)\prime}(m_2 k z) + m_2 J_1'(m_1 k_0 z) H_l^{(1)}(m_2 k_0 z)}{m_1 J_l(m_1 k_0 z) H_l^{(2)\prime}(m_2 k z) - m_2 J_1'(m_1 k_0 z) H_l^{(2)}(m_2 k_0 z)} \tag{3.5}$$

Eqs. 3.2 and 3.3 have an infinite number of roots, k_0, corresponding to the radial mode orders with complex wavevectors $k_{0,1}$, $k_{0,2}$, $k_{0,3}$.... Here, we will only examine the three lowest-order solutions corresponding to the cases where 1 to 3 intensity maxima extend in the radial direction. An example result is shown in Fig. 3.3, in which the field profile is shown for an $n = 2$ mode. As we will show below, the first-order solutions are the dominant ones experimentally in FCM structures; for $n \geq 2$, the modes tend to be lossy and usually do not appear in experiment.

We will assume that the capillary wall is lossless, but examine the effects of absorption-related losses in the fluorescent layer and in the analyte, by numerically finding the complex roots of Eqs. 3.2 and 3.3. The solutions give

a resonance wavelength ($\lambda_0 = 2\pi/Re[k]$) and Q-factor ($Q = Re[k]/2Im[k]$), as is well known (*e.g.*, Ref. [204]). The refractometric sensitivity $d\lambda/dm_1$ can be calculated by integration [203] [204], although in an FCM structure the relatively low index contrast between the film and the glass wall can lead to open resonator issues with the integration limits, similar in a sense to the case for mode volume calculations [92]. Here, we simply find the solutions to Eqs. 3.2 and 3.3 over a narrow range of refractive index in the core, and calculate $\Delta\lambda/\Delta m_1$ over this range. This method is reasonably accurate, as the sensitivity is virtually constant over a narrow range of m_1.

The detection limit, D, depends on the sensitivity and the resolution, R, of the spectrometer system: $D = R/S$, in refractive index units. R is the minimum WGM wavelength shift detectable by the spectrometer, typically within a 3σ level of certainty. A high Q-factor was generally thought necessary for a good resolution [59]; however, a complete consideration showed that high Q-factors are not strictly necessary, especially if the resonances are periodic [105]. An important question here is to determine whether there is an optimal fluorescent coating thickness for the case of a capillary structure.

3.4 Results and discussion

3.4.1 WGM field calculations

The calculated electric field profiles for the first-order radial modes are shown as a function of film thickness in Fig. 3.4. The layer index was assumed to be 1.67, in agreement with ellipsometry results for a flat quantum-dot film made by similar methods [61]. For the thinnest films, much of the mode extends into the glass capillary, although a fraction remains in the analyte. As the film becomes thicker, the mode is concentrated into the film region from both sides. The TM mode profiles (not shown) evolved similarly.

When the fluorescent film is very thin, increasing its thickness leads to a nearly exponential increase in the radiation-limited Q-factor (Fig. 3.5(b),

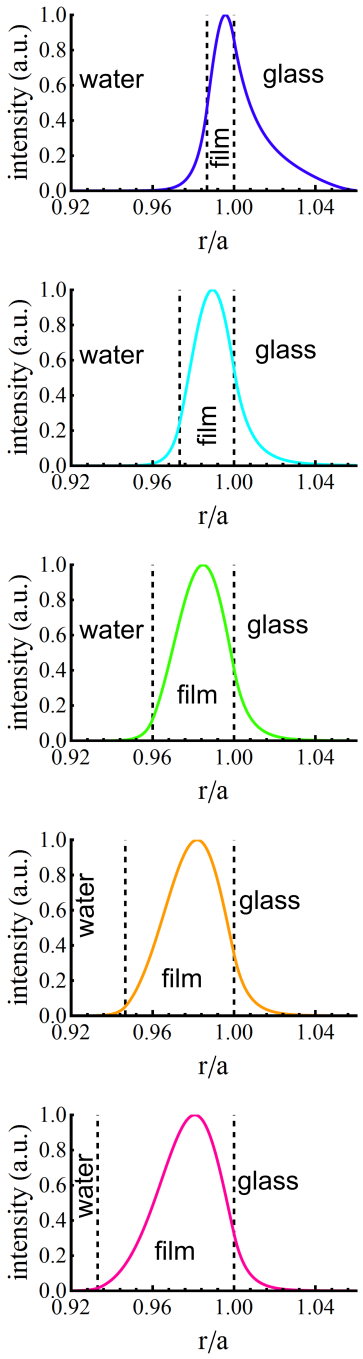

Figure 3.4: First-order mode profiles (angular mode number $l = 195$) for different film thicknesses, for a glass ($m_3 = 1.45$) capillary of inner radius 15 μm, with water in the channel ($m_1 = 1.33$). The coating thicknesses correspond to 0.2, 0.4, 0.6, 0.8, and 1.0 μm, and the refractive index is 1.67. The resonance wavelength for these modes is close to 770 nm.

similar to what happens for microspheres [206], as well as a decrease in the sensitivity (Fig. 3.5(c). However, as the film becomes thicker, the Q-factor tends to saturate. Once the mode field profile is completely inside the coating there is little further effect to increasing the thickness. The sensitivity of the first-order modes in FCM structures decreases monotonically over the calculated range of t (Fig. 3.5(c). For film thicknesses below $\sim 0.2\mu$m, the Q-factor becomes extremely low (*i.e.*, < 100), and for such thin coatings the finesse is so low that the FCMs may be impractical for refractometric sensing. Calculations also showed that the TM-polarized modes are more sensitive to refractive index changes in the analyte than are the TE-polarized ones, and have slightly lower Q-factors.

In the case of thin-walled LCORRs, the higher-order radial modes present an excellent option for improving the sensitivity [198] [207]. For the FCM structures investigated here, the situation is somewhat different. Essentially, the higher index of the wall material (compared to air in the case of LCORRs) gives the second-order radial modes a larger amplitude in the glass capillary wall (Fig. 3.6), similar to the behavior of an evanescent field of a bound waveguide mode. This implies that these modes will be much lossier than the first-order case. Thus, although the second-order modes do extend farther into the analyte for a 1-μm-thick film, the field profiles suggest that they are only weakly confining and would thus be difficult to observe in a fluorescence spectrum – in other words, FCMs are "single moded" [201], at least as long as the channel fluid index is not too high [198]. Furthermore, unlike the LCORR, in which a significant fraction of the field can extend into the analyte if the capillary walls are very thin, a relatively smaller fraction of the field extends into the FCM channel region for all coating thicknesses (essentially the WGM field profile is skewed in a manner that depends on the refractive indices of the three layers).

The Q-factors and sensitivities of the first three radial modes are compared in Fig. 3.7. The higher-order radial modes always have a greater sensitivity, although the Q-factors are orders of magnitude smaller. Thus, despite the

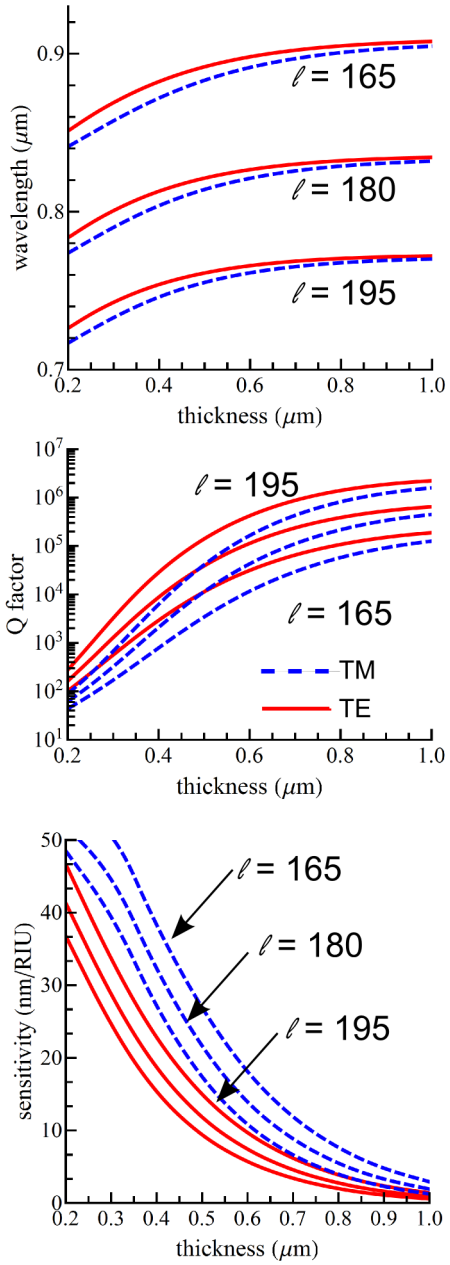

Figure 3.5: Resonance wavelength, Q-factor, and sensitivity for the first-order $l = 165, 180$, and 195 WGMs, as a function of layer thickness. In the center plot, the $l = 180$ mode occurs between the other two, but is not labeled. Solid red lines indicate TE, and dashed blue lines indicate TM polarization.

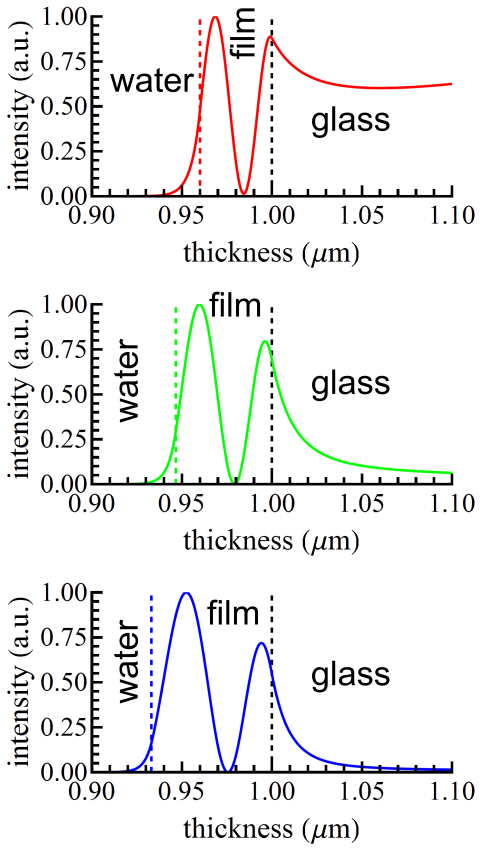

Figure 3.6: Second-order mode profiles (angular mode number $l = 195$) for different film thicknesses, for a glass ($m_3 = 1.45$) capillary of inner radius 15 μm, with water in the channel. The coating thicknesses are 0.6, 0.8, and 1.0 μm and the refractive index is 1.67. The peak wavelength for these modes is close to 705 nm. For the 600 μm film, the Q-factor is only ~ 60.

higher sensitivity, the $n = 2, 3$ modes will probably not be observable in a typical fluorescence spectrum, with a relatively low-index fluid such as water or ethanol in the capillary channel.

Fluorescent coatings may have non-negligible absorption at the emission wavelengths. In the case of the Si–QD films used in this work, the extinction coefficient was measured by ellipsometry to be $\kappa = 0.0006$ at wavelengths near 800 nm. While the structure of a flat QD film may be slightly different than it would be in a capillary, we assumed this value for the channel coating. Absorption losses do not significantly affect the resonance wavelength or the sensitivity, but they do of course limit the ultimate Q-factor achievable in an FCM device (Fig. 3.8). For $\kappa = 6 \times 10^{-4}$, the Q-factor for both polarizations saturates at around 1500 when the film thickness reaches approximately 300 nm (TE) or 400 nm (TM). This result will be compared with the experimental values shortly.

The effect of analyte absorption on the WGMs may offer an alternative transduction mechanism for sensing [208]. The total Q-factor is simply given by $1/Q_{total} = 1/Q_{rad} + 1/Q_{abs} + ...$, where Q_{rad} is the radiation limited Q-factor and Q_{abs} incorporates material-related losses such as absorption. Thus, material losses can be a dominant effect for some structures, especially for an FCM where the fluorescent layer is absorbing. In order to investigate this further, the Q-factors were calculated as a function of film thickness, for different values of the analyte extinction coefficient (Fig. 3.9). There are essentially three regimes, which depend on coating thickness. For coatings thinner than 300-400 nm, the Q-factors increase almost exponentially. In this regime, increasing the coating thickness greatly enhances modal confinement and reduces the fraction of the mode within the absorbing analyte. In the second regime, for coating thicknesses between about 0.4 and 1.5 μm, the Q-factors increase at a slower rate. In this regime, the main effect of increasing coating thickness is to decrease exposure of the mode field to the absorbing analyte. Finally, at a thickness about $\sim 1.5\mu$m, the effect of further thickening the coating becomes negligible, since there is essentially no longer any extension of the mode field

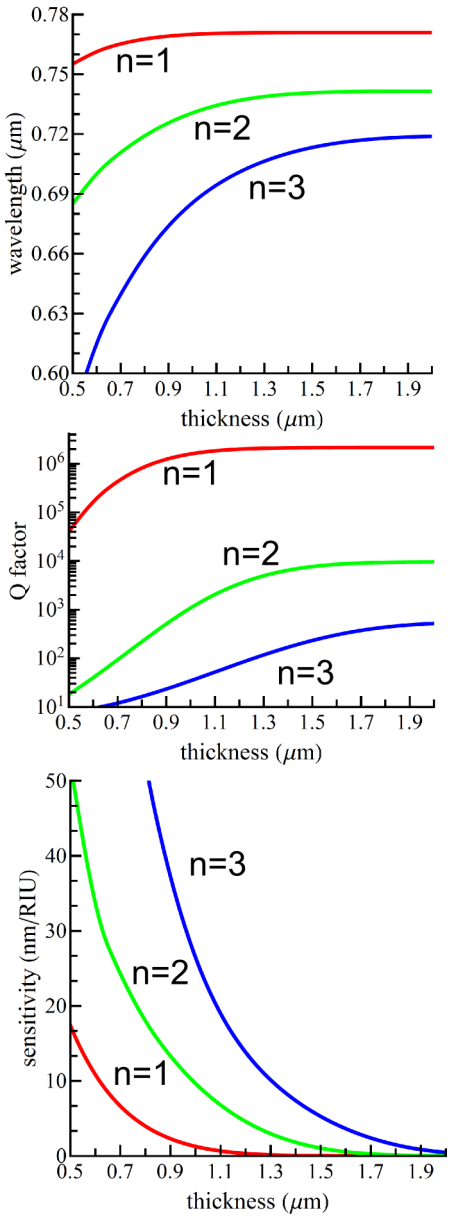

Figure 3.7: A comparison of the resonance wavelength, Q-factor, and sensitivity for the first three radial orders ($l = 195$, TM polarization).

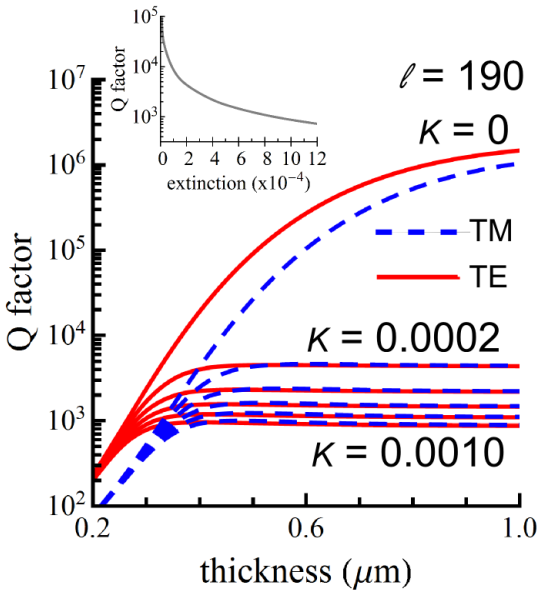

Figure 3.8: Resonance Q-factor for the first-order $l = 190$ WGM, as a function of absorbing layer thickness. The extinction coefficient steps in units of 0.0002. Solid red lines indicate TE, and dashed blue lines indicate TM polarization. The inset shows the Q-factor at saturation, as a function of extinction coefficient for a 2 μm thick coating.

into the analyte.

Of course, a real sample may have absorption both in the fluorescent coating and in the analyte. In that case, the effect of analyte absorption is smaller (in terms of a change in the Q-factor). Thus, using the change in Q due to analyte absorption as a sensing mechanism in FCMs would likely be difficult to achieve, requiring thin coatings and/or very low absorption in the QD layer.

3.4.2 Comparison with experiment

A representative capillary and the corresponding TM polarized WGM spectrum is shown in Fig. 3.10. The QD film appears as a bright line along the channel walls. Tracking a single bright band vertically along the image shows how that particular mode shifts in wavelength along the capillary due to changes in the film thickness. In the thicker-coating regions, the spectral map shows more detailed, patterned mode structure (Fig. 3.10, inset).

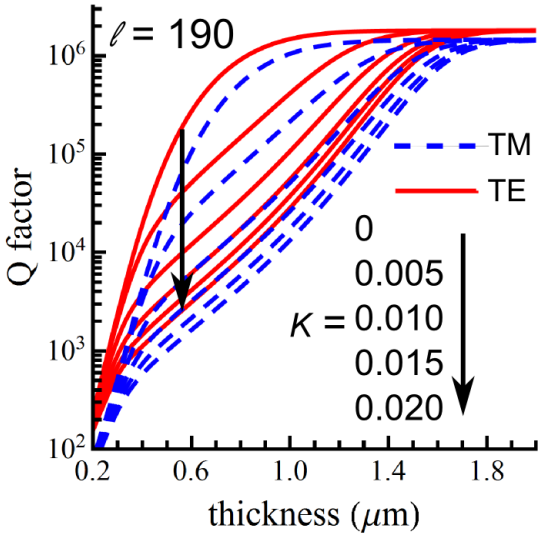

Figure 3.9: Resonance Q-factor for the first-order $l = 190$ WGM, as a function of analyte absorption. Solid red lines indicate TE, and dashed blue lines indicate TM polarization.

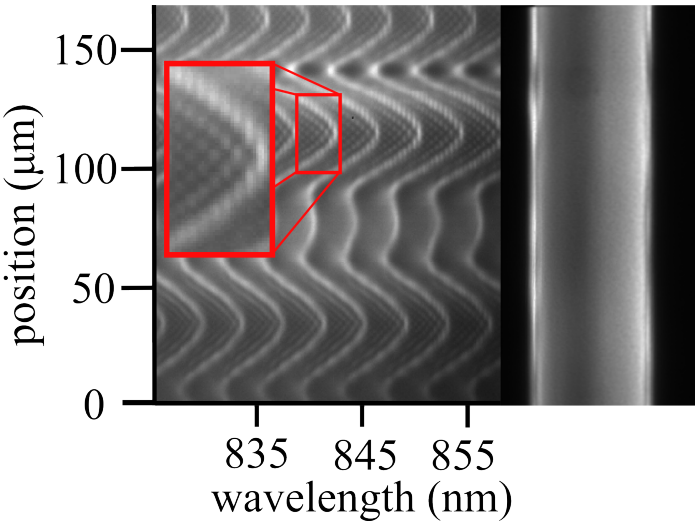

Figure 3.10: Fluorescence spatial-spectral map (left) of a section of micro-capillary and its corresponding TM spectrum. The inset shows finer mode structure in the thick region. The right side shows a fluorescence image of the capillary channel with the position scale approximately aligned to the spectral map.

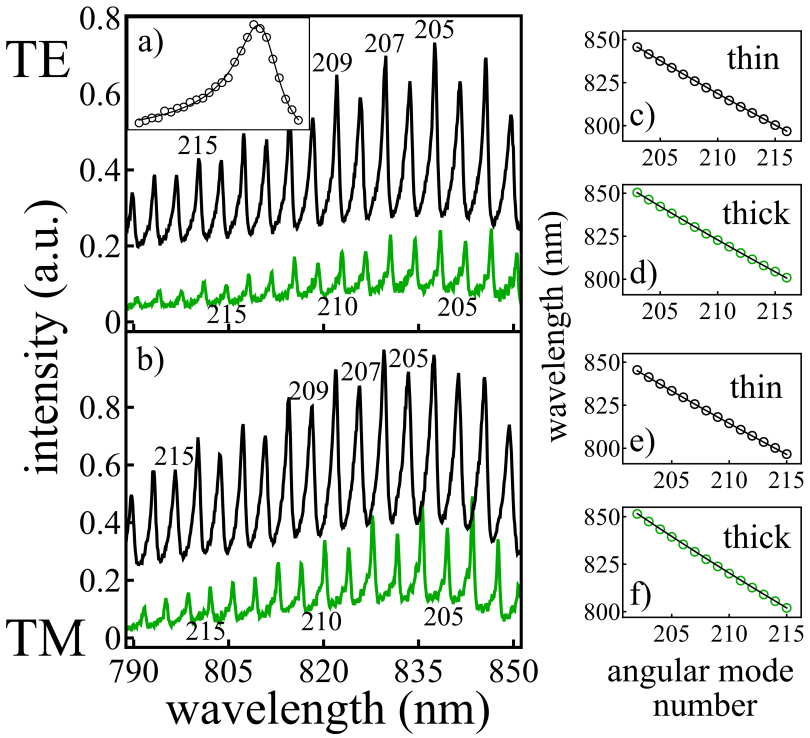

Figure 3.11: TE (a) and TM (b) polarized fluorescence spectra for thin (black lines) and thick (green lines) films on the microcapillary, with water in the channel. Data is offset for clarity. The inset in (a) shows the experimental $l = 206$ TM mode for the thin film on the microcapillary fit with the modified skewed Lorentzian function (Eq. 3.6). The sidebar (c-f) illustrates the agreement between experiment (data points) and theory (line) for films with a thickness of 695 nm (thin) and 930 nm (thick).

The WGMs are clear and well-formed in both polarizations, and are characterized by a free spectral range (FSR) of 3.6–4.0 nm, a visibility up to 0.4, and a finesse as high as 8.0 (Fig. 3.11). The modes tend to be highly asymmetrical and are skewed to shorter wavelengths. Thus, in order to estimate the resonance wavelengths, individual WGMs were cropped from the spectrum and fit with a modified skewed Lorentzian function [105] [209] given by

$$P(\lambda) = \frac{2A/\pi\gamma(\lambda)}{[1 + 4(\lambda - \lambda_0/\gamma(\lambda))^2]}. \tag{3.6}$$

Here, λ_0 is the central wavelength, A is a normalizing factor, and the peak

width γ describes the wavelength-dependence width:

$$\gamma(\lambda) = \frac{(1+B)\gamma_0}{1+Be^{a(\lambda-\lambda_0)}}. \tag{3.7}$$

Eq. 3.6 provides an excellent fit to the data (see Fig. 3.11(a), inset) and permits one to find the peak position more accurately than simply by visual estimation, although this equation does not have a specific physical meaning with respect to the WGMs.

The film thickness at any location in the capillary was estimated by modeling the peak positions of the experimental WGM spectra using Eqs. 3.2 and 3.3, and solving for the capillary radius and film thickness that matched the experimental observations. The results are shown in the sidebar of Fig. 3.11, for two regions of the FCM with water in the channel. The agreement between theory and experiment is excellent for coating thicknesses of 695 nm (thin region) and 930 nm (thick region), for both polarizations and for both fluids in the channel (water and ethanol), with a capillary radius of 17.2 μm, which is close to but somewhat outside the nominally $15 \pm 1\mu$m radius of these capillaries according to the manufacturer [210].

The mode skewing is due to a set of spiraling modes traveling with a component of the wavevector along the capillary axis [107] [211]. The data show that for thinner films, the WGMs are broadly skewed to shorter wavelengths, but no individual spiraling modes can be observed. For thicker films, the spiraling modes become better resolved into a set of small peaks on the short-wavelength side of the main one (Fig. 3.12). These modes are not simply higher-order radial modes, since they do not follow the expected spectral positions, Q-factors, or sensitivity for different fluids in the capillary channel (instead, they simply tend to closely follow the main WGM). Similar spiral mode effects have been seen previously in an LCORR structure [194], in which the spiral modes were sometimes resolvable (similar to Fig. 3.12: thick film) or otherwise appeared as a broad, short-wavelength skewing, more like the thin-coating spectra presented here. This skewing makes the measured Q-factors

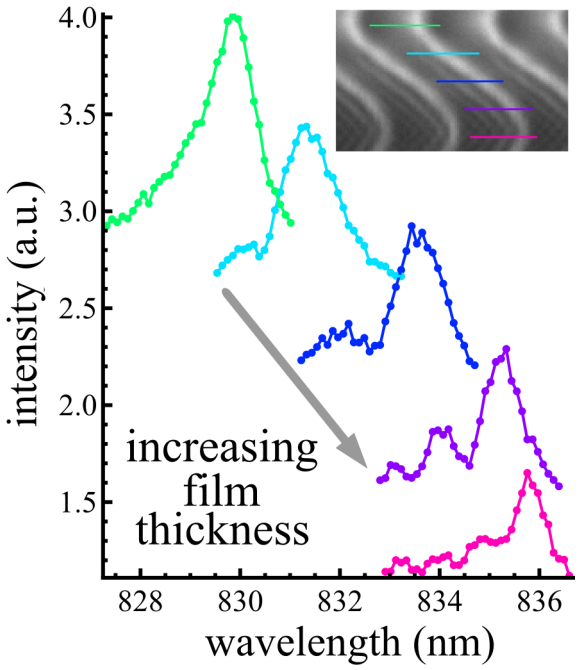

Figure 3.12: The experimental $l = 206$ TM mode for different coating thicknesses. The data has been offset for clarity. The top inset shows the spectral map from which the measurements were taken, with the line profiles color-coded to match the main spectra. The WGM Q-factor appears to increase as the skew modes become increasingly well resolved for the thicker coatings.

for the peaks shown in Fig. 3.12 lower than the theoretical ones for thinner coatings. When the main WGM becomes clearly separate from the adjacent set of spiral modes, however, the Q-factor was measured to be ~ 1450. This is in close agreement with the theoretical value shown in Fig. 3.8 for a film with $\kappa = 6 \times 10^{-4}$ (keeping in mind that the calculations described earlier do not model wave propagation along the cylinder axis).

The experimental and theoretical sensitivities are shown for two different film thicknesses in Fig. 3.13. The TM modes were always more sensitive, in agreement with theory. One surprising result in the experimental data is the appearance of an oscillation in the sensitivity of adjacent angular modes in some cases (this is especially noticeable for the "TM thin" data set). One set of alternating angular modes has sensitivities that agree well with theory, while the other set is much more sensitive. Similar effects were observed to some

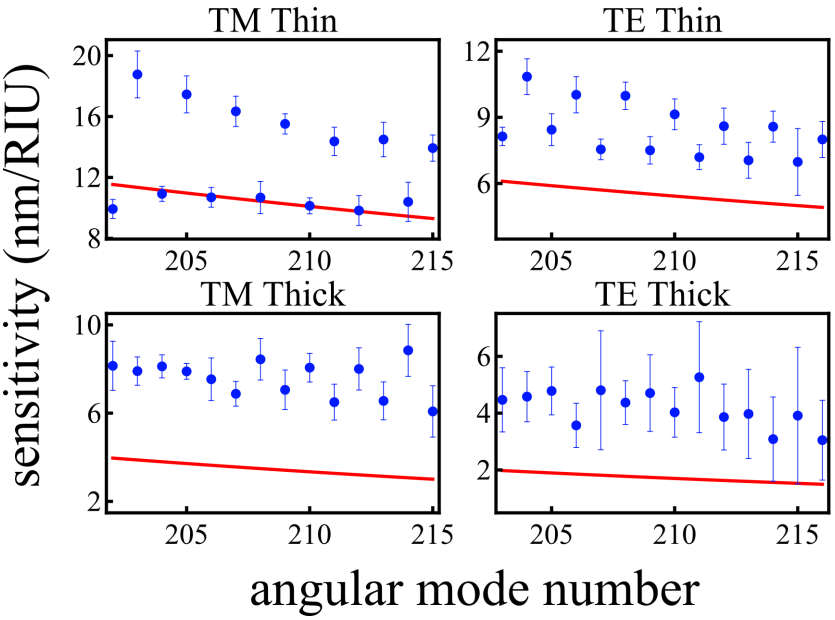

Figure 3.13: Measured (blue) and calculated (red) sensitivities as a function of angular mode number, for FCMs with a thin (695 nm) or thick (930 nm) QD coating. Note the variation in the sensitivities of alternating angular modes that is especially apparent in the thin film TM case. The theoretical sensitivity closely matches the lower-sensitivity group of modes. In the other cases, this alternating behavior is not as clear, and but all the modes are more sensitive to changes in the core index than would be predicted by theory. Error bars were calculated from the uncertainty in the peak fitting procedure for each WGM.

degree in several of the other spectra as well. In some cases, the alternating sensitivity pattern is not observable (*i.e.*, TE thick) but all of the modes are more sensitive than expected.

While a full study of the enhanced sensitivity effect is outside the scope of this work, we hypothesize that the periodic oscillations observed in Fig. 3.13 (which, in fact, correspond with intensity oscillations in some spectra in Fig. 3.11) can arise from an interference modulation effect. Fabry–Perot (F-P) type resonances in the film [212] could couple to the WGMs, but can be ruled out on account of the very large FSR for F–P resonances in the QD coating. Interior resonances of the capillary channel could also couple to the main WGMs, but these would have very low Q-factors associated with lossy external reflections

at the channel-coating interface. On the other hand, outer wall interferences similar to those reported in Ref. [213] could be important in the present case also.

Capillary wall interferences are caused by external reflection of a portion of the emitted fluorescence at the interface between the capillary wall and the outside air. Knight et al. [213] used a simple ray picture to describe the condition required for the wall reflections to interfere constructively with the core WGMs. Following their method, we find that there is nearly a 5:2 ratio for the resonance periods of the wall reflections and the core WGMs, respectively, for an outer capillary radius of 156 μm, in close agreement with the thickness measured for the same capillary with the jacket removed. This suggests the possibility that interference from wall reflections could cause the modulations observed in the peaks heights and sensitivity for alternating WGMs.

A complete investigation of this effect is outside the scope of the present work; here, we simply find that whenever a WGM moves from constructive to destructive interference with the calculated wall reflections (or vice versa) when the analyte in the channel changes, the sensitivity is higher than predicted for that mode. Analysis of the WGM spectra showed that this occurred for all the resonances in the thick film case ("high" peaks changed to "low" peaks, and vice versa, on changing from water to ethanol in the channel) so they are all "too sensitive", but for only one set of alternating angular resonances in the thin film case. If correct, this hypothesis implies that, by optimizing the capillary wall radius for a given structure, these interference modulations could in principle be used to improve the sensitivity of FCM structures beyond the values predicted from Eqs. 3.2 and 3.3.

3.5 Conclusions

In the first part of this work, we mapped the predicted behavior of the wavelength, Q-factor, and sensitivity over a wide range of coating thicknesses, for FCM-type refractometric sensors. Unlike the case for a microsphere, these

structures have no optimum coating thickness required to achieve the highest sensitivity. Instead, thinner films are always better, at least until the Q-factor degrades to the point at which the WGMs become difficult to resolve. The TM-polarized WGMs are also predicted to always have a higher sensitivity than the TE case. For thicker coatings, the Q-factors saturate at values depending on the losses in the fluorescent film. These results were in agreement with experiment, for an FCM in which silicon QDs were used as the high-index fluorescent coating layer.

By imaging the luminescence spectrum along the length of a capillary, a complete map of WGM spectral information can be obtained as a function of varying QD-coating thickness along the capillary length. This method can permit more information to be obtained than does the method used previously [61] [198], but it was found to be very sensitive to sample drift. The WGM spatial–spectra map showed considerable structure, featuring the development of spiraling modes that appeared on the short-wavelength tail of the main WGMs. These modes were always better resolved when the coating was thicker. Finally, many of the individual WGMs were more sensitive than predicted theoretically, reaching values of $\sim$ 20 nm/RIU for the first-order TM WGMs for a coating thickness of 695 nm. This could be due to an interference modulation associated with external reflections at the outer capillary wall. Coupling between core WGMs and wall interferences could be used in future to help improve the FCM sensitivity beyond the predicted limits for these devices.

3.6 Acknowledgements

The authors thank and acknowledge the NSERC Discovery and the AITF iCiNano programs for funding support, and the Veinot group for access to materials. Thanks to Ray DeCorby for a discussion on the capillary wall interferences.

Chapter 4

Refractometric sensitivity and thermal stabilization of fluorescent core microcapillary sensors: theory and experiment

A modified version of this chapter was published in Applied Optics 54 (6) 1331-1340 (2015) by S. Lane, F. Marsiglio, Y. Zhi, and A. Meldrum.

4.1 Abstract

Fluorescent-core microcapillaries (FCMs) present a robust basis for the application of optical whispering gallery modes toward refractometric sensing. An important question concerns whether these devices can be rendered insensitive to local temperature fluctuations, which may otherwise limit their refractometric detection limits, mainly as a result of thermorefractive effects. Here, we first use a standard cylindrical cavity formalism to develop the refractometric and thermally limited detection limits for the FCM structure. We then measure the thermal response of a real device with different analytes in the channel and compare the result to the theory. Good stability against

temperature fluctuations was obtained for an ethanol solvent, with a near-zero observed thermal shift for the transverse magnetic modes. Similarly good results could in principle be obtained for any other solvent (*e.g.*, water), if the thickness of the fluorescent layer can be sufficiently well controlled.

4.2 Introduction

Fluorescent-core microcapillaries (FCMs) represent a relatively new class of microcavity-based optical sensor. They are formed by coating the channel walls of a conventional glass capillary with a thin, high-refractive-index fluorescent film [136] [61] [214] [201]. The FCM is then excited with a short wavelength laser or LED, forming a cylindrical optical cavity. Because the film index is higher than that of the capillary walls, a fraction of the fluorescence emitted inside the film is confined to propagate around the inner circumference of the capillary [97]. The resulting interference leads to a modulation of the emitted fluorescence at the resonant cavity wavelengths.

These resonances are known as cylindrical whispering gallery modes (WGMs). The electric field of the WGMs can interact with analytes in the capillary channel (Fig. 3.1(a)), forming the basic sensing transduction mechanism for FCM-type devices. Changes in the refractive index of the material in the channel cause small shifts of the resonances, which can be measured by curve fitting or Fourier shift techniques [105]. This resonance shift method has been used to sense a variety of different compounds dissolved in water- or alcohol-based solvents [214] [84]. FCMs are also compatible with heavy oils [198] and can be used for protein biosensing [139].

An important issue with fluorescent core microcapillaries concerns local temperature fluctuations. Any change in the temperature of the environment can lead to a shift of the resonant wavelengths. This effect arises from thermal expansion of the capillary, and from a temperature-induced change in the refractive index of the fluorescent film and capillary wall (*i.e.*, the thermorefractive effect). While this may seem advantageous for temperature sensing,

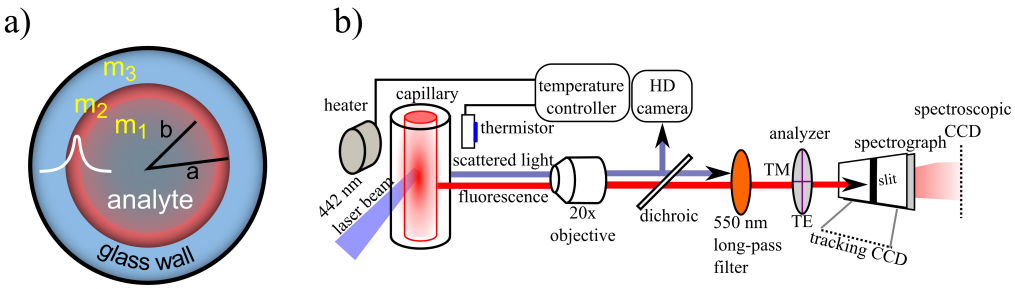

Figure 4.1: (a) Cross-sectional diagram of an FCM illustrating the channel analyte (refractive index m_1), the high-index fluorescent layer (index m_2), and the capillary wall (index m_3). The QD film thickness is given by $t = a - b$. The electric field of the WGM extends into the analyte region, as illustrated by the red shading and the white "wave" that represents the electric field profile of a resonance. (b) Diagram of the experimental setup.

thermal fluctuations can affect the lower boundary on the detection limit for chemical sensing. In other words, resonance shifts due to thermal fluctuations can compete with the refractometric shifts that one actually wants to sense. "Self-tuning" or "mode latching" effects have been shown to be able to compensate for thermal drift in evanescently pumped WGMs (as opposed to fluorescence) [215] [216], but cannot readily eliminate the effects of external (*e.g.*, laboratory) temperature variations.

Methods for compensating thermal fluctuations have been studied in liquid core optical ring resonators (LCORRs) [217] [204], microspheres [218] [219], microdisks [220] [192] [221] [222], and planar multilayer stacks [223]. LCORRs are especially applicable to the current work, since they are similar to the FCMs investigated here. LCORRs are thin-walled capillaries in which the WGMs are excited evanescently, using a tunable laser coupled to a waveguide or tapered fiber. Theory suggested an ideal wall thickness of around 1.7 μm for the first-order modes, where the negative thermorefractive effect of water is exactly balanced by the positive thermo-optic coefficient of the capillary wall. However, a zero thermal shift has not been demonstrated experimentally,

possibly because of the difficulty in creating and using such a fragile thin-walled structure [122] [125].

The purpose of the current work was, first, to examine the perturbation-based approach to calculating the sensitivity of an FCM-type WGM-based sensor. The second aim was to use both theory and experiment to investigate whether FCMs can be practically constructed to be insensitive to local temperature fluctuations. The refractive index contrast between the confining layer (the fluorescent coating) and the outside region (the glass capillary wall) is smaller in FCMs than in LCORRs, which have a glass-to-air interface. Thus, although FCMs are more robust than LCORRs, the conditions for thermal stabilization may be considerably harder to achieve.

4.3 Experiment

FCMs were synthesized using a recently developed capillary channel coating technique [140]. Briefly, commercial glass capillaries with a nominal inner radius of 15 μm and an outer radius of 360 μm were filled with a solution of hydrogen silsesquioxane (HSQ: "$H_8Si_8O_{12}$") dissolved in methyl isobutyl ketone [224]. After filling the capillaries, they were annealed in two stages. The first stage evaporates the solvent at 300 °C and leaves an oxide film on the channel walls The second stage collapses the HSQ structure at 1100 °C. This decomposes the film into fluorescent silicon quantum dots (QDs) embedded in a silica glass matrix [65], which coats the capillary channel. The Si-QD film has a refractive index near 1.67, which is significantly higher than the glass wall (index $m_1 \approx 1.45$) and thus permits the development of the WGMs. A schematic illustrating the structure is shown in Fig. 4.1(a).

The fluorescence spectra were measured with an SBIG SGS spectrograph interfaced to an ASI inverted microscope with a motorized stage. The 442 nm line of a HeCd laser was used as the excitation source, at a power about 50 mW weakly focused onto the capillary. The fluorescence spectra were calibrated with an HgAr lamp and corrected for the spectral efficiency by using

a black-body calibration light source. A polarizer in the microscope's beam path was used to select the TM modes (electric field parallel to the capillary radius; Fig. 4.1(b)), since they have a higher sensitivity than the TE case (see Section 4.4). A resistive heating apparatus was built directly around the capillary, including aluminum and plastic heat- and air-draft-shields, which permitted the temperature to be controlled to within 0.1 °C. A diagram of the experimental setup and measurement system is shown in Fig. 4.1(b). Either water, ethanol, or ethylene glycol (EG) were pumped into the capillary and the fluorescence spectrum was measured using a spectrometer with a pitch of 0.1 nm per pixel, as the temperature was raised from 25 °C to 40 °C at a ramp rate of 0.25 °C/min. The mode shifts, $d\lambda$, were extracted from the periodic WGM spectrum using Fourier shift methods (see [105]).

4.4 Theory

The sensitivity of the resonant wavevector, k_0, to refractive index perturbations in the surrounding medium was derived by Teraoka and Arnold for the case of a layered sphere [202] [203] [225]. A similar method seems to have been used by Lin et al. for a cylinder [204]. In order to model the thermal response of an FCM structure, we therefore start from the beginning, following the perturbation model of Teraoka and Arnold and applying it to the case of a layered cylinder. In order to be consistent with the sphere model, the polarization directions are defined with respect to the WGM plane of propagation. Thus, the transverse electric (TE) modes have the electric field parallel to the cylinder axis, whereas the transverse magnetic (TM) modes have a radial or azimuthal polarization of the E-field.

Adopting Stratton's notation (see [226]) but with the polarization direc-

tions as defined above, we have for the TE case assuming $k_z = 0$:

$$E_r = 0, \tag{4.1}$$

$$E_\phi = 0, \tag{4.2}$$

$$E_z = J_l(mk_0r), \tag{4.3}$$

where the subscripts r, ϕ, and z indicate the radial, azimuthal, and axial directions, respectively, J_l is the Bessel function of order l, and m is the refractive index (the symbol n is reserved to describe the radial mode order). For the TM polarization, the electric field is described according to [226]

$$E_r = \frac{-1}{k_0 m^2 r}\frac{l}{r}J_l(mk_0r), \tag{4.4}$$

$$E_\phi = \frac{-i}{k_0 m^2}\frac{d(J_l(mk_0r))}{dr}, \tag{4.5}$$

$$E_z = 0. \tag{4.6}$$

In a three-layer cylinder such as an FCM, the refractive index is a piecewise function of the radius:

$$m(r) = \begin{cases} m_1, & r \leq b \\ m_2, & b < r \leq a, \\ m_3, & r > a \end{cases} \tag{4.7}$$

where a is the inner radius of the bare capillary and b is the distance from the cylinder axis to the film of thickness $t = a - b$, shown in Fig. 4.1(a). The expressions for the electric field are somewhat different in the various regions because of the boundary conditions. For the TE modes we have

$$\vec{E} = S_l(r)e^{il\varphi}\hat{z}, \tag{4.8}$$

where the radial field function is

$$S_l(r) = \begin{cases} A_l J_l(m_1 k_0 r), & r \leq b \\ B_l H_l^{(2)}(m_2 k_0 r) + C_l H_l^{(1)}(m_2 k_0 r), & b < r \leq a. \\ D_l H_l^{(1)}(m_3 k_0 r), & r > a \end{cases} \tag{4.9}$$

We use the Bessel function $J_l(x)$ for the field in the inner layer, and the Hankel functions of the first ($H_l^{(1)}(x)$) and second ($H_l^{(2)}(x)$) kind for the outer two layers, which represent outgoing and incoming plane waves at $r \to \infty$. A_l, B_l, C_l, and D_l are proportionality constants.

For a TM mode with the appropriate boundary conditions, the electric field is described by a slightly different equation:

$$\vec{E} = \frac{-e^{il\phi}}{k_0[m(r)]^2}\left[\frac{l}{r}T_l(r)\hat{r} + i\frac{dT(m(r)k_0 r)}{dr}\hat{\phi}\right], \tag{4.10}$$

with

$$T_l(r) = \begin{cases} a_l J_l(m_1 k_0 r), & r \leq b \\ b_l H_l^{(2)}(m_2 k_0 r) + c_l H_l^{(1)}(m_2 k_0 r), & b < r \leq a. \\ d_l H_l^{(1)}(m_3 k_0 r), & r > a \end{cases} \tag{4.11}$$

For simplicity and without loss of generality we can set one of the constants equal to unity in Eqs. 4.9 and 4.11 (*e.g.*, $C_l = c_l = 1$). The radial functions $S_l(r)$ and $T_l(r)$ satisfy the cylindrical harmonic equation:

$$\frac{d^2 Z_l}{d\rho^2} + \frac{1}{\rho}\frac{dZ_l}{d\rho} + \left(1 - \frac{l^2}{\rho^2}\right) Z_l = 0, \tag{4.12}$$

where $\rho = mkr$ and Z_l is proportional to the amplitude of the electric field.

The resonant wavevector is found by applying the appropriate boundary conditions across the interfaces at a and b, as shown for a sphere in Refs. [203] [225]. For a cylinder (TE case), the fields and their derivatives are continuous

across all interfaces, yielding

$$\frac{m_3 H_l^{(1)\prime}(m_3 k_0 a)}{m_2 H_l^{(1)}(m_3 k_0 a)} = \frac{B_l H_l^{(2)\prime}(m_2 k_0 a) + H_l^{(1)\prime}(m_2 k_0 a)}{B_l H_l^{(2)}(m_2 k_0 a) + H_l^{(1)}(m_2 k_0 a)} \tag{4.13}$$

with

$$B_l = \frac{m_2 J_l(m_1 k_0 b) H_l^{(1)\prime}(m_2 k_0 b) - m_1 J_l'(m_1 k_0 b) H_l^{(1)}(m_2 k_0 b)}{-m_2 J_l(m_1 k_0 b) H_l^{(2)\prime}(m_2 k_0 b) + m_1 J_l'(m_1 k_0 b) H_l^{(2)}(m_2 k_0 b)}. \tag{4.14}$$

Similar expressions can be written for the TM polarization, with slightly different boundary conditions:

$$\frac{m_2 H_l^{(1)\prime}(m_3 k_0 a)}{m_3 H_l^{(1)}(m_3 k_0 a)} = \frac{b_l H_l^{(2)\prime}(m_2 k_0 a) + H_l^{(1)\prime}(m_2 k_0 a)}{b_l H_l^{(2)}(m_2 k_0 a) + H_l^{(1)}(m_2 k_0 a)} \tag{4.15}$$

and

$$b_l = \frac{m_1 J_l(m_1 k_0 b) H_l^{(1)\prime}(m_2 k_0 b) - m_2 J_l'(m_1 k_0 b) H_l^{(1)}(m_2 k_0 b)}{-m_1 J_l(m_1 k_0 b) H_l^{(2)\prime}(m_2 k_0 b) + m_2 J_l'(m_1 k_0 b) H_l^{(2)}(m_2 k_0 b)} \tag{4.16}$$

To avoid confusion, we write explicitly the meaning of the prime notation in the Bessel and Hankel functions: $J_l' = d(J_l(mkb))/(mk \cdot dr)$. One then uses a numerical solver (in our case, Mathematica's "FindRoot"function) to find the values of complex k_0 that satisfy Eqs. 4.13-4.16.

In order to find the sensitivity, one can next use the perturbation method to find the fractional resonance wavevector shift induced by a local change in the refractive index, as developed for a sphere by Teraoka and Arnold [203] [225]:

$$\frac{dk}{k} = -\frac{1}{2} \frac{\int_{V_p} \partial \varepsilon_r \vec{E}_0^* \cdot \vec{E}_p d^3 r}{\int_V \varepsilon_r \vec{E}_0^* \cdot \vec{E}_0 d^3 r} \tag{4.17}$$

where $\vec{E}_0$ is the electric field before the change in refractive index and $\vec{E}_p$ is the perturbed field after the change. The integration in the denominator is over all space (V), while the integration in the numerator is over only the region

in which the index of refraction has been changed (V_p), *i.e.* the innermost layer of the FCM ($0 < r < b$). The relative permittivity is $\varepsilon_r = m^2$ so $d\varepsilon = d(m^2) = 2mdm$.

The TE mode is the simplest and we proceed with it first. The denominator of Eq. 4.17 consists of three terms:

$$\int_V \varepsilon_r \vec{E}_0^* \cdot \vec{E}_0 d^3r = 2\pi m_1^2 \int_0^b r|A_l J_l(m_1 k_0 r)|^2 dr + m_2^2 \int_b^a r|B_l H_l^{(2)}(m_2 k_0 r) + C_l H_l^{(1)}(m_2 k_0 r)|^2 dr + m_3^2 \int_a^\infty r|D_l H_l^{(1)}(m_3 k_0 r)|^2 dr.$$

These integrals are dimensionless with a change of variable, $x_i \equiv m_i k_{0,1} r$, where $i = 1, 2, 3$ for each of the three regions and $k_0 = k_{0,1} + ik_{0,2}$. Using $\tilde{x} \equiv x(1 + ik_{0,2}/k_{0,1})$, we have

$$\int_V \varepsilon_r \vec{E}_0^* \cdot \vec{E}_0 d^3r = \frac{2\pi}{k_{0,1}^2}(I_1 + I_2 + I_3), \tag{4.18}$$

where

$$I_1 = \int_0^{m_1 k_{0,1} b} x|A_l J_l(\tilde{x})|^2 dx \tag{4.19}$$

$$I_2 = \int_{m_2 k_{0,1} b}^{m_2 k_{0,1} a} x|B_l H_l^{(2)}(\tilde{x}) + H_l^{(1)}(\tilde{x})|^2 dx \tag{4.20}$$

$$I_3 = \int_{m_3 k_0 a}^{\infty} x|D_l H_l^{(1)}(\tilde{x})|^2 dx. \tag{4.21}$$

Note that Eqs. 4.20–4.21 are explicitly real and are easily integrated (numerically) in standard math packages. For example, Eq. 4.20 can simply be rewritten as $I_1 = \int_0^{m_1 k_{0,1} b} x A_l J_l(x\frac{k_0}{k_{0,1}})|^2 dx$, with k_0 and $k_{0,1}$ taken from the solutions of Eqs. 4.13-4.16. The extra "x" in the integral in Eqs. 4.20-4.21 (not present, *e.g.*, in Ref. [204]) means that these terms stand for the volume-integrated energy, in the same way that Refs. [203] [225] used the Ricatti-Bessel functions to describe the refractometric sensitivity of a sphere.

In contrast, the numerator of Eq. 4.17 consists of just one term:

$$\int_{V_p} \partial\varepsilon_r \vec{E}_0^* \cdot \vec{E}_p d^3r = \frac{2\pi}{(k_{0,1}m_1)^2} d(m_1^2) I_1, \tag{4.22}$$

so that

$$\frac{dk_0}{k_0}_{TE} = \frac{-d(m_1)}{m_1} \frac{I_1}{I_1 + I_2 + I_3}. \tag{4.23}$$

Finally, the refractometric sensitivity is straightforwardly related to the fractional wavevector shifts via

$$S_{TE} = \frac{d\lambda_0}{dm_1} \tag{4.24}$$

$$= -\frac{\lambda_0}{dm_1} \cdot \frac{dk}{k_0} \tag{4.25}$$

$$= \frac{\lambda_0}{m_1} \cdot \frac{I_1}{I_1 + I_2 + I_3}. \tag{4.26}$$

For the TM modes, we first rewrite the differential equation (Eq. 4.12) as

$$r^2 \frac{d^2 Z_l}{dr^2} + r \frac{dZ_l}{dr} + ((m(r)k_0 r)^2 - l^2) Z_l = 0. \tag{4.27}$$

So now for the denominator of Eq. 4.17 we have

$$\int_V \varepsilon_r \vec{E}_0^* \cdot \vec{E}_0 d^3r = 2\pi \int \frac{1}{|k|^2 (m(r))^2} \left[(\frac{l}{r})^2 |T(mk_0 r)|^2 + \frac{dT(m(r)k_0 r)}{dr} \cdot \frac{dT^*(m(r)k_0 r)}{dr} \right] r dr, \tag{4.28}$$

where the integration is added piecewise over the three separate regions. One can simplify by integrating Eq. 4.28 by parts. For each region, concerning the term with the product of derivatives in Eq. 4.28, we let

$$u = r\frac{dT}{dr} \text{ and } dv = \frac{dT^*}{dr} dr, \tag{4.29}$$

so that

$$u = \left(r\frac{d^2T}{dr^2} + \frac{dT}{dr} \right) dr = r\left[\frac{l^2}{r^2} - (m(r)k)^2 \right] T, \tag{4.30}$$

$$v = T^*, \tag{4.31}$$

where we have used Eq. 4.27 to simplify the du term. Thus we obtain for each region

$$2\pi \left[r\frac{dT}{dr}T^*|_{r1}^{r2} + \int_{r1}^{r2} (m(r)k)^2 |T(m(r)kr)|^2 r dr \right], \tag{4.32}$$

in which the l^2 term cancels out in each case. Adding up the contributions from each layer, all the interface derivative terms cancel and we are left with

$$\int_V \varepsilon_r \vec{E}_0^* \cdot \vec{E}_0 d^3r = \frac{2\pi(k_0)^2}{|k_0|^2} \cdot \left[\int_0^b |T(m_1 kr)|^2 r dr + \int_b^a |T(m_2 kr)|^2 r dr + \int_a^\infty |T(m_3 kr)|^2 r dr \right]. \tag{4.33}$$

In order to deal with the fact that k_0 is complex but the integrals must be real, we note that Eq. 4.29 could also have been written in its conjugate form, where $u = rdT^*/dr$ and $dv = (dT/dr)dr$. With this change, we proceed as before, obtaining an identical version of Eq. 4.33, except that the numerator of the prefactor now has $(k_0^*)^2$ instead of $(k_0)^2$. The end result can be written as the half-sum of the two, yielding

$$\int_V \varepsilon_r \vec{E}_0^* \cdot \vec{E}_0 d^3r = \frac{\pi(k_0^2 + (k_0^*)^2)}{k_{0,1}^2 |k_0^4|} \left[\frac{I_1}{m_1^2} + \frac{I_2}{m_2^2} + \frac{I_3}{m_3^2} \right], \tag{4.34}$$

in which the energy terms, $I_i (i = 1, 2, 3)$, are identical in form to those shown in Eqs. 4.20-4.21, except they now use the TM solutions and coefficients.

For the numerator of Eq. 4.17, we integrate over only the first region so the boundary derivative term does not disappear, yielding

$$\int_{V_p} \partial\varepsilon_r \vec{E}_0^* \cdot \vec{E}_p d^3r = \frac{2\pi}{2|k_0|^2} \frac{d(m_1^2)}{m_1^4} \left[b\left[\frac{dT}{dr}T^* + T\frac{dT^*}{dr} \right]_b + \frac{k_0^2 + (k_0^*)^2}{k_{0,1}^2} I_1 \right] \tag{4.35}$$

Thus, for the TM case the refractometric sensitivity is

(4.36)
$$S_{TM} = \lambda_0 \frac{(2k_1^2)}{m_1^3(k_0^2 + (k_0^*)^2)} \cdot \frac{b|a_l|^2\left(\frac{dJ_l^*(m_1 k_0 r)}{dr}\|_b J_l(m_1 k_0 b) + J_l^*(m_1 k_0 b)\frac{dJ_l(m_1 k_0 r)}{dr}\|_b\right) + \frac{k_0^2+(k_0^*)^2}{k_{0,1}^2} I_1}{\left[\frac{I_1}{m_1^2} + \frac{I_2}{m_2^2} + \frac{I_3}{m_3^2}\right]}.$$

The wavelength shift due to thermal fluctuations is generally assumed to be proportional to the fractional changes in the effective refractive index, m_{eff}, and the thermal expansion of the capillary radius [204] [122], such that

(4.37)
$$\frac{d\lambda_0}{\lambda} = \frac{dm_{eff}}{m_{eff}} + \frac{da}{a}.$$

The effective refractive index is usually approximated as $m_{eff} = f_1 m_1 + f_2 m_2 + f_3 m_3$, where $f_{i,(TE)} = I_i/(I_1+I_2+I_3)$ and $f_{i,(TM)} = I_i/m_3^2/\frac{I_1}{m_1^2}+\frac{I_2}{m_2^2}+\frac{I_3}{m_3^2}$. These are slightly different than previous equation 4.18, since our definition of the "I_i" energy integrals include the m^2 factor. The thermally induced wavelength shift is obtained by dividing both sides of Eq. 4.38 by dT, yielding

(4.38)
$$\frac{d\lambda}{dT} = \lambda\left(\frac{1}{m_{eff}}\frac{dm_{eff}}{dT} + \frac{1}{a}\frac{da}{dT}\right).$$

Combining these equations yields

(4.39)
$$\frac{d\lambda_{min,TM}}{dT} = \lambda_{)}\left(\frac{(I_1/m_1^2)\kappa_1 + (I_2/m_2^2)\kappa_2 + (I_3/m_3^2)\kappa_3}{(I_1/m_1) + (I_2/m_2) + (I_3/m_3)} + \alpha\right).$$

and

(4.40)
$$\frac{d\lambda_{min,TE}}{dT} = \lambda_0\left(\frac{I_1\kappa_1 + I_2\kappa_2 + I_3\kappa_3}{m_1 I_1 + m_2 I_2 + m_3 I_3} + \alpha\right),$$

where the thermo-optic coefficient in each layer is given by $\kappa_1 = dm_1/dT$, and the thermal expansion coefficient is $\alpha = (1/a)da/dT$. Eqs. 4.39-4.40 represent the thermal sensitivity of the FCM structure. Finally, the temperature-shift-

induced detection limit is given by

$$DL_{thermal,(TE,TM)} = \left| \frac{d\lambda_{min,(TE,TM)}}{dT} \cdot \frac{dT}{S_{TE,TM}} \right|. \tag{4.41}$$

where dT/S is the ratio of the local temperature fluctuation, dT, to the refractometric sensitivity S. Equation 4.41 represents the thermal contribution to the refractometric detection limit, which is the same whether $d\lambda/dT$ is positive or negative (hence the absolute values). In a given sensor device, one wants $DL_{thermal}$ to be as close as possible to zero.

4.5 Results and discussion

These calculations allow the landscape of refractive index sensitivity, thermal shift, and detection limit to be mapped over a range of typical input parameters for an FCM structure. In Fig. 3.2(a), the sensitivity is shown as a function of QD layer thickness for 10 mode orders covering a wavelength range from approximately 720 to 770 nm, for an FCM with a radius of 15 μm. The sensitivity decreases with increasing film thickness, as more of the mode energy spreads into the capillary wall (*i.e.*, for a very thick film, almost none of the mode profile would extend into the capillary channel). The sensitivities are fairly high ($\sim$ 20–30 nm/refractive index unit (RIU)) for QD films of the thickness shown; for thicker films the experimentally measured sensitivity is of the order of $\sim 5 - 10$ nm/RIU [84]. The effect of angular mode order is more subtle, but indicates a decreasing sensitivity as the angular order increases. The sensitivity for EG is higher than it is for water, due to the higher index of refraction of the former solvent.

In order to calculate the thermal shifts and associated detection limit, we use values of $\kappa_{silica} = 11.9 \times 10^{-6}$ K^{-1}, $\alpha_{silica} = 5.5 \times 10^{-7}$ K^{-1} (from Ref. [227]), $\kappa_{water} = -0.8 \times 10^{-4}$ K^{-1}, and $\kappa_{EG} = -2.6 \times 10^{-4}$ K^{-1}. The thermo-optic coefficient for the ensembles of Si-QDs in a silica matrix, κ_{Si-QD}, should be $\sim 1 \times 10^{-5}$ K^{-1} for compositions similar to those used in the experimental

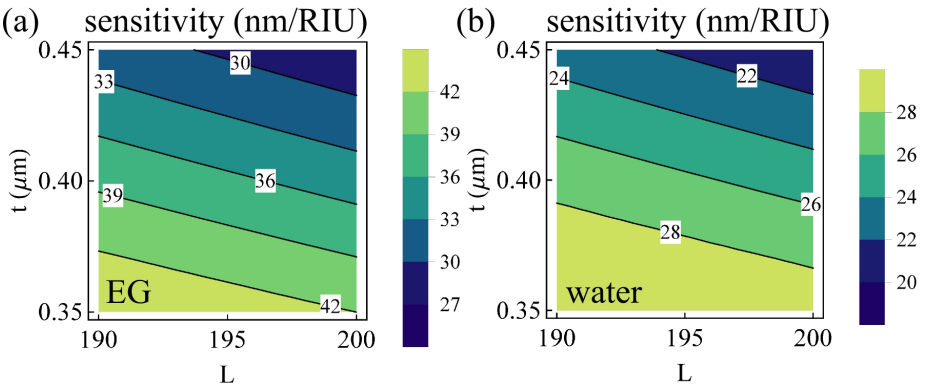

Figure 4.2: Refractometric sensitivity maps (TM polarization, $n = 1$ radial modes) for a 15-μm-radius capillary with a QD coating of thickness t and index $m_2 = 1.67$, for ethylene glycol (left) and water (right) in the channel. The angular orders, $L = 190 - 200$, cover a wavelength range of $\sim$ 720-770 nm. TE maps were essentially similar but had slightly lower sensitivities.

section discussed below [228]. FCMs generally work only with the first-order ($n = 1$) radial modes, so only these modes are mapped in Fig. 4.3. A temperature variation of 1 K was assumed to estimate the thermal-fluctuation-controlled refractometric detection limit; for different values, the DL scales proportionally. The results show that a zero thermal shift and complete thermal stability can be achieved for an EG solvent for angular orders consistent with the QD emission spectrum, for a film thickness of approximately 400 to 450 nm. In contrast, for the case of water, thermal stability cannot be achieved unless the film is thinner than those plotted in Fig. 4.3. For water, the thermal-fluctuation-limited DL is close to 10^{-4} RIU over the range of conditions shown. The DL is higher (*i.e.*, worse) for water than for EG mainly because of water's lower index of refraction, which decreases the mode energy fraction in the solvent.

One interesting structure in the shift map for water in the capillary channel is apparent in Fig. 4.3(b1), which shows a "bending backward" or reversal of the contour lines, indicating the existence of a thickness at which the thermal shift is minimized for a given L. The thermal shift depends fundamentally on the fraction of the mode energy located in each layer, weighted according to the thermo-optic coefficients. If the film is made thinner, at first, more of

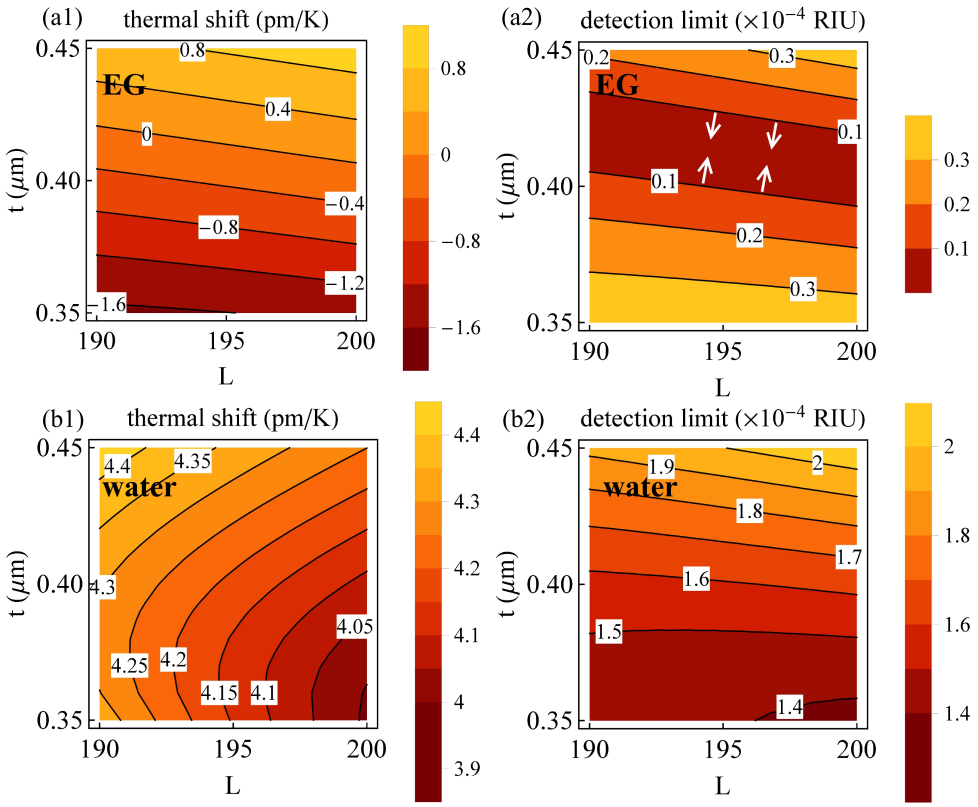

Figure 4.3: Map of thermal shifts and detection limits for various film thicknesses, for an EG- or water-filled capillary. (a1) Thermal shift map for EG solvent. (a2) Thermal-fluctuation-limited detection limit for EG. The arrows point into the zero DL valley. (b1) and (b2) Same as above, except for a water solvent.

the mode energy extends into the channel, causing a smaller thermal shift as a result of the negative κ_{water}. Eventually, however, for even thinner films a significant fraction of the mode begins to extend into the glass capillary wall and the overall thermal shift begins to increase again. This is not found over the same range of conditions for EG, mainly because of its higher refractive index and significantly more negative thermo-optic coefficient.

In order to investigate the effect of the channel fluid, one can fix the thickness (*e.g.*, at 360 or 400 nm in Fig. 4.4) and map the thermal shifts and detection limits over a range of refractive indices and thermo-optic coefficients typical of common solvents. For both coating thicknesses, the zero-detection-limit valley is located near the bottom right corner of the map, corresponding to a large m_1 and a strongly negative thermo-optic coefficient. The landscape is fairly flat as one goes from air to water in the channel, and becomes much steeper around the locations of ethanol and EG. As the coating gets thicker, the valley moves farther off to the lower right, since it would require even more extreme solvents to compensate the positive thermo-refractive shift of the QD layer and the glass capillary wall. Thus, overall, stabilization against thermal fluctuations can be achieved in FCMs, but only for relatively high-index solvents, such as ethanol or EG. For water, the QD film would have to be thinner than 350 nm (*i.e.*, thinner than we have so far been able to prepare experimentally).

According to theory, it should be possible to achieve stability against temperature fluctuations for solvents with thermo-optic and refractive properties similar to ethanol or EG, depending on the coating thickness. Comparing the effect of film thickness is experimentally difficult, however, since we cannot currently control or measure it with precision. Further, there is no obvious way to compare the film thickness in one capillary to that in another. However, a single capillary can show a varying thickness along the channel length [84], probably due to irregularities in the solvent evaporation during annealing, which causes clear shifts in the resonance wavelengths. The effect is obvious in Fig. 4.5(a), which shows a spectral image of the capillary WGMs taken with

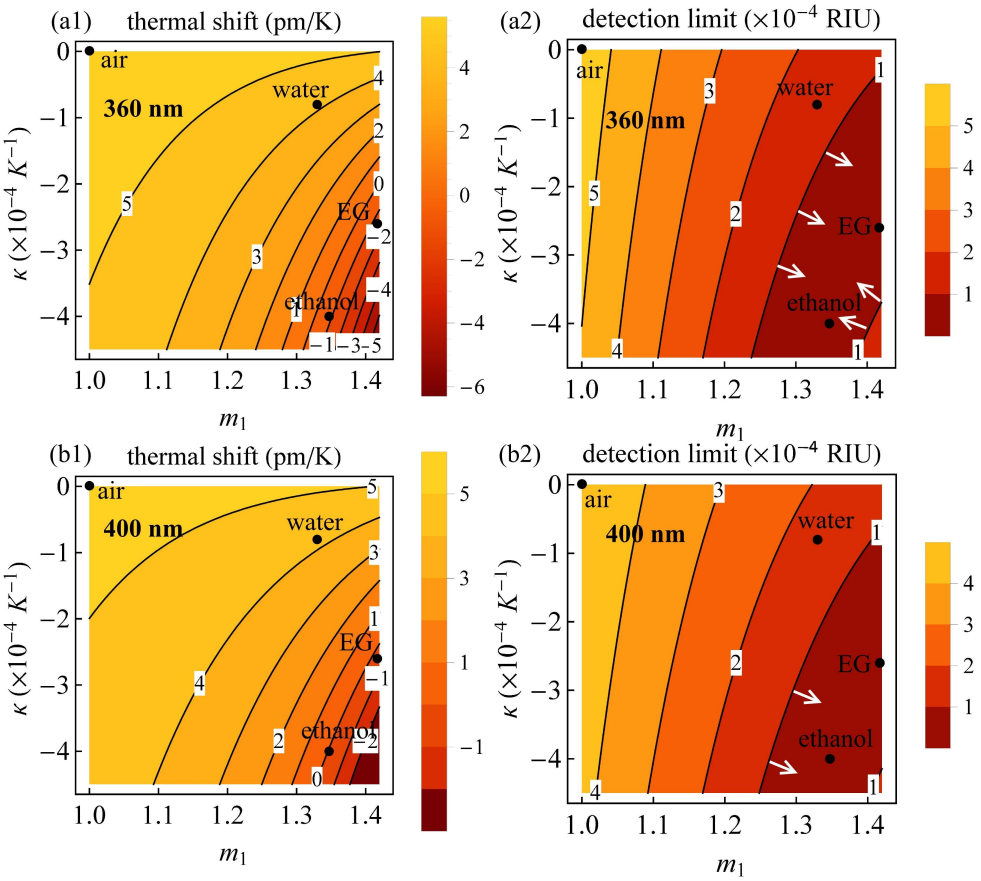

Figure 4.4: (a1), (b1) Thermal sensitivity and (a2), (b2) corresponding detection limit for thermal fluctuations of 1 K. The white arrows in (a2) and (b2) point toward the zero-DL valley. The top panels are for a 360-nm-thick QD film, and the bottom ones correspond to a 400 nm film.

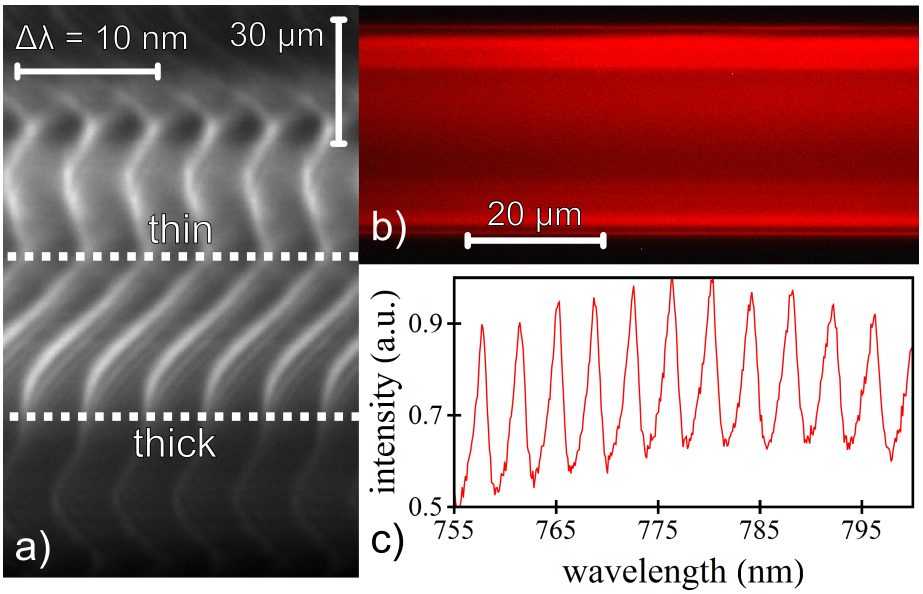

Figure 4.5: (a) Spectral map of the modes in a section of the capillary, in which the WGMs appear as bright lines. The resonance wavelengths change along the capillary length, due to variations in the QD coating thickness. (b) Luminescence image showing a length of capillary. The color fluorescence image must be taken on a different setup in our laboratory, so although the capillary is the same one, the region shown in (b) does not necessarily correlate with the spectra in (a) or (c). (c) Typical mode spectrum, representing an intensity profile along a horizontal dashed line (thin) in (a). These structures have experimental Q-factors of $\sim$ 1500 and free spectral range of $\sim$ 3.2 nm, depending on the QD film thickness.

the slit aligned parallel to the axis. The wavy appearance of the resonances is caused by film thickness variations along the channel axis. Wherever the film is thicker, the modes shift to longer wavelengths (leftward on the spectral image) due to the longer effective path length in the high-index coating. Slight variations can also be observed in the fluorescence image shown in Fig. 4.5(b). A previous mode analysis suggested that thickness variations upwards of 200 nm can be easily achieved in a single capillary [84].

The refractometric sensitivity was measured by comparing the mode positions with air, water, ethanol, and EG in the capillary channel, for both polarizations and two thicknesses (Fig. 4.6). The modes redshifted as a function of increasing fluid refractive index, yielding a sensitivity of 5 to 20 nm/RIU

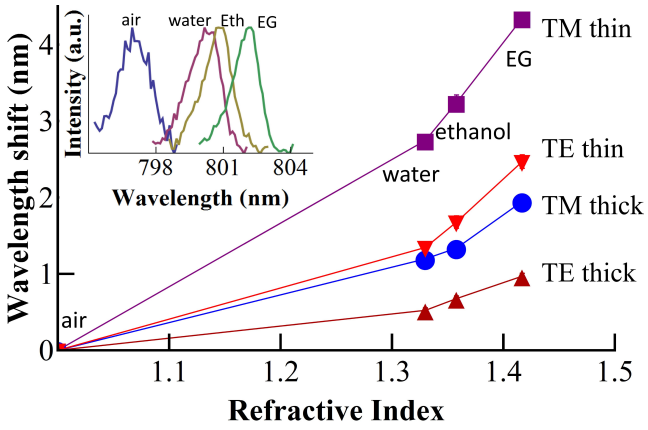

Figure 4.6: Wavelength shifts for different solvents in the capillary channel, relative to the case for air, for regions of the film, corresponding to lines labeled "thick" and "thin" in Fig. 4.5. The thin regions of the film have greater sensitivity, as do the TM-polarized modes, in agreement with theory. The inset shows a representative normalized WGM spectral peak for each solvent in the "TM thin" case. The solvents used were, in order, air, water, ethanol, and ethylene glycol from left to right.

for the TM polarization, depending on the film thickness and channel index of refraction. The smaller sensitivity was obtained in regions where the modes were redshifted (*i.e.*, corresponding to regions of thicker QD coating). Thus, a thicker film causes both a redshift of the resonance due to the increased optical path length, and a lower sensitivity due to the smaller fraction of the mode energy that sample the channel region.

The capillary was then heated from room temperature to 40 °C with spectra taken in 1 degree intervals, using air, water, ethanol, or EG stationary in the channel. Spectral images were collected at each interval and the spectral shifts, shown in Fig. 4.7, were extracted from a Fourier analysis of the whole spectrum [105]. For the thicker film, the shifts are positive and have values of 7.55 ± 0.38 pm/K (air), 6.97 ± 0.60 pm/K (water), 5.89 ± 0.34 pm/K (ethanol), and 1.56 ± 0.16 pm/K (EG). The errors represent the 1σ uncertainty in the slope of the linear fits. For this coating thickness, we see that none of the solvents can achieve a zero thermal shift and that the smallest thermal shifts are observed for EG, in agreement with theory (Fig. 4.4).

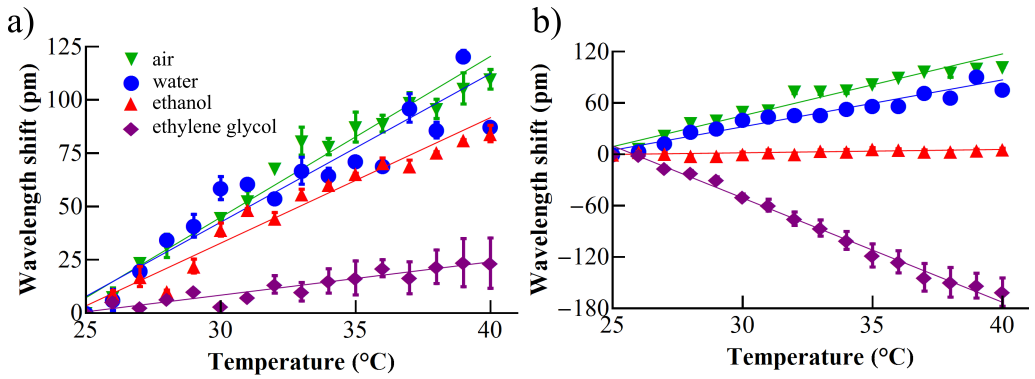

Figure 4.7: Experimental WGM shifts with different solvents in the channel of an FCM (TM modes). The results for the thick film region are shown in panel (a), while a thin region is illustrated in (b). In the latter case, thermal stability was achieved with ethanol in the capillary channel. In some cases the error bars are smaller than the symbols.

For the thinner film, the thermal shift behavior was quite different (Fig. 4.7(b)). The curves are angled downward with respect to the thick-coating case, and the one for ethanol is close to zero. The thermal sensitivities were 7.22 ± 0.42 pm/K (air), 5.48 ± 0.37 pm/K (water), 0.39 ± 0.11 pm/K (ethanol), and -12.19 ± 0.32 pm/K (EG). The decrease in the thermal shifts for the thinner coating is due to the greater fraction of the mode energy that extends into the channel. The mode energy is therefore more concentrated within the region of negative thermo-optic coefficient. The shifts for air and water in the channel are broadly similar in both cases, because the mode energy is confined mainly within the film and the glass capillary wall for both thicknesses (*i.e.*, the landscape in the upper left corner of the maps in Fig. 4.4 is fairly flat). Only for the higher indices is the field "attracted" sufficiently into the channel to begin to have a significant effect on the thermal sensitivity; in fact, for the highest index investigated (EG), the shift became negative. A negative shift is theoretically consistent for EG (Fig. 4.4).

A direct comparison between experiment (Figs. 4.6 and 4.7) and theory (Figs. 4.3 and 4.4) is not possible, since we do not know the experimental QD film thicknesses, nor the precise thermo-optic coefficients. Although magnitude of the observed thermal shifts do not agree with the theoretical ones, within

error, the observed trends are consistent, with a zero shift being theoretically possible and experimentally verified for ethanol. A similar effect for water would require a thinner film that we can currently synthesize by the described method. One option may be to etch the film to the desired thickness, similar to the case for LCORRs [5]. The results suggest that complete temperature stabilization can in principle be obtained for an FCM for any solvent, where the film thickness needed to achieve such stabilization depends on the optical properties of the solvent. Typically, films thinner than 500 nm will be needed for an Si-QD fluorescent coating, but somewhat thicker values would be needed for lower-index coatings such as fluorescent polymers [201].

While FCMs are durable and robust, they still suffer practically from higher detection limits ($\sim 10^{-4}$ RIU), as compared to 10^{-6}-10^{-7} RIU for (fragile and expensive) LCORRs [59] or surface-plasmon-type sensors [229], and 10^{-5} RIU for skew-ray fiber-optic refractive index sensors [230]. In current devices, at least, as long as the thermally limited DL is not larger than $\sim 10^{-4}$ RIU, other factors probably limit the overall DL. The first non-thermal issue is that the sensitivity of FCM-type devices is typically in the range of 5–10 nm/RIU. This low sensitivity is limited by the fairly thick films often produced by the film deposition method [168]. We have recently found a way to etch the QD film [168], which enables the formation of films of controlled thinness and offers a means to improve the sensitivity by close to an order of magnitude in theory. The second issue is the wavelength shift resolution limit of the spectrometer: in our case, we use a miniature telescope spectrograph with a pitch of ~ 0.1 nm/pixel. Higher-resolution instruments are routine; although they would increase experimental cost, the detection limit decreases by approximately the square root of the pitch [105]. Finally, mechanical drift is an issue that can cause a gradual blueshift or redshift of the resonance wavelengths. Improving the stability of the holder may require a firmer epoxy and the minimization of forces on the capillary caused by the tubing. We hope that all of these efforts might bring the DL into the range of 10^{-5} RIU or lower with appropriate temperature stabilization.

4.6 Conclusions

WGMs in FCMs offer a versatile refractometric sensing and detection platform for microfluidic analysis. However, thermal fluctuations may present a fundamental limitation on the detection limit for changes in the local index of refraction. In this paper, following the work of Teraoka and Arnold [202] [203] [225], we first calculated the refractometric sensitivity, S, for both polarizations of a layered cylindrical microcavity, using the perturbation approach. We derived formulas that allow the determination of S, including for complex values of k_0. Once the sensitivity is obtained, one can then estimate the thermal sensitivity (*i.e.*, the wavelength shift as a function of temperature change) and the refractometric detection limit associated with thermal fluctuations for FCM-type layered cylinder structures. The results showed that zero thermal sensitivity (and, therefore, minimum detection limits) is achievable for any solvent in the channel, but it depends on the layer thicknesses, refractive indices, and thermo-optic coefficients of the coating material and the solvent.

In order to demonstrate this experimentally, a microcapillary was synthesized with a high-index fluorescent coating deposited on the channel walls. The refractometric sensitivity and thermal shifts were measured for two different coating thicknesses, using the TM-polarized WGMs. For all solvents used, the observed experimental trends agreed with the theory. A near-zero thermal shift and corresponding stability against thermal fluctuations was experimentally achieved but only for an ethanol solvent. In future work, it would be desirable to demonstrate stability against thermal fluctuations using a water solvent, which is most important for biosensing applications. Thinner QD films than those currently employed will be needed in order to achieve this, likely requiring a finer control over the QD film thickness.

4.7 Acknowledgements

The authors thank NSERC and AITF iciNano for funding, and the Veinot laboratory for experimental assistance in the FCM synthesis.

Chapter 5

Protein biosensing with fluorescent microcapillaries

A modified version of this chapter was published in Optics Express 23 (3) 2577-2590 (2015) by S. Lane, P. West, A. François, and A. Meldrum.

5.1 Abstract

Capillaries with a high-index fluorescent coating represent a new type of whispering gallery mode (WGM) microcavity sensor. By coating silicon quantum dots (Si-QDs) onto the channel wall of a microcapillary, a cylindrical microcavity forms in which the optical confinement arises from the index contrast at the interface between the QD layer and the glass capillary wall. However, the ability to functionalize the QD layer for biosensing applications is an open question, since the layer consists of a mixture of Si-QDs embedded in a glassy SiOx matrix. Here, we employ a polyelectrolyte (PE) multilayer approach to functionalize the microcapillary inner surface and demonstrate the potential of this refractive index sensing platform for label-free biosensing applications, using biotin-neutravidin as a specific interaction model.

5.2 Introduction

To meet most practical needs, a label-free optical biosensor should feature low detection limits, small sample volumes, easy and low-cost analysis, and specificity to the desired analyte [231]. Achieving these requirements poses a difficult challenge, but at least two technologies appear especially promising: (i) those based on surface plasmon resonances (SPRs); and (ii) those due to the resonances of optical microcavities. Optical biosensors based on SPRs have exploded onto the scene in the last decade; progress was partly enabled by the wealth of chemical functionalization methods for gold surfaces [232]. An enormous array of specific SPR biosensor experiments have now been done, for compounds spanning the range from Dengue fever [233] to cancer biomarkers [234]. In contrast, optical microcavities are often based on silica interfaces, which have a variety of well-established functionalization chemistries (*e.g.*, silanization). Both of these approaches can be specific, require low sample volumes, and have detection limits as low as 10^{-7} refractive index units (RIU) [229] [59]. Currently, optical microcavities can detect the binding of single molecules as light as a few kDa [235]. However, expensive equipment such as a narrow-bandwidth tunable laser is necessary to make these measurements. Commercial SPR devices are historically fairly expensive as well, but there is a push toward smaller devices (*e.g.*, using cell-phone applications) [236] that could considerably lower the cost.

Of the various types of optical microcavities, whispering-gallery-mode optical resonators are currently setting records for single-molecule detection limits [235]. The most common types of WGM-based resonator include microscale spheres [237] [108] [238] toroids [239], disks [240], fibers [87], and thin-walled capillaries [241]. The basic idea behind each of these is the same: In the first four examples, light is confined by total internal reflection as it propagates around the circumference of the structure. Part of the mode field energy extends "evanescently" outside the device and samples the adjacent medium. In a thin-walled microcapillary, the situation is a bit different; here the outer

capillary wall confines radiation and forms the resonances, while the tail of the mode field samples the interior channel region (hence the need for a thin wall).

Fluorescent microcavities (FMs) can be classified as a third type of optical biosensor. These structures combine some of the properties of SPR and evanescent cavity-based sensing. Like the case for SPR devices, fluorescent microcavities feature a broadband optical detection and do not require an expensive scanning laser or a finicky evanescent coupling system. In FMs, the fluorescence generally comes from dyes or quantum dots embedded into the structure; some of the emitted light couples into the cavity modes whose electric field samples the analyte. Instead of interacting with a single WGM, the typically broadband fluorescence couples into many modes, although at the cost of having a low light intensity in each one.

Much of the work on fluorescent microcavity sensors has focused on dye- or QD-doped microspheres [242] [243] [244] [245] [246] [147] [247] [248] [108]. There are many methods for embedding a fluorophore under the surface of a microsphere (*e.g.* diffusion of dye molecules into polystyrene spheres [249], or coating polystyrene or glass with a fluorescent surface layer) [247]. An advantage of this geometry is that the fluorophores are located close to the electric field maxima of the WGMs and can couple into the modes relatively strongly, to the point that lasing from fluorophores interacting with spherical WGMs can be achieved [250]. However, microspheres inevitably require an external chamber to hold the analyte. Potential solutions include inserting the microsphere into a capillary [108], channel waveguide [251], or specialized fluid cell [252], but this adds to the complexity of the sensor system.

An intriguing option is to use the cylindrical resonances of a capillary instead. Capillaries are inherently fluidic devices; thus external chambers are not necessary. The difficulty here is that one needs a fluorescent coating inside the capillary channel, and the coating must have a higher index of refraction than the glass wall in order to confine radiation. Several methods have recently been developed to fabricate this structure; these include rolling fluorescent

multilayers into a tube-like formation [200], or injecting fluorescent polymers that dry inside the channel [201]. In the first case, coupling into the device is quite difficult; in the second case the polymer layer may not be sufficiently stable over the course of an experiment [201].

In contrast, a thin layer of fluorescent silicon QDs embedded inside a glassy silicon-oxide matrix can provide a stable, high-index fluorescent coating [61]. The effective refractive index of this layer is near 1.67 at the peak wavelength of the QD fluorescence (around 800 nm). The high refractive index helps to confine the emitted fluorescence into the WGMs and leads to reasonably good Q-factors. However, relatively little is known about the chemical methods to functionalize these structures for biosensing. In one previous example the silanization reactions yielded mainly non-specific streptavidin binding and suggested a fairly labile functionalization [139]. In this work, we aimed to develop a suitable method to enable these devices for biosensing applications. This method is based around the deposition of polyelectrolyte (PE) multilayers on the surface of the QD film in the channel. This functionalization scheme was characterized optically, and then used to test the specific detection of neutravidin on a biotinylated polyelectrolyte interface.

5.3 Experimental

Glass capillaries with inner and outer diameters of 50 μm and of 360 μm, respectively, were purchased from Polymicro Technologies. They were cut into $\sim$ 5-cm lengths and the polyimide jacket was then removed by ashing at 600 °C in flowing O_2. The silicon quantum-dot layer was formed using the "HSQ method"[140]. Essentially the capillary is filled with a solution consisting of hydrogen silsesquioxane (HSQ) dissolved in methyl isobutyl ketone (MIBK) and is then annealed at a temperature of 1100 °C for one hour in flowing 95% N_2 + 5% H_2 forming gas. This causes the solvent to evaporate and the remaining HSQ to form a solid layer on the channel surface. This layer consists of silicon QDs with a mean diameter between 3 and 4 nm, embedded in a glassy

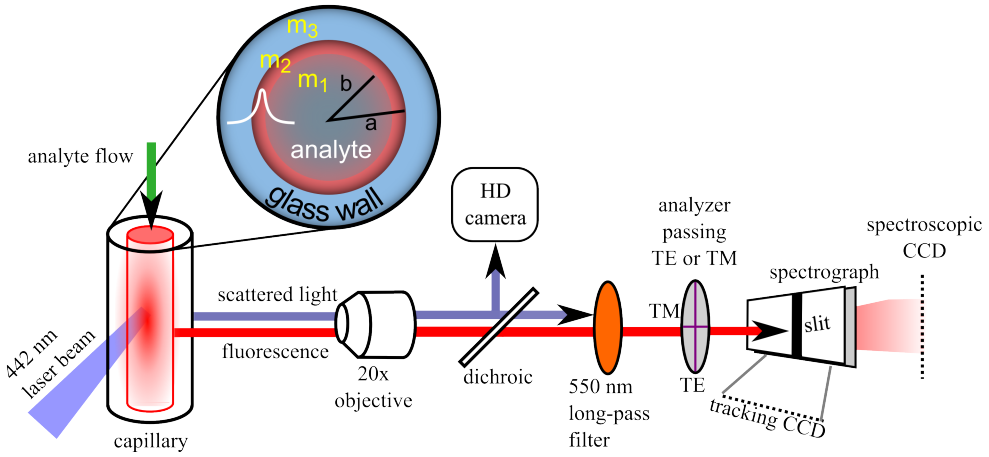

Figure 5.1: Diagram of the capillary and the experimental setup. In the cross-sectional diagram of the capillary, the refractive indices m_1, m_2, and m_3 refer to the analyte, fluorescent layer, and capillary wall, respectively. Radius "b" is measured to the QD layer while "a" is the capillary's original inner radius (*i.e.*, prior to QD layer deposition). The white wave represents a WGM electric field profile.

silicon sub-oxide film [65], forming a fluorescent capillary-type microcavity (FCM).

The capillaries were then mounted onto a microscope stage and interfaced to a syringe pump via a PTFE tubing system. The fluorescence was excited with the 442 nm line of a HeCd laser at a power of ~ 40 mW. The fluorescence was collected by the microscope objective and sent to an imaging spectrometer for analysis, as diagrammed in Fig. 5.1. The TM-polarized WGMs (radial electric field) were selected by aligning the analyzer accordingly, since these modes have a slightly higher sensitivity [84]. The WGM shifts were extracted from the spectra using an adaptation of the Fourier shift method [105] rather than by peak analysis [253].

The channel QD film was initially cleaned by pumping 10 M NaOH solution through the capillary while the fluorescence WGMs were being monitored. This procedure leaves the QD film surface clean and with a slight negative charge [81] [165]. The FCMs were then functionalized using a polyelectrolyte layering method [164], with the aim of producing well-defined PE multilayers

that would coat the channel interface (*i.e.*, the quantum dot layer). The first step was to pump a solution consisting of 2 mg/mL polyallylamine hydrochloride (PAH) dissolved in a 2.5 M NaCl solvent. This solution was pumped at a rate of 5 μL/min for 15 minutes. PAH has a positively-charged functional group that should bind electrostatically to the silica surface, with the salt concentration effectively controlling the layer thickness [7]. The FCM was then rinsed by pumping water through the channel for 25 minutes. Next, a solution of 2 mg/mL polystyrene sulfonate (PSS), also in 2.5 M NaCl solvent, was pumped through the capillary under the same conditions as for the PAH solution. PSS has a negative surface charge and should bind electrostatically to the PAH, forming a PAH-PSS bi-layer on the channel surface. This procedure was repeated up to five times to test the response of the WGMs to the layer-by-layer PE deposition on the channel walls; however, for biosensing experiments we used a PAH-PSS-PAH trilayer (Fig. 5.2). This is because the first PAH layer tends to be incomplete [254] [255] implying that a multilayering approach should give a more uniformly functionalized interface. PAH has amine groups on each monomer which could be used to covalently immobilize the carboxylic termination of biotin, using carbodiimide coupling reagents. Therefore it has to be the final layer for the biosensing experiments.

After the multilayer deposition, a baseline phosphate buffer saline (PBS) solution of pH = 7.4 was pumped into the FCM. Next, a solution consisting of 0.25 M N-hydroxysuccinimide (NHS), 0.25 M ethyl-(dimethylaminopropyl) carbodiimide (EDC), and 1 mg/mL biotin in PBS was injected into the device. The NHS/EDC mixture catalyzes the covalent binding of the carboxylic moiety of the biotin with the amine groups on the exposed PAH layer [256] [257] [258]. PBS was then pumped for 20 minutes. Next, a solution of 0.1 mg/mL neutravidin in PBS was injected into the FCM. Neutravidin was chosen specifically because the alternatives, avidin and streptavidin, will be significantly charged in the buffer solution, potentially leading to nonspecific electrostatic binding (or repulsion) with the biotin molecules or the slightly positive PAH interface [259] [260]. In contrast, neutravidin has an isoelectric point of 6.3 and will be

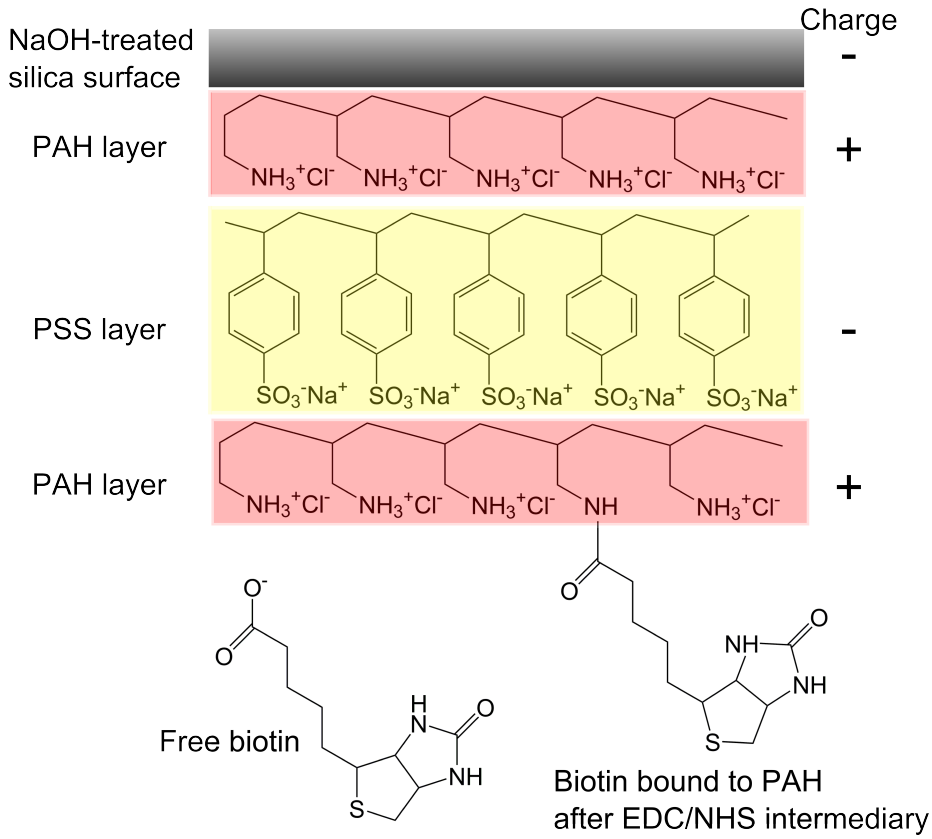

Figure 5.2: Diagram of the polyelectrolyte surface functionalization for the biosensing experiments corresponding to steps 1-10 below. The NaOH-treated glass surface has a polyelectrolyte trilayer, with the final PAH layer capturing biotin.

nearly neutral in the buffer solution. To summarize:

Step 1: 10 M NaOH etch and clean

Step 2: water rinse

Step 3: 2 mg/mL PAH in saline solution

Step 4: water rinse

Step 5: 2 mg/mL PSS in saline solution

Step 6: water rinse

Step 7: 2 mg/mL PAH in saline solution

Step 8: water rinse

Step 9: PBS buffer

Step 10: biotin/NHS/EDC solution

Step 11: PBS buffer

Step 12: neutravidin in buffer

Step 13: PBS buffer

Step 14: rejuvenate with 1-10 M NaOH solution for next experiment

Two control samples were also measured. Control 1 differed from the primary run in that the neutravidin (in step 12) was mixed in a 1:4 ratio with biotin in order to block the biotin-binding sites. In control 2, the biotin conjugation step (step 10) was omitted. The second control should test whether the neutravidin can bind nonspecifically to the PAH interface [261]. Finally, the capillary was rejuvenated between experiments (*i.e.* controls, etc.). Although the biotin and neutravidin cannot be specifically disassociated, the functionalization can be stripped using 1 to 10 M NaOH. This removes both the bio-conjugation and polyelectrolyte layers.

5.4 Results and discussion

The fluorescence emitted from the FCMs showed a clear mode structure, with a Q-factor, free spectral range, and finesse of ~ 700, ~ 2.6 nm, and ~ 2.5, respectively (Fig. 5.3). The QD films tended to show some variability along the length of the capillary; for this work, a reasonably uniform region was found

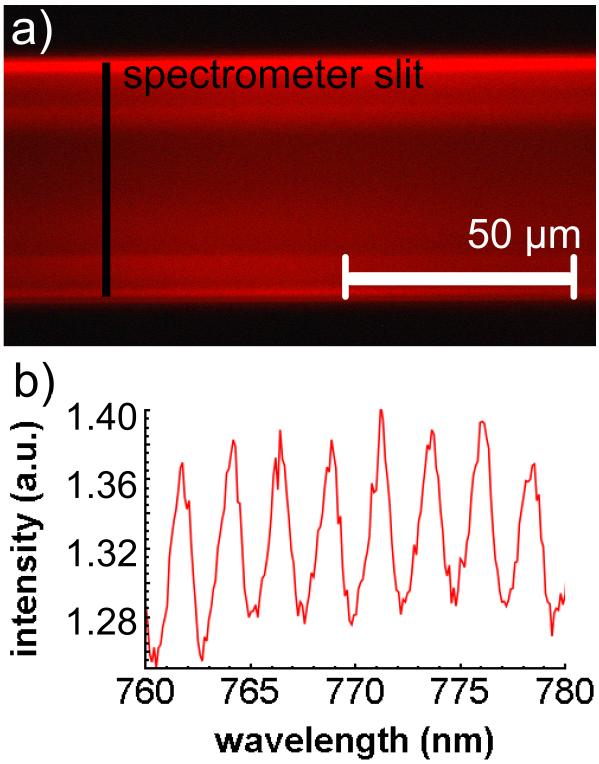

Figure 5.3: (a) Fluorescence image of the capillary channel. The red glow is due to the QD emission. The representative slit direction (perpendicular to the channel) is diagrammed. (b) A typical WGM emission spectrum over the range from 760 to 780 nm.

and the entrance slit was aligned perpendicular to the FCM axis, as illustrated in Fig. 5.3. This helps to minimize underlying WGM drifts associated with mechanical motion over the several hours needed to perform each experiment.

NaOH has been shown to etch silica [157] and other ceramic materials including silicon [262]; thus it might permit one to obtain experimental control over the QD film thickness. The QD film did in fact show signs of gradually etching as the strong NaOH solution was pumped through the channel. The WGM wavelength blue-shifted with time (Fig. 5.4 bottom left), at a rate of approximately 35 pm/h. This blueshift occurs because the effective path length decreases as the high-index material is gradually removed. The spectral shift data could be related directly to an etching rate by using standard methods to calculate the resonance wavelength for a layered cylinder [55], as

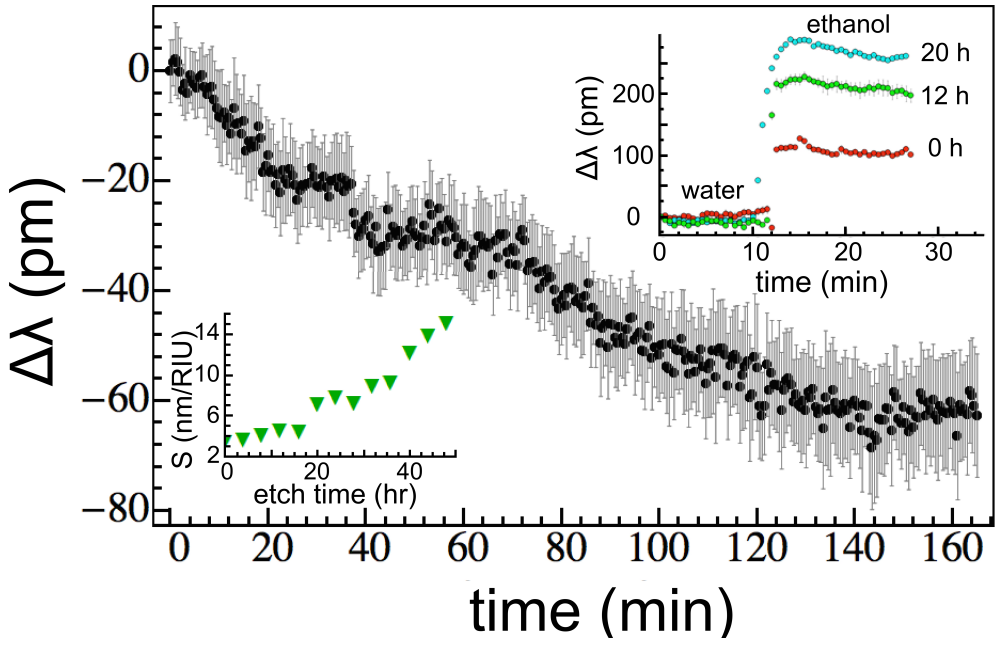

Figure 5.4: WGM wavelength shift as a function of NaOH etching time. As the QD film becomes thinner, the WGMs gradually blueshift. The upper-right inset shows sensorgrams for the water-to-ethanol transition at different etching times. The sensitivity of a single fluorescent microcavity observed at many different etching times is shown in the lower-left inset.

adapted from earlier theoretical work on TM-polarized layered spheres [225]. For the sake of brevity we do not repeat the equations here but merely state the results: for conditions matching the experimental ones the resonance is calculated to blueshift by approximately 25 pm per nm etched, yielding an etching rate for the QD film of $\sim$ 1.4 nm/h in continuously pumped 10 M NaOH solution. At the same time, the sensitivity increased, as shown in the inset to Fig. 5.4, again consistent with a thinner QD film. After 20 hours of etching, the sensitivity increased from 3.5 to 7.0 nm/RIU, representing a rate of increase of $\sim$ 0.05 pm/RIU/s.

This is the first time that the QD layer has been controllably etched in an FCM structure; it can be done without the use of hydrofluoric acid, which has been used for thinning liquid-core optical ring resonators [263]. Here, the capillary was judged suitable for biosensing experiments when it had reached a sensitivity of $\sim$ 10 nm/RIU. One slightly tricky aspect is that the NaOH

rejuvenation step is necessary to remove previously-deposited PE layers for each subsequent experiment. While a single capillary could therefore be used for dozens of runs (essentially until the capillary-tubing adhesive broke down), the sensitivity does slightly increase each time as the QD layer progressively dissolves.

One question concerns the optimal thickness of the QD layer needed to support WGMs for sensing. We recently reported the effect of the layer thickness [84], but some of the salient points can be mentioned here. First, a higher sensitivity is obtained with thinner QD films, as illustrated in Fig. 5.4. This is because, when the film is thin, more of the mode energy extends into the channel where it samples the analyte medium. However, the film cannot be made indefinitely thin or the Q-factor eventually begins to drop off noticeably. Thus, there should be an optimum thickness associated with the trade-off between the lower Q and the higher sensitivity. On the other hand, for thicker QD films, the sensitivity decreases because less of the mode energy extends into the capillary channel. The Q-factor never exceeds ~ 1500 for any thickness, however, because of absorption and scattering in the QD film [84].

In order to determine the approximate experimental thickness of the films in the present work, the electric field profiles were calculated following the methods developed in Ref [56]. For space reasons we do not repeat the derivation here but merely cite the relevant equations. Accordingly, the radial function (TM polarization) is given by:

$$T_l(r) = \begin{cases} a_l J_l(m_1 k_0 r), & r \le b \\ b_l H_l^{(2)}(m_2 k_0 r) + c_l H_l^{(1)}(m_2 k_0 r), & b < r \le a \\ d_l H_l^{(1)}(m_3 k_0 r), & r > a \end{cases} \tag{5.1}$$

where $J_l(x)$ is the cylindrical Bessel function describing the field in the inner layer, the Hankel functions of the first ($H_l^{(1)}(x)$) and second ($H_l^{(2)}(x)$) kind describe the field in the two outer two layers, and a_l, b_l, and d_l are proportionality constants. The resonant wave vector is found by solving for k_0 under the

appropriate boundary conditions, given by

$$\frac{m_3 H_l^{(1)\prime}(m_3 k_0 a)}{m_2 H_l^{(1)}(m_3 k_0 a)} = \frac{B_l H_l^{(2)\prime}(m_2 k_0 a) + H_l^{(1)\prime}(m_2 k_0 a)}{B_l H_l^{(2)}(m_2 k_0 a) + H_l^{(1)}(m_2 k_0 a)} \tag{5.2}$$

with

$$b_l = \frac{m_1 J_l(m_1 k_0 b) H_l^{(1)\prime}(m_2 k_0 b) - m_2 J_l'(m_1 k_0 b) H_l^{(1)}(m_2 k_0 b)}{-m_1 J_l(m_2 k_0 b) H_l^{(2)\prime}(m_2 k_0 b) + m_2 J_l'(m_1 k_0 b) H_l^{(2)}(m_2 k_0 b)}. \tag{5.3}$$

Finally, the refractometric sensitivity is

$$S_{TM} = \lambda_0 \frac{(2k_1^2)}{m_1^3(k_0^2 + (k_0^*)^2)} \cdot \frac{b|a_l|^2 \left(\frac{dJ_l^*(m_1 k_0 r)}{dr} \|_b J_l(m_1 k_0 b) + J_l^*(m_1 k_0 b) \frac{dJ_l(m_1 k_0 r)}{dr} \|_b \right) + \frac{k_0^2 + (k_0^*)^2}{k_{0,1}^2} I_1}{\left[\frac{I_1}{m_1^2} + \frac{I_2}{m_2^2} + \frac{I_3}{m_3^2} \right]}. \tag{5.4}$$

in which the energy terms are given by

$$I_1 = \int_0^{m_1 k_{0,1} b} x |a_l J_l(\tilde{x})|^2 dx \tag{5.5}$$

$$I_2 = \int_{m_2 k_{0,1} b}^{m_2 k_{0,1} a} x |b_l H_l^{(2)}(\tilde{x}) + H_l^{(1)}(\tilde{x})|^2 dx \tag{5.6}$$

$$I_3 = \int_{m_3 k_0 a}^{\infty} x |d_l H_l^{(1)}(\tilde{x})|^2 dx, \tag{5.7}$$

where $i = 1, 2, 3$ for each of the three regions (channel, film, and glass wall, respectively), $k_0 = k_{0,1} + ik_{0,2}$, and $\tilde{x} \equiv x(1 + ik_{0,2}/k_{0,1})$. These equations can be solved numerically using standard math packages such as Mathematica. Once the field profile has been solved, 2D plots can be obtained by simply multiplying the solution by $e^{\pm il\phi}$ and adding the two solutions to obtain the standing wave in Fig. 5.5(a).

Figure 5.5 shows the calculated energy profile for a 50-μm diameter capillary with a 500-nm-thick QD layer. Dispersion is taken into account by interpolating tables of optical constants for water [264], Si-QDs (ellipsometry measurements on flat Si-QD films taken in our lab), and silica glass [265]. The refractometric sensitivity for this particular simulation was 23.7 nm/RIU. In

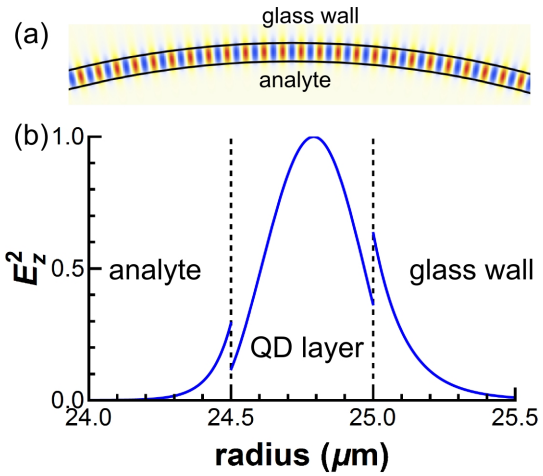

Figure 5.5: (a) Calculated 2D electric field amplitude for an $n = 1$, $l = 310$ TM mode for a 50-μm diameter capillary with 500-nm-thick QD film (marked by the black lines). Only part of the circumference is shown. (b) 1D intensity profile for the same conditions as in (a). The discontinuities in the field profile are due to the TM boundary conditions. The sensitivity of this structure is calculated from Eq. 5.4 to be 23.7 nm/RIU.

order to obtain the observed experimental sensitivities ranging from 3 to 10 nm/RIU depending on the amount of etching, one requires a QD film thickness ranging from 1.0 to 0.8 μm in thickness. These relatively large values imply room for improvement via further etching the films.

We next investigated whether the layers of PAH and PSS could be applied systematically and repeatedly to the FCM channel walls. A representative sensorgram showing the deposition of a double bilayer is shown in Fig. 5.6. The larger jumps in the WGM wavelength (red and yellow points) is due to the higher index of refraction for the PAH and PSS saline solutions, as compared to the water baseline. Evidence in favor of a layer-by-layer PE buildup is clearly observed in the "water regions" of the sensorgram labeled a-e. The net redshift after four layers was $\sim$ 170 pm, which corresponds to a mean single PE layer thickness of $\sim$ 1 nm, again estimated by using the field calculations shown in Refs. [55] and [56]. The PE layers appear stable and are not removed in water. After the double bilayer, the capillary was cleaned with a 10 M NaOH solution. The slight negative shift during the NaOH run is consistent with

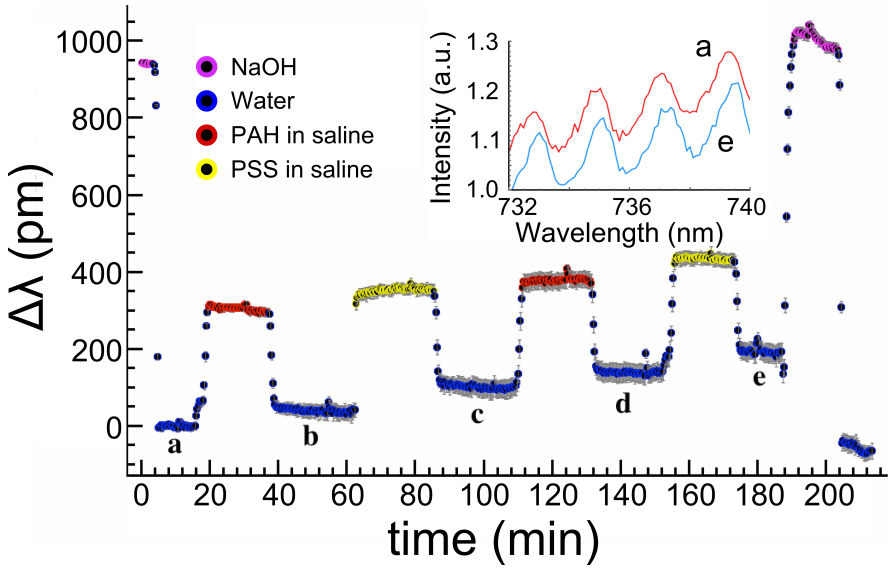

Figure 5.6: Sensorgram showing the deposition of alternating layers of PAH (red points) and PSS (yellow), followed by cleaning with 10 M NaOH solution (pink). Water is in blue, labeled a to e. The inset shows representative spectra corresponding to steps a and e.

the removal of the PE layers. The final water rinse yielded a slightly negative WGM wavelength shift, possibly due to a slight etching of the QD film during the cleaning stage.

One final observation was that the overall QD fluorescence intensity slightly decreased over the course of the PE layer deposition (Fig. 5.6, inset). We believe that this behavior is due to a gradual drift of the microscope focus over the course of several hours over which the experiment was conducted, possibly due to a gradual continuous mechanical motion of the capillary or the stage. However, this had no observable effect on the mode shifts or the sensorgrams, which were clearly independent of any changes in the collected PL intensity.

Some of the key points of the Fourier shift method can be mentioned in order to explain how one is able to obtain minimum wavelength shift resolution of a few pm using a spectrometer with a CCD pitch of about 0.1 nm per pixel and a Rayleigh resolution closer to 0.3 nm. Here, the signal-to-noise ratio (SNR) is approximately 100 (in linear units), the Q-factor is $\sim$ 700 and the

finesse is about 2.5, as discussed earlier. Inserting these values into Eq. (4) of Ref. [105], one obtains an optimal 3σ shift resolution of 14 pm using the Fourier shift technique. This calculated value is quite close to experimental the 3σ deviation of 18 pm in the present experiments, which was obtained by taking repeated measurements with flowing water in the capillary. The reason that the shift resolution is much better than the Rayleigh resolution is due to the need to measure the shift of the whole periodic waveform vs. the separation between two peaks.

An additional point is that the shift resolution is only weakly dependent on the Q-factor [105]. This should not be too surprising; for example, advanced curve-fitting methods for surface plasmon resonances (which have a very low Q) can measure refractive index changes on the order of 4×10^{-7} RIU [253]. This corresponds to shifts of a few picometres or less despite the much lower resolution of the spectral system. Similarly, for the types of measurements in the present work, the spectral shift information is encoded over the entire spectral data set and one is not limited to the analysis of a single (potentially poorly-sampled) peak. Indeed, the requirement for a high-Q-factor is really only applicable to intensity-shift methods (*i.e.*, measuring the change in transmission at a fixed wavelength on the side of a high-Q mode) and not to wavelength shift methods like those used here.

The next step was to determine whether the PE functionalization scheme can be applied to biosensing in these fluorescent-type cylindrical microcavities, using the biotin-neutravidin test system. For this experiment, a PAH-PSS-PAH trilayer was first formed on the channel walls. Injection of the biotin/EDC/NHS solution was then followed by a PBS rinsing step and the subsequent injection of a 1.67 μM neutravidin solution in PBS buffer. As the neutravidin solution was pumped into the device (grey circles in Fig. 5.7), there was a pronounced redshift of 109 ± 5 pm that occurred over a timeframe of a few minutes. This redshift was retained upon returning to pure PBS, suggesting that the neutravidin had been bound to the biotinylated layer.

In order to determine whether the neutravidin had attached specifically to

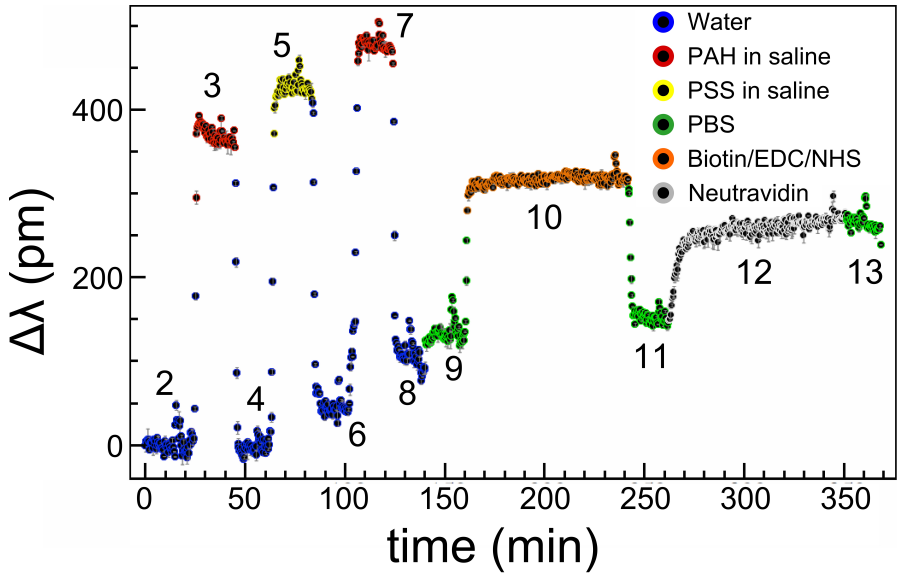

Figure 5.7: Sensorgram showing the 13-step functionalization and biosensing experiment. The numbers label the steps according to the list given in Section 5.3. The key step is (12), corresponding to the specific binding of neutravidin.

the biotinylated PAH layer, two separate control samples were run. In the first one, the neutravidin was biotinylated before being pumped through the capillary, as described in Section 5.3. This was accomplished by allowing it to react with free biotin in buffer for one hour, at a biotin concentration of four times the neutravidin one. This solution was then pumped into the capillary in step 12, in place of the unreacted neutravidin. Here, essentially no shift was observed (Fig. 5.8(a)). This is consistent with the idea the redshift reported in Fig. 5.7, step 12 was indeed due to specific neutravidin binding to the functionalized surface.

The second control was performed in order to determine whether the neutravidin could react nonspecifically, for example by binding electrostatically to the PAH layer. For this control sample, step 10 (biotinylation) was skipped (Fig. 5.8(b)). As before, the PE layers were built up and followed by water and PBS washes, but the biotin conjugation solution was not performed. This time, we observed a relatively small redshift of 32 ± 6 pm upon injection of the neutravidin solution. This suggests that a small amount of nonspecific binding

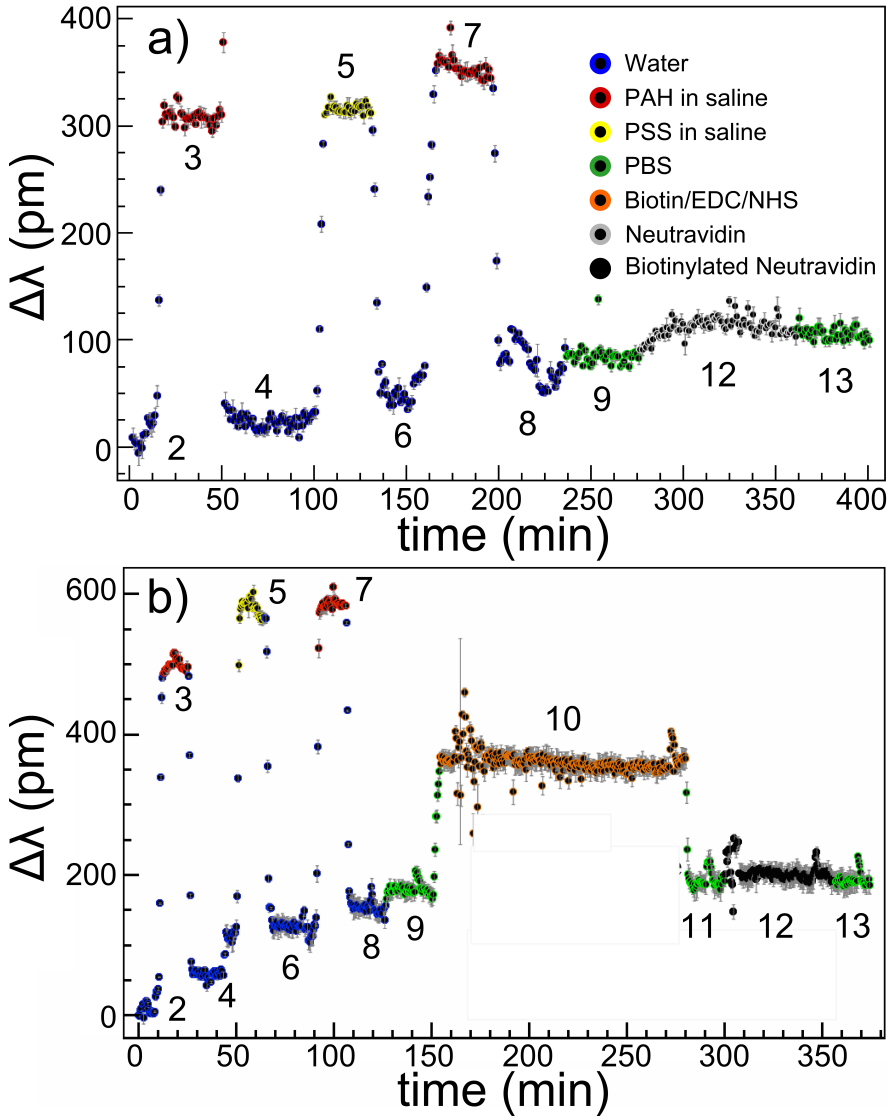

Figure 5.8: (a) Sensorgram for control sample 1. The sequence is identical to that in Fig. 5.7, except that the neutravidin (step 12) had been pre-biotinylated before being pumped into the microcavity. The slight spread in data near the start of step 10 is likely caused by a bubble in solution. (b) Sensorgram for control sample 2. Here, there is a slight redshift (grey points, step 12), likely due to a small amount of electrostatic binding of neutravidin to the PAH layer.

of neutravidin does occur, but the signal was only about 1/4 that observed in Fig. 5.7. This observation is consistent with the fact that the isoelectric point of neutravidin (pH(I)) is slightly below the pH of the buffer solution (6.3 vs. 7.4). Thus, while some nonspecific binding to the PE layer does happen, the protein detection is dominated by the specific biotin-neutravidin interaction.

The surface coverage, detection limit, and binding rate constants are important figures of merit for a microfluidic sensor device. This would be the first measurement of these values for fluorescent-WGM-type capillary sensors which are, essentially, a new class of sensor structure that shares some of the properties of fluorescent microspheres and thin-walled LCORRs. The neutravidin binding experiments were therefore repeated using several different concentrations. For these experiments, steps 1-11 were followed as before, but for step 12 the neutravidin concentration was changed from 1.67 μM to 0.8 nM. As the concentration decreased, the saturation wavelength shift decreased (Fig. 5.9). From these data, one can extract several of the key sensor parameters.

If the equilibrium binding constant, K_a, is large, as can be expected for the biotin-neutravidin reaction, then the fractional surface coverage should be close to unity. The functional avidin tetramer has dimensions of $\sim 5.6 \times 5 \times 4$ nm [266], so one can reasonably approximate the neutravidin molecule as a sphere of diameter 5 nm. This yields a maximum theoretical surface coverage of 2.8×10^{12} cm^{-2} (assuming that the projection of a sphere fills $\sim 55\%$ of a surface for random packing [267]), which corresponds to a surface mass density of $\sim$ 280 ng/cm^2 for neutravidin. This result is quite close to an experimentally-estimated value of 295 ng/cm^2 using an SPR sensor [268].

The molecular surface density, σ_p, for a capillary-type microcavity can be estimated from the experimental data according to [241] [269]:

$$\sigma_p = \frac{\delta\lambda}{\lambda_0} \cdot \frac{\varepsilon_0 a(m_2^2 - m_1^2)}{\alpha_{ex}} \tag{5.8}$$

in which ε_0 is the vacuum permittivity, a is the radius (Fig. 5.1), α_{ex} is the excess polarizability of the neutravidin molecule, and the refractive indices

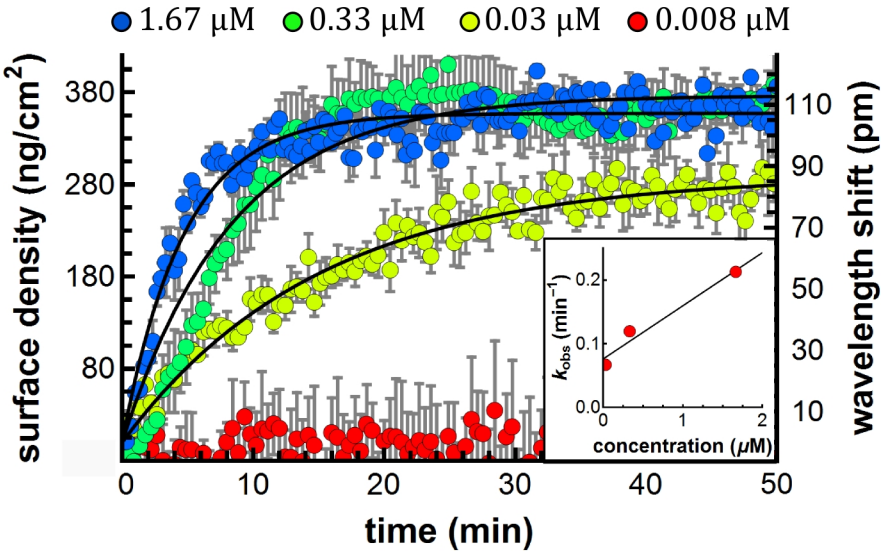

Figure 5.9: Sensorgrams for neutravidin binding, for four different concentrations. These data show only step 12 of the reaction process; for each data set the capillary was cleaned with 10 M NaOH and steps 1-11 were performed prior to the running the neutravidin solution. The black lines are fits using first-order reaction kinetics (Eq. 5.10). The inset shows k_{obs} plotted against the neutravidin concentration, along with a linear fit.

are the same as shown in Fig. 5.1. The polarizability of neutravidin can be estimated from the Clausius-Mossotti equation:

$$\alpha_n = \frac{\varepsilon_n - 1}{\varepsilon_n + 2} \cdot \frac{3M\varepsilon_0}{N_A \rho_n} \tag{5.9}$$

where N_A is Avogadro's number, M is the molar mass of neutravidin ($\sim$ 60 kg/mol), ε_n is the dielectric function of neutravidin and ρ_n is its density. For the latter two values, we take 2.25 and 1.37 g/cm^3 as typical of proteins [270]. Accordingly, α_n is estimated to be 5.1×10^{-21} cm^3, which is almost three orders of magnitude larger than that of water [271] and justifies the replacement of α_{ex} by α_n in Eq. 5.8. The surface mass density is then given by $d = M\sigma_p/N_A$, yielding a saturation mass density of $\sim$ 370 ng/cm^2 for the higher neutravidin concentrations. This is slightly larger than the theoretical value but is probably within the limits of the various approximations. The result appears consistent with the binding of a near-complete monolayer of

neutravidin. The equilibrium binding constant can also be estimated, under the assumption that it is a first-order reaction. Accordingly, the observed reaction rate at any concentration can be obtained from the relation

$$R_t = R_0[1 - exp(-k_{obs}r)], \tag{5.10}$$

in which R_t and R_0 are the signal at time t and initially, and k_{obs} is the observed reaction rate. The lines through the data in Fig. 5.3 are fits using Eq. 5.10, from which k_{obs} could be extracted for three concentrations. The data for the 8 nM neutravidin concentration could not be well fit, as the shift was too small. The intrinsic rate constants for association (k_a) and dissociation (k_d) are then related to the observed reaction rate according to

$$k_{obs} = k_a[B] + k_d, \tag{5.11}$$

where [B] is the concentration of neutravidin in the solution. Since the solution is continuously pumped, the reaction rate is not diffusion limited. Finally, the equilibrium association constant is given by $K_a = k_a/k_d$. By plotting the observed reaction rate as a function of concentration (inset to Fig. 5.9), one obtains a slope of $k_a = 8.3 \times 10^4$ $M^{-1}min^{-1}$ and an intercept of $k_d = 0.076$ min^{-1}. The estimated equilibrium association constant is then 1.1×10^6 M^{-1}. This value is about an order of magnitude smaller than that reported for streptavidin on biotinylated gold nanorods [272] and is much lower than in the dissolved form ($\sim 10^{15}$ M^{-1}), implying that the biotin-neutravidin reaction rates are affected by the underlying PE layers and/or steric hindrance on the surface monolayer. In Fig. 5.9, the lowest detected concentration was 33 nM. This corresponded to a mean 83 pm wavelength shift (or a surface density of 273 ng/cm^2). The 3σ standard deviation was $\sim$ 15 pm, yielding a detection limit of $\sim$ 6 nM; *i.e.*, quite close to the 8 nM run in which a shift could not clearly be observed. With certain improvements these values may approach the detection limits of devices such as the LCORR which, when probed by a tunable laser, has reached the picomolar range [273] although at the cost of

a more complicated, expensive, and fragile device structure and measurement method. One limitation currently appears to be a combination of mechanical and thermal instabilities that could be improved if in future the microcapillary could be physically packaged so that it is immoveable with respect to the objective lens. Also, our relatively low-resolution spectrograph (which has a pitch of slightly over 0.1 nm/pixel) and the moderate sensitivity for the QD film thicknesses used here both offer room for improvement. The latter two methods could, in principle, improve the detection limits from the range of nM to tens of pM [55].

5.5 Conclusions

In this work, we report the first example of biosensing with a capillary-type WGM cavity structure. This clearly demonstrates the feasibility of fluorescent capillaries as an alternative type of whispering gallery mode biosensor. While the detection limits do not match those for microcavities probed with a tunable laser, they do offer several attractive features. These include a simple capillary-based fluidic setup, ease of fabrication, and high durability. The devices can withstand multiple usage, they can be readily removed from a setup for cleaning, they can be easily manipulated by hand, and they strictly need only a fairly simple apparatus (a microscope objective, a miniature spectrometer, and a blue light source). As with refractometric investigations, the trade-off, at least at the moment, is in the lower detection limits. Nevertheless, the methods developed in this work – polyelectrolyte layer functionalization for capillary-type FCMs – could enable much wider application of these structures. Once the multilayer is deposited, for example, almost any type of biotin-related recognition scheme becomes possible. The method is quite robust and provides uniform results, as long as mechanical drift and temperature fluctuations can be minimized. Several methods were, finally, suggested to improve the detection limits. For example, a higher-resolution spectrograph and increased sensitivity via etching to achieve an optimal QD film thickness

should push the detection limit significantly lower.

5.6 Acknowledgements

We thank the Veinot group for materials and discussions and the West group for assistance with chemical storage. Funding was from NSERC and AITF iciNano.

Chapter 6

Conclusions and outlook

6.1 Summary of contents

The main objective of this work was to investigate the performance and applications of fluorescent-core microcapillaries. To begin, the background and nature of microfluidic sensing devices were discussed, with emphasis on the use of WGMs as the sensing transduction mechanism. Different WGM-supporting platforms were briefly reviewed, focusing their main advantages and drawbacks for sensing applications. The derivation and classification of WGMs was laid out, with some notes on the parameters that describe their spectral structure. Finally, various schema for performing biosensing were discussed, particularly protein-anchoring protocols and experiments based on assays.

In Chapter 2, the methods used to construct the fluorescent microcapillary devices were presented. These devices were built from stock materials and controlled or tuned for optimum sensing capability. They were then prepared for microfluidic applications by anchoring them on a microscope stage and gluing them to tubing fed by syringes containing the analyte. Likely sources of experimental error were discussed including thermal fluctuations and mechanical drift. Some strategies for optimum data collection were given from experience gained over course of the experiments.

Chapters 3–5 consist of a series of published papers. Chapter 3 discusses

the sensitivity of the WGMs with particular attention paid to the FCM diameter and the fluorescent layer thickness. These parameters are also discussed in relation to the Q-factor, resonance order and wavelength, and the refractometric sensitivity. The theory was compared to the experimental performance for particular mode orders and polarizations. The optimum fluorescent layer thickness could be calculated from the results and etching techniques used to reach it experimentally.

Chapter 4 showed how to reduce or eliminate thermal cross-sensitivity from FCM sensing measurements. The thermo-optic coefficients of each layer in an operating FCM (silica walls, fluorescent layer, and channel analyte) as well as thermal expansion determine the thermal response of the WGMs. We showed that these parameters can be balanced to such that all the thermal effects precisely cancel and then demonstrated this experimentally. While the demonstration was somewhat impractical in the sense that ethanol had to be used as the channel fluid, the concept could be extended to other analytes including water.

Chapter 5 shows proof-of principle biosensing using vitamin B_7 and a protein. The ability to control fluorescent layer thickness of the FCM (and thus optimize its sensitivity) was shown. Next, a layer-by-layer scheme for depositing polyelectrolytes based on ionic attraction was proposed and then demonstrated to functionalize the FCM, ultimately allowing the attachment of biotin. Then, neutravidin was bound specifically to the biotin, building up a monolayer on the inner wall. These events were all detectable via WGM spectral shifts. The device was sensitive enough to perform concentration measurements and obtain data on the reaction kinetics and ultimately showed a protein detection limit of 6 nM. This work was also featured in an SPIE newsroom article [274].

6.2 Advances in FCM-based sensing

Previous work on FCMs developed the basic fabrication techniques, characterized the WGMs, proposed sensing protocols, established Fourier-based analysis of the WGM spectral shifts, and investigated detection limits [275] [162]. Those authors laid out critical areas for improvement, including: a reliable FCM fabrication method, a way to control the SiQD film thickness, a more reliable functionalization process, a method for reusing or the sensor head after functionalization, and a method for doing live analysis of experimental data.

This thesis has advanced several of these issues. The problem of consistent and controllable FCM fabrication was solved by etching the SiQD film. Initially, FCMs had been fabricated with a 30 μm inner diameter (ID), but had a low success rate ($\sim$ 0.5%) possibly because the gas used in annealing (H_2) could not penetrate the channel sufficiently. It was discovered that SiQD-coated capillaries with a 50 μm inner diameter could be reliably created ($\sim$ 50% success rate), although with lowered sensitivity because of thicker films. NaOH etching was used to thin the SiQD film to increase the sensitivity of these 50 μm FCMs. The ability to change the film thickness post-production also allowed the film to be optimized for high- or low-refractive index analytes.

The second problem that had to be overcome was the inability to reliably functionalize the inner surface of the capillary channel and perform specific biosensing [275] [162]. The initial investigation, prior to this work, used silanization to functionalize the channel walls. That work implied the feasibility of this task, but illustrated the difficulties associated with unpredictable surface chemistry [162]. This work instead developed a more reliable and repeatable polyelectrolyte layer-by-layer deposition to show stable functionalization, as well as specific and concentration-sensitive protein detection.

The third challenge was to create a reusable sensor [162]. This was achieved using an NaOH rinse, which strips the sensor surface in seconds or minutes but is tolerated by the rest of the microfluidic assembly. This is beneficial because NaOH is safer to handle than alternative cleaning solutions like HCl/methanol

or Piranha.

This work also showed how to build a chemically resistant microfluidic system based on FCM-type sensors. Through careful selection of tubing, glue, syringes, and needles, a chemically resistant platform capable of accommodating a large range of analytes was obtained, thus extending the capability of the FCM platform to organic solvents, acids, and strong bases.

Last, although not detailed here, live data collection and real-time graphs were accomplished and used throughout the thesis work, using scripts written in Mathematica.

6.3 Future work

The FCM platform demonstrates a powerful detection capability for biosensing, antibody-based detection, plasmon-enhanced sensing, and lasing-based detection. Future work could try to capitalize on this in the following ways.

The first is a competition assay. Some biosensing targets are too small to be measured via monolayer formation using an FCM, but can be measured by their absence of signal when competing with another detectable target. As an example, initial work to measure Vitamin D [276] could be improved in this fashion. A spike made of Vitamin D could be made by conjugating some of it with a known detectable marker, say a large protein. When mixed with a sample containing an unknown concentration of unmarked Vitamin D, the resulting signal would be inversely proportional to the sample concentration. This has not been accomplished to date because of a lack of experience in conjugating the target to a marker while maintaining its specificity.

The second method is antibody-based detection. The FCM can perform standard ELISA protocols to detect antigens and antibodies in solution using a protein-functionalized surface. The requirement to achieve this is a working knowledge of how to handle antibodies in solution and a recipe for sulfhydryl or carbonyl activation. This would be a particularly powerful proof-of-concept because the ELISA is one of the fundamental detection protocols in modern

biochemical analytics. An interdisciplinary researcher with some knowledge of the FCM and biochemistry might be able to accomplish this.

The third method is plasmon-enhanced sensing. WGM-plasmon coupling has been used to improve the detection capabilities of several platforms, and could be extended to the FCM by depositing plasmonic nanoparticles on the channel surface.

Another interesting direction would be to switch the device from fluorescence into lasing-based sensing. This could improve the visibility and signal-to-noise ratio. SiQDs have not been shown to lase in FCMs to date (or reproducibly in any other structure), but dye-doped polymers may offer an alternative fluorescent layer that can be pumped above the lasing threshold. This was just recently achieved while this thesis was being written, but bleaching and WGM drift were reported to be problems. This might be rectified by protecting the lasing chromophores from oxygen and solvents, but bleaching remains a longstanding challenge associated with organic chromophores.

The FCM remains a robust, easily-fabricated platform for WGM-based sensing, with a multitude of possible improvements to its detection capabilities and diverse applications to interdisciplinary research.

Bibliography

[1] K. A. Willets and R. P. Van Duyne, "Localized surface plasmon resonance spectroscopy and sensing," *Annual Review of Physical Chemistry*, vol. 58, pp. 267–297, May 2007.

[2] G. C. Righini and S. Soria, "Biosensing by WGM microspherical resonators," *Sensors (Basel)*, vol. 16, June 2016.

[3] V. Duong Ta, R. Chen, L. Ma, Y. Jun Ying, and H. Dong Sun, "Whispering gallery mode microlasers and refractive index sensing based on single polymer fiber: Microlasers and refractive index sensing," *Laser & Photonics Reviews*, vol. 7, pp. 133–139, Jan. 2013.

[4] T. A. Birks, J. C. Knight, and T. E. Dimmick, "High-resolution measurement of the fiber diameter variations using whispering gallery modes and no optical alignment," *IEEE Photonics Technology Letters*, vol. 12, pp. 182–183, Feb. 2000.

[5] J. D. Suter, I. M. White, H. Zhu, H. Shi, C. W. Caldwell, and X. Fan, "Label-free quantitative DNA detection using the liquid core optical ring resonator," *Biosensors and Bioelectronics*, vol. 23, pp. 1003–1009, Feb. 2008.

[6] J. T. Gohring, P. S. Dale, and X. Fan, "Detection of HER2 breast cancer biomarker using the opto-fluidic ring resonator biosensor," *Sensors and Actuators B: Chemical*, vol. 146, pp. 226–230, Apr. 2010.

[7] G. Decher and J. Schmitt, "Fine-Tuning of the film thickness of ultrathin multilayer films composed of consecutively alternating layers of anionic and cationic polyelectrolytes," in *Trends in Colloid and Interface Science VI*, Progress in Colloid & Polymer Science, pp. 160–164, Steinkopff, 1992.

[8] A. François, K. Rowland, T. Reynolds, S. Nicholls, and T. Monro, "Combining whispering gallery mode lasers and microstructured optical fibers for in-vivo biosensing applications," in *Photonics North 2013*, vol. 8915, p. 891518, International Society for Optics and Photonics, 2013.

[9] Thomas Shafee.
https://en.wikipedia.org/wiki/File:Protein_structure_(full).png,
Accessed 06 Jan 2019.

[10] "Isoelectric Bovine Serum Albumin: Robust blocking agent for enhanced performance in optical-fiber,"

[11] W. B. J. Zimmerman, ed., *Microfluidics: History, Theory and Applications*. CISM International Centre for Mechanical Sciences, Wien: Springer-Verlag, 2006.

[12] J. de Jong and C. Taft, "Fluidic nonlinear computation," in *BHRA Fluidic Conference*, 1977.

[13] J. Iseman, "Circuit models of passive pneumatic fluidic compensation networks," *NASA STI/Recon Technical Report N*, vol. 76, pp. 445–484, 1976.

[14] C. Pavlin, "Applications of logic subassemblies without moving parts(fluidic setup corresponding to automatic control and digital computation circuits, discussing analog elements regulation and applications of logic subassemblies without moving parts)," *Association Francaise de Cybernetique Economique et Technique, Journees sur l'Automatisation Pneumatique et Fluidique, Lyons, France*, 1972.

[15] S. B. Cheng, C. D. Skinner, J. Taylor, W. E. Lee, M. Jolivet, G. Picelli, and D. J. Harrison, "Multichannel microchip system for rapid calibration and immunoassay," in *Micro Total Analysis Systems 2000*, pp. 533–536, Springer, 2000.

[16] M. L. Chabinyc, D. T. Chiu, J. C. McDonald, A. D. Stroock, J. F. Christian, A. M. Karger, and G. M. Whitesides, "An integrated fluorescence detection system in poly (dimethylsiloxane) for microfluidic applications," *Analytical chemistry*, vol. 73, no. 18, pp. 4491–4498, 2001.

[17] J. Wang, Y. Huang, and S. Wang, "Design and implementation of a microfluidic logic gate chip based on double-stranded DNA," in *2017 9th International Conference on Intelligent Human-Machine Systems and Cybernetics (IHMSC)*, vol. 2, pp. 259–264, Aug. 2017.

[18] L. a. Klinteberg and Kungliga Tekniska högskolan, *Computational methods for microfluidics*. PhD thesis, KTH Royal Institute of Technology, Stockholm, 2013. OCLC: 939983858.

[19] G. M. Whitesides, "The origins and the future of microfluidics," *Nature*, vol. 442, pp. 368–373, July 2006.

[20] J. Wu and M. Gu, "Microfluidic sensing: state of the art fabrication and detection techniques," *Journal of Biomedical Optics*, vol. 16, no. 8, p. 080901, 2011.

[21] C. Hempen and U. Karst, "Labeling strategies for bioassays," *Analytical and Bioanalytical Chemistry*, vol. 384, pp. 572–583, Feb. 2006.

[22] M. Manimaran and N. R. Jana, "Detection of protein molecules by surface-enhanced Raman spectroscopy-based immunoassay using 2–5 nm gold nanoparticle lables," *Journal of Raman Spectroscopy*, vol. 38, no. 10, pp. 1326–1331.

[23] Y. He, S. Zhang, X. Zhang, M. Baloda, A. S. Gurung, H. Xu, X. Zhang, and G. Liu, "Ultrasensitive nucleic acid biosensor based on enzyme–gold nanoparticle dual label and lateral flow strip biosensor," *Biosensors and Bioelectronics*, vol. 26, pp. 2018–2024, Jan. 2011.

[24] A. L. Ghindilis, P. Atanasov, M. Wilkins, and E. Wilkins, "Immunosensors: electrochemical sensing and other engineering approaches," *Biosensors and Bioelectronics*, vol. 13, pp. 113–131, Jan. 1998.

[25] E. Michelini, L. Cevenini, L. Mezzanotte, A. Coppa, and A. Roda, "Cell-based assays: fuelling drug discovery," *Analytical and Bioanalytical Chemistry*, vol. 398, pp. 227–238, Sept. 2010.

[26] L. J. Kricka, "Chemiluminescent and bioluminescent techniques.," *Clinical Chemistry*, vol. 37, pp. 1472–1481, Sept. 1991.

[27] Y. Chen, Y. Chi, H. Wen, and Z. Lu, "Sensitized luminescent terbium nanoparticles: Preparation and time-resolved fluorescence assay for dna," *Analytical Chemistry*, vol. 79, pp. 960–965, Feb. 2007.

[28] I. Hemmilä and V. Laitala, "Progress in lanthanides as luminescent probes," *Journal of Fluorescence*, vol. 15, pp. 529–542, July 2005.

[29] Y.-Y. Xu, I. A. Hemmilä, and T. N.-E. Lövgren, "Co-fluorescence effect in time-resolved fluoroimmunoassays. a review," *Analyst*, vol. 117, no. 7, pp. 1061–1069, 1992.

[30] L. E. M. Miles and C. N. Hales, "Labelled antibodies and immunological assay systems," *Nature*, vol. 219, pp. 186–189, July 1968.

[31] K. T. Brunner, J. Mauel, J.-C. Cerottini, and B. Chapuis, "Quantitative assay of the lytic action of immune lymphoid cells of 51cr-labelled allogeneic target cells in vitro; inhibition by isoantibody and by drugs," *Immunology*, vol. 14, pp. 181–196, Feb. 1968.

[32] M. R. Harrison, G. B. Thurman, and G. M. Thomas, "A simple and versatile harvesting device for processing radioactive label incorporated into and/or released from cells in microculture," *Journal of Immunological Methods*, vol. 4, pp. 11–16, Jan. 1974.

[33] A. Aicher, W. Brenner, M. Zuhayra, C. Badorff, S. Massoudi, B. Assmus, T. Eckey, E. Henze, A. M. Zeiher, and S. Dimmeler, "Assessment of the tissue distribution of transplanted human endothelial progenitor cells by radioactive labeling," *Circulation*, vol. 107, pp. 2134–2139, Apr. 2003.

[34] B. Kuswandi, Nuriman, J. Huskens, and W. Verboom, "Optical sensing systems for microfluidic devices: A review," *Analytica Chimica Acta*, vol. 601, pp. 141–155, Oct. 2007.

[35] A. G. Schuchinsky, "Surface plasmons in noble metal films," *Metamaterials*, vol. 4, pp. 61–69, Aug. 2010.

[36] H. Raether, "Surface plasmons on smooth surfaces," in *Surface Plasmons on Smooth and Rough Surfaces and on Gratings*, Springer Tracts in Modern Physics, pp. 4–39, Springer, Berlin, Heidelberg, 1988.

[37] L. Novotny and B. Hecht, *Surface plasmons*. Cambridge University Press, Sept. 2012.

[38] L. C. Oliveira, C. S. Moreira, H. Neff, and A. M. N. Lima, "Optical properties and instrumental performance of thin noble metal (Cu, Au, Ag) films near the surface plasmon resonance," *Procedia Engineering*, vol. 168, pp. 834–837, Jan. 2016.

[39] K. Takagi, S. V. Nair, R. Watanabe, K. Seto, T. Kobayashi, and E. Tokunaga, "Surface plasmon polariton resonance of gold, silver, and copper studied in the Kretschmann geometry: Dependence on wavelength, angle of incidence, and film thickness," *Journal of the Physical Society of Japan*, vol. 86, p. 124721, Dec. 2017.

[40] Y. Tang and Z. Xiangqun, "Surface plasmon resonance: An introduction to a surface spectroscopy technique," *Journal of Chemical Education*, vol. 87, no. 7, 2010.

[41] B. Liedberg, C. Nylander, and I. Lundström, "Biosensing with surface plasmon resonance - how it all started," *Biosensors and Bioelectronics*, vol. 10, pp. i–ix, Jan. 1995.

[42] E. Wijaya, C. Lenaerts, S. Maricot, J. Hastanin, S. Habraken, J.-P. Vilcot, R. Boukherroub, and S. Szunerits, "Surface plasmon resonance-based biosensors: From the development of different spr structures to novel surface functionalization strategies," *Current Opinion in Solid State and Materials Science*, vol. 15, no. 5, pp. 208 – 224, 2011.

[43] J. Homola, "Present and future of surface plasmon resonance biosensors," *Analytical and Bioanalytical Chemistry*, vol. 377, pp. 528–539, Oct. 2003.

[44] Y. Liu, Q. Liu, S. Chen, F. Cheng, H. Wang, and W. Peng, "Surface plasmon resonance biosensor based on smart phone platforms," *Scientific Reports*, vol. 5, p. 12864, Aug. 2015.

[45] H. Guner, E. Ozgur, G. Kokturk, M. Celik, E. Esen, A. E. Topal, S. Ayas, Y. Uludag, C. Elbuken, and A. Dana, "A smartphone based surface plasmon resonance imaging (SPRi) platform for on-site biodetection," *Sensors and Actuators B: Chemical*, vol. 239, pp. 571–577, Feb. 2017.

[46] P. K. Jain, X. Huang, I. H. El-Sayed, and M. A. El-Sayed, "Review of some interesting surface plasmon resonance-enhanced properties of noble metal nanoparticles and their applications to biosystems," *Plasmonics*, vol. 2, pp. 107–118, Sept. 2007.

[47] A. Moores and F. Goettmann, "The plasmon band in noble metal nanoparticles: an introduction to theory and applications," *New Journal of Chemistry*, vol. 30, no. 8, p. 1121, 2006.

[48] A. V. Whitney, J. W. Elam, S. Zou, A. V. Zinovev, P. C. Stair, G. C. Schatz, and R. P. Van Duyne, "Localized surface plasmon resonance nanosensor: A high-resolution distance-dependence study using atomic layer deposition," *The Journal of Physical Chemistry B*, vol. 109, pp. 20522–20528, Nov. 2005.

[49] A. J. Haes, S. Zou, G. C. Schatz, and R. P. Van Duyne, "A nanoscale optical biosensor: The long range distance dependence of the localized surface plasmon resonance of noble metal nanoparticles," *The Journal of Physical Chemistry B*, vol. 108, pp. 109–116, Jan. 2004.

[50] S. Arnold, V. R. Dantham, C. Barbre, B. A. Garetz, and X. Fan, "Periodic plasmonic enhancing epitopes on a whispering gallery mode biosensor," *Optics Express*, vol. 20, p. 26147, Nov. 2012.

[51] X. Jiang, A. J. Qavi, and L. Yang, "Whispering-gallery microresonators for sensing technologies," in *Chemical, Biological, Radiological, Nuclear, and Explosives (CBRNE) Sensing XIX*, vol. 10629, p. 106290R, International Society for Optics and Photonics, May 2018.

[52] F. Vollmer, S. Arnold, and D. Keng, "Single virus detection from the reactive shift of a whispering-gallery mode," *Proceedings of the National Academy of Sciences*, vol. 105, pp. 20701–20704, Dec. 2008.

[53] F. Vollmer and L. Yang, "Label-free detection with high-q microcavities: a review of biosensing mechanisms for integrated devices.," *Nanophotonics*, vol. 1, no. 3-4, pp. 267–291, 2012.

[54] "Heraeus Quarzglas: Properties of fused silica." https://www.heraeus.com/en/hqs/fused_silica_quartz_knowledge_base/properties/properties.aspx, Accessed 13 Jan 2019.

[55] A. Meldrum and F. Marsiglio, "Capillary-Type Microfluidic Sensors Based on Optical Whispering Gallery Mode Resonances," *Reviews in Nanoscience and Nanotechnology*, vol. 3, pp. 193–209(17), Sept. 2014.

[56] S. Lane, F. Marsiglio, Y. Zhi, and A. Meldrum, "Refractometric sensitivity and thermal stabilization of fluorescent core microcapillary sensors: theory and experiment," *Applied Optics*, vol. 54, pp. 1331–1340, Feb. 2015.

[57] B. R. Johnson, "Theory of morphology-dependent resonances: shape resonances and width formulas," *Journal of the Optical Society of America A*, vol. 10, pp. 343–352, Feb 1993.

[58] R. D. Chung, "Fluorescence lifetimes and refractometric sensing with cavity-coupled silicon quantum dots," Master's thesis, University of Alberta, 2016.

[59] I. M. White and X. Fan, "On the performance quantification of resonant refractive index sensors," *Optics Express*, vol. 16, pp. 1020–1028, Jan. 2008.

[60] J. Veinot, J. R. Rodriguez, P. Bianucci, and A. Meldrum, "Method for depositing silicon nanocrystals in hollow fibers," Sept. 2016.

[61] C. P. K. Manchee, V. Zamora, J. W. Silverstone, J. G. C. Veinot, and A. Meldrum, "Refractometric sensing with fluorescent-core microcapillaries," *Optics Express*, vol. 19, pp. 21540–21551, Oct. 2011.

[62] C. M. Gonzalez and J. G. Veinot, "Silicon nanocrystals for the development of sensing platforms," *Journal of Materials Chemistry C*, vol. 4, no. 22, pp. 4836–4846, 2016.

[63] J. G. C. Veinot, "Synthesis, surface functionalization, and properties of freestanding silicon nanocrystals," *Chemical Communications*, no. 40, p. 4160, 2006.

[64] C. M. Hessel, E. J. Henderson, and J. G. C. Veinot, "Hydrogen silsesquioxane: A molecular precursor for nanocrystalline Si-SiO_2 composites and freestanding hydride-surface-terminated silicon nanoparticles," *Chemistry of Materials*, vol. 18, pp. 6139–6146, Dec. 2006.

[65] C. M. Hessel, E. J. Henderson, and J. G. C. Veinot, "An investigation of the formation and growth of oxide-embedded silicon nanocrystals in hydrogen silsesquioxane-derived nanocomposites," *Journal of Physical Chemistry C*, vol. 111, pp. 6956–6961, May 2007.

[66] C. M. Hessel, M. A. Summers, A. Meldrum, M. Malac, and J. G. C. Veinot, "Direct patterning, conformal coating, and erbium doping of luminescent nc-Si/SiO_2 thin films from solution processable hydrogen silsesquioxane," *Advanced Materials*, vol. 19, no. 21, pp. 3513–3516.

[67] M. Dasog and J. G. C. Veinot, "Size independent blue luminescence in nitrogen passivated silicon nanocrystals," *Physica Status Solidi (a)*, vol. 209, no. 10, pp. 1844–1846.

[68] M. Dasog and J. G. C. Veinot, "Tuning silicon quantum dot luminescence via surface groups," *Physica Status Solidi (b)*, vol. 251, no. 11, pp. 2216–2220.

[69] K. Littau, P. Szajowski, A. Muller, A. Kortan, and L. Brus, "A luminescent silicon nanocrystal colloid via a high-temperature aerosol reaction," *The Journal of Physical Chemistry*, vol. 97, no. 6, pp. 1224–1230, 1993.

[70] J. Wilcoxon, G. Samara, and P. Provencio, "Optical and electronic properties of Si nanoclusters synthesized in inverse micelles," *Physical Review B*, vol. 60, no. 4, p. 2704, 1999.

[71] R. D. Kekatpure and M. L. Brongersma, "Fundamental photophysics and optical loss processes in Si-nanocrystal-doped microdisk resonators," *Physical Review A*, vol. 78, Aug. 2008.

[72] M. Wolkin, J. Jorne, P. Fauchet, G. Allan, and C. Delerue, "Electronic states and luminescence in porous silicon quantum dots: the role of oxygen," *Physical Review Letters*, vol. 82, no. 1, p. 197, 1999.

[73] U. Resch-Genger, M. Grabolle, S. Cavaliere-Jaricot, R. Nitschke, and T. Nann, "Quantum dots versus organic dyes as fluorescent labels," *Nature Methods*, vol. 5, no. 9, p. 763, 2008.

[74] Y. Zhong, F. Peng, F. Bao, S. Wang, X. Ji, L. Yang, Y. Su, S.-T. Lee, and Y. He, "Large-scale aqueous synthesis of fluorescent and biocompatible silicon nanoparticles and their use as highly photostable biological probes," *Journal of the American Chemical Society*, vol. 135, no. 22, pp. 8350–8356, 2013.

[75] J. Liu, F. Erogbogbo, K.-T. Yong, L. Ye, J. Liu, R. Hu, H. Chen, Y. Hu, Y. Yang, J. Yang, *et al.*, "Assessing clinical prospects of silicon quantum dots: studies in mice and monkeys," *ACS Nano*, vol. 7, no. 8, pp. 7303–7310, 2013.

[76] L. Shcherbyna and T. Torchynska, "Si quantum dot structures and their applications," *Physica E: Low-dimensional Systems and Nanostructures*, vol. 51, pp. 65–70, June 2013.

[77] S. Sanwlani, K. Rawat, M. Pal, H. B. Bohidar, and A. K. Verma, "Cellular uptake induced biotoxicity of surface-modified CdSe quantum dots," *Journal of Nanoparticle Research*, vol. 16, no. 5, p. 2382, 2014.

[78] L. Wang, H. Zheng, Y. Long, M. Gao, J. Hao, J. Du, X. Mao, and D. Zhou, "Rapid determination of the toxicity of quantum dots with luminous bacteria," *Journal of Hazardous Materials*, vol. 177, no. 1-3, pp. 1134–1137, 2010.

[79] R. Hardman, "A toxicologic review of quantum dots: Toxicity depends on physicochemical and environmental factors," *Environmental Health Perspectives*, vol. 114, no. 2, p. 165, 2006.

[80] K. R. Williams and R. S. Muller, "Etch rates for micromachining processing," *Journal of Microelectromechanical Systems*, vol. 5, pp. 256–269, Dec. 1996.

[81] S. A. Greenberg, "The depolymerization of silica in sodium hydroxide solutions," *The Journal of Physical Chemistry*, vol. 61, pp. 960–965, July 1957.

[82] M. Capek, L. Jelinek, and G. A. Vandenbosch, "Stored electromagnetic energy and quality factor of radiating structures," *Proc. R. Soc. A*, vol. 472, no. 2188, p. 20150870, 2016.

[83] M. L. Gorodetsky, A. A. Savchenkov, and V. S. Ilchenko, "Ultimate Q of optical microsphere resonators," *Optics Letters*, vol. 21, pp. 453–455, Apr. 1996.

[84] S. Lane, J. Chan, T. Thiessen, and A. Meldrum, "Whispering gallery mode structure and refractometric sensitivity of fluorescent capillary-type sensors," *Sensors and Actuators B: Chemical*, vol. 190, pp. 752–759, Jan. 2014.

[85] University of Reading, "Absorption and extinction coefficient theory." http://www.reading.ac.uk/ir-substrateopticaltheory-absorptionandextinctioncoefficienttheory.aspx, Accessed 06 Jan 2019.

[86] Y. Zhi, *Whispering gallery modes in layered microspheres: Mode structure, thermal response, and reactive sensing*. PhD, University of Alberta, 2014.

[87] P. Bianucci, J. R. Rodríguez, C. M. Clements, J. G. C. Veinot, and A. Meldrum, "Silicon nanocrystal luminescence coupled to whispering gallery modes in optical fibers," *Journal of Applied Physics*, vol. 105, p. 023108, Jan. 2009.

[88] P. Bianucci, X. Wang, J. G. C. Veinot, and A. Meldrum, "Silicon nanocrystals on bottle resonators: mode structure, loss mechanisms and emission dynamics," *Optics Express*, vol. 18, pp. 8466–8481, Apr. 2010.

[89] F. P. Payne and J. P. R. Lacey, "A theoretical analysis of scattering loss from planar optical waveguides," *Optical and Quantum Electronics*, vol. 26, pp. 977–986, Oct. 1994.

[90] M. Soltani, S. Yegnanarayanan, Q. Li, A. A. Eftekhar, and A. Adibi, "Self-sustained gigahertz electronic oscillations in ultrahigh-q photonic microresonators," *Physical Review A*, vol. 85, no. 5, p. 053819, 2012.

[91] Y.-F. Xiao, Y.-C. Liu, B.-B. Li, Y.-L. Chen, Y. Li, and Q. Gong, "Strongly enhanced light-matter interaction in a hybrid photonic-plasmonic resonator," *Physical Review A*, vol. 85, no. 3, p. 031805, 2012.

[92] I. H. Agha, J. E. Sharping, M. A. Foster, and A. L. Gaeta, "Optimal sizes of silica microspheres for linear and nonlinear optical interactions," *Applied Physics B*, vol. 83, p. 303, May 2006.

[93] W. Kim, S. K. Ozdemir, J. Zhu, and L. Yang, "Observation and characterization of mode splitting in microsphere resonators in aquatic environment," *Applied Physics Letters*, vol. 98, p. 141106, 2011.

[94] E. M. Purcell, "Spontaneous emission probabilities at radio frequencies," *Physical Review*, vol. 69, p. 681, 1946.

[95] E. Fermi, *Nuclear Physics*. University of Chicago Press, 1950.

[96] P. A. M. Dirac, "The quantum theory of the emission and absorption of radiation," *Proceedings of the Royal Society of London A*, vol. 114, no. 767, pp. 243–265, 1927.

[97] A. Meldrum, P. Bianucci, and F. Marsiglio, "Modification of ensemble emission rates and luminescence spectra for inhomogeneously broadened distributions of quantum dots coupled to optical microcavities," *Optics Express*, vol. 18, pp. 10230–10246, May 2010.

[98] J. M. Gérard, B. Sermage, B. Gayral, B. Legrand, E. Costard, and V. Thierry-Mieg, "Enhanced spontaneous emission by quantum boxes

in a monolithic optical microcavity," *Physical Review Letters*, vol. 81, pp. 1110–1113, Aug. 1998.

[99] K.-S. Hsu, W.-C. Hung, C.-C. Chang, W.-H. Lin, M.-H. Shih, P.-T. Lee, S.-Y. Lin, S.-W. Chang, and Y.-C. Chang, "Lasing action and extraordinary reduction in long radiative lifetime of type-II GaSb/GaAs quantum dots using circular photonic crystal nanocavity," *Applied Physics Letters*, vol. 107, p. 091113, Aug. 2015.

[100] M. V. Artemyev, U. Woggon, R. Wannemacher, H. Jaschinski, and W. Langbein, "Light trapped in a photonic dot: Microspheres act as a cavity for quantum dot emission," *Nano Letters*, vol. 1, pp. 309–314, June 2001.

[101] A. Belarouci and F. Gourbilleau, "Microcavity enhanced spontaneous emission from silicon nanocrystals," *Journal of Applied Physics*, vol. 101, p. 073108, Apr. 2007.

[102] G. S. Solomon, M. Pelton, and Y. Yamamoto, "Single-mode spontaneous emission from a single quantum dot in a three-dimensional microcavity," *Physical Review Letters*, vol. 86, pp. 3903–3906, Apr. 2001.

[103] J. Vučković, D. Fattal, C. Santori, G. S. Solomon, and Y. Yamamoto, "Enhanced single-photon emission from a quantum dot in a micropost microcavity," *Applied Physics Letters*, vol. 82, pp. 3596–3598, May 2003.

[104] J. Gérard, B. Legrand, B. Gayral, E. Costard, B. Sermage, R. Kuszelewicz, D. Barrier, V. Thierry-Mieg, T. Rivera, and J. Marzin, "InAs quantum boxes in GaAs/AlAs pillar microcavities: From spectroscopic investigations to spontaneous emission control," *Physica E: Low-dimensional Systems and Nanostructures*, vol. 2, pp. 804–808, July 1998.

[105] J. W. Silverstone, S. McFarlane, C. P. K. Manchee, and A. Meldrum, "Ultimate resolution for refractometric sensing with whispering gallery mode microcavities," *Optics Express*, vol. 20, pp. 8284–8295, Apr. 2012.

[106] J. A. Lock, "Morphology-dependent resonances of an infinitely long circular cylinder illuminated by a diagonally incident plane wave or a focused Gaussian beam," *Journal of the Optical Society of America A*, vol. 14, p. 653, Mar. 1997.

[107] A. W. Poon, R. K. Chang, and J. A. Lock, "Spiral morphology-dependent resonances in an optical fiber:?effects of fiber tilt and focused Gaussian beam illumination," *Optics Letters*, vol. 23, pp. 1105–1107, July 1998.

[108] Y. Zhi, T. Thiessen, and A. Meldrum, "Silicon quantum dot coated microspheres for microfluidic refractive index sensing," *Journal of the Optical Society of America B*, vol. 30, pp. 51–56, Jan. 2013.

[109] Y. Zhi, J. Valenta, and A. Meldrum, "Structure of whispering gallery mode spectrum of microspheres coated with fluorescent silicon quantum dots," *Journal of the Optical Society of America B*, vol. 30, pp. 3079–3085, Nov. 2013.

[110] N. Dubreuil, J. C. Knight, D. K. Leventhal, V. Sandoghdar, J. Hare, and V. Lefèvre, "Eroded monomode optical fiber for whispering-gallery mode excitation in fused-silica microspheres," *Optics Letters*, vol. 20, p. 813, Apr. 1995.

[111] L. Collot, V. Lefèvre-Seguin, M. Brune, J. M. Raimond, and S. Haroche, "Very high-Q whispering-gallery mode resonances observed on fused silica microspheres," *Europhysics Letters*, vol. 23, no. 5, p. 327, 1993.

[112] H.-C. Ren, F. Vollmer, S. Arnold, and A. Libchaber, "High-Q microsphere biosensor - analysis for adsorption of rodlike bacteria," *Optics Express*, vol. 15, no. 25, p. 17410, 2007.

[113] K. Gardner, Y. Zhi, L. Tan, S. Lane, Y.-F. Xiao, and A. Meldrum, "Whispering gallery mode structure in polymer-coated lasing microspheres," *Journal of the Optical Society of America B*, vol. 34, pp. 2140–2146, Oct. 2017.

[114] W. Yu, W. C. Jiang, Q. Lin, and T. Lu, "Cavity optomechanical spring sensing of single molecules," *Nature Communications*, vol. 7, p. 12311, July 2016.

[115] M. Kuwata-Gonokami and K. Takeda, "Polymer whispering gallery mode lasers," *Optical Materials*, vol. 9, pp. 12–17, Jan. 1998.

[116] S. Kushida, D. Okada, F. Sasaki, Z.-H. Lin, J.-S. Huang, and Y. Yamamoto, "Low-threshold whispering gallery mode lasing from self-assembled microspheres of single-sort conjugated polymers," *Advanced Optical Materials*, vol. 5, no. 10, p. 1700123.

[117] D. Venkatakrishnarao, C. Sahoo, R. Vattikunta, M. Annadhasan, S. R. G. Naraharisetty, and R. Chandrasekar, "2D arrangement of polymer microsphere photonic cavities doped with novel N-rich carbon quantum dots display enhanced one- and two-photon luminescence driven by optical resonances," *Advanced Optical Materials*, vol. 5, no. 22, p. 1700695.

[118] M. Humar and I. Muševič, "Surfactant sensing based on whispering-gallery-mode lasing in liquid-crystal microdroplets," *Optics Express*, vol. 19, pp. 19836–19844, Oct 2011.

[119] S. Avino, A. Krause, R. Zullo, A. Giorgini, P. Malara, P. De Natale, H. P. Loock, and G. Gagliardi, "Direct sensing in liquids using whispering-gallery-mode droplet resonators," *Advanced Optical Materials*, vol. 2, no. 12, pp. 1155–1159, 2014.

[120] X. Jiang, A. J. Qavi, S. H. Huang, and L. Yang, "Whispering gallery microsensors: a review," *arXiv preprint arXiv:1805.00062*, 2018.

[121] S. Arnold, D. Keng, S. I. Shopova, S. Holler, W. Zurawsky, and F. Vollmer, "Whispering gallery mode carousel – a photonic mechanism for enhanced nanoparticle detection in biosensing," *Optics Express*, vol. 17, p. 6230, Apr. 2009.

[122] I. M. White, H. Oveys, and X. Fan, "Liquid-core optical ring-resonator sensors," *Optics Letters*, vol. 31, pp. 1319–1321, May 2006.

[123] I. M. White, H. Zhu, J. D. Suter, N. M. Hanumegowda, H. Oveys, M. Zourob, and X. Fan, "Refractometric sensors for lab-on-a-chip based on optical ring resonators," *IEEE Sensors Journal*, vol. 7, pp. 28–35, Jan. 2007.

[124] I. M. White, H. Oveys, X. Fan, T. L. Smith, and J. Zhang, "Integrated multiplexed biosensors based on liquid core optical ring resonators and antiresonant reflecting optical waveguides," *Applied Physics Letters*, vol. 89, p. 191106, Nov. 2006.

[125] I. M. White, H. Zhu, J. D. Suter, X. Fan, and M. Zourob, "Label-free detection with the liquid core optical ring resonator sensing platform," in *Biosensors and Biodetection*, Methods in Molecular Biology, pp. 139–165, Humana Press, 2009.

[126] X. Fan, I. M. White, H. Zhu, J. D. Suter, and H. Oveys, "Overview of novel integrated optical ring resonator bio/chemical sensors," p. 64520M, Feb. 2007.

[127] T. Lu, H. Lee, T. Chen, S. Herchak, J.-H. Kim, and K. Vahala, "Nanosensing with a Silica Microtoroid," p. 2, 2011.

[128] T. Lu, H. Lee, T. Chen, and S. Herchak, "Single molecule detection with an Yb-doped microlaser," p. 2, 2013.

[129] J.-F. Ku, Q.-D. Chen, R. Zhang, and H.-B. Sun, "Whispering-gallery-mode microdisk lasers produced by femtosecond laser direct writing," *Optics Letters*, vol. 36, p. 2871, Aug. 2011.

[130] S. Chang, N. B. Rex, R. K. Chang, G. Chong, and L. J. Guido, "Stimulated emission and lasing in whispering-gallery modes of GaN microdisk cavities," *Applied Physics Letters*, vol. 75, pp. 166–168, July 1999.

[131] A. Kiraz, P. Michler, C. Becher, B. Gayral, A. Imamoğlu, L. Zhang, E. Hu, W. V. Schoenfeld, and P. M. Petroff, "Cavity-quantum electrodynamics using a single InAs quantum dot in a microdisk structure," *Applied Physics Letters*, vol. 78, pp. 3932–3934, June 2001.

[132] J. M. Ward, Y. Yang, and S. N. Chormaic, "Highly sensitive temperature measurements with liquid-core microbubble resonators," *IEEE Photonics Technology Letters*, vol. 25, pp. 2350–2353, Dec. 2013.

[133] P. Wang, J. Ward, Y. Yang, X. Feng, G. Brambilla, G. Farrell, and S. N. Chormaic, "Lead-silicate glass optical microbubble resonator," *Applied Physics Letters*, vol. 106, p. 061101, Feb. 2015.

[134] M. N. Zervas, G. S. Murugan, and J. S. Wilkinson, "Demonstration of novel high-Q fibre WGM bottle microresonators," in *2008 10th Anniversary International Conference on Transparent Optical Networks*, vol. 4, pp. 58–60, June 2008.

[135] M. Pöllinger, D. O'Shea, F. Warken, and A. Rauschenbeutel, "Ultrahigh-Q tunable whispering-gallery-mode microresonator," *Physical Review Letters*, vol. 103, July 2009. arXiv: 0901.4921.

[136] J. R. Rodríguez, J. G. C. Veinot, P. Bianucci, and A. Meldrum, "Whispering gallery modes in hollow cylindrical microcavities containing silicon nanocrystals," *Applied Physics Letters*, vol. 92, p. 131119, Mar. 2008.

[137] P. Bianucci, J. Rodríguez, F. Lenz, J. Veinot, and A. Meldrum, "Mode structure in the luminescence of Si-nc in cylindrical microcavities," *Physica E: Low-dimensional Systems and Nanostructures*, vol. 41, pp. 1107–1110, May 2009.

[138] C. P. K. Manchee, J. G. C. Veinot, and A. Meldrum, "Theory and demonstration of fluorescence-based refractometric sensing in glass micro-capillaries with a silicon nanocrystal-embedded film," pp. 1–4, IEEE, June 2011.

[139] S. McFarlane, C. P. K. Manchee, J. W. Silverstone, J. G. C. Veinot, and A. Meldrum, "Feasibility of a Fluorescent-Core Microcapillary for Biosensing Applications," *Sensor Letters*, vol. 11, pp. 1513–1518(6), Aug. 2013.

[140] S. McFarlane, C. Manchee, J. W. Silverstone, J. Veinot, and A. Meldrum, "Synthesis and operation of fluorescent-core microcavities for refractometric sensing," *J Vis Exp*, Mar. 2013.

[141] G. C. Righini, Y. Dumeige, P. Feron, M. Ferrari, G. Nunzi Conti, D. Ristic, and S. Soria, "Whispering gallery mode microresonators: Fundamentals and applications," *La Rivista del Nuovo Cimento*, p. 435, June 2011.

[142] D. Erickson, S. Mandal, A. H. J. Yang, and B. Cordovez, "Nanobiosensors: Optofluidic, electrical and mechanical approaches to biomolecular detection at the nanoscale," *Microfluidics and Nanofluidics*, vol. 4, pp. 33–52, Jan. 2008.

[143] I. M. White, H. Zhu, J. D. Suter, H. Oveys, and X. Fan, "Liquid core optical ring resonator label-free biosensor array for lab-on-a-chip development," p. 63800F, Oct. 2006.

[144] A. Schweinsberg, S. Hocdé, N. N. Lepeshkin, R. W. Boyd, C. Chase, and J. E. Fajardo, "An environmental sensor based on an integrated optical whispering gallery mode disk resonator," *Sensors and Actuators B: Chemical*, vol. 123, pp. 727–732, May 2007.

[145] F. Vollmer and L. Yang, "Review Label-free detection with high-Q microcavities: a review of biosensing mechanisms for integrated devices," *Nanophotonics*, vol. 1, Jan. 2012.

[146] H. Quan and Z. Guo, "Simulation of whispering-gallery-mode resonance shifts for optical miniature biosensors," *Journal of Quantitative Spectroscopy and Radiative Transfer*, vol. 93, pp. 231–243, June 2005.

[147] H. T. Beier, G. L. Coté, and K. E. Meissner, "Whispering Gallery Mode Biosensors Consisting of Quantum Dot-Embedded Microspheres," *Ann Biomed Eng*, vol. 37, pp. 1974–1983, Oct 2009.

[148] D. Kim and A. E. Herr, "Protein immobilization techniques for microfluidic assays," *Biomicrofluidics*, vol. 7, p. 041501, July 2013.

[149] K. Nakanishi, T. Sakiyama, Y. Kumada, K. Imamura, and H. Imanaka, "Recent advances in controlled immobilization of proteins onto the surface of the solid substrate and its possible application to proteomics," *Current Proteomics*, vol. 5, pp. 161–175, Oct. 2008.

[150] R. G. Lee and S. W. Kim, "Adsorption of proteins onto hydrophobic polymer surfaces: Adsorption isotherms and kinetics," *Journal of Biomedical Materials Research*, vol. 8, no. 5, pp. 251–259.

[151] Y. Arima and H. Iwata, "Effect of wettability and surface functional groups on protein adsorption and cell adhesion using well-defined mixed self-assembled monolayers," *Biomaterials*, vol. 28, pp. 3074–3082, July 2007.

[152] A. Gessner, R. Waicz, A. Lieske, B.-R. Paulke, K. Mäder, and R. Müller, "Nanoparticles with decreasing surface hydrophobicities: influence on plasma protein adsorption," *International Journal of Pharmaceutics*, vol. 196, pp. 245–249, Mar. 2000.

[153] M. Malmsten, "Ellipsometry studies of the effects of surface hydrophobicity on protein adsorption," *Colloids and Surfaces B: Biointerfaces*, vol. 3, pp. 297–308, Jan. 1995.

[154] J. A. Howarter and J. P. Youngblood, "Optimization of silica silanization by 3-aminopropyltriethoxysilane," *Langmuir*, vol. 22, pp. 11142–11147, Dec. 2006.

[155] Gelest, "Gelest silane coupling agents." https://www.gelest.com/wp-content/uploads/Goods-PDF-brochures-couplingagents.pdf, Accessed 06 Jan 2019.

[156] J. B. Brzoska, I. B. Azouz, and F. Rondelez, "Silanization of solid substrates: A step toward reproducibility," *Langmuir*, vol. 10, pp. 4367–4373, Nov. 1994.

[157] J. J. Cras, C. A. Rowe-Taitt, D. A. Nivens, and F. S. Ligler, "Comparison of chemical cleaning methods of glass in preparation for silanization," *Biosensors and Bioelectronics*, vol. 14, pp. 683–688, Dec. 1999.

[158] E. P. Schartner, G. Tsiminis, A. François, R. Kostecki, S. C. Warren-Smith, L. V. Nguyen, S. Heng, T. Reynolds, E. Klantsataya, K. J. Rowland, A. D. Abell, H. Ebendorff-Heidepriem, and T. M. Monro, "Taming the light in microstructured optical fibers for sensing," *International Journal of Applied Glass Science*, vol. 6, no. 3, pp. 229–239, 2015.

[159] W. Dierkes, *Twente University: Raw materials and compounds in rubber technology: Silica-Silane Reaction*, Accessed 06 Jan 2019.

[160] A. François, H. Ebendorff-Heidepriem, and T. M. Monro, "Comparison of surface functionalization processes for optical fibre biosensing applications," in *20th International Conference on Optical Fibre Sensors*, vol. 7503, p. 75030U, International Society for Optics and Photonics, Oct. 2009.

[161] A. François, Y. Zhi, and A. Meldrum, "Whispering gallery mode devices for sensing and biosensing," in *Photonic Materials for Sensing, Biosensing and Display Devices*, Springer Series in Materials Science, pp. 237–288, Springer, Cham, 2016.

[162] S. A. McFarlane, "Fluorescent-core microcapillaries: Detection limits for biosensing applications," Master's thesis, University of Alberta, 2013.

[163] C. G. L. Khoo, J. B. Lando, and H. Ishida, "Surface modification of contact-lens materials by silanization: An FTIR-ATR study," *Journal of Polymer Science: Part B: Polymer Physics*, vol. 28, pp. 213–223, 1990.

[164] G. Decher, "Fuzzy nanoassemblies: Toward layered polymeric multicomposites," *Science*, vol. 277, pp. 1232–1237, Aug. 1997.

[165] S. H. Behrens and D. G. Grier, "The charge of glass and silica surfaces," *The Journal of Chemical Physics*, vol. 115, pp. 6716–6721, Sept. 2001.

[166] N. Bassim, A. Herzing, W. Dressick, K. Wahl, D. Petrovykh, K. Fears, R. Stroud, and T. Clark, "Scanning transmission electron microscopy (STEM) tomography of layer-by-layer PAH/PSS-Au nanocomposite structures," *Microscopy and Microanalysis*, vol. 17, pp. 1012–1013, July 2011.

[167] Z. Feldötö, I. Varga, and E. Blomberg, "Influence of salt and rinsing protocol on the structure of PAH/PSS polyelectrolyte multilayers," *Langmuir*, vol. 26, pp. 17048–17057, Nov. 2010.

[168] S. Lane, P. West, A. François, and A. Meldrum, "Protein biosensing with fluorescent microcapillaries," *Optics Express*, vol. 23, pp. 2577–2590, Feb. 2015.

[169] Thermo Fisher, "Overview of Crosslinking and Protein Modification." https://www.thermofisher.com/ca/en/home/life-science/protein-

biology/protein-biology-learning-center/protein-biology-resource-library/pierce-protein-methods/overview-crosslinking-protein-modification.html, Accessed 06 Jan 2019.

[170] Thermo Fisher, "AntiBody Labeling and Immobilization Sites | Thermo Fisher Scientific." https://www.thermofisher.com/ca/en/home/life-science/antibodies/antibodies-learning-center/antibodies-resource-library/antibody-methods/antibody-labeling-immobilization-sites.html#/legacy=www.piercenet.com, Accessed 06 Jan 2019.

[171] B. B. Haab, "Antibody arrays in cancer research," *Mol Cell Proteomics*, vol. 4, pp. 377–383, Apr. 2005.

[172] Thermo Fisher, "Amine-Reactive Crosslinker Chemistry | Thermo Fisher Scientific." https://www.thermofisher.com/ca/en/home/life-science/protein-biology/protein-biology-learning-center/protein-biology-resource-library/pierce-protein-methods/amine-reactive-crosslinker-chemistry.html, Accessed 06 Jan 2019.

[173] Thermo Fisher, "AntiBody Labeling and Immobilization Sites | Thermo Fisher Scientific." https://www.thermofisher.com/ca/en/home/life-science/protein-biology/protein-biology-learning-center/protein-biology-resource-library/pierce-protein-methods/chemistry-crosslinking.html#3, Accessed 06 Jan 2019.

[174] C. Y. Lim, N. A. Owens, R. D. Wampler, Y. Ying, J. H. Granger, M. D. Porter, M. Takahashi, and K. Shimazu, "Succinimidyl ester surface chemistry: Implications of the competition between aminolysis and hydrolysis on covalent protein immobilization," *Langmuir*, vol. 30, pp. 12868–12878, Nov. 2014.

[175] Thermo Fisher, "Chemistry of Crosslinking." https://www.thermofisher.com/ca/en/home/life-science/protein-biology/protein-biology-learning-center/protein-biology-resource-

library/pierce-protein-methods/chemistry-crosslinking.html, Accessed 06 Jan 2019.

[176] N. C. Veitch, "Horseradish peroxidase: A modern view of a classic enzyme," *Phytochemistry*, vol. 65, pp. 249–259, Feb. 2004.

[177] Thermo Fisher, "Enzyme Probes | Thermo Fisher Scientific." https://www.thermofisher.com/ca/en/home/life-science/protein-biology/protein-biology-learning-center/protein-biology-resource-library/pierce-protein-methods/enzyme-probes.html, Accessed 06 Jan 2019.

[178] G. T. Hermanson, *Bioconjugate Techniques*. Academic Press, 2013.

[179] Sino Biological, "Competitive ELISA." http://www.elisa-antibody.com/ELISA-Introduction/ELISA-types/competitive-elisa, Accessed 06 Jan 2019.

[180] E. Engvall, "[28] Enzyme immunoassay ELISA and EMIT," in *Methods in enzymology*, vol. 70, pp. 419–439, Elsevier, 1980.

[181] P. J. Tighe, R. R. Ryder, I. Todd, and L. C. Fairclough, "ELISA in the multiplex era: Potentials and pitfalls," *PROTEOMICS–Clinical Applications*, vol. 9, no. 3-4, pp. 406–422, 2015.

[182] A. Voller, A. Bartlett, and D. Bidwell, "Enzyme immunoassays with special reference to ELISA techniques.," *Journal of Clinical Pathology*, vol. 31, no. 6, pp. 507–520, 1978.

[183] Thermo Fisher, "Overview of Protein Labeling | Thermo Fisher Scientific." https://www.thermofisher.com/ca/en/home/life-science/protein-biology/protein-biology-learning-center/protein-biology-resource-library/pierce-protein-methods/overview-protein-labeling.html, Accessed 06 Jan 2019.

[184] Thermo Fisher, "Antibody labeling | Thermo Fisher Scientific." https://www.thermofisher.com/ca/en/home/life-science/antibodies/antibody-labeling.html, Accessed 06 Jan 2019.

[185] A. R. Crofts, "Diffusion – useful equations." http://www.life.illinois.edu/crofts/bioph354/diffusion1.html, Accessed 06 Jan 2019.

[186] R. Chang, *Chemistry*. McGraw-Hill, 2005.

[187] California State University, "Methods of Determining Reaction Order." https://chem.libretexts.org/Core/Physical_and_Theoretical_Chemistry/Kinetics/Experimental_Methods/Methods_of_Determining_Reaction_Order, Accessed 06 Jan 2019.

[188] Biacore, "Biacore kinetic and affinity analysis: An introduction." http://web.bf.uni-lj.si/bi/sprcenter/BiacoreT100/Session5%20BasicKinetics.pdf, Accessed 06 Jan 2019.

[189] M. Srisa-Art, E. C. Dyson, A. J. deMello, and J. B. Edel, "Monitoring of real-time streptavidin-biotin binding kinetics using droplet microfluidics," *Analytical Chemistry*, vol. 80, pp. 7063–7067, 2008.

[190] V. Ilchenko and M. Gorodetskii, "Thermal nonlinear effects in optical whispering gallery microresonators," *Laser Phys*, vol. 2, no. 6, pp. 1004–1009, 1992.

[191] J. Hofer, A. Schliesser, and T. J. Kippenberg, "Cavity optomechanics with ultrahigh-q crystalline microresonators," *Physical Review A*, vol. 82, no. 3, p. 031804, 2010.

[192] A. Chijioke, Q.-F. Chen, A. Y. Nevsky, and S. Schiller, "Thermal noise of whispering-gallery resonators," *Physical Review A*, vol. 85, p. 053814, May 2012.

[193] M. Borecki, M. L. Korwin-Pawlowski, M. Beblowska, J. Szmidt, and A. Jakubowski, "Optoelectronic capillary sensors in microfluidic and point-of-care instrumentation," *Sensors*, vol. 10, pp. 3771–3797, Apr. 2010.

[194] V. Zamora, A. Díez, M. V. Andrés, and B. Gimeno, "Refractometric sensor based on whispering-gallery modes of thin capillaries," *Optics Express*, vol. 15, pp. 12011–12016, Sept. 2007.

[195] G. Yang, I. M. White, and X. Fan, "An opto-fluidic ring resonator biosensor for the detection of organophosphorus pesticides," *Sensors and Actuators B: Chemical*, vol. 133, pp. 105–112, July 2008.

[196] F. Vollmer, D. Braun, A. Libchaber, M. Khoshsima, I. Teraoka, and S. Arnold, "Protein detection by optical shift of a resonant microcavity," *Applied Physics Letters*, vol. 80, pp. 4057–4059, May 2002.

[197] H. Zhu, I. M. White, J. D. Suter, M. Zourob, and X. Fan, "Integrated refractive index optical ring resonator detector for capillary electrophoresis," *Analytical Chemistry*, vol. 79, pp. 930–937, Feb. 2007.

[198] V. Zamora, Z. Zhang, and A. Meldrum, "Refractometric sensing of heavy oils in fluorescent core microcapillaries," *Oil & Gas Science and Technology – Revue d'IFP Energies nouvelles*, vol. 70, no. 3, pp. 487–495, 2015.

[199] K. Scholten, X. Fan, and E. T. Zellers, "Microfabricated optofluidic ring resonator structures," *Applied Physics Letters*, vol. 99, p. 141108, Oct. 2011.

[200] G. Huang, V. A. Bolaños Quiñones, F. Ding, S. Kiravittaya, Y. Mei, and O. G. Schmidt, "Rolled-Up Optical Microcavities with Subwavelength Wall Thicknesses for Enhanced Liquid Sensing Applications," *ACS Nano*, vol. 4, pp. 3123–3130, June 2010.

[201] K. J. Rowland, A. François, P. Hoffmann, and T. M. Monro, "Fluorescent polymer coated capillaries as optofluidic refractometric sensors," *Optics Express*, vol. 21, pp. 11492–11505, May 2013.

[202] I. Teraoka, S. Arnold, and F. Vollmer, "Perturbation approach to resonance shifts of whispering-gallery modes in a dielectric microsphere as a probe of a surrounding medium," *Journal of the Optical Society of America B*, vol. 20, pp. 1937–1946, Sept. 2003.

[203] I. Teraoka and S. Arnold, "Enhancing the sensitivity of a whispering-gallery mode microsphere sensor by a high-refractive-index surface layer," *Journal of the Optical Society of America B*, vol. 23, pp. 1434–1441, July 2006.

[204] N. Lin, L. Jiang, S. Wang, H. Xiao, Y. Lu, and H.-L. Tsai, "Design and optimization of liquid core optical ring resonator for refractive index sensing," *Applied Optics*, vol. 50, pp. 3615–3621, July 2011.

[205] E. F. Franchimon, K. R. Hiremath, R. Stoffer, and M. Hammer, "Interaction of whispering gallery modes in integrated optical microring or microdisk circuits: hybrid coupled mode theory model," *Journal of the Optical Society of America B*, vol. 30, pp. 1048–1057, Apr. 2013.

[206] L. A. Weinstein, *Open resonators and open waveguides*. Golem Press, 1969.

[207] H. Li and X. Fan, "Characterization of sensing capability of optofluidic ring resonator biosensors," *Applied Physics Letters*, vol. 97, p. 011105, July 2010.

[208] T. Ling and L. J. Guo, "Analysis of the sensing properties of silica microtube resonator sensors," *Journal of the Optical Society of America B*, vol. 26, pp. 471–477, Mar. 2009.

[209] A. L. Stancik and E. B. Brauns, "A simple asymmetric lineshape for fitting infrared absorption spectra," *Vibrational Spectroscopy*, vol. 47, pp. 66–69, May 2008.

[210] "Polymicro technologies." https://www.polymicro.com/mx_upload/superfamily/polymicro/pdfs/capillarytubing%20_tsp_tsg.pdf.

[211] V. Zamora, A. Díez, M. V. Andrés, and B. Gimeno, "Interrogation of whispering-gallery modes resonances in cylindrical microcavities by backreflection detection," *Optics Letters*, vol. 34, pp. 1039–1041, Apr. 2009.

[212] A. Mazhorova, A. Markov, B. Ung, M. Rozé, S. Gorgutsa, and M. Skorobogatiy, "Thin chalcogenide capillaries as efficient waveguides from mid-infrared to terahertz," *Journal of the Optical Society of America B*, vol. 29, pp. 2116–2123, Aug. 2012.

[213] J. C. Knight, H. S. T. Driver, and G. N. Robertson, "Interference modulation of Q values in a cladded-fiber whispering-gallery-mode laser," *Optics Letters*, vol. 18, pp. 1296–1298, Aug. 1993.

[214] P. Bianucci, J. R. Rodríguez, C. Clements, C. M. Hessel, J. G. C. Veinot, and A. Meldrum, "Whispering gallery modes in silicon nanocrystal coated microcavities," *Physica Status Solidi (a)*, vol. 206, pp. 973–975, May 2009.

[215] T. Carmon, L. Yang, and K. J. Vahala, "Dynamical thermal behavior and thermal self-stability of microcavities," *Optics Express*, vol. 12, pp. 4742–4750, Oct. 2004.

[216] I. Teraoka, "Analysis of thermal stabilization of whispering gallery mode resonance," *Optics Communications*, vol. 310, pp. 212–216, Jan. 2014.

[217] J. D. Suter, I. M. White, H. Zhu, and X. Fan, "Thermal characterization of liquid core optical ring resonator sensors," *Applied Optics*, vol. 46, pp. 389–396, Jan. 2007.

[218] M. R. Foreman, W.-L. Jin, and F. Vollmer, "Optimizing detection limits in whispering gallery mode biosensing," *Optics Express*, vol. 22, pp. 5491–5511, Mar. 2014.

[219] Y. Zhi and A. Meldrum, "Tuning a microsphere whispering-gallery-mode sensor for extreme thermal stability," *Applied Physics Letters*, vol. 105, p. 031902, July 2014.

[220] B. Guha, J. Cardenas, and M. Lipson, "Athermal silicon microring resonators with titanium oxide cladding," *Optics Express*, vol. 21, pp. 26557–26563, Nov. 2013.

[221] L. He, S. K. Ozdemir, J. Zhu, and L. Yang, "Scatterer induced mode splitting in poly(dimethylsiloxane) coated microresonators," *Applied Physics Letters*, vol. 96, p. 221101, May 2010.

[222] J. Zhu, a. Kaya Özdemir, L. He, and L. Yang, "Optothermal spectroscopy of whispering gallery microresonators," *Applied Physics Letters*, vol. 99, p. 171101, Oct. 2011.

[223] F. Michelotti and E. Descrovi, "Temperature stability of Bloch surface wave biosensors," *Applied Physics Letters*, vol. 99, p. 231107, Dec. 2011.

[224] "Trade name FOX-15 Flowable Oxide from Dow-Corning.," tech. rep.

[225] I. Teraoka and S. Arnold, "Whispering-gallery modes in a microsphere coated with a high-refractive index layer: polarization-dependent sensitivity enhancement of the resonance-shift sensor and TE-TM resonance matching," *Journal of the Optical Society of America B*, vol. 24, pp. 653–659, Mar. 2007.

[226] Adams Stratton Julius., *Electromagnetic Theory*. Mcgraw Hill Book Company, 1941.

[227] "Silica glass (SiO_2) optical material."
https://www.crystran.co.uk/optical-materials/silica-glass-sio2,
Accessed 06 Jan 2019.

[228] S.-Y. Seo, J. Lee, J. H. Shin, E.-S. Kang, and B.-S. Bae, "The thermo-optic effect of Si nanocrystals in silicon-rich silicon oxidethin films," *Applied Physics Letters*, vol. 85, pp. 2526–2528, Sept. 2004.

[229] M. Piliarik and J. Homola, "Surface plasmon resonance (SPR) sensors: approaching their limits?," *Optics Express*, vol. 17, pp. 16505–16517, Sept. 2009.

[230] G. Y. Chen, C. A. Codemard, R. J. Lewis, L. Jankowski, J. S. Chan, P. M. Gorman, and M. N. Zervas, "Enhanced responsivity with skew ray excitation of reflection- and transmission-type refractometric sensors," *Optics Letters*, vol. 39, pp. 3822–3825, July 2014.

[231] X. Fan, I. M. White, S. I. Shopova, H. Zhu, J. D. Suter, and Y. Sun, "Sensitive optical biosensors for unlabeled targets: A review," *Analytica Chimica Acta*, vol. 620, pp. 8–26, July 2008.

[232] E. Wijaya, C. Lenaerts, S. Maricot, J. Hastanin, S. Habraken, J.-P. Vilcot, R. Boukherroub, and S. Szunerits, "Surface plasmon resonance-based biosensors: From the development of different SPR structures to novel surface functionalization strategies," *Current Opinion in Solid State and Materials Science*, vol. 15, pp. 208–224, Oct. 2011.

[233] W. R. Wong, O. Krupin, S. D. Sekaran, F. R. Mahamd Adikan, and P. Berini, "Serological diagnosis of dengue infection in blood plasma using long-range surface plasmon waveguides," *Analytical Chemistry*, vol. 86, pp. 1735–1743, Feb. 2014.

[234] J. Ladd, A. D. Taylor, M. Piliarik, J. Homola, and S. Jiang, "Label-free detection of cancer biomarker candidates using surface plasmon

resonance imaging," *Analytical and Bioanalytical Chemistry*, vol. 393, pp. 1157–1163, Feb. 2009.

[235] M. D. Baaske, M. R. Foreman, and F. Vollmer, "Single-molecule nucleic acid interactions monitored on a label-free microcavity biosensor platform," *Nature Nanotechnology*, vol. 9, pp. 933–939, Nov. 2014.

[236] P. Preechaburana, M. C. Gonzalez, A. Suska, and D. Filippini, "Surface plasmon resonance chemical sensing on cell phones," *Angewandte Chemie International Edition*, vol. 51, pp. 11585–11588, Nov. 2012.

[237] Y. Zhi, C. P. K. Manchee, J. W. Silverstone, Z. Zhang, and A. Meldrum, "Refractometric sensing with silicon quantum dots coupled to a microsphere," *Plasmonics*, vol. 8, pp. 71–78, Mar. 2013.

[238] I. Teraoka and S. Arnold, "Coupled whispering gallery modes in a multilayer-coated microsphere," *Optics Letters*, vol. 32, pp. 1147–1149, May 2007.

[239] V. S. Ilchenko, M. L. Gorodetsky, X. S. Yao, and L. Maleki, "Microtorus: a high-finesse microcavity with whispering-gallery modes," *Optics Letters*, vol. 26, pp. 256–258, Mar. 2001.

[240] S. M. Grist, S. A. Schmidt, J. Flueckiger, V. Donzella, W. Shi, S. Talebi Fard, J. T. Kirk, D. M. Ratner, K. C. Cheung, and L. Chrostowski, "Silicon photonic micro-disk resonators for label-free biosensing," *Optics Express*, vol. 21, pp. 7994–8006, Apr. 2013.

[241] H. Zhu, I. M. White, J. D. Suter, P. S. Dale, and X. Fan, "Analysis of biomolecule detection with optofluidic ring resonator sensors," *Optics Express*, vol. 15, pp. 9139–9146, July 2007.

[242] S. Pang, R. E. Beckham, and K. E. Meissner, "Quantum dot-embedded microspheres for remote refractive index sensing," *Applied Physics Letters*, vol. 92, p. 221108, June 2008.

[243] A. Francois and M. Himmelhaus, "Optical biosensor based on whispering gallery mode excitations in clusters of microparticles," *Applied Physics Letters*, vol. 92, p. 141107, Apr. 2008.

[244] A. Weller, F. C. Liu, R. Dahint, and M. Himmelhaus, "Whispering gallery mode biosensors in the low-Q limit," *Applied Physics B*, vol. 90, pp. 561–567, Mar. 2008.

[245] E. Nuhiji and P. Mulvaney, "Detection of unlabeled oligonucleotide targets using whispering gallery modes in single, fluorescent microspheres," *Small*, vol. 3, pp. 1408–1414, Aug. 2007.

[246] P. Zijlstra, K. L. van der Molen, and A. P. Mosk, "Spatial refractive index sensor using whispering gallery modes in an optically trapped microsphere," *Applied Physics Letters*, vol. 90, p. 161101, Apr. 2007.

[247] D. E. Gómez, I. Pastoriza-Santos, and P. Mulvaney, "Tunable whispering gallery mode emission from quantum-dot-doped microspheres," *Small*, vol. 1, pp. 238–241, Feb. 2005.

[248] M. Charlebois, A. Paquet, L. S. Verret, K. Boissinot, M. Boissinot, M. G. Bergeron, and C. N. Allen, "Toward automatic label-free whispering gallery modes biodetection with a quantum dot-coated microsphere population," *Nanoscale Research Letters*, vol. 5, p. 524, Mar. 2010.

[249] R. E. Benner, P. W. Barber, J. F. Owen, and R. K. Chang, "Observation of structure resonances in the fluorescence spectra from microspheres," *Physical Review Letters*, vol. 44, pp. 475–478, Feb. 1980.

[250] V. Lefèvre-Seguin, "Whispering-gallery mode lasers with doped silica microspheres," *Optical Materials*, vol. 11, pp. 153–165, Jan. 1999.

[251] Y. Panitchob, G. S. Murugan, M. N. Zervas, P. Horak, S. Berneschi, S. Pelli, G. N. Conti, and J. S. Wilkinson, "Whispering gallery mode spectra of channel waveguide coupled microspheres," *Optics Express*, vol. 16, pp. 11066–11076, July 2008.

[252] H. Zhu, J. D. Suter, I. M. White, and X. Fan, "Aptamer based microsphere biosensor for thrombin detection," *Sensors*, vol. 6, pp. 785–795, Aug. 2006.

[253] K. Johansen, R. Stålberg, I. Lundström, and B. Liedberg, "Surface plasmon resonance: instrumental resolution using photo diode arrays," *Measurement Science and Technology*, vol. 11, no. 11, p. 1630, 2000.

[254] V. Bosio, F. Dubreuil, G. Bogdanovic, and A. Fery, "Interactions between silica surfaces coated by polyelectrolyte multilayers in aqueous environment: comparison between precursor and multilayer regime," *Colloids and Surfaces A: Physicochemical and Engineering Aspects*, vol. 243, pp. 147–155, Aug. 2004.

[255] A. François, T. Reynolds, and T. M. Monro, "A fiber-tip label-free biological sensing platform: A practical approach toward in-vivo sensing," *Sensors*, vol. 15, pp. 1168–1181, Jan. 2015.

[256] M. J. E. Fischer, "Amine coupling through EDC/NHS: a practical approach," *Methods in Molecular Biology*, vol. 627, pp. 55–73, 2010.

[257] G. T. Hermanson, *Bioconjugate Techniques*. Academic Press, July 2010.

[258] D. Hayworth, "Carbodiimide Crosslinker Chemistry." https://www.thermofisher.com/ca/en/home/life-science/protein-biology/protein-biology-learning-center/protein-biology-resource-library/pierce-protein-methods/carbodiimide-crosslinker-chemistry.html, Accessed 06 Jan 2019.

[259] "Technical data sheet 779, The benefits of neutravidin over streptavidin and avidin." Polysciences, Inc., 2008.

[260] P. Vermette, T. Gengenbach, U. Divisekera, P. A. Kambouris, H. J. Griesser, and L. Meagher, "Immobilization and surface characterization of NeutrAvidin biotin-binding protein on different hydrogel interlayers," *Journal of Colloid and Interface Science*, vol. 259, pp. 13–26, Mar. 2003.

[261] I. Barinaga-Rementeria Ramirez, L. Ekblad, and B. Jergil, "Affinity partitioning of biotinylated mixed liposomes: effect of charge on biotin–NeutrAvidin interaction," *Journal of Chromatography B: Biomedical Sciences and Applications*, vol. 743, pp. 389–396, June 2000.

[262] P. Allongue, V. Costa-Kieling, and H. Gerischer, "Etching of silicon in NaOH solutions II. Electrochemical studies of n-Si(111) and (100) and mechanism of the dissolution," *J. Electrochem. Soc.*, vol. 140, pp. 1018–1026, Apr. 1993.

[263] I. M. White, S. I. Shapova, H. Zhu, J. D. Suter, S. Lacey, P. Zhang, H. Oveys, L. Brewington, J. Gohring, and X. Fan, "Applications of the liquid core optical ring resonator platform," in *Sensors for Harsh Environments III*, vol. 6757, p. 675707, International Society for Optics and Photonics, Oct. 2007.

[264] G. M. Hale and M. R. Querry, "Optical constants of water in the 200-nm to 200-μm wavelength region," *Applied Optics*, vol. 12, pp. 555–563, Mar. 1973.

[265] I. H. Malitson, "Interspecimen comparison of the refractive index of fused silica," *Journal of the Optical Society of America*, vol. 55, pp. 1205–1209, Oct. 1965.

[266] C. Rosano, P. Arosio, and M. Bolognesi, "The X-ray three-dimensional structure of avidin," *Biomolecular Engineering*, vol. 16, pp. 5–12, Dec. 1999.

[267] G. Y. Onoda and E. G. Liniger, "Experimental determination of the random-parking limit in two dimensions," *Physical Review A*, vol. 33, pp. 715–716, Jan. 1986.

[268] A. Tsortos, G. Papadakis, K. Mitsakakis, K. A. Melzak, and E. Gizeli, "Quantitative determination of size and shape of surface-bound DNA

using an acoustic wave sensor," *Biophysical Journal*, vol. 94, pp. 2706–2715, Apr. 2008.

[269] S.-F. Cheng and L.-K. Chau, "Colloidal gold-modified optical fiber for chemical and biochemical sensing," *Analytical Chemistry*, vol. 75, pp. 16–21, Jan. 2003.

[270] G. Schweiger and M. Horn, "Effect of changes in size and index of refraction on the resonance wavelength of microspheres," *Journal of the Optical Society of America B*, vol. 23, pp. 212–217, Feb. 2006.

[271] L. Weiss, A. Tazibt, A. Tidu, and M. Aillerie, "Water density and polarizability deduced from the refractive index determined by interferometric measurements up to 250 MPa," *The Journal of Chemical Physics*, vol. 136, p. 124201, Mar. 2012.

[272] C.-D. Chen, S.-F. Cheng, L.-K. Chau, and C. R. C. Wang, "Sensing capability of the localized surface plasmon resonance of gold nanorods," *Biosensors and Bioelectronics*, vol. 22, pp. 926–932, Jan. 2007.

[273] H. Zhu, I. M. White, J. D. Suter, and X. Fan, "Phage-based label-free biomolecule detection in an opto-fluidic ring resonator," *Biosensors and Bioelectronics*, vol. 24, pp. 461–466, Nov. 2008.

[274] A. Meldrum, S. Lane, A. François, and P. West, "Fluorescent microcapillaries for biosensing applications," *SPIE Newsroom*, May 2015.

[275] C.P. Kyle Manchee, "Refractometric sensing with fluorescent-core microcapillaries," Master's thesis, University of Alberta, Edmonton, Alberta, 2011.

[276] J. Chan, T. Thiessen, S. Lane, P. West, K. Gardner, A. Francois, and A. Meldrum, "Microfluidic detection of vitamin D_3 compounds using a cylindrical optical microcavity," *IEEE Sensors Journal*, vol. 15, pp. 3467–3474, June 2015.

[277] C. Dang, J. Lee, C. Breen, J. S. Steckel, S. Coe-Sullivan, and A. Nurmikko, "Red, green and blue lasing enabled by single-exciton gain in colloidal quantum dot films," *Nature Nanotechnology*, vol. 7, pp. 335–339, May 2012.

[278] N. A. Naderi, F. Grillot, K. Yang, J. B. Wright, A. Gin, and L. F. Lester, "Two-color multi-section quantum dot distributed feedback laser," *Optics Express*, vol. 18, no. 26, pp. 27028–27035, 2010.

[279] Y. Fujimoto, O. Ishii, and M. Yamazaki, "Multi-colour laser oscillation in Pr^{3+}-doped fluoro-aluminate glass fibre pumped by 442.6 nm GaN-semiconductor laser," *Electronics Letters*, vol. 45, pp. 1301–1302, Dec. 2009.

[280] F. Fan, S. Turkdogan, Z. Liu, D. Shelhammer, and C. Z. Ning, "A monolithic white laser," *Nature Nanotechnology*, vol. 10, pp. 796–803, July 2015.

[281] S. K. Y. Tang, Z. Li, A. R. Abate, J. J. Agresti, D. A. Weitz, D. Psaltis, and G. M. Whitesides, "A multi-color fast-switching microfluidic droplet dye laser," *Lab on a Chip*, vol. 9, no. 19, p. 2767, 2009.

[282] H. Zhang, T.-T. Lu, W.-Y. Lai, X.-W. Zhang, M.-K. Zhang, P. Lv, C.-F. Liu, and W. Huang, "Pyrene-cored starburst oligofluorenes with diphenylamine end-cappers: Design, synthesis, stabilized optical gain, and lasing properties," *The Journal of Physical Chemistry C*, vol. 121, no. 49, pp. 27569–27579, 2017.

[283] W. Xu, J. Yi, W.-Y. Lai, L. Zhao, Q. Zhang, W. Hu, X.-W. Zhang, Y. Jiang, L. Liu, and W. Huang, "Pyrene-capped conjugated amorphous starbursts: Synthesis, characterization, and stable lasing properties in ambient atmosphere," *Advanced Functional Materials*, vol. 25, no. 29, pp. 4617–4625.

[284] M. Fang, J. Huang, S.-J. Chang, Y. Jiang, W.-Y. Lai, and W. Huang, "Ladder-type oligo(p-phenylene)s with d–π–a architectures: design, synthesis, optical gain properties, and stabilized amplified spontaneous emission," *Journal of Materials Chemistry C*, vol. 5, pp. 5797–5809, 2017.

[285] C.-F. Liu, M. Sang, W.-Y. Lai, T. Lu, X. Liu, and W. Huang, "Design and synthesis of monodisperse macromolecular starbursts based on a triazine center with multibranched oligofluorenes as efficient gain media for organic lasers," *Macromolecules*, vol. 51, no. 4, pp. 1325–1335, 2018.

[286] A. Neumann, J. J. Wierer, W. Davis, Y. Ohno, S. R. J. Brueck, and J. Y. Tsao, "Four-color laser white illuminant demonstrating high color-rendering quality," *Optics Express*, vol. 19, no. 104, pp. A982–A990, 2011.

[287] J. J. Wierer, J. Y. Tsao, and D. S. Sizov, "Comparison between blue lasers and light-emitting diodes for future solid-state lighting: Comparison between blue lasers and light-emitting diodes," *Laser & Photonics Reviews*, vol. 7, pp. 963–993, Nov. 2013.

[288] K. Chellappan, E. Erden, and H. Urey, "Laser-based displays: a review," *Applied optics*, vol. 49, Sept. 2010.

[289] T. Hayes, "Laser projection takes its place in the spotlight." http://optics.org/news/7/3/23, Accessed 06 Jan 2019.

[290] M. Holz and E. Weidel, "System for improving the visibility in vehicles." http://patents.google.com/patent/US6552342B2/en, Apr. 2003.

[291] T. Mori, H.-G. Kim, T. Mizutani, and D.-C. Lee, "Electroluminescent properties in organic light-emitting diode doped with two guest dyes," *Japanese Journal of Applied Physics*, vol. 40, no. 9R, p. 5346, 2001.

[292] M.-T. Lee, C.-K. Yen, W.-P. Yang, H.-H. Chen, C.-H. Liao, C.-H. Tsai, and C. H. Chen, "Efficient green coumarin dopants for organic light-emitting devices," *Organic Letters*, vol. 6, pp. 1241–1244, Apr. 2004.

[293] K. Yamashita, N. Takeuchi, K. Oe, and H. Yanagi, "Simultaneous RGB lasing from a single-chip polymer device," *Optics Letters*, vol. 35, July 2010.

[294] M. Savarese, A. Aliberti, I. De Santo, E. Battista, F. Causa, P. A. Netti, and N. Rega, "Fluorescence lifetimes and quantum yields of rhodamine derivatives: New insights from theory and experiment," *The Journal of Physical Chemistry A*, vol. 116, no. 28, pp. 7491–7497, 2012.

[295] O. S. Wolfbeis, E. Lippert, and H. Schwarz, "pH-dependent fluorescence spectroscopy, 8 [1]: Photochemical reversible ring opening of 4-phenylumbelliferone," *Berichte der Bunsengesellschaft für physikalische Chemie*, vol. 84, no. 11, pp. 1115–1119, 1980.

[296] J. Ferguson and A. Mau, "Absorption studies of acid-base equilibria of dye solutions," *Chemical Physics Letters*, vol. 17, pp. 543–546, Dec. 1972.

[297] L. Lu and S. A. Jenekhe, "Poly(vinyl diphenylquinoline): A new pH-tunable light-emitting and charge-transport polymer synthesized by a simple modification of polystyrene," *Macromolecules*, vol. 34, pp. 6249–6254, Aug. 2001.

[298] O. S. Wolfbeis and R. Schipfer, "Acidity dependence of the absorption and fluorescence spectra of isoflavone and 7-hydroxyisoflavone," *Photochemistry and Photobiology*, vol. 34, no. 5, pp. 567–571.

[299] C. V. Shank, A. Dienes, A. M. Trozzolo, and J. A. Myer, "Near UV to yellow tunable laser emission from an organic dye," *Applied Physics Letters*, vol. 16, pp. 405–407, May 1970.

[300] D. Schneider, T. Rabe, T. Riedl, T. Dobbertin, M. Kröger, E. Becker, H.-H. Johannes, W. Kowalsky, T. Weimann, J. Wang, and P. Hinze, "Ultrawide tuning range in doped organic solid-state lasers," *Applied Physics Letters*, vol. 85, pp. 1886–1888, Sept. 2004.

[301] S. Kushida, S. Okabe, T. D. Dao, S. Ishii, T. Nagao, A. Saeki, M. Kijima, and Y. Yamamoto, "Self-assembled polycarbazole microspheres as single-component, white-colour resonant photoemitters," *RSC Advances*, vol. 6, no. 58, pp. 52854–52857, 2016.

[302] T. E. Bush and G. W. Scott, "Fluorescence of distyrylbenzenes," *The Journal of Physical Chemistry*, vol. 85, no. 2, pp. 144–146, 1981.

[303] A. Guerlin, F. Dumur, E. Dumas, F. Miomandre, G. Wantz, and C. R. Mayer, "Tunable Optical Properties of Chromophores Derived from Oligo(p -phenylene vinylene)," *Organic Letters*, vol. 12, pp. 2382–2385, May 2010.

[304] J. C. Sancho-García, J.-L. Brédas, D. Beljonne, J. Cornil, R. Martínez-Álvarez, M. Hanack, L. Poulsen, J. Gierschner, H.-G. Mack, H.-J. Egelhaaf, and D. Oelkrug, "Design of π-conjugated organic materials for one-dimensional energy transport in nanochannels," *The Journal of Physical Chemistry B*, vol. 109, pp. 4872–4880, Mar. 2005.

[305] A. Chaieb, A. Khoukh, R. Brown, J. François, and C. Dagron-Lartigau, "Characterization of model luminescent PPV analogues with donating or withdrawing groups," *Optical Materials*, vol. 30, pp. 318–327, Oct. 2007.

[306] C.-W. Ko and H.-C. Lin, "Doped LED polymers containing novel luminescent bispyridyl compounds," *Thin Solid Films*, vol. 363, pp. 81–85, 2000.

[307] T. Fukuda, M. Ohashi, B. Wei, T. Okada, M. Ichikawa, and Y. Taniguchi, "Transient response of blue organic electroluminescence

devices with short fluorescence lifetime of substituted phenyl/vinyl compound as an emissive layer," *Optics Letters*, vol. 32, no. 9, pp. 1150–1152, 2007.

[308] S. Vagin, A. Ott, S. Hoffmann, D. Lanzinger, and B. Rieger, "Synthesis and properties of (triptycenedicarboxylatio)zinc coordination networks," *Chemistry - A European Journal*, vol. 15, pp. 5845–5853, June 2009.

[309] K. Shen, L. Qin, and H.-G. Zheng, "Diverse structures of metal–organic frameworks via a side chain adjustment: interpenetration and gas adsorption," *Dalton Transactions*, vol. 45, no. 41, pp. 16205–16210, 2016.

[310] I.-H. Park, C. E. Mulijanto, H.-H. Lee, Y. Kang, E. Lee, A. Chanthapally, S. S. Lee, and J. J. Vittal, "Influence of interpenetration in diamondoid metal–organic frameworks on the photoreactivity and sensing properties," *Crystal Growth & Design*, vol. 16, pp. 2504–2508, May 2016.

[311] R. Kabe, H. Nakanotani, T. Sakanoue, M. Yahiro, and C. Adachi, "Effect of molecular morphology on amplified spontaneous emission of bis-styrylbenzene derivatives," *Advanced Materials*, vol. 21, pp. 4034–4038, Oct. 2009.

[312] H. Wang, F. Li, B. Gao, Z. Xie, S. Liu, C. Wang, D. Hu, F. Shen, Y. Xu, H. Shang, Q. Chen, Y. Ma, and H. Sun, "Doped organic crystals with high efficiency, color-tunable emission toward laser application," *Crystal Growth & Design*, vol. 9, pp. 4945–4950, Nov. 2009.

[313] H.-H. Fang, R. Ding, S.-Y. Lu, X.-L. Zhang, J. Feng, Q.-D. Chen, and H.-B. Sun, "Flexible lasers based on the microstructured single-crystalline ultrathin films," *Journal of Materials Chemistry*, vol. 22, no. 45, p. 24139, 2012.

[314] E. M. Ebeid, M. H. Abel-Kader, M. M. F. Sabry, and A. B. Yousef, "Photochemical and spectral behaviour of diolefinic laser dyes in microemul-

sion media," *Journal of Photochemistry and Photobiology A: Chemistry*, vol. 44, no. 2, pp. 153–159, 1988.

[315] X. Wang, H. Li, Y. Wu, Z. Xu, and H. Fu, "Tunable morphology of the self-assembled organic microcrystals for the efficient laser optical resonator by molecular modulation," *Journal of the American Chemical Society*, vol. 136, no. 47, pp. 16602–16608, 2014. PMID: 25369119.

[316] H.-C. Lin, C.-M. Tsai, G.-H. Huang, and Y.-T. Tao, "Synthesis and characterization of light-emitting H-bonded complexes and polymers containing bis(pyridyl) emitting acceptors," *Macromolecules*, vol. 39, pp. 557–568, Jan. 2006.

[317] E. Z. M. Ebeid and A. J. Lees, "Molecular association in flexible diolefinic dyes," *Journal of Physical Chemistry*, vol. 91, no. 22, pp. 5792–5795, 1987.

[318] H. Detert, O. Sadovski, and E. Sugiono, "Acidochromism of C_2 - symmetrical aza-analogues of 1,4-distyrylbenzene," *Journal of Physical Organic Chemistry*, vol. 17, pp. 1046–1050, Nov. 2004.

[319] E.-Z. M. Ebeid, R. M. Issa, M. M. Ghoneim, and S. A. El-Daly, "Emission characteristics and micellization of cationic 1, 4-bis (β-pyridyl-2-vinyl) benzene laser dye," *Journal of the Chemical Society, Faraday Transactions 1: Physical Chemistry in Condensed Phases*, vol. 82, no. 3, pp. 909–919, 1986.

[320] H. Quast and J. Schulze, "Neopentylierung von Phenolen und Hydrochinonen," *European Journal of Organic Chemistry*, vol. 1990, no. 6, pp. 509–512, 1990.

[321] S. Doddi, B. Ramakrishna, Y. Venkatesh, and P. R. Bangal, "Synthesis and spectral characterization of photoswitchable oligo(p-phenylenevinylene)–spiropyran dyad," *RSC Advances*, vol. 5, no. 70, pp. 56855–56864, 2015.

[322] Y. Iwase, K. Kamada, K. Ohta, and K. Kondo, "Synthesis and photophysical properties of new two-photon absorption chromophores containing a diacetylene moiety as the central π-bridge," *Journal of Materials Chemistry*, vol. 13, no. 7, pp. 1575–1581, 2003.

[323] Y. Guo, W. Geng, and J. Sun, "Layer-by-layer deposition of polyelectrolyte-polyelectrolyte complexes for multilayer film fabrication," *Langmuir*, vol. 25, no. 2, pp. 1004–1010, 2008.

[324] M. G. Lagorio and E. San Román, "How does light scattering affect luminescence? Fluorescence spectra and quantum yields in the solid phase," *Journal of Chemical Education*, vol. 79, no. 11, p. 1362, 2002.

[325] M. Y. Berezin and S. Achilefu, "Fluorescence lifetime measurements and biological imaging," *Chemical Reviews*, vol. 110, pp. 2641–2684, May 2010.

[326] S. M. Al-Hazmy, A. S. Babaqi, E. Daltrozzo, M. Klink, J. Sauter, and E. M. Ebeid, "A new diolefinic laser dye: 2, 5-bis-2-(2-naphthyl) vinyl pyrazine (B2nvp)," *Journal of Photochemistry and Photobiology A: Chemistry*, vol. 122, no. 1, pp. 17–22, 1999.

[327] J. N. Wilson and U. H. F. Bunz, "Switching of intramolecular charge transfer in cruciforms: Metal ion sensing," *Journal of the American Chemical Society*, vol. 127, pp. 4124–4125, Mar. 2005.

[328] J. Zhang, J. Chen, B. Xu, L. Wang, S. Ma, Y. Dong, B. Li, L. Ye, and W. Tian, "Remarkable fluorescence change based on the protonation–deprotonation control in organic crystals," *Chemical Communications*, vol. 49, no. 37, p. 3878, 2013.

[329] X.-J. Zhou, C. Chen, C.-X. Ren, J.-K. Sun, and J. Zhang, "Tunable solid-state photoluminescence based on proton-triggered structural transformation of 4,4-bipyridinium derivative," *Journal of Materials Chemistry C*, vol. 1, no. 4, pp. 744–750, 2013.

[330] T. Grossmann, S. Schleede, M. Hauser, M. B. Christiansen, C. Vannahme, C. Eschenbaum, S. Klinkhammer, T. Beck, J. Fuchs, G. U. Nienhaus, U. Lemmer, A. Kristensen, T. Mappes, and H. Kalt, "Low-threshold conical microcavity dye lasers," *Applied Physics Letters*, vol. 97, p. 063304, Aug. 2010.

[331] B. Min, S. Kim, K. Okamoto, L. Yang, A. Scherer, H. Atwater, and K. Vahala, "Ultralow threshold on-chip microcavity nanocrystal quantum dot lasers," *Applied Physics Letters*, vol. 89, p. 191124, Nov. 2006.

[332] I. V. Golovnin, A. A. Bakulin, S. A. Zapunidy, E. M. Nechvolodova, and D. Y. Paraschuk, "Dramatic enhancement of photo-oxidation stability of a conjugated polymer in blends with organic acceptor," *Applied Physics Letters*, vol. 92, p. 243311, June 2008.

Appendix A

Wide-gamut lasing from a single organic chromophore

Toward the end of my main thesis work, I began to investigate organic chromophores for application in microcavities and other structures. Since the theme is fairly different from the work that went before, this manuscript was added as an appendix. *A modified version of this chapter was published in Light Science & Applications 7:101 (2018) by S. Lane, S. Vagin, H. Wang, W. Heinz, W. Morrish, Y. Zhao, B. Rieger, and A. Meldrum.*

A.1 Abstract

The development of wide-band lasing media has deep implications for imaging, sensing, and display technologies. We show that a single chromophore can be engineered to feature wide-gamut fluorescence and lasing throughout the entire visible spectrum and beyond. This exceptional color tuning demonstrates a chemically controlled paradigm for light emission applications with precise color management. Achieving such extensive color control requires a molecular blueprint that yields a high quantum efficiency and a high solubility in a wide variety of liquids and solids, while featuring a heterocyclic structure with good steric access to the lone pair electrons. With these requirements in mind,

we designed a lasing chromophore that encloses a lasing color space twice as large as the sRGB benchmark. This record degree of color tuning can in principle be adapted to the solid state by incorporation of the chromophore into polymer films. By appropriately engineering the base molecular structure, the widest range of lasing wavelengths observed for a conventional gain medium can be achieved, in turn establishing a possible route toward high-efficiency light emitters and lasers with near-perfect chromaticity.

A.2 Introduction

Achieving widely tunable light emission from a single substance has implications for biological imaging, fluorescence- or laser-based sensing, and for realizing white-light emitters and lasers. There is a concerted effort toward the development of color-controlled light emission based on single-material systems for these applications, including quantum dots [277] [278], doped fibers [279], monolithic semiconductors [280], and microdroplets [281]. Organic chromophores present another tunable gain medium that offers exceptional structural and chemical control [282] [283] [284] [285], although they traditionally offer restricted fluorescence shifts and the lasing spectrum is usually limited within a few tens of nm. Here we show that by appropriately engineering the chromophore molecular structure, one can design extensive fluorescence control and the widest laser color gamut obtained from any single emitter.

The ability to extensively tune the wavelength suggests a possible "one-pot" option for mixed-color lasers, sensors, and biomarkers. For example, emitters whose color is especially sensitive to the chemical nature of the environment could offer a major improvement over conventional materials used for fluorescence-based sensors and biological imaging. Appropriate wavelength selection can also increase the attainable color space [286] for high-power illumination sources [287], holographic projectors [288], IMAX^{TM} screens [289], and headlights [290]. Organic chromophores are often incorporated into organic light emitting devices (OLEDs) [291] [292] but achieving the desired

color control requires the use of mutually compatible chromophores, solvents, and polymer hosts, significantly increasing the synthesis complexity [293].

One way to change the emission spectrum is to chemically alter the base structure of the chromophore in order to create derivative structures with modified energy levels [294], but this offers limited wavelength control and relies on the synthesis of fundamentally different compounds (*e.g.*, the rhodamine dye class). Another method is to use the solvatochromic effect; for example, the fluorescence maximum of 4-phenylumbelliferone, a blue-emitting coumarin derivative, can be shifted by changing the solvent from dimethyl formamide (DMF) to alkaline water [295]. Rhodamine B and polyvinyl diphenylquinoline are tunable over tens of nm by changing the local pH [296] [297]. 7-hydroxy isoflavone can be tuned over about 35 nm in the blue-green depending on the pH of the solution [298]. Exciplex structures formed from a coumarin derivative might lase over a range of wavelengths by adjusting the solution pH [299]. A lasing color range between orange and red was recently achieved in dicyanomethylene-doped polymers via energy transfer from a conjugated polymer host [300]. In an alternative approach, broad spectrum luminescence was recently reported from the whispering gallery modes of conjugated polymer microspheres [301].

Distyrylbenzenes (DSBs, Fig. A.1) are a class of fluorescent conjugated organic molecules that provide structurally defined motifs for the poly(phenylene vinylene)s (PPVs) [302]. They can be functionalized by the introduction of different substituents, heteroatoms, or functional groups at desired positions [303] [304] to achieve specific structure-property relationships [305]. Electroluminescent devices [306] [307] and coordination frameworks [308] [309] [310] have been recently fabricated using this class of materials. DSBs can also show amplified spontaneous emission and lasing both in solution and in the solid state [311] [312] [313] [314] [315], and in some cases, they may respond to protonation by shifts in the absorption, fluorescence, or lasing spectra [316] [317] [318] [319]. P2VB (1,4-bis(β-pyridyl-2-vinyl)benzene) is a DSB derivative with pyridine groups (Fig. A.1(b)) that tend to interact with the surrounding

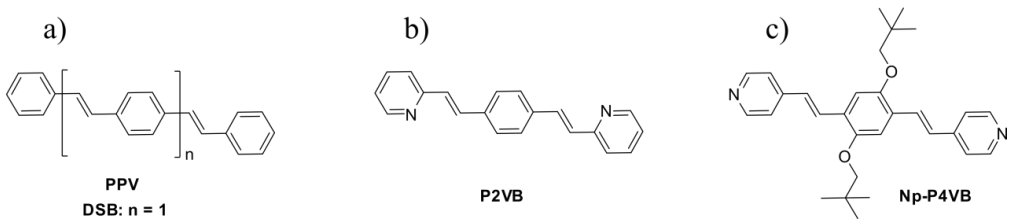

Figure A.1: Chemical structures of a) DSB (PPV), b) P2VB, and c) Np-P4VB. The key change between DSB and P2VB is the pyridine ring on each end. The difference between the P2VB and P4VB structures is the position of the nitrogen in the pyridine rings. The Np-P4VB synthesized here is similar to P4VB but with the addition of branched neopentyloxy groups on the central benzene ring.

electronic structure. P4VB (1,4-bis(4-pyridyl-2-vinyl)benzene) has the nitrogen atoms on the more accessible 4^{th} ring position, but it appears to associate more readily, and, like P2VB, it has limited solubility in organic solvents [317].

The addition of specific sidegroups to the molecular base structure might, in principle, overcome the solubility problem and could limit undesirable intermolecular interactions that decrease the efficiency of conventional chromophores. Here, we place relatively bulky and unreactive neopentyl sidegroups onto P4VB base structure to form bis(4-pyridyl)dineopentoxyl-p-phenylenedivinylene (Np-P4VB; Fig. A.1(c)). One may thus in principle combine high solubility, a high absolute quantum yield (AQY), and sterically accessible heterocyclic nitrogen atoms on the terminal pyridines in order to achieve wideband emission color control. Minor changes to the sidegroup could include carboxyl, amine or other groups aimed toward bioconjugation while maintaining many of the other beneficial features demonstrated below.

A.3 Materials and methods

All solvents and reagents used in the synthesis were purchased from commercial sources and were applied without additional purification, unless stated otherwise.

A.3.1 Synthesis of Np-P4VB

The Np-P4VB was prepared according to the four-step route shown in Fig. A.2.

Step 1:

1,4-dineopentyloxy benzene (1) was first synthesized by a modification of a procedure described by Quast et al. [320]. Hydroquinone (1.10 g; 9.99 mmol; 1.0 eq.) together with cesium carbonate (16.02 g; 45.40 mmol; 4.5 eq.) were placed in a flame dried pressure Schlenk flask, evacuated and again flooded with argon. Neopentyl bromide (3.43 mL, 4.11 g, 27.25 mmol; 2.8 eq.) in degassed and dried over molecular sieves N-methylpyrrolidon (NMP, 30 mL) was then added. The reaction mixture was gently evacuated, heated to 160 °C and stirred for three days. After cooling to ambient temperature the reaction mixture was poured into 700 mL ice-cold water and the colorless precipitate was filtered after fifteen minutes of stirring. Recrystallization from ethanol yields product (1) as colorless needles (2.48 g, 9.90 mmol; 99%).

Step 2:

1,4-bis(bromomethyl)-2,5-bis(neopentyloxy) benzene (2) was synthesized via a Blanc-type bromomethylation of product (1) similarly to a recently described procedure [321]. Product (1) (3.82 g; 15.26 mmol; 1.0 eq.) and paraformaldehyde (1.01 g; 33.57 mmol; 2.2 eq.) were evacuated, flushed with argon and then suspended in acetic acid (100 mL). A hydrogen bromide solution in acetic acid (30%; 9.05 g; 33.57 mmol; 2.2 eq.) was added. After stirring for fifteen minutes at ambient temperature, the suspension was further stirred at 65 °C overnight. After cooling to room temperature, the resulting yellow-brownish suspension was poured into ice-cold water (650 mL), stirred for ten minutes and the white precipitate filtered off. The raw product was dissolved in hot chloroform (20 mL) and precipitated by addition of methanol (180 mL). The flask was slowly cooled to 5 °C and stored overnight at this temperature. After

filtration, the solution was concentrated to 50% of its volume and again cooled to 5 °C and filtered. The collected solid fractions were dried under reduced pressure yielding product (2) (3.84 g; 8.80 mmol; 58%) as fine colorless needles.

Step 3:

1,4-bis(diethylphosphonatomethyl)-2,5-bis(neopentyloxy) benzene, which is product (3), was synthesized using the method established by Iwase et al. [322]. The bromomethyl derivative (2) (0.15 g; 0.34 mmol; 1.0 eq.) was placed in a Schlenk flask under argon. After addition of triethylphosphite (2.4 mL; 2.28 g; 13.76 mmol; 40 eq.) the mixture was stirred at 150 °C overnight. The clear solution turned into a white suspension after cooling down to ambient temperature. Residual triethylphosphite was removed via vacuum distillation. The solid crude product was vigorously stirred in 3 mL of water until a homogeneous suspension formed. After filtration and drying on air, product (3) (0.18 g; 0.32 mmol; 84%) was obtained as a colorless solid.

Step 4:

2,5-Bis(2-(4-pyridyl)-vinylene) hydroquinone dineopentyl ether (Np-P4VB) was finally synthesized following a Wittig-Horner-type reaction adapted from the methyl derivative. In a preheated Schlenk flask phosphonate (3) (0.19 g; 0.34 mmol; 1.0 eq.) and potassium tert-butoxide (0.12 g; 1.04 mmol; 3.0 eq.) were dissolved in dry tert-butanol (10.0 mL). To the resulting yellow-greenish mixture a solution of 4-formyl pyridine (0.10 mL; 0.12 g; 1.07 mmol; 3.1 eq.) in tert-butanol (1 mL) was added dropwise. During this addition, the solution turned brown and became fluorescent. The solution was then stirred at 60 °C overnight and subsequently poured into ice-cold water (100 mL). After filtration, the resulting solid was washed with 10 mL of water three times and then recrystallized from methanol to yield Np-P4VB (0.08 g; 0.18 mmol; 52%) as long needles exhibiting yellow fluorescence. Melting point 277 °C (decomp). EA calcd. C 78.91, H 7.95, N 6.13; found C 79.07, H 8.04, N 6.26 %. UV-Vis

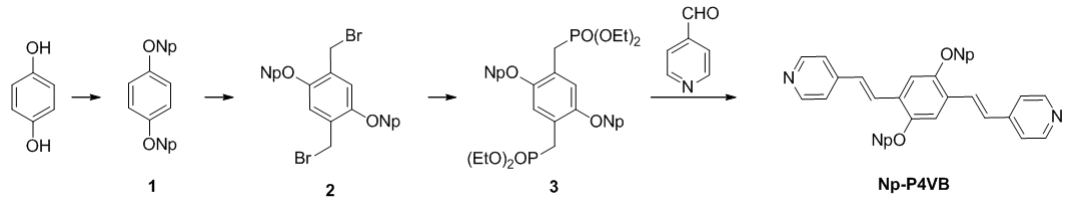

Figure A.2: Scheme showing the intermediate products during the synthesis of Np-P4VB. The products are numbered according to the step of the synthetic route. Step 4 shows the Wittig-Horner-type reaction which produces Np-P4VB.

($\lambda_{max}/\varepsilon$ (L·mol^{-1}·cm^{-1}) in CH_2Cl_2) 329 nm /22600, 401 nm /24900.

A.3.2 Preparation of dye solutions

Finally, the purified Np-P4VB was dissolved in dimethyl formamide (DMF) in order to prepare it for optical characterization. The concentrations varied from 0.05 mM to 4 mM with a measured saturation of 94.1 mM. In order to modify the electronic structure and optical properties of the Np-P4VB via protonation, we acidified the solutions by adding defined amounts of aqueous hydrochloric acid (HCl) solutions varying from 0.001 M to 12 M. In order to achieve the changes in electronic properties via the interaction with zinc ions, we added pure $Zn(NO_3)_2$ salt to concentrations varying from 1 mM to 3000 mM. Zn^{2+} was chosen as a solution dopant because it is not paramagnetic (often indicated by an unpaired electron), therefore laser quenching is minimized, and previous work has shown that the pyridinyl nitrogens chelate with zinc ions to form coordination frameworks [308].

A.3.3 NMR spectroscopy and other analytics

NMR spectroscopy was applied in order to confirm the structure of the intermediate products and of the goal compound Np-P4VB. ^{1}H NMR spectra were measured on Bruker AV-III 300 MHz spectrometer using deuterated chloroform as solvent for the intermediate products. Np-P4VB was analyzed in

CD_2Cl_2 to avoid overlapping of the residual solvent peak with the signals of aromatic protons of the compound. The signals in all spectra were referenced to the residual solvent peak (7.24 parts per million deviation in frequency for chloroform, and 5.30 ppm for CD_2Cl_2). The recorded spectra are in complete agreement with the respective structures shown in Fig. A.2. The details on the signals assignment are given in the supplemental information.

The structure of compound Np-P4VB was additionally confirmed by electron spray ionization mass-spectroscopic measurement using a Varian LC MS 500. Protonated molecular ion and doubly protonated molecular ion peaks along with a Na^+-adduct molecular peak were observed using acetonitrile (LC-MS grade) as solvent. C, H, and N elemental composition of Np-P4VB was determined at the central analytical facility of the Chemistry Department of TUM using either EA Euro 3000 (Kehatech) or Elementar Vario EL. The results are in good agreement with the values calculated for the structure in Fig. A.2.

A.3.4 Preparation of emissive polyelectrolyte films

The polyelectrolyte (PE) films were made from Np-P4VB (1 mM) dissolved in polyallylamine hydrochloride (PAH) dissolved in water (10 or 20 mg/mL) or polystyrene sulfonate (PSS) dissolved in water (20 mg/mL). Higher dye concentrations were also tested but these tended to lead to precipitation (cloudy solutions) and/or the formation of rough films. Lower concentrations worked fine in terms of film quality but are, obviously, less luminescent. We then followed a recipe similar to that developed in Ref. [323] for monolayer PE films. A drop of the PAH solution (20 mg/mL) was dropped onto a quartz wafer that was initially cleaned with concentrated NaOH solution. The droplet was immediately washed in pure water in order to leave a single PE layer bound to the surface. The orange films were produced by adding HCl to the PSS solution to a concentration of 0.01 M (hereafter called PSSo); the green ones were prepared similarly, but using $Zn(NO_3)_2$ (0.032 mM) instead of HCl (PSSg).

To produce the blue layers, NaOH was added to a PAH stock solution to a concentration of 0.01 M (PAHb). The blue-fluorescent sample consisted of PAH-(PSS-PAHb)×3; the green was (PAH-PSSg)×3, and the orange was (PAH-PSSo)×3. Finally the white film consisted of PAH-(PSS-PAHb)×4-PSS-(PAH-PSSo)×2-(PAH-PSSg)×2.

A.3.5 Absorption and photoluminescence spectroscopy

Absorption measurements were performed using a Hewlett-Packard 8452A Diode Array spectrophotometer, using a cuvette filled with the pure solvent as the blank. For photoluminescence (PL) spectroscopy we used the 405 nm ion line of a diode laser operated at an excitation power density of ~ 1250 W/m^2 as the excitation source. The PL was collected by an optical fiber (numerical aperture ~ 0.22) and directed to an Ocean Optics USB 2000+ miniature spectrometer. The efficiency of the system was corrected with either an Ocean Optics calibrated light source. Photographs of the polyelectrolyte layers were taken with a Canon Rebel T3i camera.

A.3.6 Photoluminescence dynamics

PL decay traces were taken using an Alphalas picosecond pulsed laser at a wavelength of 405 nm and nominal pulse length of 40 ps. The PL was collected using a fiber optic system, passed through a long-pass filter to remove scattered excitation light, and directed into a Becker-Hickl HPM-100-50 photomultiplier tube, which has a response time of ~ 100 ps. The decay traces were obtained using the SPC-130 module from Becker-Hickl.

A.3.7 Absolute quantum yield

AQY measurements were performed using a home-built integrating sphere. Blank or sample solutions were placed into a cuvette that was lowered into the integrating sphere on a magnetic holder. A 405 nm light emitting diode was used as the excitation source. The PL and excitation intensities were

captured through a fiber attached to the sphere and analyzed with a calibrated Ocean Optics spectrometer. The quantum yield was calculated via $AQY = (I_{PL,sample}–I_{PL,blank})/(I_{EX,blank}–I_{EX,sample})$, where I_{PL} is integrated photoluminescence intensity and I_{EX} is excitation intensity recorded inside the sphere. "Blank" measurements were taken with a cuvette filled with DMF only, whereas "sample" stands for the measured intensities with the dissolved sample present in the solution.

A.3.8 Lasing

Lasing from Np-P4VB dissolved in DMF was characterized using the double-cuvette laser cavity inside a PTI GL-302 dye laser. The first cuvette is contained in the main tunable laser cavity, while the second identical solution is used to further amplify the output (Fig. A.3). The dye laser cavity was pumped using the 337 nm output of a GL-3000 nitrogen laser operated at 3-4 Hz, with 1 ns pulses having an energy of ~ 20 μJ. The same mirror set was used for each sample, with a tiltable grating within the optical path used to tune the cavity to resonance. The Np-P4VB lasing output power was measured using a Gentec-EO Solo 2 monitor with a XLP12 thermopile, protected by an aluminum draft shield, which was allowed to stabilize for ten minutes before taking measurements.

The sample emission, if present, was attenuated using a neutral density filter or a set of polarizers and sent to the Ocean Optics miniature spectrometer, calibrated as described above. The spectrometer response function was measured to be 5 nm using the 442 nm line (bandwidth ~ 3 GHz) of a HeCd gas laser. Higher-resolution measurements were taken using a Santa Barbara Instruments Group (SBIG) ST-8 spectrometer with a tunable grating. The response function of this system was 63 pm, measured in the same way.

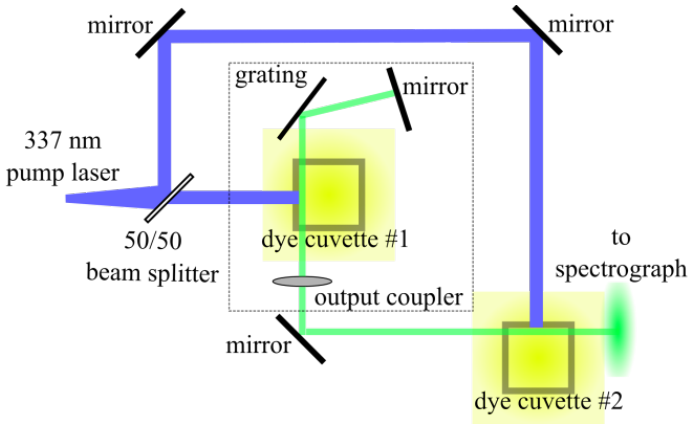

Figure A.3: Simplified diagram of the laser cavity setup. Cuvette #1 is placed in the tunable lasing cavity and is excited with 337-nm pulses from a nitrogen laser. The lasing output is directed through Cuvette #2 for further amplification before entering the spectroscopy system.

A.4 Results and discussion

The compound Np-P4VB was synthesized as described in the experimental section. The ^{1}H NMR and ESI-MS spectra (Fig. A.12-A.16) as well as the elemental analysis unambiguously verified the chemical structure shown in Fig. A.1(c). Crystallized from methanol, Np-P4VB formed agglomerations of long, prismatic needles (Fig. A.4) giving a yellowish–green fluorescence that peaked around 550 nm. When dissolved at a concentration of less than 2 mM in cyclohexane it instead took on a deep blue fluorescence; dissolved in dimethylformamide (DMF) the fluorescence appeared teal in color. Addition of other soluble impurities such as metal nitrates or acids caused the Np-P4VB to undergo a further dramatic color shift toward the green, yellow, or red, respectively (Fig. A.5).

The Np-P4VB featured two absorption bands at wavelengths depending on the solvent and dissolved additive. The short-wavelength absorption (peak 1) could be shifted from 324 to 366 nm, whereas the longer-wavelength one (peak 2) ranged from 393 to 460 nm (Fig. A.6, Table A.1). For acidified (orange-red fluorescent) solutions, the concentration-dependent changes became saturated at a 1:2 molar ratio of Np-P4VB to H^{+}, suggesting that double protonation

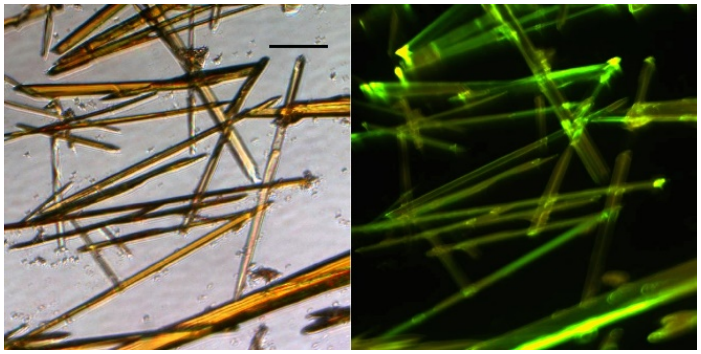

Figure A.4: Crystals of Np-P4VB in transmitted light (left) and fluorescence (right). The scale bar is 100 μm.

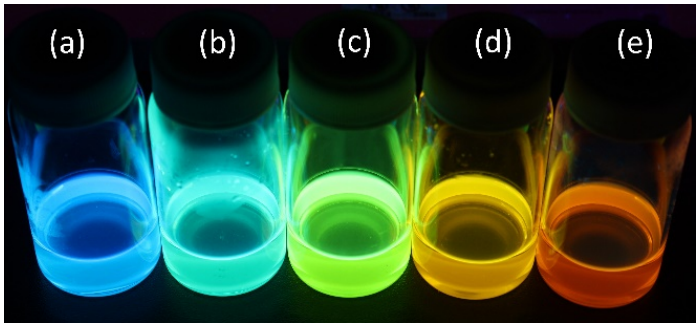

Figure A.5: Photograph of the Np-P4VB chromophore (2 mM) in solution taken under a black light (a) dissolved on cyclohexane (blue); (b) dissolved in DMF (teal); (c) dissolved in DMF with the addition of $Zn(NO_3)_2$ (green); (d) dissolved in DMF with the addition of $Hg(NO_3)_2$ (yellow); and (e) dissolved in acidified DMF (orange-red).

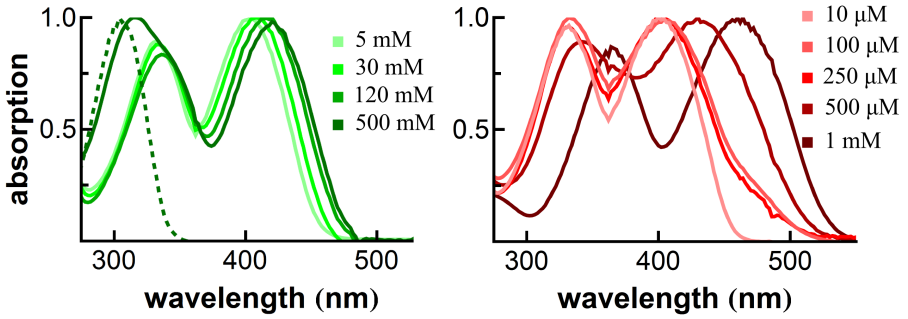

Figure A.6: a) Normalized absorption spectra of 0.07 mM Np-P4VB in DMF containing various concentrations of $Zn(NO_3)_2$. The dashed line shows the absorption of a 500 mM $Zn(NO_3)_2$ solution in DMF. b) Absorption spectra of Np-P4V in DMF with various concentrations of HCl.

(*i.e.*, one for each pyridine endmember) completes the shift. Significantly higher concentrations were required for other dissolved ions in order to achieve saturation (Fig. A.6), likely due to the reaction kinetics and equilibria that limit the concentration of the dissociated species.

The pure chromophore dissolved in cyclohexane was characterized by a broad, asymmetric fluorescence peaking at 451 nm (Fig. A.7(a); blue line). In DMF the fluorescence peaked at 475 nm (Fig. A.7(b); teal line). Upon addition of $Zn(NO_3)_2$ to a chromophore-DMF solution, the peak of the emission spectrum shifted to 537 nm (Fig. A.7(c); green) while dissolution of $Hg(NO_3)_2$ resulted in a fluorescence at 575 nm (Fig. A.7(d); yellow). Finally, the addition of an acid (*e.g.* hydrochloric, acetic, or nitric) led to a red-orange emission peaked at 591 nm (Fig. A.7(e)). The fluorescence absolute quantum yield (AQY) was 68%, 82%, 49%, 9%, and 25% for the blue, teal, green, yellow, and red solutions, respectively (Table A.1). The AQY excitation was the same in every case (405 nm) which aligns with the first absorption band of the blue and teal samples but was located between the emission bands for the other samples, thus likely populating different excited states from which a different AQY might not be surprising. For the $Hg(NO_3)_2$ in particular it was difficult to prevent crystallization even at fairly low concentrations; thus the especially low AQY in this case might be due to scattering from microcrystals

in solution [324].

The fluorescence lifetime, τ_{PL}, for each Np-P4VB solution showed a single-exponential decay (Fig. A.8(a)) with a time constant 1.5 to 3.1 ns (Table A.1). The radiative lifetime τ_R can be estimated for a two-level system (or one in which other transitions such as S2 $\longrightarrow$ S1 are fast) with $\tau_R = \tau_{PL}/AQY$, yielding 2.76, 3.02, 6.31, 16.56, and 11.32 ns for the blue, teal, green, yellow, and red emission (*i.e.*, increasing monotonically with emission wavelength). Since the emissive species is the same chromophore in each case, these changes can be expected on the basis of the increased mode density for shorter wavelengths according to Fermi's golden rule, possibly mediated by solvent effects such as refractive index or viscosity (for example, the visibly higher viscosity of the "nitrated" or acidified solutions are known to increase trans-cis photoisomerization-mediated lifetimes by restricting molecular rotation [325]). There was no appearance of a second lifetime component characteristic of exciplex formation. In contrast to similar compounds without the designed side-groups [326], these results suggest that the luminescence of Np-P4VB is essentially excimer-free single-molecule emission since there was no evidence of additional lifetime components or any significant concentration-dependent luminescence shifts.

Two absorption bands are a common feature of many conjugated organic chromophores and are likely related to two spin singlet states S1 and S2, where absorption and emission occur through the usual continuum of vibrational levels. The redshift upon addition of electron-withdrawing moieties can occur as a result of their interaction with the pyridine endgroups. Indeed, protonation of DSB derivatives leads to an increased delocalization of the LUMO across the whole molecule, which results in a lowering of the excited state energy [318] [327] [328] [329]. This process should also occur in Np-P4VB to a degree depending on the electron withdrawing ability of the additive.

As predicted, the emission color of Np-P4VB can be regulated by changing the electron withdrawing character of the solution, with the additional benefit of its extensive solubility and resistance to exciplex formation. As the sol-

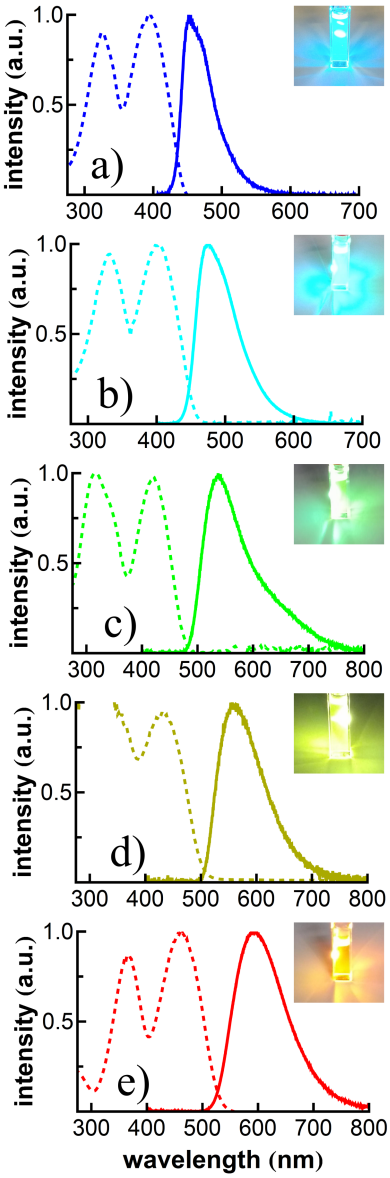

Figure A.7: Absorption (dashed) and photoluminescence (solid) spectra of Np-P4VB in (a) cyclohexane, (b) pure DMF, (c) DMF with 500 mM $Zn(NO_3)_2$, (d) DMF saturated (∼100 mM) with $Hg(NO_3)_2$, and (e) DMF with 500 mM HCl. The concentration of the chromophore for absorption measurements was 0.1 mM, while that for PL measurements was 2 mM (0.7 mM for cyclohexane). The insets show photographs of the luminescence corresponding to the spectrum for each panel.

vent becomes more polar or Lewis-acidic the electrons become more strongly delocalized, causing a decrease in emission energy. Thus, the transition from cyclohexane to DMF corresponds to a solvent polarity index increase from 0.2 to 6.4 and the fluorescence shifts from blue to teal. Adding $Zn(NO_3)_2$ or $Hg(NO_3)_2$ increases the Lewis acidity and shifts the emission to green or yellow, respectively. Addition of an acid (HCl, HNO_3, or CH_3COOH) leads to an even stronger effect, with the emission becoming orange or red. The fluorescence of Np-P4VB can therefore be tailored or designed throughout the visible spectrum simply by changing the chemical surroundings.

These combined properties suggested that this chromophore may be an excellent color-controlled lasing candidate. Clear evidence of lasing appeared in the emission spectra under 337-nm pulsed excitation in the laser cavity described in Section A.3.8 (Fig. A.8(e)-A.8(f)). For 2 mM Np-P4VB solutions (0.7 mM for cyclohexane), the output pulse powers under nominal 1650 μJ excitation pulses were 400 μJ, 286 μJ, 123 μJ, and 30 μJ, for blue, teal, green, and red laser emission, respectively. Only the yellow solution did not lase, due to a combination of low AQY and the formation of microcrystals and eventual precipitation at relatively low concentrations. The lasing was characterized by an intense emission above a pump threshold (Fig. A.8(c)) of $\sim 115-130$ μJ/cm^2 (from measurements on new solutions taken several months apart), a linewidth limited by the measured spectrometer response function (63 pm), and a beam divergence of 4.0 mrad. The optimum chromophore concentration was 1.4 mM in order to achieve the highest intensity teal output pulses (Fig. A.8(b)). At lower concentrations, the decreasing amount of gain medium increases the threshold, whereas at higher concentrations both increased absorption/scattering and intermolecular interactions typically decrease the output power of organic chromophores [330] [331]. That the lowest threshold was obtained for the teal lasing may be due to the especially good match between the absorption and the pump laser emission for that case.

In addition to this wide lasing color range, the Np-P4VB is also tunable within each color band by changing the cavity resonant wavelength (Fig.

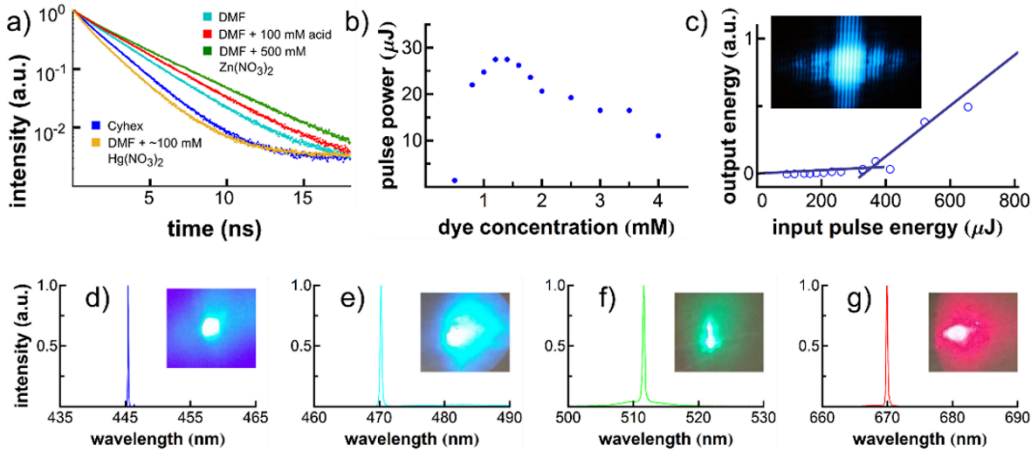

Figure A.8: (a) Lifetimes of pure, HCl (acid) doped, and $Zn(NO_3)_2$ doped solutions of Np-P4VB (3 mM). The small "blip" at $\sim$ 10 ns is a PMT afterpulse. (b) Output pulse power of various concentrations of Np-P4VB in DMF. (c) Threshold behavior of 2 mM solution of Np-P4VB in DMF when stimulated at 337 nm by an N_2 laser. The inset shows a double-slit interference pattern from the laser emission. Panels (d), (e), (f), and (g) show the Np-P4VB laser emission wavelengths for blue (0.7 mM Np-P4VB in cyclohexane) teal (2 mM Np-P4VB in DMF), green (2 mM Np-P4VB/DMF with 500 mM $Zn(NO_3)_2$), and red lasing (2 mM Np-P4VB/DMF with 0.1 M HCl) solutions.

Emission	**Abs (nm)**	**PL (nm)**	**AQY**	τ **(ns)**	$\mathbf{P}_{Th}$ **(μJ/cm^2)**
Blue	324,393	451	68%	1.88	240
Teal	330,403	475	82%	2.48	120
Green	—,419	537	49%	3.09	320
Yellow	—,430	575	9%	1.54	—
Red	366,460	591	25%	2.83	330

Table A.1: Summary of Np-P4VB absorption and emission properties. The first absorption peak in the green and yellow emission was overwhelmed by the nitrate absorption.

A.9(a)). The blue lasing can be tuned from approximately 442 to 477 nm, teal from 465 to 495 nm, green from 505 to 514 nm, and the red from 640 to 705 nm, representing the widest in-situ color range so far reported for any single laser gain medium. Moreover, if the Np-P4VB is tuned to 442 nm for blue, 514 nm for green and 700 nm for red, a vast range of the Commission Internationale de l'Éclairage (CIE) color space is enclosed (Fig. A.9(b)). The color space achievable from lasing Np-P4VB is much larger than that of the standard RGB (sRGB; 39.5% coverage) and has an area virtually equivalent to that of Adobe's wide-gamut RGB color space (77.6% coverage).

What gives Np-P4VB such a huge range of the visible color spectrum? One key aspect is the addition of the neopentyl sidechains to the P4VB base molecule, thus sterically shielding the conjugated molecular backbone. This both increases its solubility up to 94 mM in DMF (19 mM in ethanol) and prevents the aggregate formation. Aggregation leads to inter-molecular exciplex formation, causing a transition to dimer emission which can severely limit the achievable lasing wavelengths. An obvious additional benefit of the P4VB molecule lies in its end-group reactivity. While in this work we demonstrated only RGB lasing within a set of wavelength ranges for each color, we believe that the designing the Lewis acidity of the solvent could allow Np-P4VB or other similarly-engineered chromophores to fluoresce or lase at virtually any wavelength in the visible spectrum and beyond.

There are several advantages of a single wide-spectrum lasing compound.

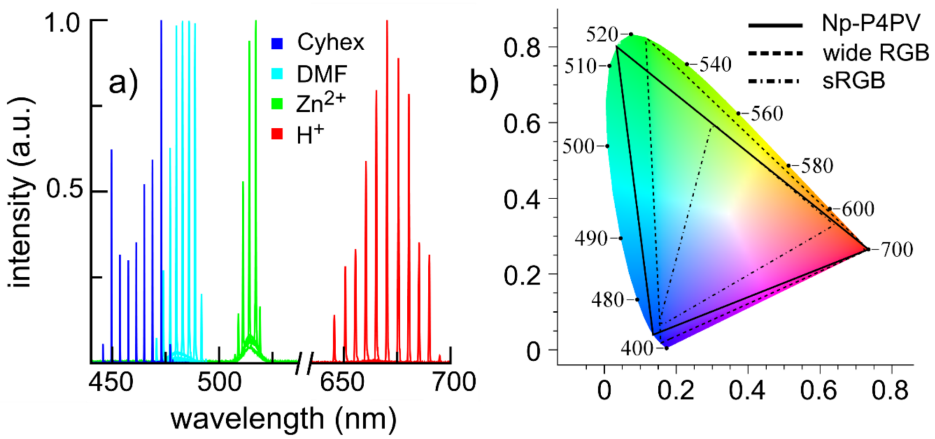

Figure A.9: (a) Lasing wavelengths for Np-P4VB in DMF achievable by tuning the laser cavity. The lasing intensity was normalized across the different groups for ease of visualization. (b) CIE 1931 chromaticity diagram showing the achievable color space from the Np-P4VB laser tuned optimally for 442 nm, 514 nm, and 695 nm, compared with the (Adobe) Wide Gamut RGB and the standard RGB color spaces.

Incorporating the various solutions into a polymer or polyelectrolyte would permit fluorescence (and possibly lasing) with extensive color control, presenting a considerable simplification over the processing required for different chromophore-polymer mixtures. While for imaging and sensing applications a solution-based and widely tunable fluorescent or lasing medium is of course of interest, for most light emission applications one needs a solid medium. Here we demonstrate color-controlled molecular layers emitting over a range of the color spectrum including white (Fig. A.10). In each case the emissive region is a Np-P4VB-doped monolayer of polyallylamine hydrochloride (teal) or polystyrene sulfonate (green-yellow and red-orange; see experimental). Stacking these layers allows a wide emissive color gamut to be obtained, which is controlled by the number of layers of each color. These results imply that white emission, or indeed, almost any color, can be achieved in solid as well as liquid media using a single emissive chromophore.

This work demonstrates extensive lasing color control over a range of wavelengths that can encompass almost the entire CIE color space. The protective sidegroups and accessible pyridine endgroups can combine a good absolute

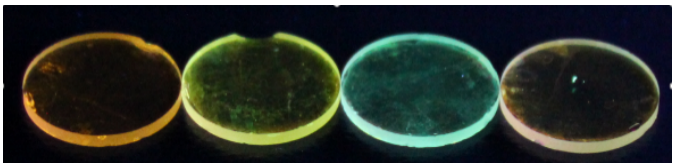

Figure A.10: Photograph (raw unprocessed data) of red-orange, yellow-green, teal, and white polyelectrolyte bilayer films containing dissolved Np-P4VB. A hand-held overhead blacklight was used for excitation. Corresponding PL spectra are shown in Fig. A.11. The wafers are 1 cm in diameter.

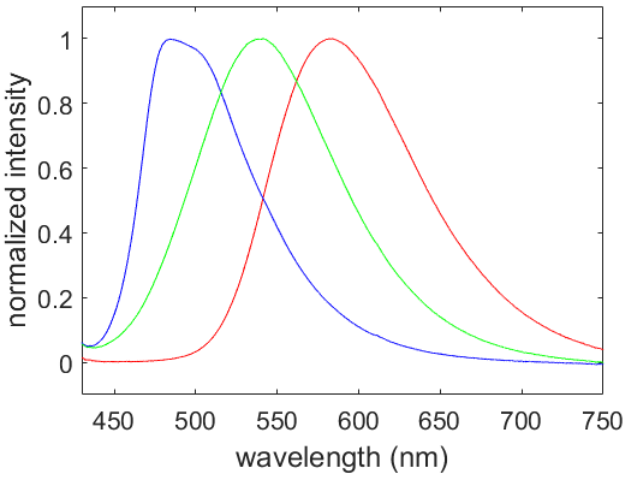

Figure A.11: Normalized photoluminescence spectra of the teal, green-yellow, and orange polyelectrolyte films.

quantum efficiency, high solubility, and minimal inter-molecular interactions, while permitting a large degree of energy-level control. The same concepts could almost certainly be applied to other organic systems to contrive massively tunable fluorescence and lasing. Of course, organic chromophores and especially the PPV-based polymers can have problems with photo-oxidation and triplet formation, which implies that the lasing will degrade over time. No noticeable degradation was observed in the solution samples after 30 minutes of lasing action (at 10 Hz), but highly viscous solutions made by the addition of polymer did show photobleaching and quenching of the lasing output. However, these issues might be minimized or even prevented via the addition of auxiliary compounds that block triplet formation, as shown for related PPV structures [332].

In summary, we demonstrate a molecular engineering blueprint for designing chromophores featuring a high solubility, high quantum efficiency, and a molecular structure that allows unprecedented energy level tunability via solvent interactions. The designed chromophore chosen to illustrate these concepts lases across almost all of the visual color spectrum as a consequence of simple Brønsted/Lewis acid-base interactions. Only complex and expensive nonlinear devices such as parametric amplifiers can currently match this method for such extensive laser wavelength control.

A.5 Acknowledgements

The authors thank DFG (IRTG 2022) and NSERC (CREATE grant 463990-2015) for financial support of the Alberta/Technische Universität München Graduate School for Functional Hybrid Materials (ATUMs).

A.5.1 Conflict of interests

The authors declare no conflict of interest.

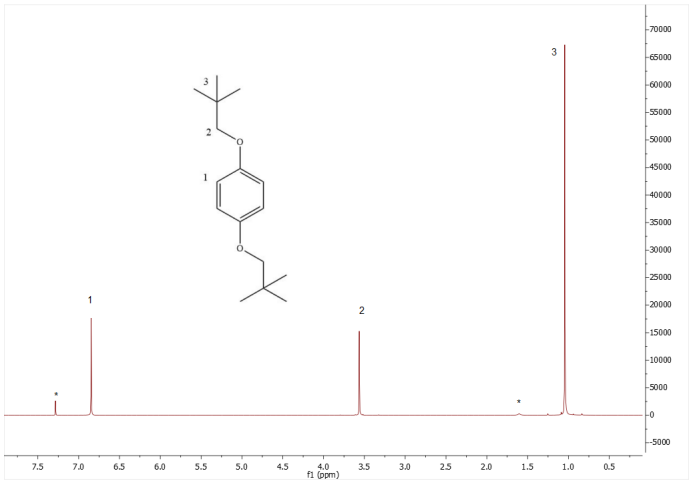

Figure A.12: Compound 1: ^{1}H-NMR (300 MHz, $CDCl_3$, 300 K): δ (ppm) = 6.85 (s, 4H, Harom), 3.56 (s, 4H, -CH_2), 1.04 (s, 18H, -CH_3). Signals of solvent impurities ($CHCl_3$, H_2O) are marked with asterisk.

A.5.2 Contributions

SL, SV, and AM contributed to all aspects of the work, conceived the experiments, and wrote the paper. SV led the synthesis and the optics work was done mainly by SL. WH contributed to the synthesis of the chromophore and the methods used therein. WM contributed to the chromaticity analysis. BR contributed to the concept behind the work, contributed to the MS, and made enabling contributions to the project. HW and YZ assisted with some experiments.

A.6 Supplemental information

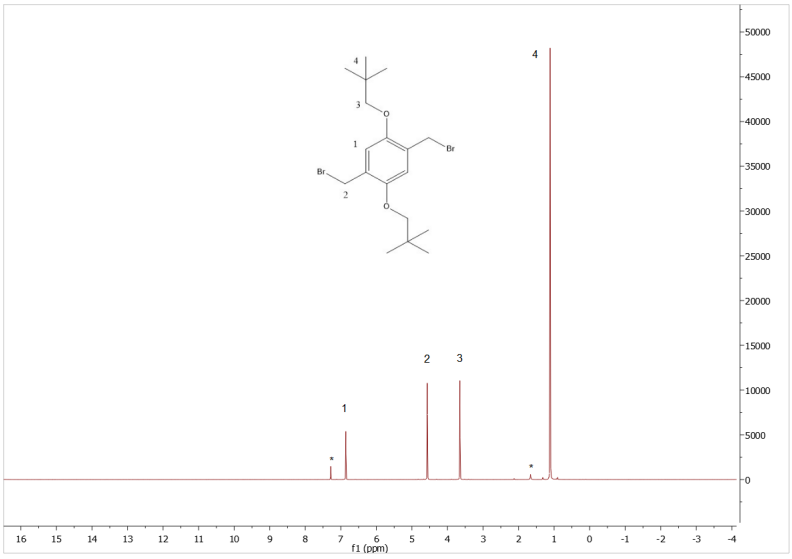

Figure A.13: Compound 2: ^{1}H-NMR (300 MHz, $CDCl_3$, 300 K): δ (ppm) = 6.86 (s, 2H, Harom), 4.57 (s, 4H, -CH_2Br), 3.65 (s, 4H, -OCH_2), 1.11 (s, 18H, -CH_3). Signals of solvent impurities ($CHCl_3$, H_2O) are marked with asterisk.

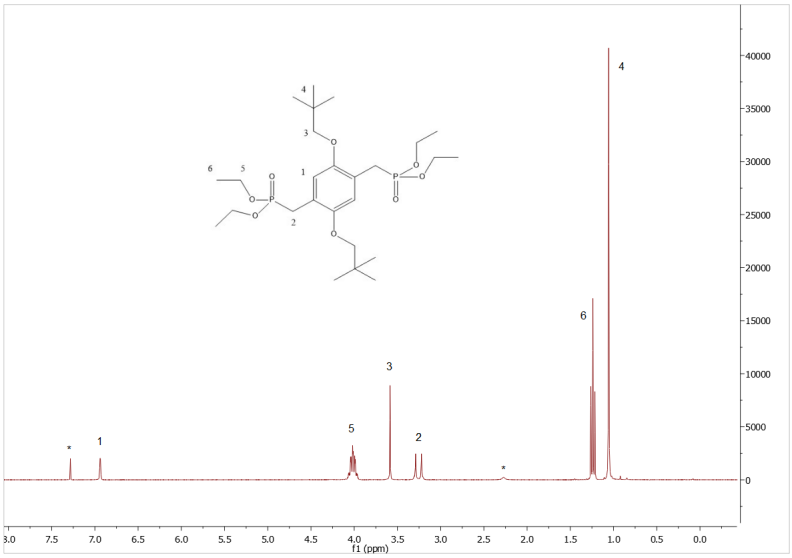

Figure A.14: Compound 3: ^{1}H-NMR (300 MHz, $CDCl_3$, 300 K): δ (ppm) = 6.95 (s, 2H, Harom), 4.09 – 3.96 (m, 8H, -OCH_2CH_3), 3.59 (s, 4H, -OCH_2), 3.26 (d, $^{2}J_{H-P}$ =20.3 Hz, 4H, -CH_2P), 1.25 (t, $^{3}J_{H-H}$ = 7.1 Hz, 12H, -OCH_2CH_3), 1.06 (s, 18H, -CH_3). Signals of solvent impurities ($CHCl_3$, H_2O) are marked with asterisk.

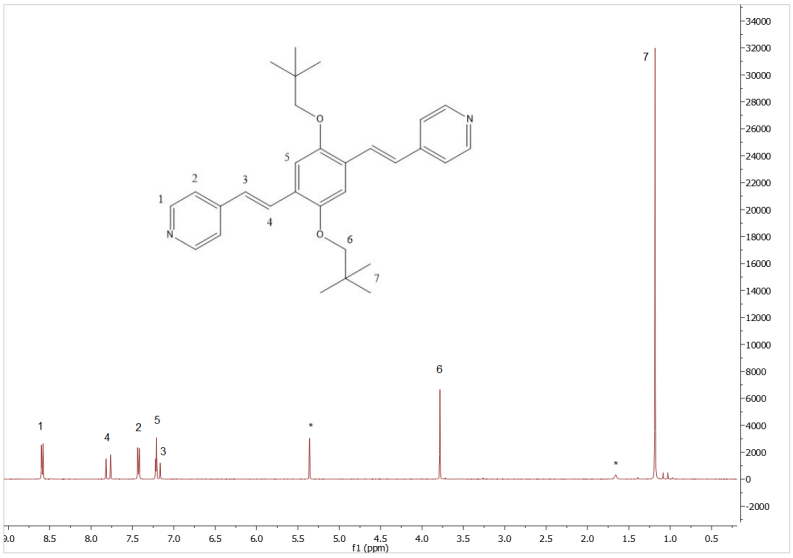

Figure A.15: Compound Np-P4VB: ^{1}H-NMR (300 MHz, CD_2Cl_2, 300 K): δ (ppm) = 8.55 (d, 3J = 6.2 Hz, 4H, $py - H_{ortho}$), 7.75 (d, ^{3}J = 16.5 Hz, 2H, inner vinylene H), 7.39 (d, ^{3}J = 6.2 Hz, 4H, py-H_{meta}), 7.17 (s, 2H, -CH_{arom}), 7.15 (d, ^{3}J = 16.5 Hz, 2H, outer vinylene H), 3.75 (s, 4H, -OCH_2), 1.15 (s, 18H, -CH_3). Signals of solvent impurities ($CHDCl_2$), H_2O) are marked with asterisk.

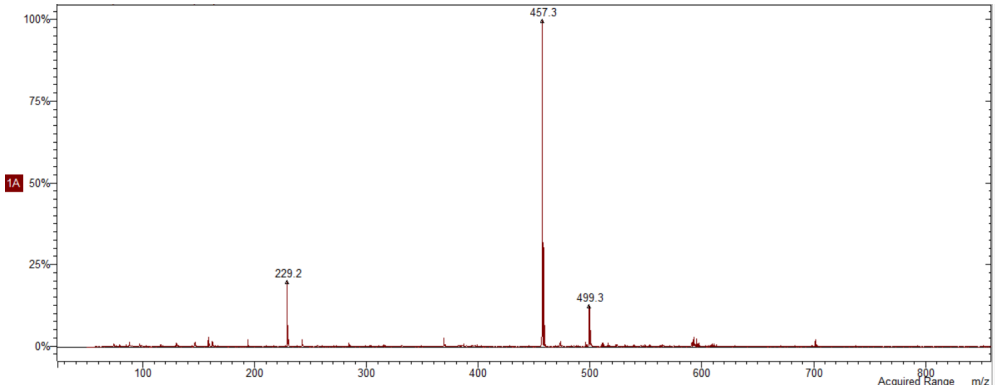

Figure A.16: Compound Np-P4VB: ESI-MS (MeCN): 229 $[M+2H]^{2+}$, 457 $[M+H]^{+}$, 499 $[M+Na]^{+}$.